
On the Dynamics of Cytoskeletal Filaments

Filament Regulation by Molecular Motors and Nucleation

Louis Reese



München 2014

On the Dynamics of Cytoskeletal Filaments

Louis Reese

Dissertation
an der Fakultät für Physik
der Ludwig-Maximilians-Universität
München

vorgelegt von
Louis Reese
aus Penzberg

München, den 17. Februar 2014

Erstgutachter:

Prof. Dr. Erwin Frey (Ludwigs-Maximilians-Universität München)

Zweitgutachter:

Prof. Dr. Thomas Franosch (Universität Innsbruck)

Tag der mündlichen Prüfung: 27. Juni 2014

Preface

Zusammenfassung

Das ZYTOSKELETT ist ein Netzwerk bestehend aus Protein Filamenten im Inneren eukaryotischer Zellen. Dieses Netzwerk ist in vielerlei Hinsicht heterogen, sowohl bezüglich seiner physikalischen Eigenschaften als auch in Bezug auf die Bausteine aus denen es besteht. Es gibt drei verschiedenen Klassen von Zytoskelett Filamenten: Mikrofilamente oder auch Aktin Filamente genannt, Mikrotubuli, und Intermediärfilamente. Jede dieser Klassen ist für eine Vielzahl bestimmter Aufgaben in der Zelle zuständig, und an diese Aufgaben spezifisch angepasst. Intermediärfilamente stabilisieren die Zelle mechanisch und bilden ihr Gerüst. Mikrotubuli dienen als Autobahnen für molekulare Motoren um Material und Organellen zu transportieren. Mikrotubuli fungieren auch als makromolekulare Maschinen, weil sie durch Polymerisation und Depolymerisation Kräfte erzeugen. Diese dienen zum Beispiel während der Zellteilung dazu die Chromosomen zu trennen. Auch Aktin Filamente können Kräfte erzeugen, dabei spielt die Polymerisation der Filamente eine entscheidende Rolle. Der Polymerisationsprozess von Aktin wird von vielen Proteinen koordiniert. Diese Proteine erwirken zum Beispiel dass Aktin Filamente verschlaufte Netzwerke bilden, die großen Kräften widerstehen können. Im Kollektiv erzeugen Aktin Filamente genügend Kraft um Zellen vorwärts zu bewegen und um die Form einer Zelle zu bestimmen.

Die dynamischen Eigenschaften des Zytoskeletts werden durch verschiedenste Enzyme beeinflusst und gesteuert. Dabei unterscheidet man zwischen Signalproteinen die regulatorische Aufgaben übernehmen, und Enzymen die direkt Bausteine des Cytoskeletts beeinflussen. Einige dieser Enzyme werden im Lauf dieser Arbeit vorgestellt. Grob kann zwischen zwei Klassen von Proteinen unterschieden werden: Manche Proteine sind für die Nukleation von Filamenten zuständig, während andere deren Dynamik verändern in Form von Polymerisations- oder Depolymerisationsraten. In dieser Arbeit werden spezifische Prozesse studiert, die zu den erwähnten Aufgaben beitragen:

Das erste System welches untersucht wird sind molekulare Motoren die

Mikrotubuli depolymerisieren. Diese Proteine gehören zur Familie der molekularen Motoren Kinesin-8.

Das zweite System das studiert wird ist die Nukleation von Filamenten. Dabei wird kein spezielles Protein betrachtet sondern es wird versucht ein möglichst allgemeingültiges, effektives Modell zu entwickeln.

Mikrotubuli sind Polymere die einer dynamischen Instabilität unterliegen. Die Filamente schalten stochastisch zwischen einem wachsenden und einem schrumpfenden Zustand hin und her. Dieses Phänomen ist durch GTP Hydrolyse angetrieben. Eine Fülle von Proteinen in der Zelle binden an Mikrotubuli und beeinflussen deren Dynamik. Eines dieser Proteine ist der molekulare Motor Kinesin-8, welcher aus der Klasse der Motorproteine heraussticht: Erstens, Kinesin-8 kann einen Mikrotubulus depolymerisieren. Zweitens, wenn Kinesin-8 Proteine an das Mikrotubulus binden und beginnen zu laufen, dann können die Motoren unter entsprechenden Bedingungen einen Stau ausbilden. Um diese Beobachtungen zu quantifizieren wurde in dieser Arbeit ein Gittergas Modell entwickelt welches ausschliesslich auf den mikroskopischen Eigenschaften der Motoren beruht.

Das Modell bestätigt experimentelle Ergebnisse und erlaubt Vorhersagen über die bisher bekannten Phänomene hinaus. In der darauffolgenden Arbeit im Rahmen dieser Dissertation, wurde dieses minimale Modell erweitert um mögliche Mechanismen aufzudecken, die zur Längenregulation von Mikrotubuli durch molekulare Motoren beitragen. In Abhängigkeit davon, ob Kinesin-8 den Anbau von Tubulin Dimeren verhindert oder nicht, ergibt sich unterschiedliches Verhalten bezüglich der Längenfluktuationen im Modell. Für den Fall das ein Mikrotubulus unabhängig von Motoren an der Spitze wächst, stellt sich eine feste Länge ein. Für den Fall, das Kinesin-8 den Anbau von Tubulin verhindert, ergibt sich eine stochastische Dynamik von zufälligem hin und her schalten zwischen Wachsen und Schrumpfen des Mikrotubulus. Dabei wird das Phänomen der Phasenkoexistenz beobachtet und zwar als eine stochastische Bistabilität.

Die Analyse mittels einer Molekularfeldnäherung zeigt den Ursprung des spontanen Wechsels zwischen den unterschiedlichen Phasen. Zudem wird aufgeklärt wie aus den mikroskopischen Details des Modells auf makroskopische Eigenschaften des Systems geschlossen werden kann.

Der zweite Teil dieser Dissertation widmet sich dem Thema der Nukleation von Filamenten im Allgemeinen und von Aktin Filamenten im Besonderen. Die Nukleationsreaktion dieser Filamente stellt einen kinetischen Engpass dar, der dazu führt das es sehr unwahrscheinlich ist das ein Filament

entsteht: Aktin Dimere und Trimere sind sehr instabil und haben somit eine sehr kurze Lebenszeit, etwa in der Größenordnung von 10^{-8} Sekunden. In der Zelle wird dieser Engpass umgangen, indem spezielle Nukleationsproteine die Dimere und Trimere stabilisieren. In der vorliegenden Arbeit wurde ein Modell entworfen, welches beide Möglichkeiten – den Engpass und die Nukleation mittels Helferproteinen – berücksichtigt.

Durch umfangreiche stochastische Simulationen mit einem finiten Vorrat an Aktin Monomeren konnte die Bedeutung des Engpasses für die Nukleationsreaktion untersucht werden. Als Parameter wurden dabei die Zerfallsraten von Dimeren und Trimeren gewählt. Die Filamente wurden als eindimensionale Brown'sche Bewegung modelliert um bei einer möglichst einfachen Beschreibung zu bleiben.

Im stationären Zustand lassen sich drei Phasen unterscheiden, die je eine unterschiedliche Phänomenologie aufweisen. Für den Fall stabiler Dimere und Trimere sind alle Monomere gebunden, und es steht kein Material zur Verfügung für Wachstum einzelner Filamente. Diese Phase läßt sich als Kondensation in Dimere und Trimere verstehen.

Im Gegensatz dazu entsteht für den Fall instabiler Dimere und Trimere genau ein Filament, welches aus allen verfügbaren Monomeren besteht. Zwischen diesen beiden Phasen, für mittlere Lebzeiten der Dimere und Trimere, existiert ein stationärer Zustand mit einer konstanten Anzahl von Filamenten. Eine heuristische Analyse führt zu Skalengesetzen welche die unterschiedlichen Phasen voneinander abgrenzt.

Diese Ergebnisse erklären qualitativ die exponentielle Längenverteilung von Aktin Filamenten *in vitro* und warum *in vivo* die Filamente kurz und dynamisch sind. Eine sorgfältige Analyse und Quantifizierung des Modells steht jedoch noch aus, da im Moment die notwendigen Ratenkonstanten noch nicht gemessen werden konnten.

Synopsis

THE CYTOSKELETON is a network of protein filaments inside eukaryotic cells. This network is heterogeneous with respect to several of its properties and constituents. There are three classes of cytoskeletal filaments: microfilaments (actin filaments), microtubules, and intermediate filaments. Each of these classes obeys many particular tasks in the cell, for which they are ideally suited. Intermediate filaments provide mechanical scaffolding and support. Microtubules serve as intracellular tracks enabling molecular motors to deliver cargoes to or from the peripheries. Microtubules also function as macromolecular machines that tear sister chromosomes apart during cell division via depolymerization. This is in contrast to actin filaments which exert forces by polymerization. The polymerization process of actin filaments is orchestrated by nucleation factors and a plethora of enzymes. The resulting meshwork of filaments generates forces – strong enough to drive cell motility and cell shape changes.

The assembly and disassembly of the cytoskeleton is performed by different proteins. One has to distinguish between signaling proteins that regulate upstream of the physical changes of filaments, and the enzymes that actually modify the filaments. Many of these enzymes are known for actin filaments and microtubules, and some of them are subject of this work. The proteins available in the cytoplasm to provide enzymatic regulation of filaments can be roughly divided into two classes: There are proteins that influence filament nucleation, and proteins that influence the dynamics of filaments. There is a large variety in each of these types of protein factors, where some of them are molecular machines that consume ATP and others are enzymes that lower the activation energy for a process. In this work two specific of the above mentioned processes are studied. The first system investigated is the microtubule depolymerizing molecular motor kinesin-8. The second system studied is the nucleation of filaments.

Microtubules are rigid, tube-like polymers that stochastically switch between growth and shrinking. This dynamics is called microtubule dynamic instability. It is driven by GTP hydrolysis which enables microtubule polymers to push and pull against loads. There is a plethora of proteins in the cell that control the fate of microtubules. One of these enzymes is the molecular motor kinesin-8. There are two reasons that render this motor protein special and stand out from other kinesin motors. First, it depolymerizes microtubules by tightly binding to tubulin heterodimers and breaking them apart at the lattice end. Second, when bound to the microtubule lattice,

kinesin-8 motors interact via hard core exclusion and form traffic jams. To account for this behavior, a driven lattice gas model is developed. Building on data from *in vitro* depolymerization experiments with kinesin-8, the relevant rate constants are quantified with respect to the motor properties and microtubule depolymerization. The model confirms that kinesin-8 depolymerizes microtubules in a length-dependent manner due to the linear increase in motor density along the microtubule lattice. We identify this effect to lie in a density limited regime, and compare it to a rate limited regime for slowly depolymerizing motors. The two regimes can be interpreted as different phases of traffic in the system. In subsequent work we extend this minimal model for depolymerization towards a model for length-regulation of microtubules with kinesin-8. Depending on whether kinesin-8 inhibits the addition of tubulin dimers or not, the system shows strikingly different behavior: accurate length-regulation is achieved if growth of the filament is independent of the presence of kinesin-8 at the tip. This is in stark contrast to the situation when kinesin-8 inhibits microtubule growth while bound to the tip. In the latter case the system displays intermittent dynamics and coexistence of phases of different traffic. The analysis within a mean-field approach reveals the particular phase structure of the process and shows that switching between phases is driven by motor density fluctuations at the microtubule tip. Within the theoretical description obtained in this work, it is possible to distinguish different microscopic scenarios from macroscopic observations as made in experiments.

The second part of this work is on the nucleation of filaments, in particular actin filaments. These are known to have a nucleation „bottleneck“, which means that the formation of a filament from dimeric and trimeric actin is very unlikely. The mechanism behind this is that the latter oligomers are very unstable molecules and their lifetime is extremely short, of the order of 10^{-8} seconds. In the cell, however, this bottleneck is resolved with the help of nucleation proteins that largely stabilize the precursors of actin filaments. Most prominently the ARP2/3 complex has multiple binding sites for actin monomers and is considered a key enzyme for activating actin nucleation by stabilizing actin dimers and trimers. Within this work, a model is defined that captures both of the above mentioned cases and lays out a possible role for nucleation bottlenecks. Extensive stochastic simulations were performed with a finite amount of monomers in a small volume to mimic the situation of a cell or a cellular compartment. For simplicity, a filament is assumed to perform a random walk. The system is investigated systematically with respect to the decay rates, *i.e.* the lifetimes of dimers

and trimers, and the amount of available monomers. As a result the dynamic behavior of filaments can be classified into three different phases. For stable dimers and trimers all monomers are sequestered and no monomers are available for the growth of filaments. For unstable dimers and trimers one filament will emerge and contain all the available monomers. For intermediate dimer and trimer lifetimes a dynamic steady state evolves. Therein as many filaments nucleate *de novo* as filaments dissolve. A heuristic analysis reveals scaling laws for the different regimes. From a phenomenological perspective, these results explain the existence of long and exponentially distributed filaments *in vitro* and why *in vivo* filaments are short and dynamic. A thorough quantification of these results, however has yet to be achieved because experimentally measured rate constants are not available at the moment.

*Men love to wonder, and that is
the seed of science.*

Ralph Waldo Emerson

Die letzten Momente eines Lebensabschnitts. Die Musik ist gut und Entspannung tritt ein. Bald ist es vollbracht, Täler durchschritten Berge genossen und überwunden. Zeit für einen shout-out. An Alle die mich auf meinen Wegen in den letzten Jahren begleitet haben.

Zuallererst gilt mein Dank Erwin Frey. Dafür das dieser Platz ein Ort der Kreativität ist. Dafür das an diesem Ort soviel Freiheit und Entfaltung möglich ist. Dafür das sich hier immer wieder eine erstaunliche Gruppe junger Menschen zusammenfindet. Und dafür das diese Seiten unter vollster Zufriedenheit des Verfassers, *i.e.* mit einem Lächeln auf den Lippen, zu Ende gebracht werden können. Vielen Dank Erwin für Dein Vertrauen, Deine Inspiration, Deine Unterstützung, und Dein Verständnis das Du mir in den letzten Jahren entgegengebracht hast.

Mein Dank gilt Anna Melbinger. Immer genau dann wenn es wichtig war warst Du da. Ich erinnere mich an den Schafreiter im letzten Sommer - lächelnd. Vielen Dank für Deine Freundschaft, Anna. Vielen Dank für unsere fruchtbare Zusammenarbeit in den letzten Jahren.

Mein Dank gilt Matthias Rank und Emanuel Reithmann. Welch ein Vergnügen hat es mir bereitet mit Euch zu diskutieren und zusammenzuarbeiten! Vielen herzlichen Dank dafür.

Ich danke Alvaro Crevenna. Dear Alvaro, venturing at the edge of actin nucleation with you was incredibly exciting. Thank you for the many exciting discussions we had and your openness and appreciation of a theorist's - sometimes awkward - ideas.

Ich danke Don Lamb. Für die Zeit die ich in seiner Arbeitsgruppe verbringen durfte und das Vertrauen mich in seinem Labor experimentieren zu lassen.

Im Laufe der letzten Jahre hatte ich Gelegenheit zu Diskussion mit einer Handvoll Personen welche mein Denken über Motorproteine in interessante Bahnen gelenkt haben. Ich bedanke mich bei Dr. Cécile Leduc, Dr. Thomas Surrey, und Dr. Christian Tischer.

I thank the Physiology Class of 2013! You guys liberated my scientific spirits – incredible – Thank you!

Ich möchte mich außerdem bei Marilena Pinto und Beate Köhler bedanken, für die richtigen Worte zur richtigen Zeit. Bei Criss Hohmann bedanke ich mich für ein fantastisches Biophysical Journal Titelblatt.

In den letzten Jahren habe ich es unglaublich genossen Teil einer so herzlichen und offenen Arbeitsgruppe zu sein, dem LS Frey. Herzlichen Dank an Alle dafür. Mein Besonderer Dank geht an meine Bürokollegen Christoph Weber und Jacob Halatek für die gemeinsame Zeit.

Mein Dank gilt auch all jenen die sich mit der Korrektur dieser Arbeit beschäftigt haben, Michael Brunnhuber, Alexander Buchner, Patrick Hillenbrand, Monika Hochholzer, Anna Melbinger, Olav Stetter, Anton Winkler. Zu besonderem Dank verpflichtet bin ich Emanuel Reithmann und Matthias Rank, deren Anregungen weit über Korrekturen hinaus gingen.

Begleitet auf meinem Weg. Da denke ich an Simon, an Jan mit Caro und Felix. Und auch an Michal mit Teresa und Maya. Irgendwie müsst Ihr jetzt hier stehen. Ich danke Euch.

Besonders bedanken möchte ich mich auch bei meinen Mitbewohner auf dem Walserhof. Eure Unterstützung war grandios. Bernhard – für die Musik, Nadine, Marius, Monika, Marlene, Didi, Felix, Sebastian, Julia, und Josef und Johanna – für das Sein.

Mein herzlicher Dank für eine stete Begleitung und Fürsorge gilt meiner lieben Tante Hanni.

Zu Guter letzt möchte ich mich bei meinen Eltern und meiner Schwester Nadine bedanken. Für Eure immerwährende Unterstützung. Dafür das Ihr mein Ruhepol seid. Meine Kraftquelle zu jeder Zeit. Danke das Ihr da seid.

At the beginning of this Thesis, I briefly summarize each of its chapters and outline their contents. Further, I wish to make a statement on key ideas that were contributed from others to this work. Also, I would like to clarify my contributions to the work carried out by students I had the opportunity to supervise.

Chapter 1. In this chapter I lay out my current personal view on the cytoskeleton field from a perspective of theoretical modeling and physics understanding. I try to describe different approaches to address biological questions employing methods from mathematics and physics. Also I span a model-space constituted from a set of components including actin, and microtubules and their respective interactions with nucleation factors and molecular motors. To this end the molecular players – the proteins involved – are introduced.

Chapter 2. In the second chapter I present a theoretical approach to *driven lattice gases* that allows to understand collective effects in molecular motor traffic. This is a central theme throughout this work. Particles move along a lattice with on-site exclusion and towards the lattice end. This dynamics is called *totally asymmetric simple exclusion process* (TASEP). Such systems have been studied extensively over the last two decades, and only recently the system has been extended to incorporate lattice dynamics. The methods that allow to obtain a solution for the particle density profile and the phase diagram are explained, and quantities of interest are discussed. The procedure presented in this chapter can be utilized in general to analyze systems with both, lattice dynamics coupled to molecular motors.

Chapter 3. The third chapter constitutes the core of this thesis. I introduce a very general model for molecular motors and how they interact with microtubule ends. Starting from this model which includes seven different rate constants, I will explain the role each parameter plays in regulating filament dynamics. Subsequently the model is cut into several, more manageable, pieces that allow to understand the emerging phenomena bit by bit in terms of stochastic simulations and analytic theory. As a result, this approach leads to a comprehensive picture of different scenarios. Each of these scenarios constitutes a separate motif – or functional unit. And each of these units ensues a particular prediction for the behavior of motors and microtubules. The perspective obtained in this chapter provides a thorough

understanding of the relevant processes for microtubule length-regulation. It opens up several questions regarding our current knowledge of microtubule dynamics.

Chapter 4. In this chapter the second important class of cytoskeletal filaments is introduced – actin filaments. An individual based particle approach was developed, and studied within stochastic simulations. It turns out that the system displays rich phase behavior, where the number of available monomers and the lifetime of filament precursor oligomers are critical control parameters. The circumstances under which filaments assemble are analyzed, and the coupling between nucleation and filament dynamics is investigated.

Science is a team sport. So, let me give credit to my coworkers here:

First to mention is Anna Melbinger. Starting with my Diploma project, we kicked-off our endeavor to understand the complexity that emerges when molecular motors depolymerize microtubules. It was a great pleasure to work with Anna during the last couple of years. Anna conceived the idea of how to generalize the extremal current principle for length-dependent systems, which made analytic solutions possible, and resulted in our work on „Microtubule Length Regulation by Molecular Motors“ (Section 3.2).

Second, I worked with Matthias Rank during his Diploma Thesis. We designed a project and developed a research question concerning the movement of molecular spider teams. It was a great delight to work with Matthias during his step into the molecular spider field. Matthias conceived the idea of how to simplify vast reaction networks by introducing equivalence classes. My contributions to his paper „Cooperative effects enhance the transport properties of molecular spider teams“ were research design, interpretation of results, and writing the paper. It can be found in the appendix of this Thesis (Appendix A).

Thirdly, I worked with Emanuel Reithmann during his Master's thesis. He investigated diffusing motor molecules that interact with microtubule ends. It was great fun to work with Emanuel during his sneak attack on mean-field theories. He conceived the idea of how long-range type correlations can be accounted for in a *correlation mean-field* approach. My contributions to his work „Quantifying Protein Diffusion and Capture on Filaments“ were research design, interpretation of results, writing the paper. The manuscript can be found in the appendix of this Thesis (Appendix B). My contributions to Emanuels work „Spatial Correlations in Protein Diffusion and Capture on Filaments“ were research design, interpretation of results, and writing the paper. The manuscript can be found in the appendix of this thesis (Appendix B).

Contents

Preface	v
Zusammenfassung	v
Synopsis	viii
Danksagung Acknowledgements	xii
Prolog	xiv
Chapters	xiv
Contributions	xvi
1. Introduction	1
1.1. The molecular parts	5
1.1.1. Microtubules	6
1.1.2. Molecular motors	12
1.1.3. Actin filaments	15
1.2. The experimental toolbox	16
1.3. Finite sized systems	17
2. Dynamic Lattices	21
2.1. Boundary induced transitions	22
2.2. Dynamic lattices	25
2.3. Domain wall theory	26
3. Microtubules and Kinesin-8	29
3.1. Microtubule depolymerization	32
3.2. Microtubule length regulation	44
3.3. Molecular mechanisms of microtubule length regulation	50
3.4. Phase transitions and length fluctuations	63
3.5. Traffic dynamic instability	67
4. Nucleation of Filaments	81
4.1. Model definition	82
4.2. Phase transitions	84
4.3. Application to actin filaments	90
4.4. Discussion	91

5. Epilog	93
A. Molecular Spider Teams	99
B. Facilitated Diffusion	115
Bibliography	125

Introduction

– Molecular Motors and Cytoskeletal Filaments

MOLECULAR MOTORS are a paradigm in modern cell biology [1]. They convert chemical fuel into molecular motion and mechanical force. This physical view of molecular motors has been confirmed for several „biological motors“. Some of them are bound to the cell membrane. They perform rotary motion to beat cilia and flagella that lead to cell motility, or act as pumps that maintain and generate concentration gradients across membranes. Other motors are responsible for translation and transcription of genetic material (RNA and DNA) or protein synthesis. The action of these machines is limited by available biochemical resources, nucleic acids and amino acids, of which genetic material and proteins are made of, respectively.

CYTOSKELETAL FILAMENTS are polymers that consist of protein subunits and that constitute the cytoskeleton of cells. These polymers can be roughly divided into three classes: microtubules, actin filaments and intermediate filaments [2]. Each type has its particular roles in the cell and they appear in essentially all species across the tree of life, from bacteria to humans. The individual protein subunits are highly conserved from an evolutionary point of view. However their tasks are specialized and multifaceted at a time. To illustrate this functional diversification, consider the process of chromosome segregation during cell division. In bacteria the mechanism of chromosome segregation depends on the protein ParM, which is a homologue of *actin*. The assembly of ParM filaments beginning in the middle of the cell pushes the two sets of DNA to the ends of the bacteria which then divides in the middle. This contrasts with the mechanism employed by eukaryotic cells where *tubulin* is responsible for chromosome segregation via depolymerization. It is remarkable that two completely different proteins, can evolve to fulfill identical functions across different organisms. This observation illustrates not only the versatility of

these polymers, but also how they serve as macromolecular machines that carry out specific tasks in the cell. The driving force of this polymer machinery is their assembly and disassembly dynamics powered by nucleotide hydrolysis.

Molecular motors organize, regulate, and maintain the cytoskeleton.

In this Thesis, the first focus is on molecular motors, that are associated to the cytoskeleton of cells. Such motors are ATP-driven enzymes that move along cytoskeletal filaments, microtubules and actin filaments, and are able to generate force against loads. As biological machines they contribute to the cellular organization in multiple ways: They seem to organize, regulate, and maintain the cytoskeleton in an accurate and robust manner. This is important throughout the development of organisms and the life cycle of cells, from meiosis to mitosis.

Cytoskeletal filaments drive biological processes by assembly and disassembly.

The second focus of this Thesis are the dynamics of growth and shrinking of filaments and their nucleation. Microtubule polymerization and depolymerization are fueled by GTP hydrolysis and are influenced by many associated proteins and molecular motors [3]. These influencing factors help to assemble and maintain cellular structures, for example the mitotic spindle [2]. They are necessary in the major microtubule driven processes, such as cytokinesis and the separation of chromosomes. Actin filaments are very different from microtubules and perform cellular tasks orthogonal to what microtubules do. Filaments are much smaller and less rigid than microtubules, but similarly their assembly and disassembly dynamics is driven by ATP hydrolysis. The structures actin filaments form range from branched networks, effected by branching proteins like ARP2/3, to bundles of filaments as organized by linker proteins like filamin, fascin, α -actinin, or the family of myosin motor proteins. The structures of actin networks are essential to cell motility and shape deformations, and also to force generation in muscle fibers. Notably the nucleation of actin filaments is a highly regulated process, which is controlled by a variety of nucleation proteins and so called nucleation promoting factors. In contrast to the case of microtubules, where nucleation happens at a microtubule organization center and microtubules stay there fixed, the nucleation of actin happens almost everywhere in the cell. This ensues that there is a very high turnover of actin filaments – filaments are created and disassembled continuously.

Having gained a rough overview of molecular motors, cytoskeletal filaments, and some cellular phenomena, one might wonder about how such cellular phenomena are orchestrated. This constitutes an excellent starting point to begin a scientific journey. The questions arises [1]:

„How does it work?“

The following paragraph maps out how and to what extent this question could be answered, and which method is deployed here. Also a brief introduction to the experimental and theoretical methodology in biophysics is provided.

THREE main routes lead the way to find answers to the question „How does it work?“ in cell biology. Each of these routes contributes answers to the above question and they complement each other in important ways: *a)* perform experiments, *b)* derive phenomenological models, or *c)* derive quantitative theoretical models. There are two basic experimental approaches: In the first approach – *in vivo* – living cells are investigated. Specific genetic methods allow us to compare wild type cells with genetically manipulated cells. A typical modification is that the expression level of a certain protein is changed. This happens through the deletion or insertion of the desired sequence. As a consequence the cellular concentrations of protein increases or decreases. Other modifications of a specific protein include point mutations, that selectively perturb the system and thus enlighten the functionality of a protein of interest¹. The *in vivo* approach identifies the role of a molecule in the living organism. The challenge that arises from the obtained data, is to link the phenomenologically observed behavior (phenotype) to the underlying genetic code (genotype). To date, this mapping constitutes *the* major problem in biology. The second approach are reconstitution experiments with purified proteins², also called *in vitro* experiments. In a suitable setup the interactions between proteins can be directly observed under the microscope. This approach led to the discovery of the molecular motor kinesin: In 1985, Vale *et al.* [4] showed that kinesin moves on microtubules and carries cargoes. In recent years the complexity of reconstituted systems has vastly increased, consider for example actin based motility [5], microtubule tip tracking [6], or the immunological synapse [7].

In addition to experimental efforts, mathematical modeling approaches have turned an essential tool for the biological sciences [8]. There are two basic strategies. The first strategy aims at deriving simplified phenomenological models that allow to reproduce the observed biological phenomenon

¹Point mutations are of special interest, because a single mutation in a gene might switch the functionality of a protein on or off.

²Protein purification can be a very difficult and costly process and has led to the scientific discipline of biochemistry.

using mathematical or computational methods. The strength of this strategy is, that it captures the essential dynamics of a system without explicit knowledge of molecular details. This process is called coarse-graining and in Turing's pioneering work this idea has been conceived [9]. He was aware that his simple mathematical treatises of morphogenesis does not describe the biological process on a molecular level. But he anticipated that his approach could be extremely helpful to learn about the truly „real“ biological phenomenon, when comparing it to simplified models with mathematical assumptions [9]. This perception has proven true, regarding the plethora of reaction-diffusion systems that are employed to model biological processes [10]. Similarly, computational models of the cytoskeleton allow to investigate motor induced interactions between filaments [11, 12] and organizational processes during cell division and in the mitotic spindle [13, 14].

The recently obtained high temporal and spatial resolution in microscopy allows to rigorously quantify kinetic rates and the localization of proteins in a cell. These developments enable a rigorous approach of microscopic quantitative mathematical modeling in biophysics [15]. Often such studies are joint efforts between theory and experiment and constitute a difficult endeavor, that needs many back-and-forth iterations between team members of both disciplines, physics and biology [16, 17]. Most importantly, accurate rate constants are necessary to derive quantitative theoretical models [8]. In the case that key experiments have been done, a theoretical model should find the appropriate level of description, and comply with *all* the available experimental data [18, 19]. However, explicit numbers for rate constants or numbers of molecules are lacking in many cases, therefore experiments and theoretical modeling have to be conducted side by side [20–26]. In some cases this endeavor also leads to ingenious experimental methods [27, 28].

The approach of microscopic theoretical modeling is pursued in this thesis. The particular level of theoretical description can be characterized as a „bottom-up“ approach, because molecular details as observed in experiments are translated to appropriate mathematical descriptions. The resulting theoretical models are analyzed employing stochastic simulations and analytical methods from nonequilibrium statistical mechanics.

1.1. The molecular parts

The molecules that are considered the basic units in this work are molecular motors, and the building blocks of cytoskeletal filaments – actin and tubulin. Each of these molecules has been investigated in great detail using biochemical and biophysical tools [29, 30]. Because of these studies, our understanding of proteins has reached a point where molecular details as recorded from single molecule experiments and revealed by biochemical assays can be related to specific phenotypes. However the reasons for certain phenotypes remain obscure. They are hidden in complex signaling pathways, enzymatic cascades, gene regulation, and the cell metabolism. None of these complexities in cell biology can be understood without knowing the molecules involved. They are genetic and enzymatic players, of which one would also like to know their mutual interactions. All these complications do not exclude though, that there are basic principles withstanding and organizing those complexities. Such biological principles might constitute „fundamental laws“ for biology, similar to the principles which underlie the „fundamental laws“ of physics³.

The present work considers minimal models for the regulation of filaments in space and time. Different regulatory units are investigated and it is attempted to identify mechanisms which are relevant to these different units. One could view these units as the cytoskeletal analog to „functional motifs“ as defined in terms of gene regulatory networks [32].

The three players that are subject of this thesis, molecular motor, microtubules, and actin, have one theme in common. Both filaments as well as molecular motors use chemical energy to perform work: to grow, to shrink, or to move. The chemical energy in cells is available in the forms of adenosine triphosphate (ATP) and guanine triphosphate (GTP), and the energy is set free via hydrolysis to ADP and GDP, respectively, and inorganic phosphate. Hydrolysis is an exergonic reaction and reads:



where X may stand for the respective nucleotide. In the case of ATP this reaction releases a Gibbs free energy of $\Delta G^\circ = -35 \text{ kJ/mole}$; under cellular conditions this value is even higher $\Delta G = -50 \text{ kJ/mole}$. Often the ionic conditions have a strong effect on ΔG compared to the standard

Energy sources are ATP and GTP

³One has to be careful about what „fundamental laws“ are, and what their precise meaning is. The interested reader is referred to the philosophical literature, where Ref. [31] could be a suitable starting point.

conditions. A prominent example that illustrates the importance of ions is the polymerization of actin, which does not occur in the absence of Mg^{2+} . Another subtle example of how important salt conditions are, is given in Ref. [22]. Therein the authors achieved to tune the run length of molecular motors on the microtubule by increasing and decreasing salt concentration.

1.1.1. Microtubules

Microtubules are tube-like protein filaments that are part of the cytoskeleton and form cilia and flagella in eukaryotes [2]. They are stiff polymers which fulfill many different functions in various organisms. They also enhance the mechanical stability of a cell and contribute to cellular dynamics in many ways. For example, beating flagella propel sperm cells, and sensory cilia serve the nematode worm *C. elegans* to sense its environment. In prokaryotes, tubulin-like proteins (FtsZ) are directly involved in cell division, *i.e.* the scission of one cell into two daughter cells. Probably most prominently, microtubules are indispensable during cell division in eukaryotes because they constitute the machinery that separates the chromosomes known as mitotic spindle apparatus⁴. Their dynamics and their structure seems particularly adapted to perform this task as will be explained in the following.

Microtubules have
internal *polarity*

Microtubules are hollow tubes made of 13 linear protofilaments that are assembled from protein subunits, tubulin heterodimers, in the presence of GTP. One tubulin dimer consists of two different subunits, one α - and one β -tubulin. Together they form a dimer, and associate head to tail to form a protofilament with internal polarity. At the end where β -tubulin is exposed, the microtubule end is called the plus (+) end or plus tip. On the other end of the filament, where α -tubulin is exposed, the microtubule grows slowly and thus this end is called minus (−) end. These particular structural features are the reason for microtubule polarity, and gives rise to directed motion of molecular motors [33].

The consequences of microtubule polarity are far reaching throughout cell biology. On a single filament scale, polarity allows molecular motors to move on the filament into one particular direction, and to function as transporters: kinesin motors move towards the plus end, and dynein motors move towards the minus end [34]. On a cellular scale microtubule polarity has far reaching implications. It can serve as an organizational principle to cells. Let us consider a particularly striking example which reflects this

⁴This important role in the mitotic process has made tubulin a primary target for anti-mitotic drugs, which are important in cancer treatments today.

larger scale organization: Nerve cells consist of a cell body (also called soma), dendrites, and one axon [2]. In a simplified picture dendrites serve as antennae with which neurons can receive signals, while axons allow to send signals and to connect to other neurons by forming a synapse. The microtubules play an important role for the feasibility of this generic architecture in the brain⁵. The filaments are organized differently in dendrites and axons: While in the axon microtubule plus ends point towards the synapse – away from the soma – in dendrites the plus ends point towards the soma [2].

Having discussed how the principle of head-to-tail assembly, which determines microtubule polarity on a molecular scale, affects large scale architecture of cells, let us consider an intermediate scale next.

Zooming out from the level of individual proteins to a level where interactions between protofilaments are important, let us think about why protofilaments form a tube like structure. The most important reason for this are lateral interactions between the tubulin heterodimers and thus the individual protofilaments. There are different ways of how protofilaments form a microtubule lattice. These diverse structures can be observed under different polymerization conditions in the experiment. Microtubules can be polymerized into tubules of 13, 14, or even 15 protofilaments. Also lattice defects have been observed [35], similar to what is known as line defects in solid state physics [36]. The 13-protofilament microtubule is considered the regular case, while for example 14-protofilament-microtubules form in the presence of GMPCPP. If this slowly hydrolyzable GTP analog is incorporated into the microtubule lattice it prevents dynamic instability [37, 38]. In contrast to the *in vitro* situation, where microtubules form spontaneously at high concentrations, in the cell the genesis of microtubules is initiated very specifically. The organelle responsible for this task is the *microtubule organization center* or centrosome [39]. There are two centrosomes in a dividing cell and each daughter cell inherits one centrosome⁶. From these organizing centers microtubules nucleate and elongate, and microtubule asters are formed as precursor of the mitotic spindle, as observed for example in *Xenopus laevis* egg extracts [41]. The molecular details of this nucleation mech-

Microtubule
architecture

⁵Microtubules are highly abundant in nerve cells which makes bovine and porcine brain tissue a primary source of tubulin.

⁶Centrosomes are commonly linked to the origin of tumors. For example aberrations in the centrosome replication cycle that lead to a wrong number of centrosomes in the cell are a common cause for genome instability. This was actually realized as early as 1914 and is known as the Hansemann-Boveri hypothesis, see Ref. [40] for more details.

anism are known in some detail: There is a third tubulin species, γ -tubulin, involved which is responsible for microtubule nucleation [42]. Although not so much is known about the constitution of centrosomes, it is widely accepted that the organelle consists of amorphous protein material of which γ -tubulin is an integral part of. γ -tubulin assembles into a ring complex (γ -TuRC), which then serves as a seed to template microtubule growth. The γ -TuRC stays at the microtubule minus end as a cap.

Intriguingly there are also higher order microtubule structures in living organisms. One example for the controlled assembly of multiple microtubules are cilia and flagella [43]. The cytoskeleton inside these structures consists of a specific number of microtubule doublets (*nine*) that are arranged in a ring structure called the axoneme. They consist of one „normal“ microtubule and one laterally connected, second microtubule which is however consisting of fewer protofilaments. At the root of the axoneme, where the cilium is connected to the cell, there is a structure called basal body, which for its part consists of *nine* microtubule triplets⁷.

The principles of cilliogenesis, *i.e.* how these structures are initiated and assembled are a broad field of research [43] beyond the scope of the overview this section shall provide. The described observations however invite to wonder about the principles of cellular microtubule organization.

*Post-translational
modification of
microtubules*

Let us turn to a remarkable biochemical aspect of microtubules. Microtubules are subject to post-translational modifications [45, 46]. These are controlled enzymatic modifications of the surface of individual tubulin molecules, that happen in the cytoplasm after the ribosomes have assembled the protein. These biochemical modifications have far reaching effects on how microtubules organize in the cell and which molecules associate with them. In the microtubule related biophysics field, this aspect often remains disregarded. It would be easier if there were only one type of microtubules. But since this is not the case, and because the effects arising from post-translational modifications can be severe regarding the dynamic and static properties of microtubules, it is worth to discuss this topic briefly. Post-translational modifications of microtubules are particularly relevant to *in vitro* experiments, because the enzymatic modifications of isolated tubulin strongly depend on the species from which it was ob-

⁷At this point the reader could be tempted to ask: „Why *nine* again?“ To answer this question it is instructive to consider other prominent answers to questions, for example *forty two*. In that specific case the question was on „life, the universe and everything“ [44]. Eventually the context of cell biology is narrow enough and the question sufficiently clear that an explanation can be expected sooner or later.

tained [47]⁸. These modifications are for example responsible for the degree of activation or inhibition of molecular motor's ATPase activity. Some motors move faster on porcine microtubules, while others are faster on yeast microtubules [48]. A specific post-translational modification of tubulin, which is of particular interest to the topic of this thesis, is the tyrosination and detyrosination of α -tubulin by an enzyme called tubulin-tyrosine ligase. Microtubules with the latter modification are a better substrate for microtubule-depolymerizing molecular motors. The depolymerization activity of the motor proteins from the kinesin-13 family is stimulated by tyrosination and it is inhibited by detyrosination [49]. Hence, in a simplified picture, microtubule post-translational modifications are switches which influence the stability of microtubules, as well as their quality as a track for molecular motor motion.

So far we have considered elementary characteristics of the microtubule building blocks – tubulin, and we have also discussed how the filaments are organized in higher order assemblies like cilia and flagella and in the cytosol with the help of a microtubule organization centers. Knowing about the cellular organization of microtubules it remains to be said that microtubules are macroscopic molecular machines able to generate strong forces. These forces can be pushing or pulling forces depending on polymerization or depolymerization of the microtubules [50, 51]. Or they can emerge from interactions with molecular motors. To highlight the versatility of these machines, an example is in order. Recently Laan *et al.* constructed micron sized chambers with functionalized surfaces to investigate how cell nuclei are centered. Dynein motor proteins are tethered to the wall of the chamber and regulate the microtubules that radiate from the center of the chamber in an aster like manner. Together molecular motors and filaments constitute a centering mechanism to the nucleus, because the forces generated by the motor molecules and the microtubules balance in the system.

Microtubules
generate *forces*

DYNAMIC INSTABILITY is the phenomenon of switching between periods of growth and periods of shrinking as observed for microtubules [52]. Recently, dynamic instability has also been discovered for actin like filaments in bacteria, ParM [53]. Mitchison and Kirschner were able identify the origin of stochastic switching. In their experiment they observed the stable coexistence of growing and shrinking microtubules and concluded,

⁸Common sources of tubulin are bovine and porcine brain tissue. The resulting tubulin naturally contains many post-translational modifications while yeast tubulin is much less modified, however the latter is more difficult to obtain.

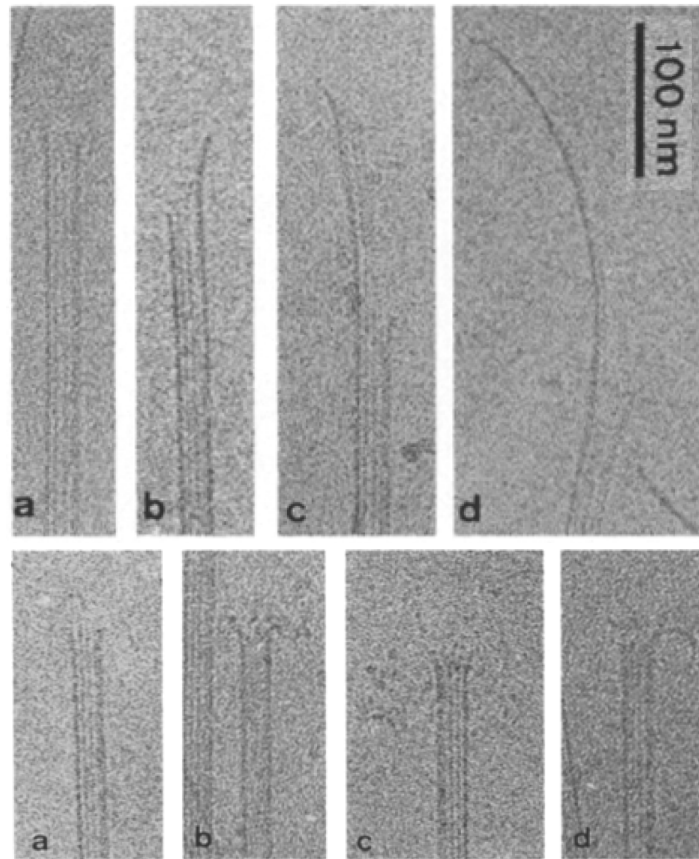


Figure 1.1.: MICROTUBULE STRUCTURE of growing (TOP) and shrinking (BOTTOM) filaments as seen by Chrétien *et al.* using electron microscopy [54].

that switching between the two processes is due to a particular feature at the microtubule tip. They hypothesized that GTP hydrolysis is the driving force for switching. Electron microscopy data largely supports this view. Shrinking microtubules are splayed out and individual protofilaments are curved as well as the individual tubulin heterodimers in the GDP state. In the GTP state the tubulin heterodimers have a straight conformation and add to a growing microtubule to form a non-splayed microtubule tip. Figure 1.1 shows electron micrographs of growing and shrinking microtubules.

Tubulin assembles into microtubules with GTP bound, and tubulin dissociates from the microtubule in the GDP bound state [33]. This renders

the hydrolysis rate an important parameter for microtubule dynamics [55]. This intrinsic parameter can be influenced in experiments in a subtle way. Because there are different kinds of GTP homologs that have a different hydrolysis rates, it is possible to incorporate these into the microtubule instead of GTP. For example GMPCPP is known to stabilize microtubules since the nucleotide is practically non-hydrolyzable. Another nucleotide substitute, GTP γ S mimics the structural features of the microtubule tip [56]. Recent cryo-electron microscopy experiments also revealed that the structure of the growing microtubule tip depends on the nucleotide state and leads to strong interactions with end binding proteins (EBs) [57]. At ambient conditions the investigation of the nucleotide state has remained challenging [38]. The difficulty is that indirect measures, like for example microtubule binding proteins or antibodies, are necessary to resolve the nucleotide state of tubulin dimers in the microtubule [58, 59] by optical microscopy. Precise data with sub-nanometer resolution has yet to be obtained. Reverse engineering the question however, allows to study the influence of the nucleotide state on microtubule dynamics nevertheless: Microtubules can be created *in vitro* with differently patterned nucleotide states. This allows to learn how the nucleotide states influence the dynamics depending on the predefined composition of the microtubule [37]. Although microtubule dynamics has largely remained elusive on a molecular scale, within a systems level understanding the situation is clarified. Microtubule depolymerization is a particular molecular machine which is strong enough to tear chromosomes through the cytoplasm [50, 60, 61].

Microtubule dynamic instability has also attracted lots of theoretical attention. First to mention is Hill, who pioneered the view that switching between distinct states of microtubule growth and shrinking induce dynamic instability [62]. There are many more models available today for microtubule dynamic instability. Generally these model qualitatively distinguish between *bounded* and *unbounded* growth, see *e.g.* Refs. [63–66], and compare to experimental data obtained in the form of dilution experiments [55, 67, 68], or develop mechanical understanding of microtubule structure and dynamics [69–71].

To conclude this section on microtubules, there are many factors that influence microtubules. Molecular mechanisms of microtubule assembly and disassembly are known as basic principles that have been hypothesized [72]. Conclusive agreement, however, between experiment and theory has yet to be obtained. This leaves a formidable question regarding microtubule dynamics unanswered: What is actually dynamic instability and how does it work?

1.1.2. Molecular motors

There is a plethora of molecular motors in the cell. The motors associated with the cytoskeleton and microtubules in particular are dynein and kinesin. These two classes of motors differ from each other in many aspects. In the following a brief overview is provided into these differences. What they have in common is that both appear in a large variety of different variants that pursue different cellular functions. From a perspective of evolutionary biology molecular motor have diversified and specified across many different organisms [34].

On first sight the main difference between kinesin and dynein is that the former walks to the microtubule plus end while the latter walks to the minus end. On a molecular scale this difference is rooted in the mechanisms both motors employ for movement. Dynein is a huge molecule consisting of many different subunits. By contrast kinesin is a relatively small, often dimeric molecule. Further the mechanism of dynein movement and force generation is very different from that of kinesin. Dynein is suited to exert large forces, for instance to hold the nucleus at the center of a cell [23], and kinesin might be suited to transport material through the cytoplasm because of its high processivity. A brief look „under the hood“ of the two motors supports this view: Dynein employs at least 6 ATPases for force generation, while kinesin has only two ATPases. This is like comparing an SUV with a motorcycle. However, the tug-of-war between these two molecules [73] has inspired lots of theoretical and experimental work.

If many molecular motor interact with many filaments, large scale organizational dynamics is observed that leads to a variety of patterns and intermittent dynamics. Some examples include the formation of aster-like structures in mixtures of microtubules and certain kinesin motors [74]. Once the formation of these structures is complete, they settle to a steady state. Quantitative insights into such processes can rarely be obtained due to the complicated nature of the interactions between its components. One interesting candidate for a system of motors and filaments where a quantification is possible is the formation of microtubule bundles by molecular motors [75, 76].

A quantification of protein-filament systems is more feasible if the influence of motor molecules on only one filament is considered. There are several proteins that interact with filaments in interesting ways. In particular the enzymatic elongation or shortening has received much attention recently [3]. In the following one kind of such an enzyme, which is also a molecular motor is presented more thoroughly.

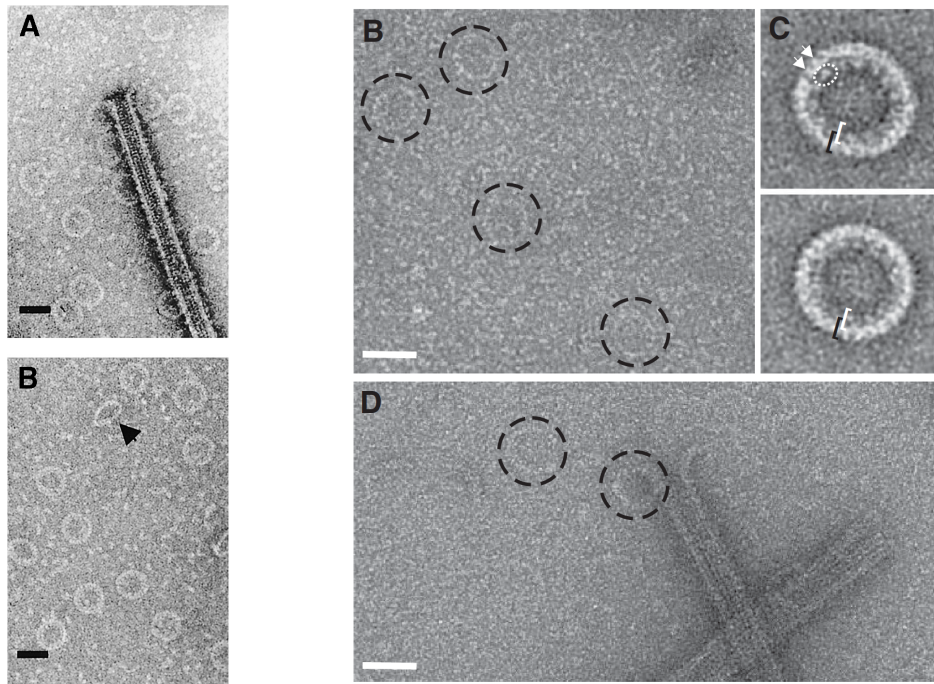


Figure 1.2.: DEPOLYMERIZING PROTEINS induce tubulin rings. Shown are rings induced by the kinesin-13 protein pKinI [80] (LEFT A&B), scale bar 40 nm. And kinesin-8 induced rings [81] (RIGHT B&D) and average structures (RIGHT C), where the inner ring is kinesin-8s (white) and the outer ring is tubulin, scale bar 50 nm.

KINESIN MOTORS tend to depolymerize microtubules [77, 78]. The first kinesin that was discovered to destabilize microtubules was KinI [79], also known as mitotic centromer associated kinesin (MCAK). This protein constitutes a main player of the kinesin-13 protein family, which is one of the two families of microtubule depolymerizing proteins. The second protein family is kinesin-8. Both kinds of proteins bend protofilaments into curved conformations, similar to those observed during microtubule depolymerization. Using electron microscopy it can be seen how motors bend the tubulin protofilaments into rings, see Fig. 1.2.

In the following, both types of protein are briefly introduced and their

differences are lined out. First consider kinesin-13. It is the most studied of its kind and has a role during mitosis in spindle regulation. It binds to both microtubule tips in the presence of ATP [82] and has been shown to diffuse on the microtubule lattice and to depolymerize it by tearing apart tubulin heterodimers from the microtubule tip [83]. The precise hydrolysis cycle of the depolymerization step has been studied [84] and the residues relevant for depolymerization were identified [85]. MCAK has also been shown to stay bound to the depolymerizing microtubule tip [85]. This behavior is called processive depolymerization and has been investigated in theoretical work for diffusing [86] as well as walking molecular motors [87].

Such processive behavior is also called tip-tracking and it arises in other situations as well. For example Bieling *et al.* have identified a minimal system for tip tracking consisting of three components, a molecular motor, an end-binding protein, and a linker molecule. There is a whole protein network which interacts with microtubule tips [88], and it is known that cellular functions are associated with it. These include the regulation of microtubule dynamics [3] as well as for example the possibility that material is transported to the cell membrane via microtubule tips [89].

Tip tracking can be regarded as a core mechanism for enzymes that regulate microtubule growth and shrink rates, because not only depolymerizing proteins MCAK, but also polymerizing enzymes XMAP215 employ this mechanism [90]. For a recent theoretical analysis of this mechanism see Ref. [91] and Appendix B of this Thesis.

The second depolymerizing protein is kinesin-8, which differs in multiple ways from the previously discussed kinesin-13. It is a plus-end directed molecular motor which tightly binds to the microtubule lattice. The best studied kinesin-8 motors are those from budding yeast (kip3p [92–94]) and humans (Kif18a [95–97]), and also fission yeast (klp5/6 [48, 89, 98]). These molecular motors walk on the microtubule towards the plus-end using ATP. In doing so they bind strongly to the microtubule lattice, which renders kinesin-8 an extremely slow motor. What might look like a drawback is indeed an advantage for the function of the motor as depolymerase, because its motion on the microtubule is extremely persistent. It stays bound for many minutes and walks dozens of micrometers to reach the microtubule tip [22]. This strong and long binding has been shown to be due to the tail domain of the motor [99–101].

Besides their activity as depolymerizing molecular motors kinesin-8 also forms traffic jams on microtubules [22], as predicted in recent theoretical work for a driven lattice gas with attachment and detachment kinetics [102]. Why have traffic jams not been observed before? The answer to

this question is that, unlike all other kinesin motors, kinesin-8 exhibits a extremely long run length. The resulting small detachment rate from the microtubule leads to massive amounts of motors on the microtubule, so that interactions between the motors become important. These interactions can be regarded as hard-core repulsion as the agreement between theory and experiment suggests [22, 102]. In the meanwhile also other motors were shown to underlie this traffic behavior [103].

A detailed quantification of the experiments with kinesin-8 has been achieved within this thesis and is presented in Section 3.1.

1.1.3. Actin filaments

When microtubules are filigree structures that contribute in subtle ways to the life of a cell during „moments of truth“ like cell division for example, then actin is a tireless power horse which is in action all the time and everywhere. It forms the cortex of a cell, which is a two-dimensional filament network that is tethered to the membrane and provides mechanical rigidity. Actin is actively remodeled at the membrane and generates pushing forces for cell motility. Similar to molecular motors actin filaments exerts forces under consumption of ATP [104, 105]. Because one actin filament is simply too small to generate strong cellular forces, it teams up with many others of its kind [106–108]. Actin filaments form tight bundles or branched network structures depending on the linker molecule that is present. For example linker proteins fascin induces actin to form tight bundles, while α -actinin or filamin proteins lead to the formation of network structures [109, 110].

One important aspect of actin is that it is maintained and regulated via a plethora of associated proteins that incessantly regulate actin's activity. Actin filaments have a time dependent particular temporal and spatial structure. The spatial structure of growing actin filaments allows various proteins to attach to different regions of the filament, that essentially differ by the nucleotide state of the actin monomers in the filament. At the barbed end actin monomers assemble with the *ATP* nucleotide bound. After the nucleotide is hydrolyzed on a timescale of seconds, the phosphate atom stays bound to the filament *ATP • P*, and only after some time again the phosphate is released, and the filament has arrived in the *ADP* state, which is the configuration at the pointed end of the filament. Actin is influenced by many different enzymes, that for example influence filament polymerization, like formins, or serve the stabilization of filaments like phalloidin. One important class of actin related enzymes are nucleation proteins [111]. These are of particular interest here, because they help form a filament

from precursor nuclei that are very short-lived in the absence of nucleation proteins. The most important players are introduced in greater detail in Section 4.

1.2. The experimental toolbox

In the last decades many biological problems were addressed using approaches that originally were brought up in physics. Since then both disciplines approached each other, in that biology has turned into a more quantitative science, and that physics has evolved a new discipline – biophysics.

Many of the novel approaches in biology arose from experiments that were developed in physics, and then have become versatile tools for research on biological samples. There are numerous examples that can be found in the literature. Two of these are chosen here due to their particular importance in physics and biology:

- i)* Force spectroscopy
- ii)* Optical microscopy

Both constitute landmarks of new developments in biophysics. The first technique has revealed the role of forces in cell biology, and the second technique elucidates the spatial and the temporal dynamics of molecules inside cells. Together these approaches are extremely useful in understanding biological systems as briefly outlined in the following. Interestingly both of these approaches were accompanied by theoretical and computational advances which provide foundations to interpret the experimental data. The little detour that is undertaken here is beneficial for two particular reasons: Any theoretical work needs explicit numbers to become meaningful. And such numbers are obtained from experiments. So if theorists do ignore where these numbers come from there is a chance that their theoretical work will neither provide a reasonable explanation for experimental data nor hold any predictive power. To know the experiments thoroughly is also important to biologists in order to know what can be learned from the data – and probably even more importantly – what can *not* be learned from the data.

The field of force spectroscopy for example broadens our understanding of the energy landscape of protein folding [112], how a bond breaks [113], and also how cellular signals are derived from force sensing molecules [114].

Molecular forces also play a role in „pure“ cell biological fields like genetics for example [115], where helicases have to unwind the twisted genetic material DNA or RNA. For a recent overview on force spectroscopy methods, see for example Ref. [116]. Important theoretical contributions to the field are the seminal work by Evans and Ritchie on the strength of molecular bonds and by Hummer and Szabo, who showed how to convert data obtained from (non-equilibrium) pulling experiments into equilibrium rate constants. These theories significantly contributed to our current understanding of forces on the nanoscale.

Modern microscopy started with the development of differential interference contrast (DIC) microscopy and a video camera mounted to a microscope [119, 120]. Since then microscopy has become an art in many ways. On the biochemical side, the work on Green Fluorescent Protein by Shimomura, Chalfie and Tsien initiated a protein engineering race of fluorescent probes for (almost) everything in the cell. There are even fluorescent proteins that „sens“ forces inside cells [121]. In addition, over the past few years super-resolution microscopy techniques have been developed, that focused on high spatial resolution. These techniques allow to localize cellular structures at a nanometer resolution, however this gain in resolution came at the price of very long acquisition times. Only recently several groups have succeeded to also improve the time resolution of imaging, such that the biologically relevant timescale of seconds is obtained [122, 123]. In addition, and particularly in embryology, it is desirable to image for extend periods of time to monitor all stages of embryo development. These very long timescales – say days – are challenging on their own right, because very mild imaging techniques are essential, such as not to influence the biological processes [124].

This brief overview on recent experimental advances shall help to assess the possibilities that are emerging in the future. These possibilities will also shape the demands on theoretical biophysics. „Which process is relevant at a certain timescales and why?“ This and similar questions will certainly be one of the most important ones that call for answers and quantification.

1.3. Finite sized systems

The experimental methods presented in the previous section are aiming at observations of single molecules. This possibility is unprecedented and has interesting consequences for the theoretical approaches that try to explain the observed nanoscale phenomena. In particular the classical statistical

mechanics approach, which connects microscopic details to macroscopic quantities, is put to test. In statistical mechanics there are two important properties that determine whether or not the approach is „working“. The first one is that, in general, there are extensive and intensive parameters that describe the state of a system. Extensive parameters are those dependent on the system size while intensive parameters are independent of the system size, the number of particles N . Second and related, it has to be possible to take the „thermodynamic limit“ of a system, that is to send the number of particles N to infinity, and also the volume of the system V , while the density (or number concentration) of particles $\rho = N/V$ is constant. The latter is corresponding to the concept of amount concentration in chemistry where the amount of a substance in mole is considered per volume of a mixture with solvent V [125]. One mole corresponds to an elementary number of entities, $N_A = 6.022 \times 10^{23}$ called Avogadro’s number. The astronomical size of this number has ever since justified to take the thermodynamic limit in chemistry and physics.

However, in the small world inside of cells, and inside of bacteria and viruses the situation is quite different. Take for example the volume of the bacterium *Escherichia coli* which can be roughly estimated to be $1 \mu\text{m}^3$ [2]. In this tiny volume a „concentration“ of $1 \mu\text{M}$ corresponds to only $N = 600$ particles. Which is very small when compared to 10^{23} particles of Avogadro’s number. This rough estimate leads to the severe question, if the current concept of concentrations is not misleading in a sense that it would rather be appropriate to consider finite particle numbers instead of concentrations when thinking about intracellular processes.

In chapter 4 of this thesis the particularities of actin nucleation from a finite pool of monomers and in a small volume is investigated. This compartmentalized view on complex chemical reactions strongly supports that chemical reactions occur differently on such small scales [126]. It provides a basis for future experiments, where volume as well as particle number are experimentally well controlled [18, 127–141].

THE SIZE of organelles is a matter of intense research at the moment, and recent work has revealed principles that determine organelle size [142, 143]. Novel microscopy techniques, allow to reconstruct three dimensional images and thus volumetric measurements are possible at accuracies never achieved before. As a specific and well-studied example related to the microtubule cytoskeleton, the mitotic spindle [144, 145] is discussed in terms of a graphical illustration. It highlights how various processes contribute to the physics of the mitotic spindle and tries to show a bigger picture.

However, it remains a challenge for the future to put these factors together. Meanwhile the following (incomplete) list could be a starting point to pursue this endeavor:

- ① Size limits due to microtubule length [146].
- ② Centrosome size determines spindle size [147].
- ③ Depolymerizing motor kinesin-8 [148]
- ④ Depolymerizing motor MCAK [149]
- ⑤ Microtubule severing protein Katanin [150]
- ⑥ Nucleation of microtubules inside the spindle [27]
- ⑦ XMAP determines spindle mass [151].
- ⑧ Cytoplasmic volume [152]

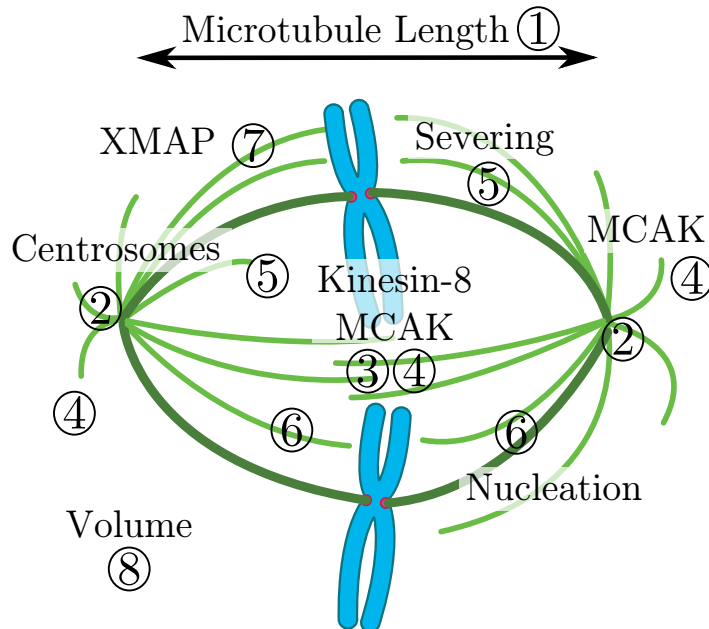


Figure 1.3.: MITOTIC SPINDLE APPARATUS. Several recently established determinants of spindle size are indicated. The numbers ① – ⑧ roughly indicate where enzymes interact with spindle constituents. Diagram by Lordjupiter / CC BY 3.0

Growing & Shrinking Lattice Gases

– A Domain Wall Theory for Dynamic Lattices

Driven diffusive systems are a class of models employed in statistical physics to study non-equilibrium phenomena. One of the first system belonging to the class driven diffusive lattice gases was originally proposed as a mechanical experiment with small particles that diffuse through a narrow channel (see Fig. 2.1), that connects two reservoirs of particles [153]. In the channel the particles diffuse in a single file, with a net current if the two reservoirs have different particle densities. Already this simplest possible system displays particular properties, because particles can not pass each other in the narrow channel. For example if one puts a tracer particle amidst the other particles in the channel, the mean square displacement of the tracer particle scales as $\sim \sqrt{t}$ [154]. Comparing this result with one dimensional diffusion of a single particle, one observes a qualitatively different behavior, because the mean square displacement of a single particle scales linearly with time $\sim t$. The presence of many particles and their excluded volume interaction changes the physical characteristics of a system. Note that this result is valid only for one dimensional systems and does not exist in two or three dimensions, although interactions between particles generally play a role in higher dimensions as well. One example is the Van-der-Waals gas in which particles have a non-zero volume leading to effective increase of pressure [155]. In the cell biological context, interactions between the proteins inside a cell lead to sub-diffusive behavior due to macromolecular crowding effects [156].

Although Hodgkin and Keynes intended to investigate ion conduction across a nerve fiber with their experiment, their idea of a one dimensional channel with diffusing, interacting particles, became very successful as a model for a variety of situations. The model is known as *simple exclusion process* (SEP) or single file diffusion. One important generalization of this model is that particles move *asymmetrically* (ASEP). The probability to move to the right differs from the probability to move to the left as in

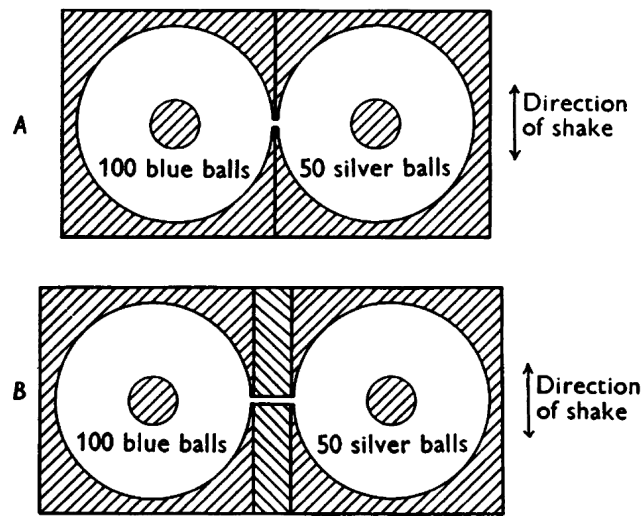


Figure 2.1.: SIMPLE EXCLUSION PROCESS in a simple mechanical model as suggested by Hodgkin and Keynes to study the ionic conductance of nerve fibers [153].

a random walk with drift. The ASEP constitutes a large class of models comprising many special cases. In the following we consider a particular situation, where the movement of particles is *totally asymmetric*, the TASEP. In this case particles move as Poisson steppers in one direction. This lattice gas was first proposed by MacDonald *et al.* [157] as a model for multiple ribosomes that move along a messenger RNA to synthesize proteins. Since then many interesting phenomena were described in this system, including phase transitions, of which one important class is discussed in more detail in the following.

2.1. Boundary induced phase transitions

A first remarkable observation is that TASEP exhibits boundary induced phase transitions [158]. Depending on the microscopic rules for particles at the lattice boundaries to enter or leave the system as illustrated in Fig. 2.2, boundary induced phase transition are observed. These can be derived intuitively, because the density of particles on the lattice is affected on a macroscopic scale. The system may contain a traffic jam (high density, „HD“), exhibit fluent movement of all particles (low density, „LD“), or

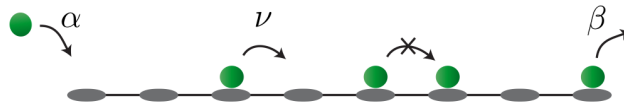


Figure 2.2.: TOTALLY ASYMMETRIC SIMPLE EXCLUSION PROCESS is a standard model for non-equilibrium physics. At the left particles are fed onto the lattice at rate α , and taken out of the lattice at the right at rate β . Hopping occurs at rate unity.

the lattice could carry a maximal capacity of particles while optimizing the current through the system (maximal current, „MC“). These different kinds of phases are relevant to all projects described in chapter 3 of this thesis.

To obtain some more intuition for the phase transitions it is important to consider the bulk current through the system

$$J = \rho(1 - \rho), \quad (2.1)$$

where ρ is the density of particles – the probability to find a particle on a site. The second term is the probability for a site to be empty. The above relation holds for particles that move at unit velocity, but is very general and applies to many situations in exclusion processes [159]. Here we specify to the case of open systems, where particles can be fed onto the lattice at the left end (minus-end) of the system and are leaving the system at the right (plus-end). Following the rules of particle exclusion, the currents at the input (IN) site and at the exit (EX) site are

$$J_{\text{IN}} = \alpha(1 - \rho), \quad (2.2)$$

$$J_{\text{EX}} = \beta\rho. \quad (2.3)$$

The conservation of current in the steady state $\partial_t J = 0$ implies that the rate constants α and β , at which particles are added to and removed from the lattice respectively, take special roles. Consider for example the case of $\beta < \alpha$. Then less particles are taken out of the system than particles are fed into the system. It is intuitively clear that particles pile up at the plus-end, and the traffic in bulk is reduced to $J = J_{\text{EX}}$. As a consequence also the density in bulk is adjusted to this situation: $\rho_{\text{EX}} = 1 - \beta$, as can be easily checked. The system is in the EX phase or also called the HD phase. Figure 2.3 shows the complete phase diagram of TASEP. All remaining phases of the system can be determined along similar lines, which is postponed to

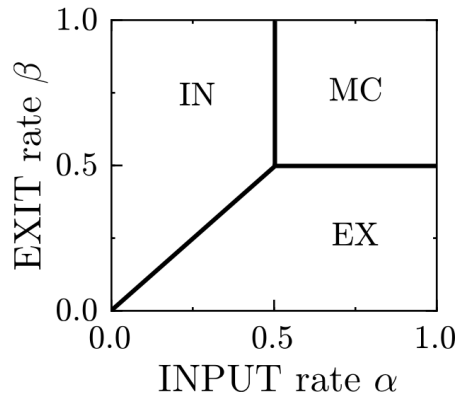


Figure 2.3.: PHASE DIAGRAM of the TASEP in terms of the entrance and exit rates. Note, the currents in high and low density phases are independent of parameters α and β respectively.

a more interesting example later. The procedure as such is nicely and less qualitatively explained in [160].

All the results obtained for the TASEP with methods similar to the argument for the EX phase above were also derived analytically [161, 162]. A particularly beautiful and simple way to the solution is via transfer matrices [163]. In this thesis a different route is pursued, the mean-field approach. Let $n_i \in \{0; 1\}$ be the occupation number of the i th lattice site. Then the mean current from site i to site $i + 1$ is $J_{i+1} = \langle n_i(1 - n_{i+1}) \rangle$, where $\langle \cdot \rangle$ denotes the average. The probability to find a particle on site i is thus $\rho_i = \langle n_i \rangle$. A priori it is however not clear how to treat the product $n_i n_{i+1}$ when the average is applied $\langle n_i n_{i+1} \rangle$. The mean field assumption states that $\langle n_i n_{i+1} \rangle = \langle n_i \rangle \langle n_{i+1} \rangle$. As a consequence simple solutions are possible in TASEP.

Despite its surprising simplicity only few situations are known where simple mean-field approaches fail to describe the qualitative behavior of a system. In these cases, there are particular methods to refine the accuracy of the approach [164], or combine it with analytic results obtained for a subsegment of the process [165, 166]. One example in which this factorization scheme is not valid, is given in chapter B and Ref. [91]. Therein, a separation of time scales between tip-related enzymatic processes and diffusion in bulk forbids a simple procedure as outlined above.

Much more can be learned about the applications of driven diffusive sys-

tems because they are broadly relevant in fields as different as car traffic phenomena [?] and biology [167]. There are several reviews available [168–170]. Notably Ref. [171] provides a hands-on tutorial to matrix product states, and Refs. [172, 173] review very recent developments, *e.g.* what can be learned from large deviation functions, and what are applications of the theory. There is also an excellent textbook [159], which provides a course-level introduction to the field. The reader interested in exact solutions is deferred to Ref. [174], in which the long standing problem of current fluctuations in ASEP has been solved.

In the more recent literature TASEP was extended to many different situations. These can be categorized as follows¹. Internal degrees of freedom of particles were varied in different ways to account for spin transport, the stepping cycle of motor molecules and also multilane transport [175–188]. A second direction of systems studied recently were transport properties on networks [73, 189–193], and under certain resource limitation [133–136, 139, 194, 195]. A different and interesting idea is to include population dynamics in a driven diffusive system [196]. The last direction of research to be mentioned here are modified hopping rules. These modifications – although they seem not much different from the usual case – are very different from the original driven diffusive system². They include TASEP with global hopping [197], which is surprisingly similar to the case with attachment and detachment kinetics [198], systems where particles push each other from behind „facilitated exclusion“ [199], or particles are accelerated by other particles [200, 201].

2.2. Dynamic lattices

Recently, driven lattice gases were studied on dynamic lattices. In these models, a lattice either grows or shrinks dynamically. In the following an overview is provided on this particular topic. Sugden and Evans proposed the *dynamically extending exclusion process* [202, 203], where each particle that arrives at the lattice boundary, extends the lattice by one site. They determine the phase diagram and describe nontrivial density profiles due to the coupling of lattice growth- and particle dynamics. In further

¹This categorization can be considered as a loose classification, which is in parts motivated by the actual details of the systems. For example internal degrees of freedom and transport on multiple lanes with particle interactions across lanes can be identical in limiting cases.

²In some cases these systems are not solvable with standard methods like the matrix products or the Bethe Ansatz.

work, this model was extended to also account for attachment and detachment of motors along the lattice [204]. Similarly, phenomena to those found by Muhuri [204] occur also on shrinking lattices [205], which suggests that growing and shrinking lattices with TASEP and on/off kinetics are connected by symmetry, similar to particle/hole symmetry for the case of a static lattice [198]. The growing or shrinking dynamics of lattice gases are of interest in several biological situations like bacterial flagellum growth [206] where particles diffuse through the flagellum to reach the tip of the microtubules. But also the growth of filopodia and stereocilia is an application for growing and shrinking lattice gases [207].

Besides systems, in which a lattice is *either* growing *or* shrinking as discussed above, there are also systems in which the lattice is allowed to grow *and* shrink. Thereby one has to distinguish between different molecular interactions at the dynamic lattice end: Nowak *et al.* [208] considered a fluctuating lattice, while particles are supposed to have a „stabilizing“ effect on the lattice. This model opposes the possibility of particles *destabilizing* a stable but dynamic lattice [209–212]. Alternatively, a finite run-length of particles in a transport process also may define a dynamic lattice length [213].

2.3. Domain wall theory

In this section a method is introduced that allows to determine the phase behavior of particles on growing or shrinking lattices. It extends what is known about driven system on static lattices [160], and allows to obtain the phase behavior of all the processes related to the kinesin-8 molecular motor subject to this thesis.

To this end consider the bulk current J_b to be a function of the particle current in one domain of the lattice, and a function of the probability that the tip of the lattice is occupied, $J_b(\rho_b, \rho_+)$. The dependency on the tip density arises for lattices that grow and shrink, because growing and shrinking give rise to currents away and towards the lattice tip, respectively. Growth and shrinking dynamics can thus be interpreted as parallel update of all particles in the system. To understand the phase behavior of such a system, a the domain wall theory and the extremal current principle [160, 214–216] have to be modified to account for the semi-infinite and dynamic lattice.

The domain wall velocity v_{DW} describes the movement of a domain wall

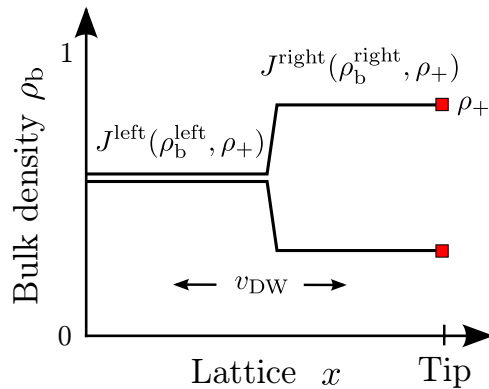


Figure 2.4.: A DOMAIN WALL in bulk of a dynamic lattice. The cartoon shows also the relevant quantities and their dependencies on bulk and tip densities.

in the bulk of the lattice. It reads

$$v_{\text{DW}} = \frac{J^{\text{left}} - J^{\text{right}}}{\rho^{\text{left}} - \rho^{\text{right}}}, \quad (2.4)$$

where *left* and *right* denote the densities and currents on either side of a domain wall on the dynamic lattice. The sign of v_{DW} determines whether a shock is traveling to the left ($v_{\text{DW}} < 0$) or the right ($v_{\text{DW}} > 0$). For an illustration see Fig. 2.4.

Evaluating all domain wall velocities with the respective current of different phases of the system, it is possible to determine if a certain tip density is stable. Because if a shock is traveling to the left, the system is taken over by J^{right} and ρ^{right} . On the other hand if the shock is traveling to the right, then the system assumes the density and currents from the left of the system J^{left} and ρ^{left} . In general, Eq. (2.4) is an arbitrary function and it is assumed that the system is semi-infinite here. However, there is evidence that this equation also holds for finite and dynamics lattice sizes, where the density at the minus end can also be included in the analysis³.

Let us turn to the second step that has to be performed to determine the complete phase diagram of the system. The stability of a particular phase depends on whether the bulk density is stable against perturbations or not. The quantity which provides this stability criterion is the collective velocity

³This statement is based on findings by Matthias Rank, who investigated finite systems of microtubules and molecular motors [217].

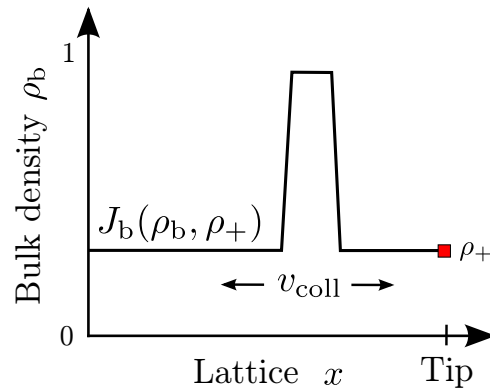


Figure 2.5.: Illustration of a DENSITY PERTURBATION in the bulk of a dynamic lattice. The collective velocity, v_{coll} , denotes the spreading velocity of the perturbation in a background density ρ_b .

of the system. It reads

$$v_{\text{coll}} = \partial_{\rho_b} J_b(\rho_b, \rho_+). \quad (2.5)$$

The collective velocity probes the stability of a small density perturbation in a background bulk density ρ_b , as illustrated in Fig. 2.5.

Generally the collective velocity indicates the phase behavior of the system. The EX phase for example is characterized by $v_{\text{coll}} < 0$, because in a high background density a small perturbation moves to the left [160]. A positive collective velocity $v_{\text{coll}} > 0$ transports particle onto the lattice and the IN phase prevails [160]. There are particular lines in the phase diagram when perturbations do not travel in any direction but rather spread out diffusively. If this is the case the system is in the maximal current phase, MC.

To conclude and summarize this chapter, a basic toolbox was presented that allows investigations of semi-infinite driven diffusive systems with non-linear boundary coupling. In the following this method is employed to the case of depolymerizing molecular motors.

Microtubules and Kinesin-8

– How Molecular Motors Influence Microtubule Dynamics

This chapter is devoted to microtubule depolymerizing molecular motor as introduced above — kinesin-8. These motors follow the rules of TASEP with attachment and detachment kinetics on the microtubule [22] and can regulate filament length *in vivo* [218].

Employing methods from non-equilibrium statistical mechanics introduced in the previous chapter 2 allows an investigation of the traffic dynamics of molecular motors on the microtubule and the specific interactions of motor proteins with the microtubule tip. This system, although relatively simple in its definitions, shows a rich phenomenology in terms of phase behavior and stochastic properties. Further, some features of the phase behavior can be attributed to different regimes that were observed in recent experiments [94]. These, and the observation of traffic jams on the microtubule [22] – as predicted in Refs. [140] and [102] – propose that the theoretical results presented here could be observed in suitable experimental setups.

Very generally it is suggested that the molecular arrangement of molecular motor and enzymes close to and at the MT tip has important consequences for their regulation, and probably also microtubule function *in vivo*. Thinking of the mitotic spindle, where microtubules find the chromosomes and attach to complex enzyme assemblies like kinetochores, it is hard to imagine that the microtubule tips are not a crowded place and come all alone. Rather it is likely that many players interact with each other, probably in even more complicated ways than we can think of at the moment [219].

However, in the following five sections the current model of depolymerizing molecular motor kinesin-8 will be stepwise passed on to higher complexity. First, a simple depolymerization assay is analyzed. Secondly, a principle for microtubule length-regulation is suggested. Third, it is unveiled that boundary conditions induce not only reliable length-regulation,

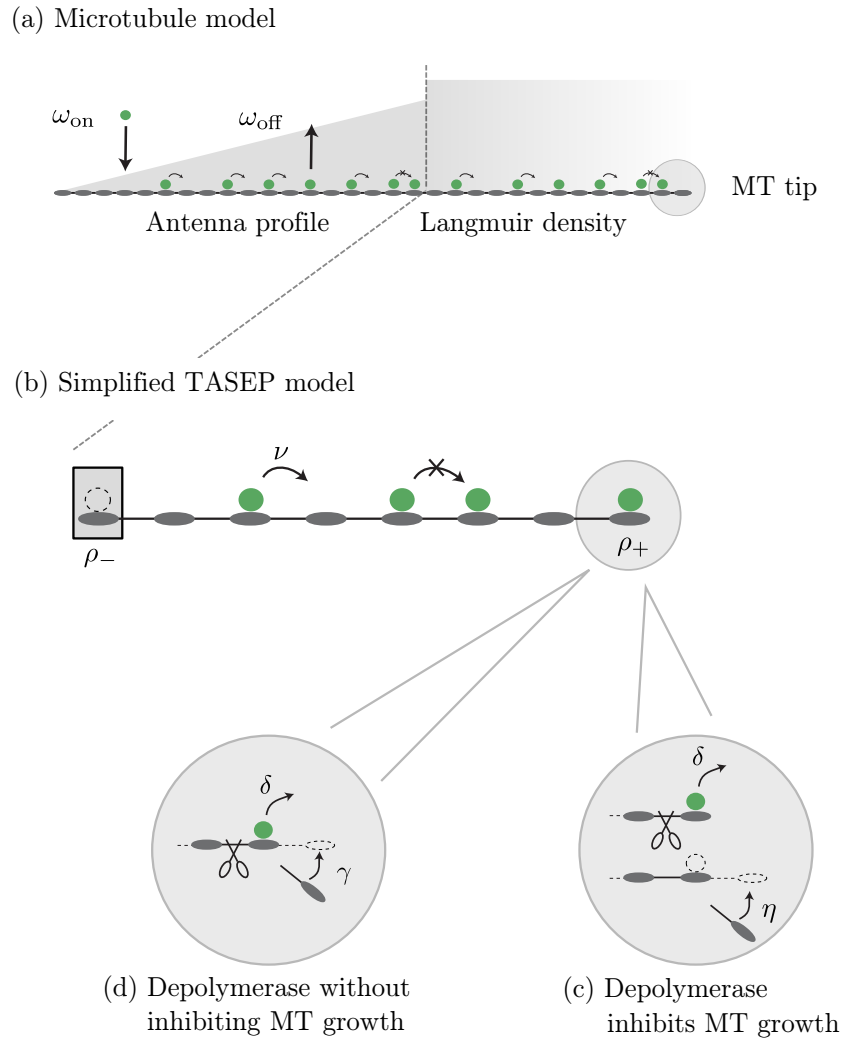


Figure 3.1.: MODEL FOR KINESIN-8 in terms of a driven lattice gas with and without particle attachment/detachment and for various growth and depolymerization scenarios at the microtubule tip.

but also persistent intermittent dynamics. Fourth, the different boundary conditions are compared with respect to their ability of length-regulation. And finally, the current understanding of mean-field theories is maxed out to learn about fluctuations at the phase transitions. Taken together the model comprises several parameters that are important to different aspects of the dynamics as summarized in Fig. 3.1. Those parameters relevant at the boundary of the system are microtubule growth rates for two different modes, one where growth is independent of a motor at the tip γ , and another mode where growth depends on the *absence* of a motor at the tip η . Further there are the motor induced depolymerization rate of the microtubule δ , and the detachment rate of motors from the microtubule tip β . In the bulk of the system two parameters are sufficient to describe the motor kinetics: the attachment of motors to the lattice ω_{on} and their detachment ω_{off} . In this work these are often written in a concentration dependent manner $c\omega_{\text{on}}$, and as the association constant $K = c\omega_{\text{on}}/\omega_{\text{off}}$.

In terms of the relevant phase transitions, the tip-related rate constants imply boundary induced phase transitions [158], and the bulk related rate constants determine the density profile on the microtubule and eventually phase coexistence [102].

3.1. Crowding of molecular motors determines microtubule depolymerization

The experiments by Varga *et al.* were the first to contain all the necessary experimental data to directly deduce a theoretical model. In particular they measured the microscopic attachment rate of motors per binding site on the microtubule, which has never been done before. Knowing this number allowed to map the dynamics onto the TASEP with Langmuir kinetics and a particular boundary condition for depolymerization.

There are essentially two regimes for depolymerization. Either the microtubule is depolymerized at the maximum depolymerization speed of the depolymerizing motor, or the depolymerization speed is determined by the time interval between two motors arriving at the microtubule tip. Further, by measuring dwell times of motors at the tip it is possible to distinguish between enzymatic depolymerization by one motor molecule or whether two consecutive motors are necessary to depolymerize the microtubule, via a „bump-off“ mechanism [94].

There is also an alternative mathematical model [87] that claims to explain kinesin-8 depolymerization data presented earlier [92]. Therein it is assumed that kinesin-8 follows the microtubule tip via processive depolymerization. At the same time this was shown to be not the case for the budding yeast kinesin-8 kip3p [94], however this case might still be relevant for different molecular motors.

On the following pages the original version of the publications is provided.

Crowding of Molecular Motors Determines Microtubule Depolymerization

Louis Reese, Anna Melbinger, and Erwin Frey*

Arnold Sommerfeld Center for Theoretical Physics and Center for NanoScience, Department of Physics, Ludwig-Maximilians-Universität München, Munich, Germany

ABSTRACT The assembly and disassembly dynamics of microtubules (MTs) is tightly controlled by MT-associated proteins. Here, we investigate how plus-end-directed depolymerases of the kinesin-8 family regulate MT depolymerization dynamics. Using an individual-based model, we reproduce experimental findings. Moreover, crowding is identified as the key regulatory mechanism of depolymerization dynamics. Our analysis reveals two qualitatively distinct regimes. For motor densities above a particular threshold, a macroscopic traffic jam emerges at the plus-end and the MT dynamics become independent of the motor concentration. Below this threshold, microscopic traffic jams at the tip arise that cancel out the effect of the depolymerization kinetics such that the depolymerization speed is solely determined by the motor density. Because this density changes over the MT length, length-dependent regulation is possible. Remarkably, motor cooperativity affects only the end-residence time of depolymerases and not the depolymerization speed.

INTRODUCTION

Microtubules (MTs) are cytoskeletal filaments that serve a central role in intracellular organization (1,2) and several cellular processes, including mitosis (3,4), cytokinesis (5), and intracellular transport (6). They can cope with these diverse tasks because they are highly dynamic structures that continually assemble and disassemble through the addition and removal of tubulin heterodimers at their ends. GTP hydrolysis is the energy source that drives switching between persistent states of growth and shrinkage, in a stochastic process termed dynamic instability (7–10). Each cellular process uses a specific set of MT-associated proteins (MAPs) to tightly regulate the rates of growth and shrinkage as well as the rate of transition between these states (11–13).

Depolymerases from the kinesin-8 and kinesin-13 protein families (e.g., Kip3p and MCAK, respectively) are important regulators of MT dynamics. They are thought to promote switching of MTs from growth to shrinkage (catastrophes) (12). Whereas MCAK lacks directed motility and diffuses along MTs (14), Kip3p is a highly processive plus-end-directed motor (15,16). Proteins from the kinesin-8 family are important for regulating MT dynamics in diverse organisms. Kif18A is a key component in chromosome positioning in mammalian cells (17–19), where it regulates plus-end dynamics. Its orthologs, the plus-end-directed motors Kip3p in budding yeast (16) and Klp5/6 in fission yeast (20–22), show depolymerizing activity. A notable feature shared by these MT plus-end depolymerases is that they depolymerize longer MTs more rapidly than they do shorter ones (15,17,21,23). A similar length-dependent regulation of MT assembly by kinesin-5 motors was observed in *in vivo* studies of chromosome congression in

budding yeast (24). The key experimental observations from *in vitro* studies of Kip3p (23) are that 1), the end-residence time of Kip3p at the tip depends on the bulk concentration of Kip3p and correlates inversely with the macroscopic depolymerization speed; and 2), the macroscopic depolymerization rate is directly proportional to the flux of Kip3p toward the MT plus-end.

It is thought that length-dependent depolymerization kinetics serves several purposes (2). For example, positioning of the nucleus at the cell center during interphase is achieved by growing MTs that push against the cell poles while remaining attached to the nucleus. A higher rate of catastrophes for longer MTs implies that shorter MTs have an increased contact time with the cell poles. Computer simulations show that this leads to a higher efficiency of nuclear positioning during interphase (25).

There is convincing experimental evidence that molecular traffic along MTs strongly affects the MT depolymerization dynamics. However, *in vitro* experiments cannot yet fully explore the underlying traffic dynamics. Theoretical investigations using individual-based models can be instrumental in furthering a mechanistic understanding of this process. Fortunately, such models can be constructed on the basis of substantial quantitative data available from *in vitro* experiments (15,23) characterizing the binding kinetics and the motor activity of plus-end-directed motors. Therefore, we sought to identify the molecular mechanisms underlying the observed correlation between depolymerization dynamics and molecular traffic along MTs.

In this study, we constructed an individual-based model for the coupled dynamics of MT depolymerization and molecular traffic of plus-end-directed motors. This model quantitatively reproduces previous experimental results (15,23). Moreover, we make precise quantitative predictions for the density profiles of molecular motors on the MT and

Submitted April 28, 2011, and accepted for publication September 2, 2011.

*Correspondence: frey@lmu.de

Editor: R. Dean Astumian.

© 2011 by the Biophysical Society
0006-3495/11/11/2190/11 \$2.00

doi: 10.1016/j.bpj.2011.09.009

demonstrate that molecular crowding and ensuing traffic jams regulate the depolymerization dynamics. We find two qualitatively distinct regimes of depolymerization dynamics: At low bulk concentrations of depolymerases, the depolymerization speed of MTs is density-limited and is a function of the bulk concentration and average motor speed alone. There is a sharp threshold in bulk depolymerase concentration above which macroscopic traffic jams emerge and the depolymerization speed is simply given by the microscopic depolymerization rate. Of note, none of these features are affected by the degree of cooperativity in the depolymerization kinetics. In contrast, the end-residence time of a depolymerase (i.e., the typical time it spends at the plus-end) is strongly correlated with cooperativity. We outline how these predictions from our theoretical analysis can be tested experimentally.

RESULTS

Model definition

We use an individual-based model, as illustrated in Fig. 1, to describe the dynamics of plus-end-directed depolymerases. Motor proteins, present at a constant bulk concentration c , are assumed to randomly bind to and unbind from the MT lattice with rates ω_a and ω_d , respectively. Bound motors are described as Poisson steppers (A more detailed biochemical model for motors on MTs has to await further experimental analysis. One of the different possible schemes has recently been studied by Klumpp et al. (26).) that processively walk along individual protofilaments toward the plus-end at an average speed u (27). These motors hinder each other sterically because individual binding sites $i = 1, \dots, L$ on each protofilament can be either empty ($n_i = 0$) or occupied by a single motor ($n_i = 1$). Because switching between protofilaments is rare (27), transport along each of the protofilaments can be taken as independent, and the model becomes effectively one-dimensional (28) (Fig. 1 B). Models of this type were recently discussed as minimal models for intracellular transport (29–32). In its given formulation, where the cytosol is considered as a homogeneous and constant reservoir of motors, it is equivalent to the driven lattice gas model known as the totally asymmetric simple exclusion process with Langmuir kinetics (TASEP/LK) (29). A central finding from this model is that the interplay between on-off (Langmuir) kinetics and directed transport along protofilaments can result in “traffic jams” in which the density profile of motors along a protofilament shows a sharp increase from a low-density to a crowded high-density regime (29,31). Crowding effects such as these (33,34) are important for a molecular understanding of MT dynamics. Previous theoretical studies on this topic largely disregarded crowding effects or considered parameter regimes in which they are unimportant (35–37). Depolymerization, including crowd-

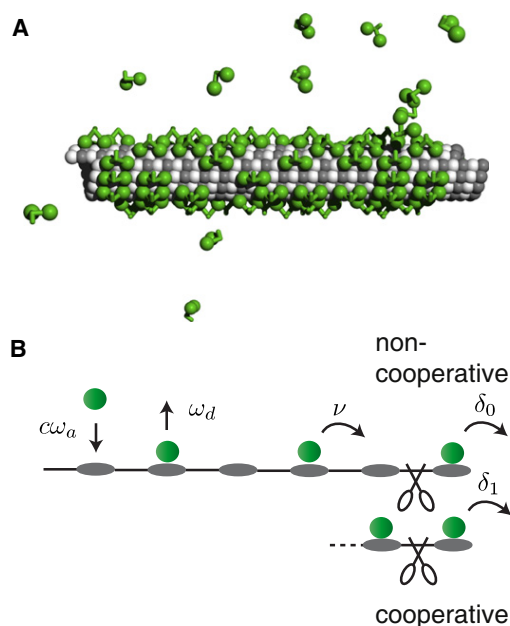


FIGURE 1 Illustration of MT and motor dynamics. Molecular motors present at concentration c randomly attach to unoccupied tubulin dimers along the MT lattice with rate ω_a . While bound, they processively move toward the plus-end at rate ν , and unbind with rate ω_d . Because motors do not switch lanes (protofilaments), the MT lattice (A) becomes effectively one-dimensional (B). Each lattice site n_i (with $i = 1, \dots, L$ numbering the sites) may be empty ($n_i = 0$) or occupied by a single motor ($n_i = 1$). At the plus-end, the motors act as depolymerases (indicated by scissors) either alone with rate δ_0 or cooperatively with rate δ_1 .

ing effects, has also been investigated for diffusive depolymerases such as MCAK (38).

At the plus-end of the systems, we consider depolymerization dynamics that arise due to the interaction of molecular motors with the MT tip. Motivated by recent experiments (23), we assume nonprocessive depolymerization, i.e., a molecular motor dissociates from the lattice after triggering depolymerization. Because the molecular mechanisms are not yet fully resolved, we study two scenarios of depolymerization (see Fig. 1 B). In the noncooperative scenario, the dissociation rate depends only on whether the last site is empty or occupied by a motor. If the last site is occupied, $n_L = 1$, the MT depolymerizes at rate δ_0 . However, recent single-molecule studies indicate that Kip3p may act cooperatively (23), which we consider as our second scenario. After arriving at the plus-end, the motor is observed to pause and depolymerize a tubulin dimer only after a second Kip3p has arrived behind it. In this scenario, a tubulin dimer is depolymerized with rate δ_1 if both the last and the second-to-last sites are occupied, $n_{L-1} = n_L = 1$. Therefore, the total depolymerization rate can be written as:

$$\Delta = \delta_0 n_L + \delta_1 n_{L-1} n_L. \quad (1)$$

For stabilized MTs, the spontaneous depolymerization rate is small (23) and thus is not considered here. The relative

magnitude of the noncooperative rate δ_0 and the cooperative rate δ_1 determines the degree of cooperativity of the depolymerization kinetics. In an average over many realizations of the stochastic process (ensemble average), the depolymerization speed V_{depol} depends on the occupation of the last two binding sites by depolymerases (Fig. 1 B):

$$V_{\text{depol}} = (\delta_0 \rho_+ + \delta_1 \kappa_+) a, \quad (2)$$

where a is the lattice spacing. Here $\rho_+ := \langle n_L \rangle$ is the probability that the last site is occupied (i.e., the expected motor density at the plus-end), and $\kappa_+ := \langle n_{L-1} n_L \rangle$ denotes the probability that both the last and second-to-last sites are occupied. We analyzed this model via stochastic simulations and analytic calculations (for further details, see the [Supporting Material](#)).

Validation of the model and its parameters

The model parameters are, as far as they are available, fixed by experimental data. The motor speed, u , the motor run length, ℓ , and motor association rate, ω_a , were measured previously (23):

$$\begin{aligned} u &= 3.2 \mu\text{m min}^{-1}, \\ \omega_a &= 24 \text{ nM}^{-1} \text{ min}^{-1} \mu\text{m}^{-1}, \\ \ell &\approx 11 \mu\text{m}. \end{aligned}$$

Using an MT lattice spacing of $a = 8.4 \text{ nm}$, we derive the corresponding parameters in our model as follows: The motor speed v corresponds to 6.35 lattice sites per second, i.e., a hopping rate of $v = u/a = 6.35 \text{ s}^{-1}$. The inverse hopping rate $\tau := v^{-1} = 0.16 \text{ s}$ and the size a of a tubulin dimer serve as our basic timescale and length scale, respectively. Then, the measured association rate corresponds to a rate $\omega_a \approx 5.3 \times 10^{-4} \text{ nM}^{-1} \text{ site}^{-1} \tau^{-1}$. The dissociation rate, $\omega_d = u/\ell$, is derived as the ratio of the mean motor speed, v , and the mean motor run length, ℓ . The latter equals 1310 lattice sites. Thus, the dissociation rate is expressed as $\omega_d \approx 7.6 \times 10^{-4} \text{ site}^{-1} \tau^{-1}$. In contrast to the transport behavior on the MT, the parameters concerning the depolymerization rates, $\delta_{0/1}$, cannot be directly extracted from experiments. However, there is evidence for a depolymerization rate as high as the motor speed, u (15,23). As a starting point for the following discussion, we tentatively take $\delta_0 = v$.

Using the above set of parameters, we now phenomenologically compare the results from numerical simulations of our model with observations from experiments. Specifically, we consider kymographs of the MT, which show how the MT length and the motor density on the MT evolve over time. For the simulation data shown in Fig. 2, we consider an MT consisting of 14 independent protofilaments and investigate the dynamics for the noncoopera-

tive scenario and a range of motor concentrations, $c = 1.2, 1.8, 2.6 \text{ nM}$ (Fig. 2, A–C). Surprisingly, as shown later, neither the cooperativity of the motors nor a decrease in the depolymerization rates led to different shapes of kymographs (see also Fig. S1).

We find an initial time period in which, starting from an empty MT lattice, the motors first fill up the lattice (39,40). This is followed by a time window in which the motor density exhibits a quasi-stationary profile, i.e., the density at a certain distance from the minus-end does not change except for boundary effects induced by the plus-end. The corresponding density profiles are illustrated in Fig. 2 E and discussed in more detail in the following section. In this quasi-stationary regime, the depolymerization dynamics shows qualitatively different behavior depending on the concentration of free motor molecules: At a low concentration, $c < 1.4 \text{ nM}$, and thus a low density of motors on the MT, depolymerization slows down gradually in the course of time (Fig. 2 A). When the motor concentration increases to larger values, $c > 1.4 \text{ nM}$, an intermediate regime emerges in which the depolymerization speed stays roughly constant (Fig. 2, B and C). Remarkably, we find that during this regime, the depolymerization speed is directly proportional to the motor density, $V_{\text{depol}}(L) = \rho_-(L) u$ (Fig. 2 D). At a third stage in the depolymerization process, there is a rather abrupt change in the depolymerization speed right where the density profile also shows a steep drop (Fig. 2, C–E). After we have elaborated more on the theoretical model, we will discuss why there is such a tight correlation between the depolymerization dynamics and the density profile.

All of these qualitative features of MT dynamics are identical to those found experimentally (15,23), and suggest that the density profile and, in particular, traffic jams formed on the MT lattice are the main determinants of the depolymerization dynamics. Moreover, the timescales of the dynamics agree quantitatively well with experimental results for the same motor concentrations (15,23). This validates our theoretical model because up to the depolymerization rate δ , all of the model parameters were derived from experimental data (23).

Density profiles at the minus-end (bulk density)

The above observations strongly point toward a tight correlation between the depolymerization speed and the motor density profile at the minus-end, $\rho_-(x)$, which we henceforth call the bulk (motor) density. The quasi-stationary bulk density profiles shown in Fig. 2 E were obtained by assuming very long lattices; effects caused by the plus-end are not visible in the vicinity of the minus-end. A more detailed discussion of these simulations can be found in the [Supporting Material](#). Because this bulk density will play an important role in the following analysis, we summarize its features here as obtained from analytical calculations detailed in the [Supporting Material](#).

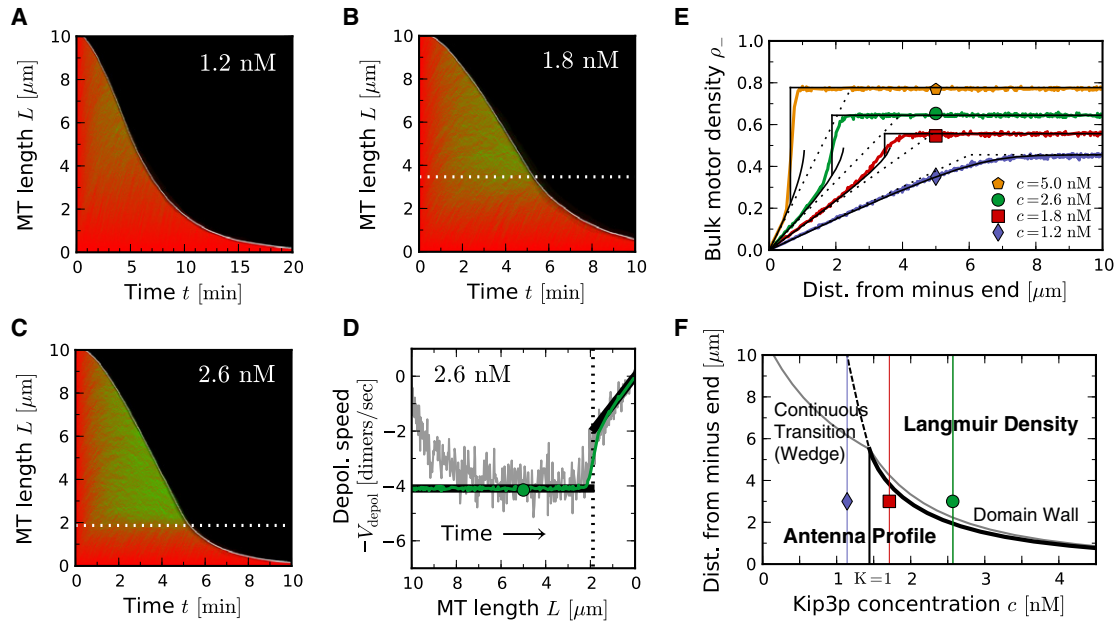


FIGURE 2 Validation of the theoretical model. (A–C) Time-space plots of stochastic simulations for a range of motor concentrations and depolymerization rate $\delta_0 = 6.35$ sites s^{-1} . The density of molecular motors is shown as the bright area (green), and the MT is shown as the dim area (red; for details, see Supporting Material). For low concentrations, $c < 1.4$ nM, depolymerization slows down gradually (23). At higher concentrations, $c > 1.4$ nM, there is a rather abrupt change in MT shortening. This change is correlated with a steep decrease in the motor density (DW), indicated as dotted lines. (D) The depolymerization speed, V_{depol} , as a function of the length of the shrinking MT $L(t)$, extracted from the simulation data shown in the kymograph (gray). The position of the DW (dotted), and the predicted depolymerization speed, $V_{\text{depol}} = u\rho(L)$ (see also Eq. 10), using the linear approximation for the motor density profile (black) and the density profile extracted from stochastic simulations (green), coincide very well with the observed depolymerization speed; $u = 6.35$ sites s^{-1} is the walking speed of the motors. (E) Density profiles at the minus-end from stochastic simulations (lines with symbols), exact solutions (solid), and linearized theory (dotted) are shown. (F) As a function of the motor concentration, c , and the distance from the minus-end, there are distinct types of density profiles. At motor concentration lower than $c = 1.4$ nM (thin black), the density of motors along the MT is low and the profile is smooth. The Langmuir density is reached continuously after a certain MT length (dashed, numerical). At high concentrations, $c > 1.4$ nM, there are two regions along the MT separated by an intervening DW (black, exact; see Supporting Material): an approximately linear antenna profile and a flat profile (Langmuir density). Linear approximations for the continuous and discontinuous transitions (Eq. 4) are shown as well (gray). Thin lines refer to the density profiles shown in E.

At the minus-end, the density profiles show an initial linear increase. This is an “antenna effect” (15), as illustrated in Fig. 3 A. Motors that attach in proximity to the MT minus-end immediately move toward the plus-end, thereby generating an approximately linearly increasing accumulation of motors. The slope is given by K/ℓ , where $K = c\omega_a/\omega_d$ denotes the binding constant. At sufficiently large distances from the minus-end, the density profile becomes flat and dominated by Langmuir kinetics with the ensuing Langmuir density:

$$\rho_{\text{La}} = \frac{K}{1+K} = \frac{c\omega_a}{c\omega_a + \omega_d}. \quad (3)$$

The full density profile is obtained by concatenating the antenna profile and the flat Langmuir profile such that the motor current is continuous along the MT. We find two qualitatively distinct scenarios (Fig. 2 E). For low concentrations of molecular motors, c , the antenna profile matches the asymptotic Langmuir density continuously, resulting in a wedge-like profile. In contrast, above a certain threshold value for the concentration, determined by the

binding constant $K_c^- = 1$, the two profiles can no longer be matched continuously and the density profile displays a sharp discontinuity, also termed a “domain wall” (DW) (29). In other words, if the Langmuir density rises above a critical value of $\rho_{\text{La}}^c = 0.5$, a crowding-induced traffic jam will result (41) (Fig. 3 A). The density profiles obtained from the analytic calculations and the stochastic simulations agree nicely, as illustrated in Fig. 2 E. In particular, the theoretical analysis gives an explicit expression for the width of the antenna-like profile:

$$\ell^- \approx \ell \begin{cases} \frac{1}{1+K} & \text{for } K < 1, \\ \frac{1}{K(1+K)} & \text{for } K > 1. \end{cases} \quad (4)$$

This result reduces to the average run length of molecular motors, $\ell = u/\omega_d$, in the limit of a very low binding constant, $K \ll 1$, where crowding effects can be neglected (37). However, with increasing K , the regime with an antenna-like profile becomes significantly shorter than ℓ (Fig. 2 F).

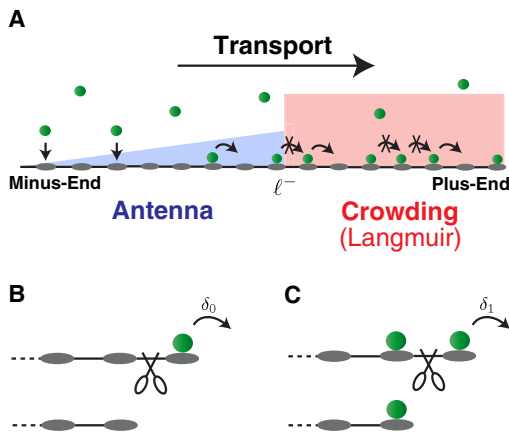


FIGURE 3 Illustration of the antenna and crowding regimes, and cooperativity. (A) Starting from an empty MT, motors start to accumulate on the MT lattice by attachment and subsequent transport to the plus-end. The combined effect of Langmuir kinetics and steric exclusion between the motors leads to two sharply separated regimes. Starting from the minus-end, the motor density increases linearly (antenna profile). At a certain critical length ℓ^- , a macroscopic traffic jam arises because particles hinder each other and crowding dominates the MT density. (B and C) Illustration of noncooperative (B, nc) and fully cooperative (C, fc) depolymerization kinetics. With regard to the depolymerization speed, both models are effectively equal (see main text).

Depolymerization dynamics is independent of cooperativity

We now address how the cooperativity of the depolymerization kinetics affects the macroscopic depolymerization speed. There are two limiting cases: noncooperative depolymerization (nc) with $(\delta_0, \delta_1) = (\delta, 0)$, and fully cooperative depolymerization (fc) with $(\delta_0, \delta_1) = (0, \delta)$ (for an illustration, see Fig. 3, B and C). Remarkably, we find from our stochastic simulations, shown in Fig. 4, that there is no difference in depolymerization speed for these two limiting cases. Even when the depolymerization dynamics contains cooperative as well as noncooperative terms, we do not find any significant differences in the depolymerization speed (Fig. 4 B).

This observation from our stochastic simulations can be explained by the following molecular mechanism: Consider a model with fully cooperative depolymerization kinetics. Then, after the first motor has arrived at the plus-end, the terminal site of the MT will remain occupied from that time on. Depolymerization only occurs if another motor arrives at the second-to-last site. In other words, while the last site remains occupied, the second-to-last site triggers the depolymerization. Hence, as far as the depolymerization speed is concerned, the fully cooperative model is identical to a noncooperative model with the same molecular rate δ . In the noncooperative model, the terminal tubulin dimer is removed at rate δ once a molecular motor has arrived at the last site (Fig. 3 B). In the fully cooperative model, the terminal tubulin dimer is removed once a molecular motor

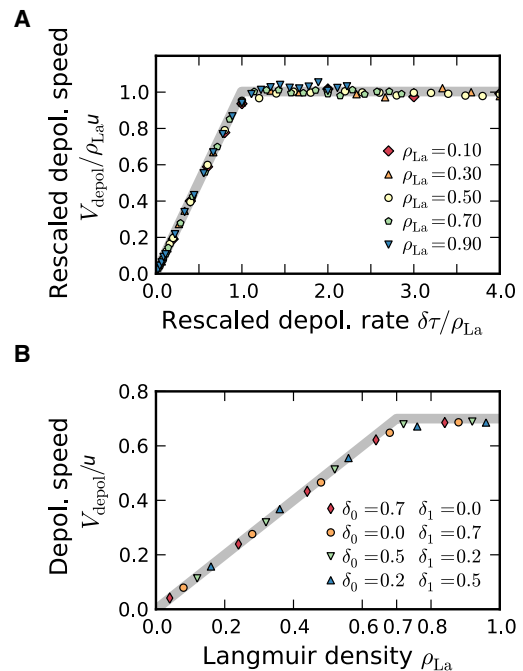


FIGURE 4 Scaling plot for the depolymerization speed V_{depol} . (A) Upon rescaling, both the macroscopic depolymerization speed, V_{depol} , and the microscopic depolymerization rate, δ , with the Langmuir density, ρ_{La} , all data collapse onto one universal scaling function \mathcal{V} (solid gray). A sharp transition at $\delta\tau = \rho_{\text{La}}^*$ distinguishes the rate-limited regime from the density-limited regime. (B) Comparison of cooperative and noncooperative depolymerization, with the macroscopic depolymerization speed V_{depol} as a function of Langmuir density ρ_{La} . For $\delta := \delta_0 + \delta_1 = 0.7\nu$ different degrees of cooperativity are displayed as indicated in the graph.

has arrived at the second-to-last site next to a permanently occupied last site (Fig. 3 C).

Depolymerization dynamics is strongly affected by crowding

To gain further insights in the correlation between the depolymerization speed and the density of motors on the MT, we performed stochastic simulations focusing on the MT plus-end by regarding the dynamics in a comoving frame. Instead of simulating the full-length MT with an antenna profile and a subsequent flat Langmuir density, we considered a reduced model in which the density at the left end is set equal to the Langmuir density ρ_{La} . For long MTs, the Langmuir density is always reached, so that the reduced system is fully equivalent to the original model. Our simulations show two clearly distinct regimes of depolymerization dynamics (Fig. 4): For small, microscopic depolymerization rates, $\delta\tau < \rho_{\text{La}}$, the polymerization speed is rate-limited: $V_{\text{depol}} = a\delta$. In contrast, for rates $\delta\tau > \rho_{\text{La}}$, the depolymerization speed is density-limited, and the Langmuir density is the limiting factor: $V_{\text{depol}} = \rho_{\text{La}}u$. The boundary between the two regimes is remarkably sharp and given by

$$\rho_{La}^* = \delta\tau. \quad (5)$$

This implies that the depolymerization speed can switch between being density-limited and rate-limited by changing the concentration c or the values of the biochemical rates of depolymerases binding to and unbinding from the MT lattice. Overall, the depolymerization speed obeys a scaling law

$$V_{\text{depol}} = \rho_{La} u \mathcal{V}\left(\frac{\delta\tau}{\rho_{La}}\right) = \begin{cases} a\delta & \text{for } \delta\tau \leq \rho_{La} \\ \rho_{La} u & \text{for } \delta\tau > \rho_{La} \end{cases}, \quad (6)$$

where $\mathcal{V}(x)$ is a universal scaling function with the simple form $\mathcal{V}(x) = x$ for $x < 1$ and $\mathcal{V}(x) = 1$ for $x > 1$. Experimentally, this implies that one should find data collapse when using such a scaling plot (Fig. 4 A).

To gain a molecular understanding of these remarkable features of the depolymerization speed, one needs to have a closer look at the density profile of the molecular motors at the MT tip. If the depolymerization rate is small, $\delta < \nu$, motors leave the tip more slowly than they arrive. Therefore, the MT tip acts as a bottleneck for molecular transport that disturbs the density profiles either locally or macroscopically. A weak bottleneck induces a local perturbation (“spike”) (33). These spikes are sharp changes of the density profile with a typical extension that scales with the size of a heterodimer. However, if the strength of a bottleneck exceeds a threshold value, the spike extends to a macroscopic perturbation (“traffic jam”) (33). Fig. 5 A illustrates how, for a given Langmuir density, $\rho_{La} = 2/3$, the effect on the density profile changes from a spike (blue) to an extended traffic jam (red and green) when the depolymerization rate is δ .

Let us now analyze the conditions and consequences of such bottlenecks in more detail. Suppose we are in a parameter regime where the plus-end disturbs the density profile only locally, i.e., on the scale of a heterodimer. Then, we may take the bulk density to be equal to the Langmuir density, ρ_{La} , up to the last site (the plus-end) where it jumps to some higher or lower value ρ_+ . The particle loss current at the plus-end due to MT depolymerization is then given by

$$J_{\text{depol}} = (1 - \rho_{La})\rho_+\delta. \quad (7)$$

The factor $1 - \rho_{La}$ arises because the particle number decreases only if a particle depolymerizes the MT and the second-to-last site, $L - 1$, is unoccupied. Otherwise, the depolymerization dynamics and the associated frame shift of the MT lattice do not change the occupation of the last site. This particle loss has to be balanced by the incoming particle flux,

$$J_{La} = \rho_{La}(1 - \rho_{La})\nu. \quad (8)$$

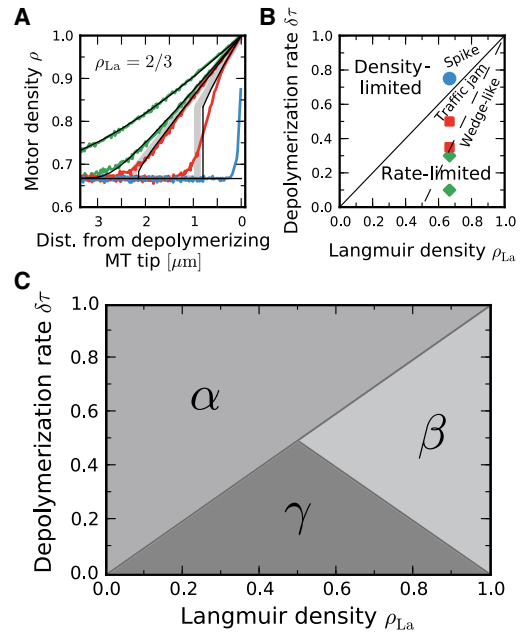


FIGURE 5 Density profiles at the plus-end, corresponding phase diagram, and depolymerization scenarios. (A) Density profiles at the MT plus-end in the comoving frame for $c = 2.9$ nM, and $\delta = 0.1, 0.3$ (left), 0.35, 0.5 (middle), and 0.8ν (right). The simulation results and analytical solutions (black; see Supporting Material) agree nicely. (B) Depending on the value of δ and the density of motors, ρ_{La} , there are three different classes of density profiles at the plus-end: wedge-like (diamonds), traffic jams with a DW (square), and spikes (circles). The transition between profiles with an extended traffic jam and a localized spike (solid line) also marks a qualitative change in the depolymerization speed. Whereas the depolymerization speed is density-limited in the spike regime, it is rate-limited in the DW and wedge regime. Symbols correspond to parameters as displayed in panel A. (C) Depending on the value of δ and the density of motors, ρ_{La} , there are three different regimes of depolymerization dynamics. In regime α , depolymerization is density-limited for arbitrary MT length. In contrast, depolymerization is rate-limited for long MTs and density-limited for short MTs in regimes β and γ . For details, see the main text.

Equating these particle fluxes (Eqs. 7 and 8) implies the following condition for the motor density at the plus-end:

$$\rho_+ = \begin{cases} \frac{\rho_{La}}{\delta\tau} & \text{for } \rho_{La} \leq \delta\tau \\ 1 & \text{for } \rho_{La} > \delta\tau \end{cases}, \quad (9)$$

where the fact that the motor density is bounded $\rho_+ \leq 1$ is already accounted for. The particle density on the last site, in turn, determines the depolymerization speed. For $\rho_{La} < \delta\tau$, one obtains according to Eqs. 2 and 9:

$$V_{\text{depol}} = \rho_+\delta a = \rho_{La} u. \quad (10)$$

Remarkably, here the effect of the depolymerization kinetics (δ) cancels out such that the macroscopic depolymerization speed is independent of the molecular details of depolymerization kinetics and is solely determined by the Langmuir density, i.e., the motor density in the bulk,

$\rho_-(x)$, and not at the tip of the MT. This result crucially depends on the presence of a microscopic spike. It explains the hitherto puzzling experimental result that the depolymerization speed is directly proportional to the bulk motor current along the MT (23) (Fig. S2).

Because the density is bounded, $\rho_+ \leq 1$, density profiles with a spike are only possible if the densities are not too large, $\rho_{La} < \delta\tau$. This is the case for the blue curve in Fig. 5 A. For densities exceeding the critical density, $\rho_{La}^* = \delta\tau$, the bottleneck-induced perturbation in the density profile can no longer remain a local spike, but has to become macroscopic in extent (33) (see *green and red curves* in Fig. 5 A and the Supporting Material).

One finds that over an extended region, the binding sites at the plus-end then remain permanently occupied such that $\rho_+ = 1$. This immediately implies that the depolymerization speed becomes density-independent and proportional to the microscopic depolymerization rate:

$$V_{\text{depol}} = a\delta. \quad (11)$$

There is a tight correlation between the shape of the density profiles and the macroscopic depolymerization speed. The analytic results explain the molecular mechanism behind the numerically observed scaling law (Eq. 6), with a sharp transition from density-regulated to rate-limited depolymerization dynamics at a critical value of $\rho_{La}^* = \delta\tau$ (cf. the classification of density profiles and depolymerization regimes shown in Fig. 5 B).

Actually, the above calculations can be generalized to the regime in which the motor density exhibits an antenna-like linear profile, i.e., for MT length shorter than ℓ^- . As detailed in the Supporting Material, we find that the depolymerization speed is rate-limited, $V_{\text{depol}} = a\delta$, if MTs are shorter than ℓ^- but still longer than a second threshold length:

$$\ell_d := \frac{\delta a}{c\omega_a} = \frac{\ell \delta\tau}{K}. \quad (12)$$

In contrast, for $\ell_d > \ell^-$, the depolymerization speed in the antenna regime is always length-dependent and strictly follows the shape of the antenna profile, $\rho_-(x)$:

$$V_{\text{depol}} = \rho_-(L)u. \quad (13)$$

Using Eq. 4, the condition $\ell_d > \ell^-$ on the threshold lengths is equivalent to $\delta\tau > \rho_{La}$ for $K < 1$, and to $\delta\tau > 1 - \rho_{La}$ for $K > 1$.

Combining all of the above results, we find three mechanisms that govern the depolymerization dynamics, as illustrated in Fig. 5 C:

α . For $\delta\tau > \rho_{La}$, the depolymerization speed is always density-regulated and given by $V_{\text{depol}}(L) = \rho_-(L)u$, where L is the time-dependent length of the MT. In this parameter regime, the depolymerization speed is a direct map of the bulk motor density profile on the

MT, $\rho_-(x)$, a feature that can be exploited experimentally to measure the profile.

- β . For $\rho_{La} > \delta\tau > 1 - \rho_{La}$, the depolymerization speed is rate-limited for MTs longer than ℓ^- , and becomes density-limited as soon as the MT length falls below ℓ^- , where the density profile is antenna-like. This implies that there is a discontinuous jump in the depolymerization speed right at $L = \ell^-$.
- γ . Finally, for all other values of $\delta\tau$, the depolymerization speed of the MT remains rate-limited for lengths larger than a threshold length ℓ_d . At ℓ_d , which is smaller than ℓ^- in this parameter regime, there is again a discontinuous jump to a density-limited depolymerization dynamics.

If the depolymerization rate is larger or equal to the hopping rate of molecular motors, $\delta\tau \geq 1$, then $\delta\tau > \rho_{La}$ is always obeyed simply because $\rho_{La} \leq 1$. In this regime, all of the molecular details of the depolymerization kinetics are irrelevant. Neither the cooperativity nor the actual value of the depolymerization rate matters in terms of the depolymerization speed; instead, only the bulk density regulates the speed. Note that this was the case for the data shown in Fig. 2, where we tentatively made the parameter choice $\delta\tau = 1$. If the motors are faster than the depolymerization process, $\delta\tau < 1$, we have to distinguish between the parameter regimes (α , β , and γ , Fig. 5 C). Here the value of the depolymerization rate matters if the bulk density exceeds a certain threshold concentration, $\rho_{La} > \delta\tau$, and the MTs are long enough. Finally, the depolymerization speed always becomes density-dependent and hence length-dependent if the MT length is short enough; the corresponding threshold length is $\ell_{\text{reg}} = \min[\ell^-, \ell_d]$.

The end-residence time strongly depends on cooperativity

In contrast to the depolymerization speed, the mean end-residence time τ_{res} is strongly affected by the degree of cooperativity. Fig. 6 displays τ_{res} as obtained from our stochastic simulations for noncooperative and fully cooperative depolymerization kinetics. Our simulations show that the end-residence time for the fully cooperative model is identical to the average lifetime of a terminal tubulin dimer $\tau_{\text{res}}^{\text{fc}} = \tau_d := a/V_{\text{depol}}$ (Fig. 6 A). Even for the noncooperative model, $\tau_{\text{res}}^{\text{nc}}$ equals τ_d for large residence times and deviates from it only at small values. The relatively sharp transition to a constant lifetime of the terminal tubulin dimer occurs right at $\tau_{\text{res}}^{\text{nc}} = \tau/\rho_{La}$, i.e., the end-residence time equals the waiting time for a molecular motor to arrive at the MT tip. For $\tau_{\text{res}}^{\text{nc}} < \tau/\rho_{La}$, the lifetime of the terminal tubulin dimer is identical to the arrival time (Fig. 6, A and B). Once the arrival time becomes shorter than the inverse depolymerization rate, the end-residence time levels off at $\tau_{\text{res}}^{\text{nc}} = 1/\delta$. These results show that the dependence of the end-residence time on density can be used to quantify the

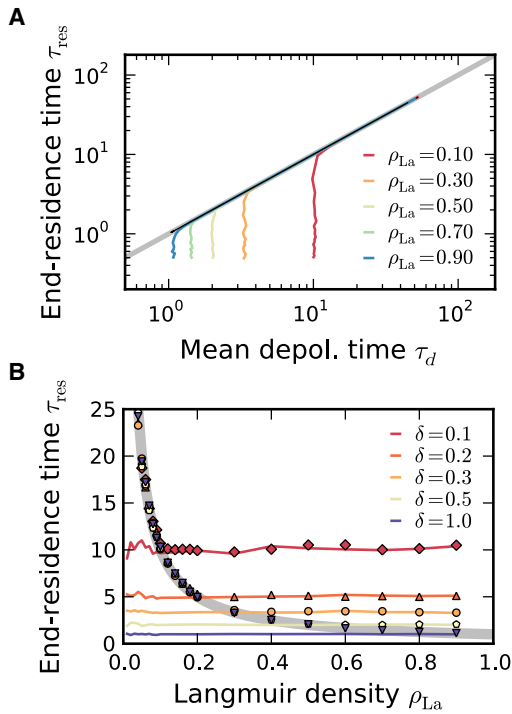


FIGURE 6 Motor end-residence times τ_{res} for cooperative and noncooperative depolymerization. (A) Mean end-residence time τ_{res} plotted against the mean depolymerization time τ_d . Data were recorded for a range of depolymerization rates $\delta = 0.02 \dots 2\nu$. Noncooperative (shaded) and cooperative (black) dynamics are shown for different densities. (B) Mean end-residence time τ_{res} as a function of the Langmuir density ρ_{La} for various depolymerization rates (in units of ν). For noncooperative depolymerization, τ_{res} is given by $1/\delta$ (shaded lines). For the fully cooperative scenario (symbols), τ_{res} depends on whether the system is in the density-limited ($\delta\tau > \rho_{\text{La}}$) or in the rate-limited ($\delta\tau < \rho_{\text{La}}$) regime. While, for $\delta\tau > \rho_{\text{La}}$, the end-residence time is given by $\tau_{\text{res}} = \tau/\rho_{\text{La}}$ (solid gray line), for $\delta\tau < \rho_{\text{La}}$, it is density-independent and determined by the microscopic depolymerization rate $\tau_{\text{res}} = 1/\delta$ (see also Eq. 16).

degree of cooperativity. This would require experiments with motor densities on the MT larger than those studied up to now (15,23).

The observation that the depolymerization speed is independent of the degree of cooperativity seems to be at odds with the experimental finding that the end-residence time, τ_{res} , of Kip3p depends on the total Kip3p concentration and is inversely proportional to the macroscopic depolymerization speed (23). Actually, however, there is no contradiction and the findings are readily explained within our theoretical model: For a noncooperative model, $\tau_{\text{res}}^{\text{nc}}$ is simply given by the depolymerization rate, because after they arrive, the particles stay at the tip until they depolymerize the MT:

$$\tau_{\text{res}}^{\text{nc}} = \frac{1}{\delta}. \quad (14)$$

For a fully cooperative model, $\tau_{\text{res}}^{\text{fc}}$ depends not only on δ but also on the rate at which the second-to-last site

becomes populated. Say the probability for the second-to-last site to be occupied is ρ_+ . Then, $\tau_{\text{res}}^{\text{fc}}$ is given by a sum of two contributions arising from the cases in which the second-to-last site is empty or occupied, respectively:

$$\tau_{\text{res}}^{\text{fc}} = (1 - \rho_+) \left(\frac{\tau}{\rho_{\text{La}}} + \frac{1}{\delta} \right) + \rho_+ \frac{1}{\delta}. \quad (15)$$

If the second-to-last site is empty (which is the case with probability $1 - \rho_+$) τ_{res} is the sum of arrival time τ/ρ_{La} and depolymerization time $1/\delta$. Otherwise, the end-residence time τ_{res} simply equals $1/\delta$.

As shown in the previous section, two distinct scenarios arise: For small bulk densities such that $\rho_{\text{La}} < \delta\tau$, the density profile at the plus-end exhibits a microscopic spike with $\rho_+ = \rho_{\text{La}}/\delta\tau$. For large densities, $\rho_{\text{La}} > \delta\tau$, a macroscopic traffic jam emerges such that $\rho_+ = 1$. This result obtained for the motor density at the MT tip (Eq. 9) may now be used to calculate $\tau_{\text{res}}^{\text{fc}}$ using Eq. 15:

$$\tau_{\text{res}}^{\text{fc}} = \begin{cases} \frac{1}{\delta} & \text{for } \rho_{\text{La}} > \delta\tau, \\ \frac{\tau}{\rho_{\text{La}}} & \text{else.} \end{cases} \quad (16)$$

This agrees well with the results from stochastic simulations displayed in Fig. 6. A comparison with Eq. 6 shows that the end-residence time equals the typical depolymerization time, i.e., the expected lifetime of a terminal tubulin dimer, $\tau_{\text{res}}^{\text{fc}} = \tau_d$. This is in agreement with experimental findings regarding the unbinding rate of motors at the plus-end (23) and strongly supports the conclusion that depolymerization of MTs by Kip3p is fully cooperative. Varga et al. (23) measured the end-residence time of motors on double stabilized MTs, i.e., where depolymerization is switched off. They observed that the end-residence time is inversely correlated with the concentration of Kip3p, and fit their data with an exponential using a cutoff. This is in accordance with our results shown in Fig. 6 B. However, because depolymerization has been switched off in the experiment, the rate δ , corresponding to the cutoff, now has to be interpreted as an unbinding-rate of motors at the plus-end. It would be highly interesting to design experiments in which the depolymerization kinetics remains switched on, because this would allow one to measure the magnitude of the microscopic depolymerization rate δ .

DISCUSSION

In this work, we analyzed the effect of crowding and cooperativity on the depolymerization dynamics of MTs. To that end, we constructed an individual-based model for the coupled dynamics of plus-end-directed motor traffic and MT depolymerization kinetics. The model is based on well-established molecular properties of motors from the

kinesin-8 family, i.e., the motors move on single protofilaments with high processivity at an average speed u , and exchange of motors between the bulk and the MT follows Langmuir kinetics. All parameters of the model, including the average walking speed, run length, and attachment rate, were directly extracted from available *in vitro* data (23). We validated our model by reproducing the onset of length-dependent depolymerization as studied recently (15,23). Without using any additional fitting parameter, we found the same regimes of density profiles and ensuing depolymerization dynamics as in the experiments, i.e., a linear antenna-profile with a length-dependent depolymerization speed and a flat profile with a constant depolymerization speed. Moreover, we identified a threshold density of motors above which a crowding-induced traffic jam emerges at the minus-end. The predicted shape and extent of these traffic jams should be amenable to experiments that raise the depolymerase concentration c or change its rates of binding to and unbinding from the MT.

The interplay between motor traffic and depolymerization kinetics at the MT plus-end leads to strong correlations between the depolymerization dynamics and density profiles of depolymerases. The plus-end acts as a bottleneck, and crowding effects cause traffic jams. We find two qualitatively distinct regimes: Motor densities below a critical threshold value, $\rho_{La}^* = \delta\tau$, always show a local spike-like perturbation at the plus-end, the extent of which is the size of a heterodimer. Above this threshold density, macroscopic traffic jams may emerge. These distinct density profiles at the plus-end affect the depolymerization speed and the end-residence time in qualitatively different ways. A quantitative analysis of the model using stochastic simulations as well as analytical calculations led to the following main results:

The end-residence time of a depolymerase strongly depends on the degree of cooperativity. Whereas for noncooperative depolymerization kinetics the end-residence time is given by the microscopic depolymerization rate δ , it is density-dependent in the fully cooperative case: Increasing the Langmuir density above the threshold value $\rho_{La}^* = \delta\tau$, the end-residence time changes from being inversely proportional to the density ρ_{La} to a constant value δ^{-1} . These results suggest an interesting way to determine the cooperativity of depolymerization kinetics and measure the value of the depolymerization rate δ . Although when the concentration c is increased, the end-residence time should be independent of concentration for noncooperative kinetics, it should strongly depend on concentration in the cooperative case. Experimental evidence points toward the latter (23).

In contrast, the depolymerization speed does not depend on the degree of cooperativity of the depolymerization kinetics. Noncooperative and fully cooperative versions of the model give identical results. As a function of depolymerase concentration and the MT length, the depolymerization

dynamics exhibits two qualitatively distinct regimes: The depolymerization speed is either density-limited and determined by the bulk density of molecular motors, $\rho_-(x)$, or rate-limited and dictated by the value of the microscopic depolymerization rate, δ . Both regimes emerge due to crowding of molecular motors at the plus-end, which acts as a bottleneck for molecular traffic.

Density-limited regimes are correlated with microscopic traffic jams (“spikes”) at the plus-end: The density profile self-organizes into a shape that cancels out all the effects of the depolymerization kinetics such that the depolymerization speed is solely determined by the bulk motor density, $\rho_-(x)$, and the average motor speed, u . Note that only in this regime length-dependent regulation is possible, because the density changes over the MT length. As emphasized above, if the depolymerization rate δ is larger than the hopping rate of the molecular motors, $\delta > \nu$, this remains the only regime of depolymerization dynamics. Then, the depolymerization speed is limited by the velocity of the plus-end directed motors, which is in accordance with recent experimental findings for Kip3p (23). In a parameter regime where motors depolymerize more slowly than they walk, $\delta < \nu$, there is a second rate-limited regime above the threshold density ρ_{La}^* and for MTs longer than some threshold length l_{reg} where $V_{depol} = a\delta$. In this regime, the plus-end acts as a strong bottleneck for molecular traffic. This causes a macroscopic traffic jam such that the motor density steeply rises to full occupation of all lattice sites at the plus-end of the MT. The cellular system sacrifices its ability to regulate the speed of depolymerization and only regains it once the MT length falls below l_{reg} , where the depolymerization speed again becomes density-regulated. From an evolutionary perspective, one might speculate that the system has evolved toward $\delta = \nu$, because this would allow regulation of the depolymerization dynamics over the broadest possible range.

Beyond these observations, other predictions of our stochastic model can be put to the test in experiments. By varying the motor concentration, two interesting observations could be made: First, the phase diagram for the density profiles at the minus-end could be scrutinized experimentally. Second, the predictions on the density-profiles at the plus-end and their predicted strong correlations to the macroscopic depolymerization dynamics might be accessible to single-molecule studies. Manipulation of the molecular properties of the motor (e.g., the run length, attachment rate (42), average speed, and depolymerization rate) would change the intrinsic biochemical rates of the system and could potentially lead to new parameter regimes. In addition, our results regarding the length and concentration dependence of the depolymerization process might be relevant *in vivo*, e.g., for mitotic chromosome alignment (18). In our theoretical studies, we explored the full parameter range, and therefore clear predictions are available for comparison.

We believe that in a more general context, our theoretical work provides new conceptual insights into the role of collective and cooperative effects in MT assembly and disassembly dynamics. Future research could focus on the antagonism between polymerases and depolymerases (12,43,44), spontaneous MT dynamics mediated by GTP hydrolysis, the abundance of molecular motors in a cell, or more-detailed modeling of molecular motors (26). This may finally lead to a molecular understanding of the regulatory mechanisms of cellular processes in which MT dynamics plays a central role.

SUPPORTING MATERIAL

Additional details, 37 equations, one table, two figures, and references are available at [http://www.biophysj.org/biophysj/supplemental/S0006-3495\(11\)01063-0](http://www.biophysj.org/biophysj/supplemental/S0006-3495(11)01063-0).

The authors thank Cécile Leduc for discussions; Varga et al. (23) for kindly providing their data; Ulrich Gerland, Günther Woehlke, and Jonas Cremer for critical readings of the original manuscript; Anton Winkler for helpful suggestions on the revised manuscript; and Andrej Vilfan for drawing Fig. 1 A.

This work was supported by the Deutsche Forschungsgemeinschaft in the framework of the SFB 863 and the German Excellence Initiative via the program “Nanosystems Initiative Munich”.

REFERENCES

- Hayles, J., and P. Nurse. 2001. A journey into space. *Nat. Rev. Mol. Cell Biol.* 2:647–656.
- Tolić-Nørrelykke, I. M. 2010. Force and length regulation in the microtubule cytoskeleton: lessons from fission yeast. *Curr. Opin. Cell Biol.* 22:21–28.
- Sharp, D. J., G. C. Rogers, and J. M. Scholey. 2000. Microtubule motors in mitosis. *Nature.* 407:41–47.
- Karsenti, E., and I. Vernos. 2001. The mitotic spindle: a self-made machine. *Science.* 294:543–547.
- Eggert, U. S., T. J. Mitchison, and C. M. Field. 2006. Animal cytokinesis: from parts list to mechanisms. *Annu. Rev. Biochem.* 75:543–566.
- Hirokawa, N., Y. Noda, ..., S. Niwa. 2009. Kinesin superfamily motor proteins and intracellular transport. *Nat. Rev. Mol. Cell Biol.* 10:682–696.
- Mitchison, T., and M. Kirschner. 1984. Dynamic instability of microtubule growth. *Nature.* 312:237–242.
- Dogterom, M., and S. Leibler. 1993. Physical aspects of the growth and regulation of microtubule structures. *Phys. Rev. Lett.* 70:1347–1350.
- Desai, A., and T. J. Mitchison. 1997. Microtubule polymerization dynamics. *Annu. Rev. Cell Dev. Biol.* 13:83–117.
- Howard, J., and A. A. Hyman. 2003. Dynamics and mechanics of the microtubule plus end. *Nature.* 422:753–758.
- Wordeman, L. 2005. Microtubule-depolymerizing kinesins. *Curr. Opin. Cell Biol.* 17:82–88.
- Howard, J., and A. A. Hyman. 2007. Microtubule polymerases and depolymerases. *Curr. Opin. Cell Biol.* 19:31–35.
- Howard, J., and A. A. Hyman. 2009. Growth, fluctuation and switching at microtubule plus ends. *Nat. Rev. Mol. Cell Biol.* 10:569–574.
- Helenius, J., G. Brouhard, ..., J. Howard. 2006. The depolymerizing kinesin MCAK uses lattice diffusion to rapidly target microtubule ends. *Nature.* 441:115–119.
- Varga, V., J. Helenius, ..., J. Howard. 2006. Yeast kinesin-8 depolymerizes microtubules in a length-dependent manner. *Nat. Cell Biol.* 8:957–962.
- Gupta, Jr., M. L., P. Carvalho, ..., D. Pellman. 2006. Plus end-specific depolymerase activity of Kip3, a kinesin-8 protein, explains its role in positioning the yeast mitotic spindle. *Nat. Cell Biol.* 8:913–923.
- Mayr, M. I., S. Hümmer, ..., T. U. Mayer. 2007. The human kinesin Kif18A is a motile microtubule depolymerase essential for chromosome congression. *Curr. Biol.* 17:488–498.
- Stumpff, J., G. von Dassow, ..., L. Wordeman. 2008. The kinesin-8 motor Kif18A suppresses kinetochore movements to control mitotic chromosome alignment. *Dev. Cell.* 14:252–262.
- Du, Y., C. A. English, and R. Ohi. 2010. The kinesin-8 Kif18A dampens microtubule plus-end dynamics. *Curr. Biol.* 20:374–380.
- Unsworth, A., H. Masuda, ..., T. Toda. 2008. Fission yeast kinesin-8 Klp5 and Klp6 are interdependent for mitotic nuclear retention and required for proper microtubule dynamics. *Mol. Biol. Cell.* 19:5104–5115.
- Tischer, C., D. Brunner, and M. Dogterom. 2009. Force- and kinesin-8 dependent effects in the spatial regulation of fission yeast microtubule dynamics. *Mol. Syst. Biol.* 5:250.
- Grissom, P. M., T. Fiedler, ..., J. R. McIntosh. 2009. Kinesin-8 from fission yeast: a heterodimeric, plus-end-directed motor that can couple microtubule depolymerization to cargo movement. *Mol. Biol. Cell.* 20:963–972.
- Varga, V., C. Leduc, ..., J. Howard. 2009. Kinesin-8 motors act cooperatively to mediate length-dependent microtubule depolymerization. *Cell.* 138:1174–1183.
- Gardner, M. K., D. C. Bouck, ..., D. J. Odde. 2008. Chromosome congression by kinesin-5 motor-mediated disassembly of longer kinetochore microtubules. *Cell.* 135:894–906.
- Foethke, D., T. Makushok, ..., F. Nédélec. 2009. Force- and length-dependent catastrophe activities explain interphase microtubule organization in fission yeast. *Mol. Syst. Biol.* 5:241.
- Klumpp, S., Y. Chai, and R. Lipowsky. 2008. Effects of the chemomechanical stepping cycle on the traffic of molecular motors. *Phys. Rev. E.* 78:041909.
- Howard, J. 1996. The movement of kinesin along microtubules. *Annu. Rev. Physiol.* 58:703–729.
- Ray, S., E. Meyhöfer, ..., J. Howard. 1993. Kinesin follows the microtubule’s protofilament axis. *J. Cell Biol.* 121:1083–1093.
- Parmeggiani, A., T. Franosch, and E. Frey. 2003. Phase coexistence in driven one-dimensional transport. *Phys. Rev. Lett.* 90:086601.
- Parmeggiani, A., T. Franosch, and E. Frey. 2004. Totally asymmetric simple exclusion process with Langmuir kinetics. *Phys. Rev. E.* 70:046101.
- Lipowsky, R., S. Klumpp, and T. M. Nieuwenhuizen. 2001. Random walks of cytoskeletal motors in open and closed compartments. *Phys. Rev. Lett.* 87:108101.
- Klumpp, S., and R. Lipowsky. 2003. Traffic of molecular motors through tube-like compartments. *J. Stat. Phys.* 113:233–268.
- Pierobon, P., M. Mabilia, ..., E. Frey. 2006. Bottleneck-induced transitions in a minimal model for intracellular transport. *Phys. Rev. E.* 74:031906.
- Telley, I. A., P. Bieling, and T. Surrey. 2009. Obstacles on the microtubule reduce the processivity of kinesin-1 in a minimal in vitro system and in cell extract. *Biophys. J.* 96:3341–3353.
- Govindan, B. S., M. Gopalakrishnan, and D. Chowdhury. 2008. Length control of microtubules by depolymerizing motor proteins. *Europhys. Lett.* 83:40006.
- Brun, L., B. Rupp, ..., F. Nédélec. 2009. A theory of microtubule catastrophes and their regulation. *Proc. Natl. Acad. Sci. USA.* 106:21173–21178.

37. Hough, L. E., A. Schwabe, ..., M. D. Betterton. 2009. Microtubule depolymerization by the kinesin-8 motor Kip3p: a mathematical model. *Biophys. J.* 96:3050–3064.
38. Klein, G. A., K. Kruse, ..., F. Jülicher. 2005. Filament depolymerization by motor molecules. *Phys. Rev. Lett.* 94:108102.
39. Vilfan, A., E. Frey, ..., E. Mandelkow. 2001. Dynamics and cooperativity of microtubule decoration by the motor protein kinesin. *J. Mol. Biol.* 312:1011–1026.
40. Frey, E., and A. Vilfan. 2002. Anomalous relaxation kinetics of biological lattice-ligand binding models. *Chem. Phys.* 284:287–310.
41. Frey, E., A. Parmeggiani, and T. Franosch. 2004. Collective phenomena in intracellular processes. *Genome Inform.* 15:46–55.
42. Cooper, J. R., M. Wagenbach, ..., L. Wordeman. 2010. Catalysis of the microtubule on-rate is the major parameter regulating the depolymerase activity of MCAK. *Nat. Struct. Mol. Biol.* 17:77–82.
43. Kinoshita, K., I. Arnal, ..., A. A. Hyman. 2001. Reconstitution of physiological microtubule dynamics using purified components. *Science.* 294:1340–1343.
44. Brouhard, G. J., J. H. Stear, ..., A. A. Hyman. 2008. XMAP215 is a processive microtubule polymerase. *Cell.* 132:79–88.

3.2. Microtubule length regulation by molecular motors

There is an intuitive argument that captures the essence of length-regulation: The main mechanism identified for length regulation in this work is that the particle density at the dynamic plus end, ρ_+ , couples to the density profile in bulk of the lattice ρ_b . Due to attachment kinetics, this density profile is linearly increasing along the filament. A linearly increasing bulk density profile of depolymerizing motor molecules immediately ensues a balance of filament shortening and growth, which leads to regulation of length.

This core mechanism – the linear density profile – is very general: It holds for treadmilling filaments as shown by Johann *et al.*, and in the case of non-motile proteins [220]. On a more coarse grained picture length-regulation has also been investigated including dynamic instability due to GTP hydrolysis [212], and a probabilistic description of molecular motors [221].

The question if length regulation is possible has an interesting analogy in exclusive queuing processes [222]. In a recent study Arita and Schadschneider investigated when a queue is in a *divergent* (continuously growing) or in a *convergent* phase (constant length), similar to *growing* and *shrinking* lattices.

On the following pages the original version of the publication is provided.

Microtubule Length Regulation by Molecular Motors

Anna Melbinger,* Louis Reese, and Erwin Frey†

Arnold Sommerfeld Center for Theoretical Physics (ASC) and Center for NanoScience (CeNS), Department of Physics,
Ludwig-Maximilians-Universität München, Theresienstrasse 37, 80333 München, Germany

(Received 5 March 2012; published 22 June 2012)

Length regulation of microtubules (MTs) is essential for many cellular processes. Molecular motors like kinesin-8, which move along MTs and also act as depolymerases, are known as key players in MT dynamics. However, the regulatory mechanisms of length control remain elusive. Here, we investigate a stochastic model accounting for the interplay between polymerization kinetics and motor-induced depolymerization. We determine the dependence of MT length and variance on rate constants and motor concentration. Moreover, our analyses reveal how collective phenomena lead to a well-defined MT length.

DOI: [10.1103/PhysRevLett.108.258104](https://doi.org/10.1103/PhysRevLett.108.258104)

PACS numbers: 87.16.Ka, 05.40.-a, 87.16.Nn, 87.16.Uv

During the lifespan of a eukaryotic cell microtubules (MTs) perform highly dynamic tasks. For instance, during mitosis, they form the mitotic spindle, which searches, captures, and separates the double set of chromosomes [1]. To achieve such complex dynamic behavior there need to be molecular mechanisms which allow a dynamic control of MT length. There is much evidence that these mechanisms rely on an intricate interplay of GTP hydrolysis [2], mechanical forces [3], and regulatory proteins [4]. In particular, the role of the molecular motor families kinesin-5 and kinesin-8 has been investigated: Several *in vivo* experiments showed that both, the presence and the concentration of such proteins, strongly affect the functionality of the mitotic spindle [5,6]. This is supported by *in vitro* experiments which specifically studied the molecular mechanisms of interactions between motor proteins and microtubules [7–13]. In general, it is accepted that kinesin-8 hampers MT growth. In particular, it was found that the plus end directed motor kinesin-8 of budding yeast, Kip3p, depolymerizes MTs at the tip. To gain a deeper understanding for the molecular mechanisms underlying these depolymerization dynamics Varga *et al.* [7,8] studied the interaction of Kip3p with stabilized MTs not exhibiting dynamic instability [2,14]. The key result of these experiments is that depolymerization is length dependent, i.e., longer MTs depolymerize faster than shorter ones. One main determinant of the observed length dependence are molecular traffic jams which can successfully be described by driven diffusive processes [15]. These findings suggest, that length-dependent depolymerization in combination with polymerization allows a cell to regulate the length of MTs [7,8]. There are by now several theoretical studies addressing length regulation ranging from MTs [16,17], over actin filaments [18] to fungi [19] and flagellae [20].

In this Letter, we study the combined influence of spontaneous MT polymerization and motor-induced depolymerization. In our model we neglect MT dynamics at the minus end as there the dynamic rates are much smaller than

the ones at the plus end [1]. Furthermore, under physiological conditions often the minus end dynamics are completely suppressed due to capping proteins [21]. We build on a recently validated quantitative model for MT depolymerization [8,15], and extend it by introducing polymerization dynamics at the fast-growing plus end [1]. This accounts for MT growth mediated by spontaneous [2] or enzymatically catalyzed [22] attachment of tubulin heterodimers to the tip. This approach enables us to study the basic principles underlying length regulation which is achieved by the antagonism between length-dependent depolymerization and spontaneous polymerization dynamics. We predict quantitative criteria for the parameter regime where regulation is feasible. In addition, we calculate both the mean length and the corresponding standard deviation, and thereby determine the accuracy at which regulation is achieved.

To describe the MT dynamics we employ a driven diffusive lattice gas model [23,24] as illustrated in Fig. 1. Since MT protofilaments serve as independent tracks for the motors [25,26], a MT can effectively be described by a one-dimensional lattice of dynamic size $L(t)$. The size of a tubulin heterodimer sets the basic length scale of the lattice. The state of each site, i , is described by its occu-

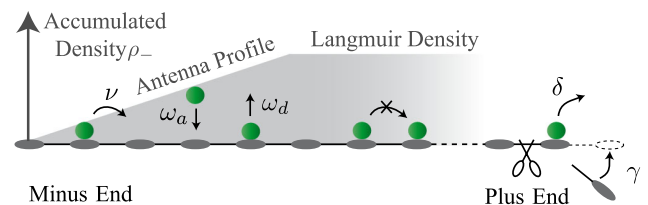


FIG. 1 (color online). Illustration of the model. Motors attach to and detach from the MT lattice at rates $\omega_a = c\tilde{\omega}_a$ and ω_d , respectively. On the lattice particles hop to the right at rate ν provided that the next site is empty. At the right boundary, the MT plus end, particles remove the last lattice site at rate δ and the MT lattice grows at rate γ . The resulting antennalike density profile $\rho_-(x)$ is sketched in light gray.

pation number, $n_i \in \{0, 1\}$, where $n_i = 0$ and $n_i = 1$ signify an empty and occupied site, respectively. On the MT lattice the dynamics follow the *totally asymmetric simple exclusion process* with Langmuir kinetics [24]: Motors can attach to and detach from the MT at rates $\omega_a = c\tilde{\omega}_a$ and ω_d , respectively, where c is the motor concentration in the surrounding fluid; the binding constant is defined as $K := \omega_a/\omega_d$. On the lattice, particles move to right at rate ν provided that the next site is empty; $\nu = 1$ sets the basic time scale. The combined effect of motor attachment in proximity of the minus end and subsequent movement towards the plus end leads to an accumulation of motors, which finally results in an antennalike steady state profile [8,15,27] as illustrated in Fig. 1. At a certain distance from the minus end the density profiles saturate to the equilibrium Langmuir density $\rho_{La} = K/(K+1)$ [28]. The resulting accumulated density profiles in vicinity of the minus end, $\rho_-(x)$, can be described by Lambert W functions [15,24]. Moving further towards the right boundary (MT minus end), the density profile is determined by the interplay of motor current and the boundary conditions at the plus end. This entails a rich variety of collective phenomena and leads to nontrivial density profiles [29,30]. In the present study, the right *boundary is dynamic*. Motivated by the recent studies on kinesin-8 [6–12], we consider the following scenario: When a motor arrives at the MT tip, it detaches by removing the last MT site at rate δ [15]. In addition, subsuming the effects of spontaneous and enzymatic polymerization, the MT is assumed to polymerize through the attachment of single tubulin heterodimers at an effective rate γ . These boundary conditions lead to a dynamic MT length which is determined by the combined effect of the particle current onto the last site, polymerization, and depolymerization rates. A related model has been suggested in Ref. [31].

The dynamic length of the MT, $L(t)$, is determined by the particle density at the MT plus end $\rho_+(L)$,

$$\partial_t L(t) = -\delta\rho_+(L) + \gamma. \quad (1)$$

This equation defines a critical density $\rho_+^c = \gamma/\delta$, at which the MT length is in a steady state, $\partial_t L = 0$. For tip densities smaller or larger than ρ_+^c the MT grows or shrinks, respectively. As the tip density is fed by the motor current towards the tip, it depends on the accumulated motor density in bulk $\rho_-(x)$. This suggests the following mechanism for MT length regulation: On short MTs, the accumulated motor density is low, and therefore also the tip density $\rho_+(L)$. As long as $\rho_+(L) < \rho_+^c$ the MT grows. In contrast, for longer MTs higher accumulated motor and tip densities are reached which eventually result in MT depolymerization once $\rho_+(L) > \rho_+^c$. However, this mechanism is only expected to work if the tip is not growing too fast: Above a critical polymerization rate the particle current feeding the tip density can no longer follow the advancing tip.

To quantify these heuristic arguments and determine the precise conditions under which length regulation is feasible and which length is adjusted, the tip density has to be determined. This requires analyzing the intricate interplay between molecular crowding due to high motor density [23,24] and transport bottlenecks at the plus end [15,32]. In addition, this boundary is highly dynamic, and calculations of the tip density are more intricate than for standard driven diffusive models for which the size of the lattice is constant [29,30,33].

To make further progress, we first consider a simplified model where we disregard spatial variations of the density profile. In detail, we assume a constant density ρ_- that serves as a particle reservoir at the left boundary, neglect attachment and detachment kinetics, but leave the dynamics at the plus end unchanged; see Fig. 2(a). This allows us to focus on the dynamics at the plus end and to unravel how they depend on the reservoir density ρ_- . Since we find that the density profiles adapt adiabatically to a dynamic lattice size [34], the results for the full model can be inferred upon replacing ρ_- by $\rho_-(x)$. As the length of the lattice is dynamic, we perform our calculations in a comoving frame fixed to the right boundary. In this frame, a polymerization event corresponds to the simultaneous movement of all particles on the lattice to the minus end by one unit, while depolymerization results in an instantaneous shift to the right. Thus, in a mean-field approximation [$\langle n_i n_j \rangle = \langle n_i \rangle \langle n_j \rangle = \rho_i \rho_j$] the particle current in bulk is given by

$$J(\rho_b, \rho_+) = \rho_b(1 - \rho_b) - \gamma\rho_b + \delta\rho_+\rho_b, \quad (2)$$

where ρ_b is the motor density in bulk. The first term describes the hopping processes, the second and third term account for simultaneous movement of all particles

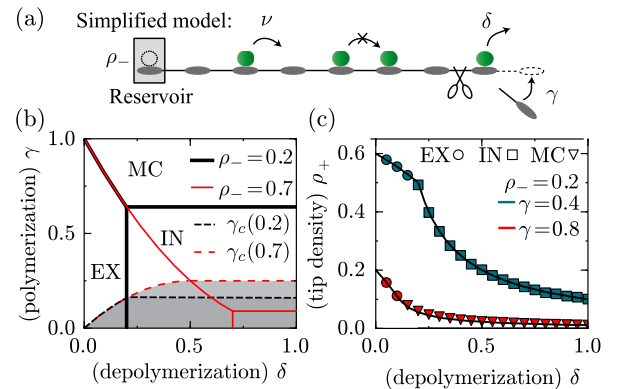


FIG. 2 (color online). (a) Illustration of the simplified model. (b) Phase diagram as a function of the rates δ and γ . The gray shaded area indicates regions in phase space in which regulation is possible in the full model. The gray area indicates regions in phase space where the MT shrinks in the simplified model. In the full model, for $\rho_- = \rho_{La}$ length regulation is only possible in the gray area as explained in detail in the main text. (c) Comparison of simulation data with analytical results for the tip density ρ_+ .

due to polymerization and depolymerization, respectively. Importantly, the bulk current explicitly depends on the tip density and thereby on the right boundary.

To determine the phase behavior we employ the Extremal Current Principle (ECP) [35–37] relying on two velocities: The *collective velocity* $v_{\text{coll}}(\rho) = \partial_{\rho} J$ determines the direction in which a local density perturbation spreads. Thereby, one is able to determine whether a certain bulk density is stable against perturbations, i.e., for a density ρ stable at the left (right) boundary $v_{\text{coll}}(\rho) > 0$ ($v_{\text{coll}}(\rho) < 0$) holds. The boundary conditions result in densities at the plus and the minus end, respectively, whose stabilities can now be tested employing v_{coll} . If these densities are stable against small perturbations, we call them ρ^{left} and ρ^{right} as they are given by the system's left and right boundary, respectively. If either one or both of these boundary densities are not stable, perturbations change these densities and ρ^{left} and ρ^{right} are given by the first stable density which is determined by $v_{\text{coll}}(\rho) = 0$. The *shock velocity* $v_{\text{shock}}(\rho^{\text{left}}, \rho^{\text{right}}) = [J(\rho^{\text{left}}) - J(\rho^{\text{right}})]/(\rho^{\text{left}} - \rho^{\text{right}})$ determines the direction in which a virtual domain wall between the densities at the left and the right, ρ^{left} and ρ^{right} , moves and thereby which of these densities is realized in bulk. In more detail, for $v_{\text{shock}} > 0$ the left density, ρ^{left} , dictates the bulk density, while for $v_{\text{shock}} < 0$ the right density, ρ^{right} , is realized. In our model particles are transported to the right and therefore jams spread from right to left. Hence, the virtual domain wall arises at the right boundary and the tip densities ρ_+^{left} and ρ_+^{right} determine v_{shock} ; see the Supporting Material [38].

Because of particle conservation at the plus end of the MT, $\partial_t \rho_+ = J(\rho_b, \rho_+) - \rho_+ \delta$, the stationary value of the bulk and tip density are related through

$$\rho_+ \delta = J(\rho_b, \rho_+). \quad (3)$$

This implies that the values of these densities as well as the nature of the ensuing nonequilibrium steady state are strongly interlinked. In general, one expects three phases [35,39]: the steady state may either be dominated by the motor densities at the plus end (EX phase) and the minus end (IN phase), respectively, or by the transport capacity (maximal current) of the lattice itself (MC phase). We first consider the IN phase where $\rho_b^{\text{IN}} = \rho_-$ holds, and Eq. (3) leads to the tip density

$$\rho_+^{\text{IN}}(\rho_-) = \rho_-(1 - \rho_- - \gamma)/[\delta(1 - \rho_-)]. \quad (4)$$

This solution is stable against perturbations only if the collective velocity $v_{\text{coll}}(\rho_-) = \partial_{\rho} J[\rho, \rho_+^{\text{IN}}(\rho)]|_{\rho=\rho_-}$ is positive, which holds for reservoir densities smaller than the bulk density in the MC phase $\rho_b^{\text{MC}} = 1 - \sqrt{\gamma}$. If the reservoir density exceeds this value, the ECP implies that the tip density becomes constant and independent of the reservoir density $\rho_+^{\text{MC}} = (1 - \sqrt{\gamma})^2/\delta$. For the EX phase, the right boundary determines the bulk density $\rho_b^{\text{EX}} = \rho_+^{\text{EX}}$, and Eq. (3) leads to $\rho_+^{\text{EX}} = 1 - \gamma/(1 - \delta)$. According to

the ECP, this solution is stable if the corresponding collective velocity $v_{\text{coll}}(\rho_+^{\text{EX}}) = \partial_{\rho} J(\rho, \rho_+^{\text{EX}})|_{\rho=\rho_+^{\text{EX}}}$ is negative. Since in the relevant parameter regime $v_{\text{coll}} < 0$ is always fulfilled, the density ρ_+^{EX} is always stable and $\rho_+^{\text{right}} = \rho_+^{\text{EX}}$ holds.

In summary, we have found the following results for the densities at the left and right boundary of the MT:

$$\rho_+^{\text{left}} = \text{Min}[\rho_+^{\text{IN}}, \rho_+^{\text{MC}}], \quad \rho_+^{\text{right}} = \rho_+^{\text{EX}}. \quad (5)$$

With these expressions at hand, we can now map out the phase diagram upon evaluating the shock velocity $v_{\text{shock}}(\rho_+^{\text{left}}, \rho_+^{\text{right}})$; cf. Fig. 2. The IN-phase is determined by $\gamma < (1 - \rho_-)^2$ and $\delta > \rho_-$. Importantly, it is the only phase in which the tip density is a function of ρ_- ; see Eq. (4). As ρ_- corresponds to the spatially varying density profile $\rho_-(x)$ in the full model, length regulation is feasible in this range of parameters. In contrast, in the EX phase [$\gamma < (1 - \delta)^2$ and $\delta < \rho_-$] and the MC phase [$\gamma > (1 - \delta)^2$ and $\gamma > (1 - \rho_-)^2$] neither the tip nor the bulk densities depend on ρ_- . To confirm these and the following analytic results, we performed extensive stochastic simulations employing the Gillespie algorithm [40]. For both the simplified and the full model discussed in the following, calculations are in excellent agreement with simulations; cf. Figs. 2(c) and 3.

Moreover, upon combining the results for the tip densities in the various phases with the critical density $\rho_+^c = \gamma/\delta$, we are able to calculate the critical growth rate γ_c , at which the MT length becomes stationary

$$\gamma_c(\rho_-) = \begin{cases} \delta(1 - \delta) & \text{EX phase,} \\ \rho_-(1 - \rho_-) & \text{IN phase,} \\ 1/4 & \text{MC phase.} \end{cases} \quad (6)$$

For $\gamma > \gamma_c$ the lattice grows to infinity, while it shrinks indefinitely for $\gamma < \gamma_c$.

Up to now, the discussion was restricted to a simplified system, and we have learned how a constant reservoir density translates into the tip density and in which parameter regimes the MT grows and shrinks, respectively. In the following we transfer the so-far obtained results to the full spatial model, in which the reservoir density is replaced by the density profile: $\rho_- \rightarrow \rho_-(x)$. This implies that also the tip density becomes length dependent, $\rho_+ \rightarrow \rho_+(L)$ in the IN phase, see Eq. (4). Let us first consider how these spatial density profiles affect the critical growth rate, γ_c , in the full model, and thereby derive a condition for the parameter regime where length regulation is feasible: Growth is unbounded only if the highest accumulated density $\rho_-(L)$ does not result in strong enough depolymerization dynamics to overcome MT growth due to polymerization. Recall that the accumulated density profile increases from left to right until it saturates to the Langmuir density, ρ_{La} . Thus, growth is unbounded if $\gamma > \gamma_c(\rho_{\text{La}})$. In contrast, in the

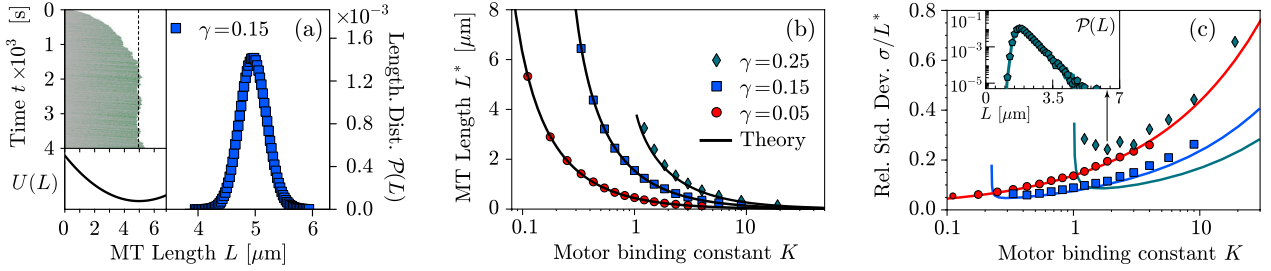


FIG. 3 (color online). (a) Kymograph (upper left): Molecular motors (green shaded traces) accumulate along the lattice (gray) resulting in a steady MT length (dashed). Corresponding potential $U(L)$ (bottom left) and length distribution $\mathcal{P}(L)$ (right) for $K = 1.5$. (b) Analytical [lines, Eq. (8)] and numerical results (symbols) for the typical MT length L^* are compared. (c) Standard deviation of the MT length σ in units of its typical length L^* for the same values for γ as in (b). Inset: $\mathcal{P}(L)$ for $\gamma = 1/4$ shows an exponential tail. [Parameters: $\delta = 0.5$ (a)–(c), $\omega_d = 2 \times 10^{-4}$ (a), and $\omega_d = 1 \times 10^{-3}$ (b),(c)].

depolymerizing regime, $\gamma < \gamma_c(\rho_{La})$, the MT shortens until the tip enters the antenna profile. Within this regime, the accumulated density and thereby the tip density decreases with every depolymerization event until the MT length reaches a stable fixed point L^* , at which growth and shrinkage balance each other. As the corresponding restoring force is conservative, the length regulation dynamics can be described by a potential U . It follows from $-\partial_L U = -\delta\rho_+(L) + \gamma$ and leads to an adjusted length fluctuating around the mean, as observed in the MT dynamics; see Fig. 3(a).

To calculate the adjusted MT length L^* , the full spatial density profile $\rho_-(x)$ as obtained from mean-field theory [24], and the stochastic growth and shrinkage have to be considered. They can be combined in an effective master equation, where the degrees of freedom from the occupation numbers, n_i , are adiabatically eliminated:

$$\partial_t \mathcal{P}(L) = [(\mathbb{E}^+ - 1)\delta\rho_+(L) + (\mathbb{E}^- - 1)\gamma]\mathcal{P}(L). \quad (7)$$

Here, \mathbb{E}^\pm are step operators which increase or decrease the lattice length; $\rho_+(L)$ is the density at the tip depending on L . In the IN phase, in which regulation is feasible, $\rho_+(L) = \rho_-(L)[1 - \rho_-(L) - \gamma]/[\delta(1 - \rho_-(L))]$ holds, where $\rho_-(x)$ is the spatial density profile given by Lambert W functions [15,24]. We solve the master equation approximately using the van Kampen system size expansion [41]: The deterministic dynamics $\ell(t)$ is separated from the fluctuations ξ employing the ansatz $L = \Omega\ell(t) + \sqrt{\Omega}\xi$. As expansion parameter we consider $\Omega = 1/\omega_a$ because the typical length scale of the accumulated density profile which triggers length regulation is given by $1/\omega_a$. Additionally, time has to be rescaled according to $\tau = \omega_a t$ since the equilibration time also scales with this length scale. An expansion of Eq. (7) in terms of $1/\sqrt{\Omega}$ yields the mean MT length

$$L^* = \frac{\rho_{La}}{\omega_a} \left(1 - \sqrt{1 - 4\gamma} + \frac{K - 1}{K + 1} \times \ln \left| \frac{(K + 1)\sqrt{1 - 4\gamma} + K - 1}{2K} \right| \right). \quad (8)$$

As can be inferred from Fig. 3(b), this result is in excellent agreement with numerical data. We observe that the stationary MT length is independent of δ , and a monotonically decreasing function of the binding constant K . The latter behavior reflects the increase of the slope of the antenna profile with larger K implying that the density at which regulation arises is reached for shorter MTs. The van Kampen approximation also gives the variance,

$$\sigma^2 = \frac{2\gamma^2}{\omega_a} \frac{K}{-1 + \sqrt{1 - 4\gamma} + 2\gamma(1 + K)}. \quad (9)$$

For small values of γ , the standard deviation σ is below 10% of the filament length in a range of approximately 1–20 μm . The variance actually diverges with $\gamma \rightarrow \rho_{La}(1 - \rho_{La})$ for $K \leq 1$, while for $K > 1$ regulation remains possible for $\gamma = \rho_{La}(1 - \rho_{La})$. In this regime, the MT length distribution $\mathcal{P}(L)$ develops an exponential tail. This tail cannot be described by the van Kampen expansion, which explains the deviations between the numerical and the analytical results in Fig. 3(c).

In this Letter, we investigated how motor-induced depolymerization in combination with spontaneous polymerization can result in length regulation of biological filaments. We found a broad parameter regime in which length regulation is feasible, due to collective phenomena of molecular motors which also act as depolymerases. Even though the regime where length regulation is possible depends on the depolymerization rate, the adjusted filament length is independent of the depolymerization rate δ , because of microscopic traffic jams forming at the tip. Our model provides a proof of principle that spatial dependences in the growth and shrinkage rates of filaments, which arise from motor transport in this case, can result in a well-defined filament length. It may serve as a basis for mechanistically more detailed analyses which account for multiple protein species [42], dynamic instability [43,44], internal states of MTs or motors [45], assemblies of MTs [46], or the abundance of molecules in the cell [47]. We expect, however, that the main idea—feedback between polymerization dynamics and collective motor dynamics—remains the core mechanism.

This project was supported by the Deutsche Forschungsgemeinschaft in the framework of the SFB 863 and the German Excellence Initiative via the program “Nanosystems Initiative Munich” (NIM). A. M. and L. R. contributed equally to this work. We thank K. Kruse and coworkers for sharing their related manuscript [31].

*Present address: Institut Pasteur, Paris, France.

[†]frey@lmu.de

- [1] B. Alberts, A. Johnson, J. Lewis, M. Ra, K. Roberts, and P. Walter, *Molecular Biology of the Cell* (Garland Science, New York, 2002), 4th ed.
- [2] T. Mitchison and M. Kirschner, *Nature (London)* **312**, 237 (1984).
- [3] G. Goshima and J. M. Scholey, *Annu. Rev. Cell Dev. Biol.* **26**, 21 (2010); S. Dumont and T. J. Mitchison, *Curr. Biol.* **19**, R749 (2009).
- [4] L. Wordeman, *Curr. Opin. Cell Biol.* **17**, 82 (2005); J. Howard and A. A. Hyman, *ibid.* **19**, 31 (2007).
- [5] G. Goshima, R. Wollman, N. Stuurman, J. M. Scholey, and R. D. Vale, *Curr. Biol.* **15**, 1979 (2005).
- [6] M. L. Gupta, P. Carvalho, D. M. Roof, and D. Pellman, *Nat. Cell Biol.* **8**, 913 (2006); M. I. Mayr, S. Hümmer, J. Bormann, T. Gruner, S. Adio, G. Woehlke, and T. U. Mayer, *Curr. Biol.* **17**, 488 (2007); J. Stumpff, G. von Dassow, M. Wagenbach, C. Asbury, and L. Wordeman, *Dev. Cell* **14**, 252 (2008); C. Tischer, D. Brunner, and M. Dogterom, *Mol. Syst. Biol.* **5**, 250 (2009).
- [7] V. Varga, J. Helenius, K. Tanaka, A. A. Hyman, T. U. Tanaka, and J. Howard, *Nat. Cell Biol.* **8**, 957 (2006).
- [8] V. Varga, C. Leduc, V. Bormuth, S. Diez, and J. Howard, *Cell* **138**, 1174 (2009).
- [9] M. K. Gardner, M. Zanic, C. Gell, V. Bormuth, and J. Howard, *Cell* **147**, 1092 (2011).
- [10] Y. Du, C. A. English, and R. Ohi, *Curr. Biol.* **20**, 374 (2010).
- [11] X. Su, W. Qiu, M. L. Gupta, J. B. Pereira-Leal, S. L. Reck-Peterson, and D. Pellman, *Mol. Cell* **43**, 751 (2011).
- [12] L. N. Weaver, S. C. Ems-McClung, J. R. Stout, C. Leblanc, S. L. Shaw, M. K. Gardner, and C. E. Walczak, *Curr. Biol.* **21**, 1500 (2011).
- [13] P. Bieling, I. A. Telley, and T. Surrey, *Cell* **142**, 420 (2010).
- [14] M. Dogterom and S. Leibler, *Phys. Rev. Lett.* **70**, 1347 (1993).
- [15] L. Reese, A. Melbinger, and E. Frey, *Biophys. J.* **101**, 2190 (2011).
- [16] B. S. Govindan, M. Gopalakrishnan, and D. Chowdhury, *Europhys. Lett.* **83**, 40006 (2008).
- [17] C. Tischer, P. Rein ten Wolde, and M. Dogterom, *Biophys. J.* **99**, 726 (2010).
- [18] C. Erlenkämper and K. Kruse, *Phys. Biol.* **6**, 046016 (2009).
- [19] K. E. P. Sugden and M. R. Evans, *J. Stat. Mech.* (2007) P11013; K. E. P. Sugden, M. R. Evans, W. C. K. Poon, and N. D. Read, *Phys. Rev. E* **75**, 031909 (2007).
- [20] M. Schmitt and H. Stark, *Europhys. Lett.* **96**, 28001 (2011).
- [21] A. Desai and T. Mitchison, *Annu. Rev. Cell Dev. Biol.* **13**, 83 (1997).
- [22] G. J. Brouhard, J. H. Stear, T. L. Noetzel, J. Al-Bassam, K. Kinoshita, S. C. Harrison, J. Howard, and A. A. Hyman, *Cell* **132**, 79 (2008).
- [23] R. Lipowsky, S. Klumpp, and T. M. Nieuwenhuizen, *Phys. Rev. Lett.* **87**, 108101 (2001); S. Klumpp and R. Lipowsky, *J. Stat. Phys.* **113**, 233 (2003).
- [24] A. Parmeggiani, T. Franosch, and E. Frey, *Phys. Rev. Lett.* **90**, 086601 (2003); *Phys. Rev. E* **70**, 046101 (2004).
- [25] S. Ray, E. Meyhöfer, R. Milligan, and J. Howard, *J. Cell Biol.* **121**, 1083 (1993).
- [26] A. Vilfan, E. Frey, F. Schwabl, M. Thormählen, Y. H. Song, and E. Mandelkow, *J. Mol. Biol.* **312**, 1011 (2001).
- [27] L. E. Hough, A. Schwabe, M. A. Glaser, J. R. McIntosh, and M. D. Betterton, *Biophys. J.* **96**, 3050 (2009).
- [28] C. Leduc, K. Padberg-Gehle, V. Varga, D. Helbing, S. Dietz, and J. Howard, *Proc. Natl. Acad. Sci. U.S.A.* **109**, 6100 (2012).
- [29] G. M. Schütz, in *Phase Transitions and Critical Phenomena*, edited by C. Domb and J. L. Lebowitz (Academic Press, London, 2000), Vol. 19 p. 1.
- [30] T. Chou, K. Mallick, and R. K. P. Zia, *Rep. Prog. Phys.* **74**, 116601 (2011).
- [31] D. Johann, C. Erlenkämper, and K. Kruse, *Phys. Rev. Lett.* **108**, 258103 (2012).
- [32] P. Pierobon, M. Mobilia, R. Kouyos, and E. Frey, *Phys. Rev. E* **74**, 031906 (2006).
- [33] S. A. Nowak, P.-W. Fok, and T. Chou, *Phys. Rev. E* **76**, 031135 (2007).
- [34] This assumption is valid for tip dynamics slower than the motor speed, which is true in the parameter regime where length regulation is possible.
- [35] J. Krug, *Phys. Rev. Lett.* **67**, 1882 (1991).
- [36] A. B. Kolomeisky, G. M. Schütz, E. B. Kolomeisky, and J. P. Straley, *J. Phys. A* **31**, 6911 (1998).
- [37] V. Popkov and G. M. Schütz, *Europhys. Lett.* **48**, 257 (1999).
- [38] See Supplemental Material at <http://link.aps.org/supplemental/10.1103/PhysRevLett.108.258104> for details.
- [39] B. Derrida, E. Domany, and D. Mukamel, *J. Stat. Phys.* **69**, 667 (1992); G. Schütz and E. Domany, *ibid.* **72**, 277 (1993); B. Derrida, M. R. Evans, V. Hakim, and V. Pasquier, *J. Phys. A* **26**, 1493 (1993).
- [40] D. T. Gillespie, *J. Phys. Chem.* **81**, 2340 (1977); *J. Comput. Phys.* **22**, 403 (1976).
- [41] N. G. Van Kampen, *Stochastic Process in Physics and Chemistry* (Elsevier, Amsterdam, 2007) 3rd ed.
- [42] M. Ebbinghaus, C. Appert-Rolland, and L. Santen, *Phys. Rev. E* **82**, 040901 (2010).
- [43] L. Brun, B. Rupp, J. J. Ward, and F. Nedelec, *Proc. Natl. Acad. Sci. U.S.A.* **106**, 21173 (2009).
- [44] R. Padinhateeri, A. B. Kolomeisky, and D. Lacoste, *Biophys. J.* **102**, 1274 (2012).
- [45] K. Nishinari, Y. Okada, A. Schadschneider, and D. Chowdhury, *Phys. Rev. Lett.* **95**, 118101 (2005).
- [46] O. Campàs, J. Casademunt, and I. Pagonabarraga, *Europhys. Lett.* **81**, 48003 (2008).
- [47] C. A. Brackley, M. C. Romano, C. Grebogi, and M. Thiel, *Phys. Rev. Lett.* **105**, 078102 (2010).

3.3. Molecular mechanisms for microtubule length regulation by kinesin-8 and XMAP215 proteins

So far it has been shown that the different depolymerization and polymerization conditions lead to distinct phenomenological behavior. The two different scenarios discussed so far „exclusive“ and „non-exclusive“ depolymerization can both serve as mechanism for length regulation of microtubules. In the following it is shown that microtubule polymerizing enzymes, like XMAP215 [90], together with depolymerizing molecular motors constitute a mechanism for length-regulation as a duo with particular properties. It is also shown that the „exclusive“ scenario is well-suited to describe the case where XMAP215 and kinesin-8 work in parallel. However, as already became clear in the previous section, the phase behavior is particular in the „exclusive“ scenario. The situation investigated in the following reveals that in the absence of motor detachment from the microtubule tip, $\beta = 0$, the process is sensitive to the initial conditions. The reason for this is that the stability of the system critically depends on the tip densities. A phase diagram is obtained and the efficiency in length-regulation is discussed in view of the different mechanisms of growth and depolymerization.

On the following pages the original publications is provided.

Research



Cite this article: Reese L, Melbinger A, Frey E. 2014 Molecular mechanisms for microtubule length regulation by kinesin-8 and XMAP215 proteins. *Interface Focus* 4: 20140031. <http://dx.doi.org/10.1098/rsfs.2014.0031>

One contribution of 13 to a Theme Issue 'Biophysics of active systems: a themed issue dedicated to the memory of Tom Duke'.

Subject Areas:

biophysics

Keywords:

microtubule dynamics, molecular motors, kinesin-8, XMAP215

Author for correspondence:

Erwin Frey
e-mail: frey@lmu.de

Molecular mechanisms for microtubule length regulation by kinesin-8 and XMAP215 proteins

Louis Reese^{1,2}, Anna Melbinger^{1,3} and Erwin Frey^{1,2}

¹Arnold Sommerfeld Center for Theoretical Physics and Center for NanoScience, Department of Physics, Ludwig-Maximilians-Universität München, Theresienstraße 37, 80333 Munich, Germany

²Nanosystems Initiative Munich (NIM), Ludwig-Maximilians-Universität München, Schellingstraße 4, 80333 Munich, Germany

³Department of Physics, University of California, San Diego, CA 92093, USA

LR, 0000-0002-0818-900X

The cytoskeleton is regulated by a plethora of enzymes that influence the stability and dynamics of cytoskeletal filaments. How microtubules (MTs) are controlled is of particular importance for mitosis, during which dynamic MTs are responsible for proper segregation of chromosomes. Molecular motors of the kinesin-8 protein family have been shown to depolymerize MTs in a length-dependent manner, and recent experimental and theoretical evidence suggests a possible role for kinesin-8 in the dynamic regulation of MTs. However, so far the detailed molecular mechanisms of how these molecular motors interact with the growing MT tip remain elusive. Here we show that two distinct scenarios for the interactions of kinesin-8 with the MT tip lead to qualitatively different MT dynamics, including accurate length control as well as intermittent dynamics. We give a comprehensive analysis of the regimes where length regulation is possible and characterize how the stationary length depends on the biochemical rates and the bulk concentrations of the various proteins. For a neutral scenario, where MTs grow irrespective of whether the MT tip is occupied by a molecular motor, length regulation is possible only for a narrow range of biochemical rates, and, in particular, limited to small polymerization rates. By contrast, for an inhibition scenario, where the presence of a motor at the MT tip inhibits MT growth, the regime where length regulation is possible is extremely broad and includes high growth rates. These results also apply to situations where a polymerizing enzyme like XMAP215 and kinesin-8 mutually exclude each other from the MT tip. Moreover, we characterize the differences in the stochastic length dynamics between the two scenarios. While for the neutral scenario length is tightly controlled, length dynamics is intermittent for the inhibition scenario and exhibits extended periods of MT growth and shrinkage. On a broader perspective, the set of models established in this work quite generally suggest that mutual exclusion of molecules at the ends of cytoskeletal filaments is an important factor for filament dynamics and regulation.

1. Introduction

Microtubules (MTs) are essential constituents of the cytoskeleton of eukaryotic cells. They provide mechanical support and are involved in a wide range of cellular functional modules. For instance, they serve cells to build cilia and flagellae which are slender extensions of the cell used for migration and sensory tasks. In addition, MTs are important during cell division, where they build the mitotic spindle and separate chromosomes. To facilitate this variety of tasks, there have to be mechanisms that control the dynamics of MTs [1]. Such capabilities are crucial for the MT cytoskeleton in order to accomplish such diverse tasks as cell division [2] and migration [3], and further, to

determine cell size and shape [4], and to position the nucleus in the centre of the cell [5,6]. Molecular motors and MT-associated proteins seem to play a crucial role in this regulation process [7,8]: motors move along the MT and interact specifically with the filament at its end. Other associated proteins that influence the dynamics of MTs also bind directly to the MT tip [9]. Biochemical reconstitution experiments have led to considerable insights into the interactions between MTs and associated molecules [10]. In the following, we highlight two specific proteins that are important for the length dynamics of MTs.

Kip3p is an MT depolymerizing molecular motor [11,12] of the kinesin-8 protein family [13]. It binds strongly to the MT lattice and, therefore, exhibits a long run-length [14]. For kinesin-8 the molecular mechanisms that lead to depolymerization are elusive. However for kinesin-13, which is also a depolymerizing molecular motor, it was shown that strong motor binding to the terminal tubulin heterodimer induces depolymerization [15]. Interestingly, Kip3p shows a length-dependent depolymerization activity mediated by the accumulations of motors along the MT, as shown in experiments [11,16] and recent theoretical work [17]. *In vitro* experiments have unveiled many molecular properties of kinesin-8: the tail of the motor has been shown to be responsible for long residence times on the MT lattice and it influences MT dynamics [18–20] and spindle size [21]; for a brief review of these findings, see [22]. In the mathematical analysis, we will concentrate on the depolymerizing activity of the motor and treat those molecular details effectively in terms of rate constants for movement, depolymerization activity, and attachment/detachment kinetics of the motors.

XMAP215 is an MT-associated protein [23] that has been shown to significantly amplify the growth rate of MTs [24], and to influence the dynamic properties of MTs in the cytosol [25,26]. Recent *in vitro* experiments investigated the interaction of XMAP215 with single MTs [27] and the interplay with other end-binding proteins, which act as cofactors [28,29]. Specifically, it was found that XMAP215 is a polymerizing enzyme to the MT plus-end; a single XMAP215 is able to polymerize several rounds of tubulin heterodimers to the MT [27]. Similar properties have also been observed for other end-binding proteins (e.g. [30]).

Combining the observations described above suggests that kinesin-8s and XMAP215 may constitute a minimal functional unit able to regulate MT dynamics [25,31] and antagonistically influence MT length. This view is supported by recent experiments on cilia [32] showing that the molecular motor Kif19a, which belongs to the kinesin-8 protein family, regulates the cilia length in a concentration-dependent manner: high motor concentrations lead to short cilia, whereas low motor concentrations lead to long cilia. On a molecular scale, the ability to regulate length is traced back to the observed length-dependent depolymerization speed [7]. In more detail, longer MTs are observed to depolymerize faster than shorter ones. This has been explained as follows [16,17]: molecular motors in the cytosol attach to the MT and subsequently move towards the MT tip. The unidirectional movement of motors towards the MT tip leads to an accumulation of motors and the motor density increases from the minus- to the plus-end of the MT, which finally results in an *antenna-like* steady-state profile of molecular motors. Therefore, there are more motors present at the tip for longer MTs than for shorter ones, which in turn leads to the observed

length dependence in the depolymerization speed. In combination with MT polymerization, which is either spontaneous or catalysed by XMAP215, this is a promising starting point to achieve MT regulation [7,33].

In this work, we elaborate on two possible molecular mechanisms of how molecular motors could interact with the MT tip. We specifically distinguish two scenarios, one where molecular motors prevent the addition of tubulin heterodimers at the MT tip (inhibition scenario), and another neutral scenario where MT growth is possible irrespective of whether the MT tip is occupied by motors or not. These differences in the interaction of motors with the MT tip give rise to a rich dynamics of MT length ranging from accurate length control to intermittent dynamics.

This article is organized as follows. In §2, we introduce a model for the dynamics of molecular motors on an MT. Further, we define different possible molecular scenarios for how kinesin-8s may interact with the MT tip during the depolymerization process, including the case when XMAP215 acts as a polymerase. In §3, we present our main results: we begin with an outline of the theoretical framework, and then employ it to study MT length dynamics. Our analytical calculations are complemented by stochastic simulations. Taken together, this allows us to identify the parameter regimes where length regulation is possible, and to provide a comprehensive analysis on how the ensuing stationary length depends on biochemical rates and protein concentrations. Moreover, we investigate the role of stochastic effects in length regulation, and discuss why there are dramatic differences between the considered scenarios. Finally, we conclude in §4 by discussing our results in terms of their possible biological relevance and their importance for driven diffusive lattice gases.

2. Model definition

To describe an MT, we consider a one-dimensional lattice gas model of finite length L [34,35] as illustrated in figure 1. This approximation is valid if the 13 protofilaments of an MT are independent and non-interacting. Motor proteins (kinesin-8), present at a constant bulk concentration c , are assumed to randomly attach to and detach from the MT lattice with rates ω_{on} and ω_{off} , respectively, defining the binding constant $K = c\omega_{\text{on}}/\omega_{\text{off}}$. Once bound, these motors move towards the plus-end at a constant hopping rate v ; we fix the time scale by setting $v = 1$ (corresponding to approx. 6.35 steps s^{-1} in the case of Kip3p [16]). As these motors hinder each other sterically, individual binding sites on MTs can at most be occupied once. This lattice gas model is known as the totally asymmetric simple exclusion process (TASEP) with Langmuir kinetics (LK) [36–38].

The right boundary is considered to be dynamic: when a Kip3p motor arrives at the MT plus-end, which is the boundary in our model, it acts as a depolymerase, i.e. it removes the last MT subunit at rate δ [17]. As we consider stabilized MTs following recent experiments [11,16], we do not include spontaneous depolymerization and MT dynamic instability. In addition, the MT is assumed to polymerize through the attachment of single tubulin heterodimers. Unfortunately, there is insufficient experimental information on the detailed molecular cycle for MT growth in the presence of kinesin-8 motors. We hypothesize the following different but equally plausible mechanisms for MT growth:

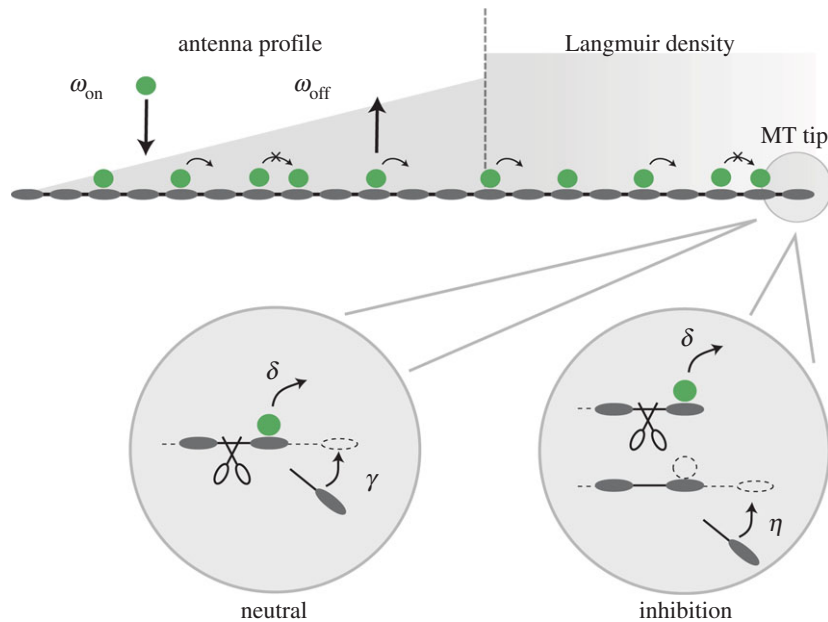


Figure 1. Illustrations of motors on an MT and different regulation scenarios at the MT plus-end. Starting from an empty MT lattice motors start to accumulate on the MT lattice by LK (with rates ω_{on} and ω_{off}) and subsequent transport with rate ν to the plus-end. The combined effect of LK and steric exclusion between the motors leads to an antenna-like profile which saturates at the Langmuir density ρ_{La} . At the MT tip, Kip3p depolymerizes the MT lattice and blocks MT growth in the *inhibition scenario* while it does not affect MT growth in the *neutral scenario*. (Online version in colour.)

- (i) The MT only grows at rate η if the last site at the plus-end is *not* occupied by a kinesin-8 motor. Because kinesin-8 inhibits MT growth we call this the *inhibition scenario* (cf. figure 1).
- (ii) The MT grows at rate γ independently of whether the tip is occupied or not. This *neutral scenario* has been considered previously in [33] (cf. figure 1).
- (iii) MT polymerization is facilitated by a second protein species, like for instance XMAP215. This enzyme, in the absence of kinesin-8, attaches to and detaches from the MT tip with rates k_{on} and k_{off} , respectively. Once bound, XMAP215 prevents kinesin-8 from reaching the tip, and processively polymerizes the MT at rate η_{X} , i.e. the enzyme immediately binds to the newly formed tip site after polymerization has occurred.

We use the remainder of this section to give a concise summary of the results obtained recently for the *neutral scenario* [33]: the combined effect of motor attachment in proximity of the minus-end (left boundary) and subsequent movement towards the plus-end (right boundary) leads to an accumulation of motors, which results in an antenna-like steady-state profile [16,17]. At a certain distance from the minus-end, the density profiles saturate to the equilibrium Langmuir density $\rho_{\text{La}} = K/(K+1)$ [14]. The resulting density profiles in the vicinity of the minus-end are position-dependent, $\rho_-(x)$, and can be described by Lambert- W functions [38]. Moving further towards the MT plus-end, the density profile is determined by the interplay of motor current and the boundary conditions at the plus-end, which gives rise to a particular tip density $\rho_+(L)$. In a mean-field description [35], this determines the length dynamics

$$\partial_t L(t) = -\delta \rho_+(L) + \gamma. \quad (2.1)$$

Steady state is reached at a critical density $\rho_+^c = \gamma/\delta$, where $\partial_t L(t) = 0$. Depending on whether the tip density $\rho_+(L)$ is smaller or larger than ρ_+^c the MT grows or shrinks.

Because the motor current to the tip depends on the accumulation of motors along the MT, $\rho_-(x)$, the tip density depends on the actual length $L(t)$ of the MT. As a consequence a mechanism for MT regulation emerges: on a short MT, when the accumulation of motor density is low, also the tip density is low and the MT grows because the tip density lies below the critical threshold density, $\rho_+(L) < \rho_+^c$. This is in contrast to the case of a long MT where a higher density of motors accumulates along the MT and also the tip density is higher. Once the tip density exceeds the critical threshold value $\rho_+(L) > \rho_+^c$ the MT depolymerizes.

Figure 2 illustrates this mechanism. Shaded areas indicate density profiles for MTs of different length and also schematically account for the fact that the tip density is length-dependent and has a spike-like shape. The dashed line shows a threshold value for the tip density, above and below which the MT shrinks and grows, respectively.

3. Motor and microtubule dynamics

Though at first sight the *neutral* and the *inhibition* scenario as introduced above appear very similar, there are actually strong qualitative differences in the ensuing length dynamics. Figure 3*a,b* shows kymographs for the neutral and the inhibition scenario, respectively, as obtained from stochastic simulations employing Gillespie's algorithm [40]. While in the neutral scenario the overall length of the MT stays approximately constant with only small fluctuations, the length dynamics for the inhibition scenario is intermittent with extended episodes of filament growth and shrinkage, reminiscent of the dynamic instability [41]. Note that for the inhibition scenario there is significant accumulation of motors at the MT tip during periods of depolymerization.

To understand how the system alternates between periods of growth and shrinkage, let us turn to a mathematical description of the dynamics. As already noted in the previous section, the length change of the MT is determined

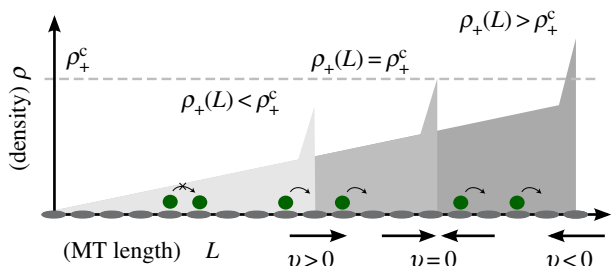


Figure 2. Illustration of a linear motor density profile (shaded areas) and the threshold density ρ_+^c (dashed line) for MT regulation. Low tip density $\rho_+(L)$ results in a growing MT, and a high tip density results in a shrinking MT. Note that the density at the tip generally has a spike-like shape [39]. (Online version in colour.)

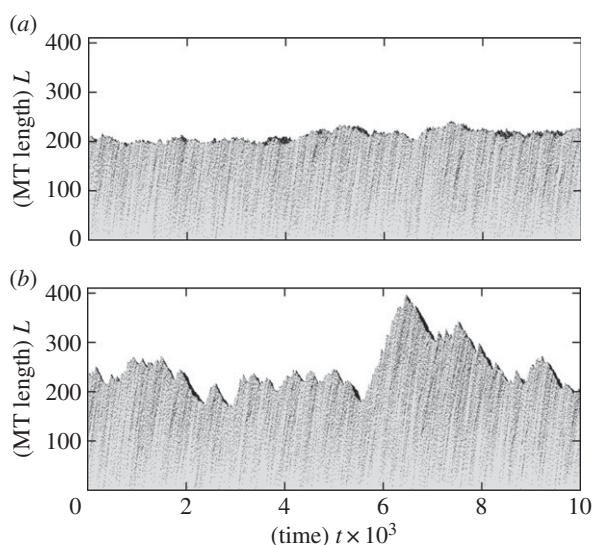


Figure 3. Kymographs of how molecular motors regulate an MT. In the neutral case (a), the system displays a higher accuracy in length regulation ($\delta = 0.2$, $\gamma = 0.1316$). This is in contrast to the case of growth inhibition (b) where the system displays intermittent dynamics ($\delta = 0.2$, $\eta = 0.385$). Attachment and detachment rates are $c\omega_{on} = 0.001$ and $\omega_{off} = 0.003$.

by the tip density ρ_+ , e.g. the probability that the MT tip is occupied by a molecular motor,

$$\partial_t L = \begin{cases} -\delta\rho_+ + \gamma & \text{(neutral scenario),} \\ -\delta\rho_+ + \eta(1 - \rho_+) & \text{(inhibition scenario).} \end{cases} \quad (3.1)$$

Here the first term on the right-hand side stands for depolymerization, and the second term describes polymerization dynamics of the neutral and the inhibition scenario, respectively. Equation (3.1) shows that depending on the magnitude of the tip density, ρ_+ , the MT either grows or shrinks: for large tip densities, depolymerization is strong and the MT shrinks, while the MT grows for small tip densities (figure 2). The critical tip densities, ρ_+^c , where the filament length becomes stationary read

$$\rho_+^c = \begin{cases} \frac{\gamma}{\delta} & \text{(neutral scenario),} \\ \frac{\eta}{\delta + \eta} & \text{(inhibition scenario).} \end{cases} \quad (3.2)$$

To make further progress, one needs to determine the actual tip densities employing a mean-field approach for the motor dynamics along the MT [33].

Table 1. Quantification of model parameters for kinesin-8 and XMAP215.

kinesin-8	model	experiment [16]
speed	$\nu = 1$	$6.35 \text{ steps s}^{-1}$
attachment	ω_{on}	$24 \text{ (nM min } \mu\text{m)}^{-1}$
detachment	ω_{off}	$4.8 \times 10^{-3} \text{ s}^{-1}$
depolymerization	δ	n/k [17]
tip detachment ^a	β	$0.1 - 0.01 \text{ s}^{-1}$
MT growth	model	experiment ^b
neutral	γ	n/k
inhibition	η	n/k
XMAP215	model	experiment [27]
attachment	k_{on}	$0.1 \text{ (nM s } \mu\text{m)}^{-1}$
detachment	k_{off}	3.8 s^{-1}
polymerization	η_x	$6.6 \text{ dimers s}^{-1}$

^aTip dwell times of different kinesin-8 constructs are: 10–55 s [18], 20–40 s [19], 80 s [16]. In [16], it is shown that dwell times at the tip depend on motor concentration, suggesting cooperative effects of motors at the tip. A theoretical analysis is given in [17].

^bMT growth speeds in the presence of kinesin-8s *in vivo* are $1.3 \mu\text{m min}^{-1}$ [12], $2 \mu\text{m min}^{-1}$ [4,42]. Rate constants of individual growth events, however, are not available to our knowledge and the complexity of the process [43] renders it difficult to quantify the damping effects of kinesin-8 [44].

3.1. Phase behaviour and tip densities

For biologically relevant parameter ranges, the time scales of the tip dynamics and the motor dynamics are comparable (cf. table 1). Therefore, the motor density profile quickly adapts to changes in the tip density and one can readily assume that the tip density and the bulk density are adiabatically coupled [33]. Moreover, experimental data also show that both the attachment and the detachment rates, ω_{on} and ω_{off} , are very small [16]. This suggests considering a *simplified model* where one neglects the attachment and detachment kinetics and assumes that a constant density ρ_- serves as a particle reservoir at the left end of a lattice with fixed size L (figure 4). This allows us to focus on the dynamics at the plus-end and unravel how it depends on the reservoir density ρ_- . Owing to the adiabatic coupling between boundary and bulk, the results for the full model can be inferred from the simplified model upon replacing ρ_- by the actual spatially varying profile $\rho_-(x)$.

Since there is particle conservation, the dynamics of the tip density is given by

$$\partial_t \rho_+ = J_b(\rho_b, \rho_+) - J_{exit}(\rho_+), \quad (3.3)$$

where J_b and $J_{exit} = \delta\rho_+$ denote the bulk current and the loss rate of motors due to depolymerization, respectively. Calculations are conveniently performed in a frame comoving with the MT tip. Then the bulk currents for the neutral (N) and the inhibition (I) scenario read in a mean-field approximation [33]

$$J_b^N = \rho_b(1 - \rho_b) - \gamma\rho_b + \delta\rho_+\rho_b \quad (3.4a)$$

and

$$J_b^I = \rho_b(1 - \rho_b) - \eta\rho_b(1 - \rho_+) + \delta\rho_+\rho_b. \quad (3.4b)$$

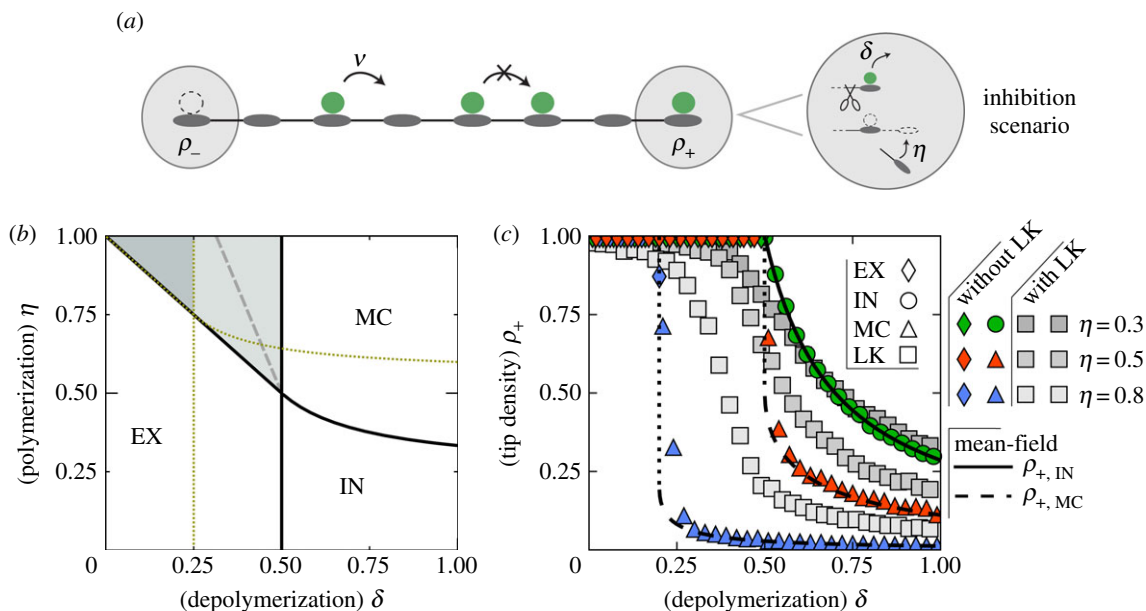


Figure 4. (a) Illustration of the simplified model with a constant particle reservoir ρ_- at the minus-end, and where LK is not accounted for. (b) Mean-field phase diagram for the simplified model (inhibition scenario) for two different values of the reservoir density: $\rho_- = 0.5$ (solid black), and $\rho_- = 0.25$ (dotted). Dashed line indicates the phase boundary obtained from stochastic simulations of the simplified model including LK with on- and off-rates $c\omega_{\text{on}} = \omega_{\text{off}} = 0.005$. (c) Mean-field solutions for tip densities at various growth rates η indicated in the graph compared to simulation data with and without LK. Different phases (IN/EX/MC) are indicated by symbols and lines and refer to analytic results (cf. equations (3.8) and (3.11)). The dotted line indicates a discontinuous transition between the EX and MC phase. The lattice was initiated with random configurations of motors with bulk density $\rho_b = 0.5$. (Online version in colour.)

Here ρ_b denotes the motor density in the bulk of the MT, and the first term describes the current due to hopping processes accounting for particle exclusion on neighbouring sites. The remainder of the terms indicates polymerization and depolymerization currents, which in a comoving frame simply correspond to simultaneous movement of all particles on the MT lattice to the left and right end, respectively.

The stationary state of the model is determined by a balance of currents, or, in other words, the fixed point of equation (3.3): $\rho_+ \delta = J_b(\rho_b, \rho_+)$. Solving for the tip density one finds

$$\rho_+ = \rho_+(\rho_b, \delta, \eta) = \frac{\rho_b(1 - \eta - \rho_b)}{\delta(1 - \rho_b) - \eta\rho_b}, \quad (3.5)$$

for the inhibition scenario. The tip density is determined by the bulk particle flux towards the tip and, at the same time, the bulk density depends on the molecular processes at the MT tip. To make progress with the analytical calculations, it is necessary to have some knowledge about the nature of the density profiles and their stability with respect to fluctuations. For exclusion processes, there are in general three distinct phases, each of which corresponds to different bulk densities ρ_b and ensuing bulk currents [45,46]:

- *IN phase.* In this phase, the particle current that enters the system at the minus-end determines the bulk density. For TASEP, this phase is also called *low-density phase*.
- *EX phase.* The bulk density is determined by the current of particles that leave the system at the right boundary (TASEP: *high-density phase*).
- *MC phase.* In this phase, the *maximal current* (MC) through the system determines the bulk density. It corresponds to a local maximum in the current density relation $J_b(\rho_b)$. In contrast to the two other phases, the bulk density in the MC phase is independent of the boundary conditions.

Moreover, for exclusion processes, there are two possibilities to account for the boundary conditions at the left and right end. Either there is a domain wall (DW) delineating a low-density region, ρ_- , from a high-density region, ρ_+ , or there are boundary layers [47] at one of the MT ends.

3.1.1. Density perturbations and domain wall theory

To make progress on the phase diagram, we need to investigate the stabilities of the aforementioned DW and bulk density. To this end, we introduce two important criteria that allow us to analyse the stability of perturbations in exclusion processes known as DW theory and the extremal current principle (ECP) [48–50]. First we consider the stability of a bulk density ρ_b against a density perturbation. Such a perturbation travels at the collective velocity [48,49]

$$u_{\text{coll}} = \partial_\rho J_b(\rho, \rho_+) |_{\rho=\rho_b}. \quad (3.6)$$

Since for $u_{\text{coll}} < 0$ density perturbations move towards the minus-end, they do not affect the tip density and thereby the EX phase remains stable. By contrast, for $u_{\text{coll}} > 0$, perturbations move towards the plus-end which renders the IN phase stable against density fluctuations. Note that the collective velocity $u_{\text{coll}} = 0$ in the MC phase (by definition). Second, we consider the stability of DWs. A DW between a left ρ^{left} and right density ρ^{right} travels at a velocity

$$u_{\text{DW}} = \frac{J_b(\rho^{\text{left}}, \rho_+) - J_b(\rho^{\text{right}}, \rho_+)}{\rho^{\text{left}} - \rho^{\text{right}}}. \quad (3.7)$$

Depending on the sign of this velocity the phase corresponding to ρ^{left} or ρ^{right} is stable [49]. Taken together, u_{coll} and u_{DW} lead to analytic results for bulk and tip densities in the various phases (table 2).

3.1.2. Phase diagram for the inhibition scenario

With the methods introduced in the previous section, it is a straightforward task to derive the densities and the ensuing

Table 2. Analytic results for the tip densities ρ_+ in the different phases IN/EX/MC and the critical growth rates η_c and γ_c for the inhibition and neutral scenario, respectively. Note that ρ_+^{EX} is obtained from the phase boundary of the EX phase as derived in the main text.

tip density			
inhibition	$\rho_+^{\text{IN}} = \frac{\rho_-(1-\eta-\rho_-)}{\delta-\rho_-(\eta+\delta)}$	$\rho_+^{\text{EX}} = 1$	$\rho_+^{\text{MC}} = \frac{\eta(\eta+\delta-1)+\delta-2\sqrt{\delta\eta(\eta+\delta-1)}}{(\eta+\delta)^2}$
neutral [33]	$\rho_+^{\text{IN}} = \frac{\rho_-(1-\gamma-\rho_-)}{\delta(1-\rho_-)}$	$\rho_+^{\text{EX}} = 1 - \frac{\gamma}{1-\delta}$	$\rho_+^{\text{MC}} = \frac{1-\sqrt{\gamma}}{\delta}$
critical growth			
inhibition	$\eta_c^{\text{IN}} = \frac{\delta\rho_-(1-\rho_-)}{\delta-\rho_-(1-\rho_-)}$	$\eta_c^{\text{EX}} = 1 - \delta$ (see equation (3.12))	$\eta_c^{\text{MC}} = \frac{\delta}{4\delta-1}$
neutral [33]	$\gamma_c^{\text{IN}} = \rho_-(1-\rho_-)$	$\gamma_c^{\text{EX}} = \delta(1-\delta)$	$\gamma_c^{\text{MC}} = \frac{1}{4}$

phase behaviour of the simplified model. Since the neutral scenario has already been discussed [33], we here focus on the inhibition scenario. In the IN phase, the bulk density is (by definition) given by the reservoir density at the left boundary: $\rho_b^{\text{IN}} = \rho_-$. With the stationarity condition, equation (3.5), one finds that the tip density is a function of the reservoir density

$$\rho_+^{\text{IN}}(\rho_-, \delta, \eta) = \frac{\rho_-(1-\eta-\rho_-)}{\delta(1-\rho_-)-\eta\rho_-}. \quad (3.8)$$

Note, however, that this is a stable solution of equation (3.3) only outside of the shaded area indicated in the phase diagram shown in figure 4b. In the EX phase, the bulk density is given by the right boundary, $\rho_b^{\text{EX}} = \rho_+$, and equation (3.5) leads to the striking result that the MT tip is *always* occupied by a molecular motor,

$$\rho_+^{\text{EX}} = 1, \quad (3.9)$$

in stark contrast to the corresponding result in the neutral scenario (table 2). It implies that an MT always depolymerizes for those parameter regimes where the system is in the EX phase. As in Reese *et al.* [17], we attribute this behaviour to the slow depolymerization rate in the EX phase, $\delta < \rho_-$. It implies that motors leave the tip more slowly than they arrive. Then the MT tip acts as a bottleneck for molecular transport and induces a traffic jam with $\rho_+^{\text{EX}} = 1$ at the plus-end. For the MC phase, the bulk density is given by the maximum of the bulk current J_b^{\dagger}

$$\rho_b^{\text{MC}} = \frac{\delta - \sqrt{\delta\eta(\delta + \eta - 1)}}{\delta + \eta}. \quad (3.10)$$

Using this bulk density in equation (3.5) gives a constant value for the tip density in the MC phase which is independent of the reservoir density

$$\rho_+^{\text{MC}} = \frac{\delta + \eta(\eta + \delta - 1) - 2\sqrt{\eta\delta(\eta + \delta - 1)}}{(\delta + \eta)^2}. \quad (3.11)$$

Knowing the tip densities, we can now use the DW theory explained above (see §3.1.1) to determine the transition lines between the various phases. The DW velocity gives the direction in which a DW between two densities, one from the left and one from the right, travels. To employ these criteria, we first have to identify the respective densities. Let us start with ρ_{left} : the density at the minus-end is in general determined by the entering current, corresponding to a tip density $\rho_{\text{IN}}^{\dagger}$, equation (3.8). This tip density, however, is only stable

against small perturbations if $u_{\text{coll}} \geq 0$. For parameters where $u_{\text{coll}} < 0$ the density from the left is decreased to $\rho_{\text{left}} = \rho_{\text{MC}}^{\dagger}$. This sign-change of the collective velocity defines the phase boundary between the IN and MC phase: $\eta = \delta(\rho_- - 1)^2/(\delta - \rho_-^2)$. Taken together, the density on the left of the DW is given by $\rho_{\text{left}} = \text{Min}[\rho_{\text{IN}}^{\dagger}, \rho_{\text{MC}}^{\dagger}]$. The density at the right of the DW, ρ_{right} , is determined analogously. Since in that regime the collective velocity is strictly negative we simply have $\rho_{\text{right}} = \rho_{\text{EX}}^{\dagger} = 1$. Using the above expressions for ρ_{left} and ρ_{right} in equation (3.7) gives the remaining phase boundaries: with $\rho_{\text{left}} = \rho_-$, $\rho_{\text{right}} = 1$ and $\rho_+ = 1$ one obtains $u_{\text{DW}} = \delta - \rho_-$, implying that the phase boundary between the IN and EX phase is given by $\delta = \rho_-$. The boundary line $\delta + \eta = 1$ signifies that above this line the stationary solution given by equation (3.8) becomes unstable. This instability gives rise to interesting motor dynamics, in particular, a subtle dependence of the ensuing stationary profile on the initial condition. While these effects are certainly worthwhile studying they are irrelevant for our main focus, namely MT regulation, and, hence, we refrain from further analysing this regime here.

Taken together, the above analysis gives the phase diagram shown in figure 4b for two different values of the reservoir density ρ_- . The general trend is that with decreasing reservoir density the parameter domain where the IN phase is stable expands.

The analytical results obtained from mean-field theory agree nicely with the stochastic simulations (figure 4c) in the case where LK is neglected. For a depolymerization rate $\eta = 0.3$, concomitant with the phase transition from the IN to the EX phase, the tip density increases upon lowering the depolymerization rate δ and then continuously saturates at $\rho_+ = 1$ as the EX phase is reached. By contrast, for $\eta \geq 0.5$, there is a *discontinuous jump* in the tip density as one passes from the MC into the EX phase; see discussion above.

The stochastic simulations with LK show a quite significant increase in the magnitude of the tip density in the MC phase, in particular in the shaded area of the phase diagram, figure 4b. We attribute this to the fact that the Langmuir density in bulk, ρ_{La} , acts as a source for kinesin-8 motors which tends to increase the motor density on the MT and at the tip. Although these effects are interesting and worthwhile studying, they are not important for our main concern here, namely regulation of MT length. As discussed previously [33], and elaborated on later in §3.4, MT regulation is possible only if the density profile is determined by the particle current at the minus-end, i.e. if the system in its stationary state is in the IN phase. In that case,

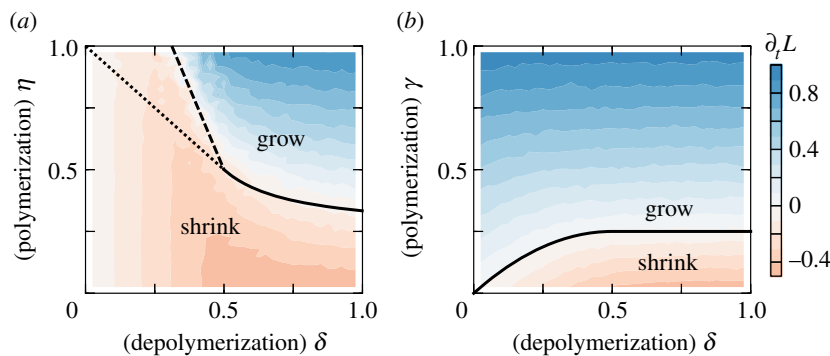


Figure 5. Drift velocity of the MT tip, $v = \partial_t L$, as a function of the polymerization and depolymerization rates for the (a) inhibition and the (b) neutral scenario obtained from stochastic simulations for the simplified model with LK; colour code indicates the magnitude of the drift. Solid lines indicate where the MT velocity is zero, $\eta_c(\delta)$ and $\gamma_c(\delta)$, as obtained from the analytical calculations (table 2). The dotted line is obtained from the analytical theory; it coincides with the boundary line $v = 0$ and agrees well with numerical simulations where LK has been turned off. The dashed line is the numerically determined boundary η_c when LK is turned on. Stochastic simulations including LK were performed with motor attachment and detachment rates $c\omega_{\text{on}} = \omega_{\text{off}} = 0.005$, $\rho_- = 0.5$ and system size 200. (Online version in colour.)

even adding LK in the simulations has only a minor effect on the magnitude of the tip density, and we can safely use the analytical mean-field results to further analyse the stationary MT length.

3.2. Dynamics of the microtubule length

Figure 5 shows the results of our stochastic simulations with LK for the MT drift velocity, $v = \partial_t L$ as a function of the depolymerization and the polymerization rates for both the inhibition and the neutral scenario. There are well-defined boundaries, $\eta_c(\delta, \rho_-)$ and $\gamma_c(\delta, \rho_-)$, separating regimes in which MTs grow and shrink, respectively. Since the tip density, ρ_+ , dictates MT dynamics (see equation (3.1)), those boundaries can be readily calculated upon comparing the tip densities listed in table 2 with the critical tip density, equation (3.2). For the inhibition scenario, we find that for $\delta < \rho_-$ the critical tip density coincides with the phase boundary of the EX phase

$$\eta_c = 1 - \delta, \quad (3.12)$$

while for $\delta > \rho_-$ it lies either within the MC or the IN phase:

$$\eta_c = \begin{cases} \frac{\delta\rho_-(1-\rho_-)}{\delta-\rho_-(1-\rho_-)} & \text{for } \rho_- < \frac{1}{2}, \\ \frac{\delta/4}{\delta-1/4} & \text{for } \rho_- > \frac{1}{2} \end{cases} \quad (3.13)$$

(see table 2 for a summary together with the results for the neutral scenario). These analytical results are in perfect accordance with our stochastic simulations (figure 5) with one interesting exception for the inhibition scenario, namely the boundary line of the EX phase for $\delta < \rho_-$. Since we recover agreement between stochastic simulations and analytical calculations by switching off LK in our stochastic simulations, we can fully attribute this difference to the effect of attachment and detachment of motors in bulk, as discussed in §3.1.2; cf. dotted and dashed lines in figure 5a. Furthermore, the differences between both scenarios are significant, cf. figure 5a,b, respectively. In the inhibition scenario, the regime where MTs shrink—and hence regulation becomes possible—is much broader since kinesin-8 inhibits MT growth when bound to the tip: for small depolymerization rate δ , motors reside at the MT end for a relatively long time, which dramatically broadens the regime of MT shrinkage.

3.3. Interplay between kinesin-8 and polymerase XMAP215

In this section, we compare the dynamics of the inhibition scenario with a model which explicitly accounts for a second protein, XMAP215, that enzymatically facilitates MT growth (figure 6a and §2). In a case where XMAP215 and kinesin-8 mutually exclude each other at the MT tip, one expects strong similarities between those scenarios. In order to compare with an analytically tractable lattice gas model, we performed the stochastic simulations for the simplified model without LK.¹ Figure 6b shows the regimes of MT growth and shrinkage as a function of kinesin-8 and XMAP215 densities for a set of depolymerization rates δ . The general trend is that the regime where MTs shrink is enlarged with smaller depolymerization rates.

At the mean-field level, the equilibrium density of XMAP215 at the MT tip is given by the product $\rho_x = \rho_x^{\text{eq}}(1 - \rho_+)$, where $1 - \rho_+$ is the probability that kinesin-8 is not bound and ρ_x^{eq} denotes the Langmuir isotherm for XMAP215 binding

$$\rho_x^{\text{eq}} = \frac{c_x k_{\text{on}}}{c_x k_{\text{on}} + k_{\text{off}}}. \quad (3.14)$$

Here c_x is the XMAP215 concentration in solution, and k_{on} and k_{off} are the attachment and detachment rates of the enzyme to and from the MT tip, respectively. This mean-field approximation neglects that the presence of XMAP215 at the MT tip influences the current of kinesin-8 to the MT end, because it could block the motor particles [51]. Fortunately, as the polymerization rate of XMAP215, η_x , and the walking speed, v , of kinesin-8 are almost the same [16,27] the two molecules rarely interact. This implies that a model explicitly accounting for XMAP215 can be reduced to the inhibition scenario with an effective polymerization rate given by

$$\eta = \eta_x \rho_x^{\text{eq}}. \quad (3.15)$$

Indeed, as can be inferred from figure 6b, the predictions of the effective inhibition scenario agree nicely with the numerical simulations. Taken together, this implies that the inhibition scenario may serve as a minimal model to include other MT-associated proteins that antagonize the depolymerization activity of kinesin-8. It remains an open question, however,

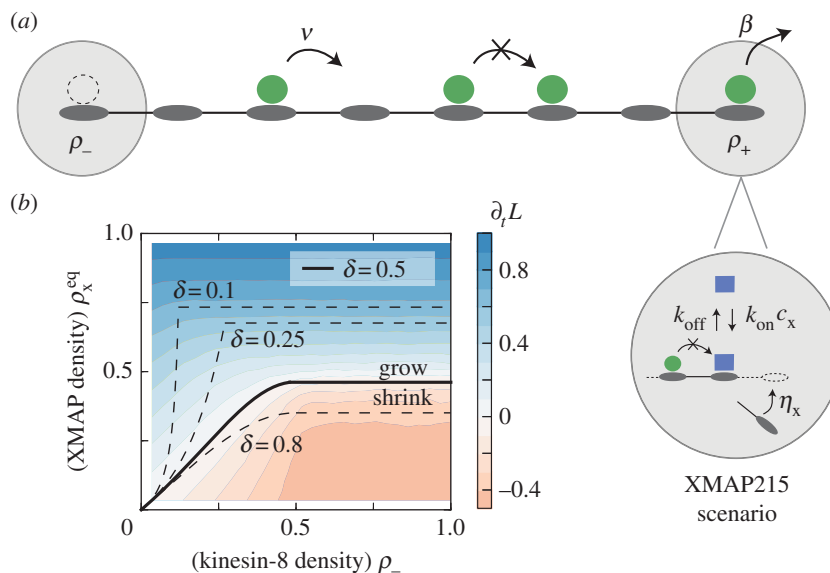


Figure 6. MT dynamics with kinesin-8 and XMAP215. (a) Simplified model with motor detachment from the tip (rate β) and tip-binding of XMAP215. (b) MT growth velocity as a function of kinesin-8 and XMAP215 density. A XMAP215 density of $\rho_x^{\text{eq}} = 0.5$ corresponds to $c_x \approx 10 \mu\text{M}$, and the concentration of kinesin-8 is approximately $c \approx 1.5 \text{ nM}$ for a half-filled lattice $\rho_b = 0.5$ (table 1). (Online version in colour.)

as to what extent our assumption of mutual exclusion between proteins at the MT tip is justified. Because MTs consist of multiple protofilaments, one could think of a multi-lane scenario where kinesin-8 and XMAP215 are simultaneously present at the MT tip. To model this scenario, it would be necessary to rethink the interactions between the different proteins and also between the proteins and the MT.

3.4. Microtubule regulation

We now consider the full model for an MT of finite length L , where LK leads to an accumulation of kinesin-8 motors along the MT. As discussed in §2, the ensuing antenna-like profile $\rho_-(x)$ can be calculated within the framework of the TASEP/LK model [37,38]; these theoretically predicted profiles have recently been confirmed by *in vitro* experiments [14]. Now length regulation becomes possible if this spatially varying profile translates into a length-dependent velocity $v(L)$ of the MT tip [7,33]. This requires that the tip density $\rho_+(L)$ depends on $\rho_-(L)$ which is the case only for the IN phase (see equation (3.8)). Then the tip density reads

$$\rho_+(L) = \rho_+^{\text{IN}}(\rho_-(L), \delta, \eta). \quad (3.16)$$

Upon inserting the ensuing length-dependent tip density into equation (3.1), one obtains a length-dependent velocity $v(L)$. It is instructive to define an *effective potential*

$$U_{\text{eff}}(L) = - \int_0^L dx v(x), \quad (3.17)$$

whose minimum defines the stationary MT length L^*

$$\rho_+(L^*) = \rho_+^{\text{IN}}(\rho_-(L^*), \delta, \eta) = \rho_+^c, \quad (3.18)$$

as illustrated in figure 7a–c. Tight length regulation is restricted to the regime where the critical density $\rho_-^c := \rho_-(L^*)$ falls well into the linearly increasing antenna profile. The closer ρ_-^c is to the Langmuir plateau ρ_{La} the less well defined is the stationary length; note that the effective spring coefficient

$$k(L) := U_{\text{eff}}''(L) = \begin{cases} \delta \rho_+'(L) & \text{(neutral scenario)} \\ (\delta + \eta) \rho_+'(L) & \text{(inhibition scenario)} \end{cases} \quad (3.19)$$

is proportional to the slope of the profile, where prime denotes derivative (see also figure 7c).

As can be inferred from figure 8a,b, the stochastic simulations agree nicely with the above analytical results for the stationary MT length L^* in both scenarios, neutral and inhibition. Previous studies [33] have shown that the variance of the length can be obtained well upon using a van Kampen expansion for the stochastic dynamics of the MT length $L(t)$, which assumes that the tip density is adiabatically coupled to the motor density along the MT. This essentially amounts to saying that the MT length performs a random walk in the effective potential $U_{\text{eff}}(L)$. Such a picture is fully consistent with results obtained from our stochastic simulations: the observed stochastic trajectories resemble those of random walks in confinement (figure 3a). More importantly, the numerically observed value for the probability that the MT tip is occupied, $p_+(L)$, agrees well with the mean-field tip density $\rho_+(x)$ (figure 7d). This implies that the stochastic trajectory samples the values of MT length $L(t)$ with a statistical weight determined by the effective potential $U_{\text{eff}}(L)$. Surprisingly, as can be inferred from figure 7e, this is not the case for the inhibition model which immediately invalidates a description of the stochastic dynamics in terms of a continuous random walk in the potential landscape shown in figure 7b. The latter would actually give rise to stochastic trajectories strongly confined to the stationary value L^* . By contrast, the actual stochastic trajectories for the inhibition scenario shown in figure 3b rather resemble an intermittent dynamics with abrupt transitions between growing and shrinking states. Even though the magnitude of the length fluctuations resembles MT dynamic instability [41], the microscopic origin of fluctuations in our model differs.

The key to understand this anomalous dynamics lies in realizing that the stochastic length dynamics in the inhibition scenario is a *dichotomous process* with only two states: while, if the MT tip is empty, the MT grows with a rate η , it shrinks with a rate δ if the MT tip is occupied by a kinesin-8 protein. In other words, depending on whether the MT tip is occupied or not, it is either in a shrinking or a growing state,

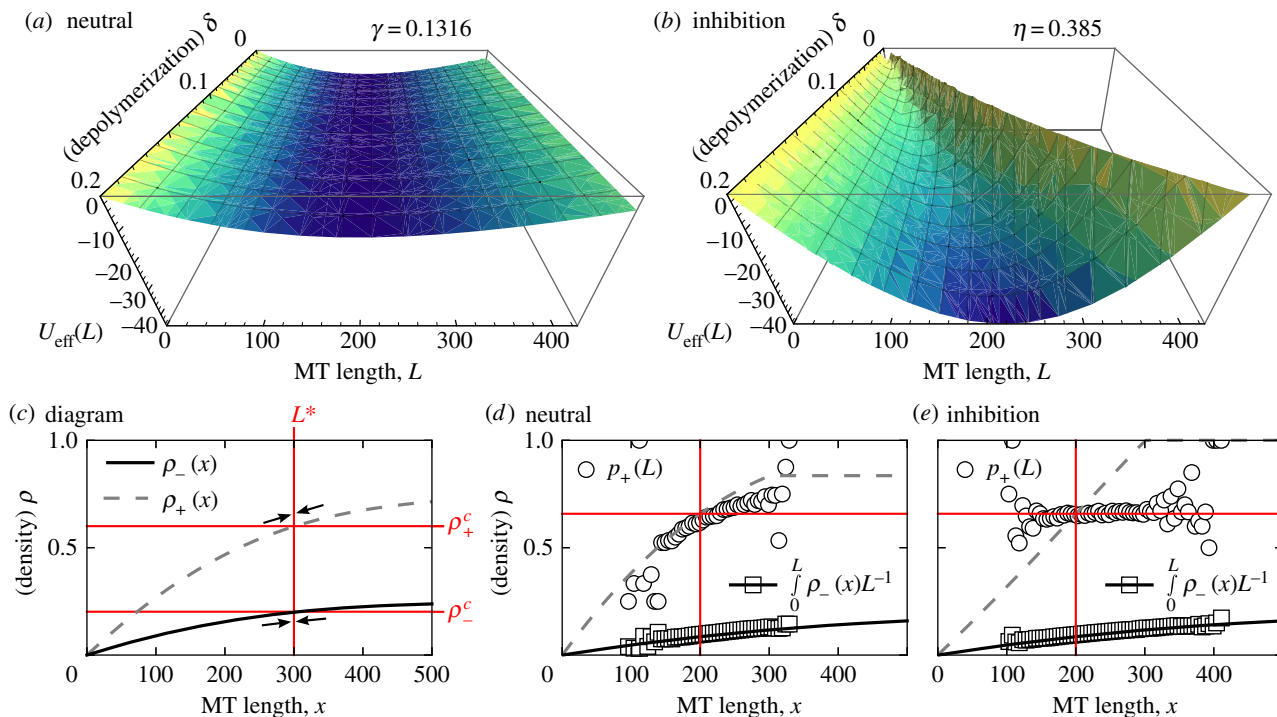


Figure 7. (a,b) Effective potentials for the inhibition and the neutral scenario for the trajectories shown in figure 3. The diagram in (c) illustrates how threshold densities for the tip density $\rho_+(x)$ and minus-end density $\rho_-(x)$ are defined, and how both quantities together set MT length L^* . (d,e) Data for the accumulated density, and the ensuing probability of tip occupation $p_+(L)$. For the inhibition scenario $p_+(L)$ is constant, while in the neutral scenario it is length-dependent and thus samples the effective potential, i.e. $p_+(L) = \rho_+(L)$. (Online version in colour.)

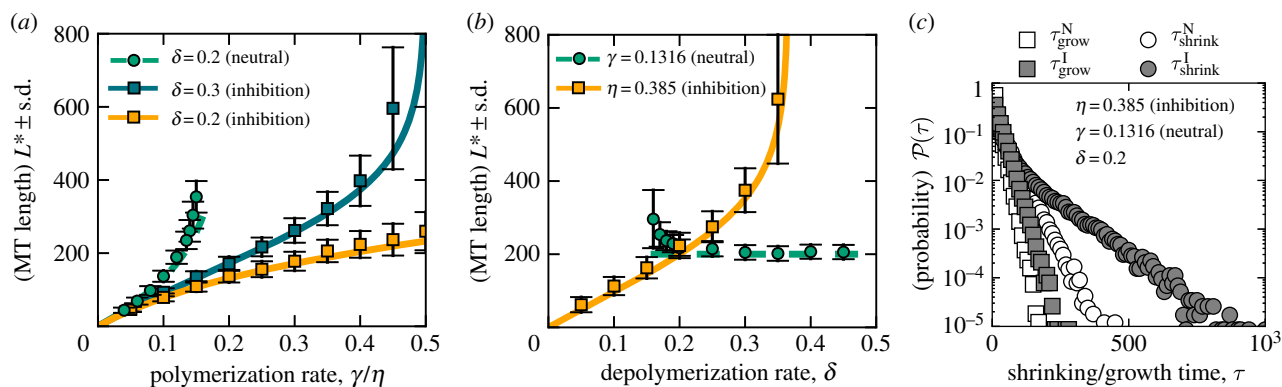


Figure 8. Comparison of MT length L^* for the inhibition (solid) and neutral (dashed) scenario with respect to polymerization (a) and depolymerization rates (b). The data were obtained as single trajectories $L(t)$. Data points correspond to the most probable length of the process L^* ; error bars denote the standard deviation of $L(t)$. Motor attachment and detachment rates are $c\omega_{on} = 0.001$ and $\omega_{off} = 0.003$. In (c) probability distributions of the times during which MTs shrink and grow are shown for parameter values as in figure 3. The exponential tails of the distributions support the view that the inhibition scenario follows dichotomous switching dynamics (see main text for details). (Online version in colour.)

respectively [52]. Consider a configuration where the tip is empty, and, hence, the MT is in a growing state (with average speed η). Then it will remain in this state for some time τ_{grow} until the motor closest to the tip actually reaches the tip. Figure 8c shows the probability distribution of τ_{grow} for the same parameters as in figure 8b. The distribution is clearly exponential with a typical time of the order of approximately $23/v$. On the other hand, if the MT tip is occupied by a kinesin-8 protein, it will remain in this state and not depolymerize the tip for a time of the order of δ^{-1} . During this time, the filament neither grows nor shrinks, and the kinesin-8 protein at the MT tip acts as a strict bottleneck. As a consequence, an extended traffic jam may emerge at the MT tip by motors queuing up behind this bottleneck. These traffic jams can

be clearly seen in figure 3b as black clusters. The formation of such clusters is a nucleation process, and the duration of the shrinking state is determined by a subtle interplay between particles gained by stochastic arrival at the left end and depolymerization dynamics. Interestingly, the probability distribution of τ_{shrink} shows two typical time scales, and, in particular, a broad exponential tail with a typical time of the order of approximately $112/v$. We leave a more detailed investigation of these interesting stochastic effects for future work. The main results we emphasize here are that we have identified two distinct time scales characteristic for prolonged growing and shrinking states. These time scales are macroscopic in the sense that they are much larger than the hopping time of individual motors (which

we have set to 1). This implies that also the typical lengths covered during the growing and the shrinking state are rather large; for the examples shown in figure 8c they are on average approximately 8 and 22 lattice sites during polymerization and depolymerization, respectively. These large length scales explain why the probability to occupy the MT tip as obtained from the stochastic simulations is only weakly dependent on MT length.

Taken together, we find that in the neutral scenario MT length is tightly controlled. The variance in MT length is mainly determined by the width of the effective potential, or, equivalently by the effective spring coefficient $k(L) = \delta \rho'_+(L)$. Hence, the slope of the antenna profile is the key determinant of length fluctuations. By contrast, for the inhibition scenario, extended periods of MT growth and shrinkage lead to large length fluctuations as can be seen from the kymographs in figure 3. These large fluctuations result in characteristic exponential tails in the filament's length distributions; the characteristic width of this distribution is shown as error bars in figure 8b. Note also the different dependencies of the two models with respect to the depolymerization rate. While in the neutral scenario the length of the MT is independent of the depolymerization rate δ , it strongly affects MT length in the inhibition scenario.

4. Discussion

We have analysed distinct molecular mechanisms of MT regulation by proteins which are able to catalyse growth and shrinkage of MTs. Specifically, our interest was in the interplay of Kip3p acting as depolymerase when bound to the MT tip and MT growth processes which are either spontaneous or also catalysed by proteins like XMAP215. We investigated two distinct scenarios: in a *neutral scenario* MTs grow independently of whether a kinesin-8 motor is bound to the tip or not. By contrast, in an *inhibition scenario* the MT only grows if the MT tip is not occupied by a depolymerase. Even though these scenarios were motivated by the MT depolymerizing motor Kip3p, our results can be applied to other molecular motors as well. For example, the human kinesin-8, Kif18a, has been shown to dampen MT dynamics [44] and even to block MT growth entirely [53]. Another example is kinesin-4, which inhibits the growth of MTs in anti-parallel MT overlaps [54].

Experiments with the MT polymerizing enzyme XMAP215 [27] suggest a high binding rate for the MT tip through facilitated diffusion. Then, to a first approximation, one may model XMAP215 as a tip-binding protein which excludes binding of kinesin-8. As we have shown, this tip site exclusion leads to a dynamics which is equivalent to the inhibition scenario.

The results obtained here show how interactions between individual proteins and the MT tip play an important role for MT regulation. There are three main findings: (i) MT regulation is directly affected by motor traffic. It is influenced by the MT growth rate, and attachment and detachment kinetics of motors to and from the MT. Both parameters can be tuned in experiments through the tubulin concentration and the motor and salt concentrations [14], respectively. (ii) Regimes of MT growth and shrinkage critically depend on the probability that a kinesin-8 motor is bound to the MT tip. (iii) Protein–MT interactions at the MT tip are key

to distinguish different mechanisms of MT regulation, like for example intermittent dynamics or tight length control.

The parameter regimes where motor traffic constrains MT growth differ dramatically for the two scenarios (cf. figure 5). For the neutral scenario, this parameter regime is relatively small and, in particular, limited to slow growth rates. It is characterized by relatively tight length control [33]. By contrast, for the inhibition scenario, the regime where length regulation is possible is extremely broad and includes high growth rates, however, at the cost of accurate length control: MT dynamics is intermittent with extended periods of MT growth and shrinkage, reminiscent of MT dynamic instability. Therefore, in the view of the regulation of MT length, these findings suggest the inhibition scenario as a mechanism for large length fluctuations, while the neutral scenario provides a mechanism for precise length control. To test these theoretical ideas, we suggest experiments which vary the protein concentration of kinesin-8, tubulin and XMAP215. The specific predictions of our theory will allow one to discern between different molecular mechanisms at the MT tip, simply by analysing how changes in the concentrations affect macroscopic quantities like the MT length and the speed of MT growth and shrinkage.

Besides its biological relevance for MT-related cellular processes, our study also contributes to the field of driven diffusive systems. We not only show how systems with a dynamic length can be treated analytically, but the technique we propose also gives conceptual insights into the determination of boundary-induced phases. This is achieved by extending the ECP [48] to dynamic systems. For instance, we found that a shock forming dynamically at the right boundary (not in bulk) determines whether the system is in the IN or EX phase. In addition, we could identify an unstable region in the phase diagram (between EX and MC phase for the inhibition scenario), where the system not only depends on the boundaries, but also on the initial conditions. This behaviour is to our knowledge not common for driven diffusive systems, and an interesting topic for future studies. Even though the main dynamic behaviour, as MT length, is governed by currents which are determined by the boundaries, also bulk phenomena are important as observed in [14,36,37], especially for lattice length fluctuations. We restricted our analysis to boundary-induced transitions, leaving it as a challenge for the future to capture also the bulk dynamics of motors on the MT.

From a broader perspective, the presented findings support the view that length-dependent disassembly and/or assembly rates due to molecular motor transport are likely to constitute a general mechanism to influence the length of one-dimensional structures in biology regardless of mechanistic details [55]. Specifically, MT tips are crowded spots in the cell, where space limitations for protein binding, inferring mutual exclusion, are relevant factors. Future experimental work needs to study dwell times of molecules at MT tips at the highest possible accuracy, because dwell times encode important information about the underlying molecular interaction networks [56]. Future theoretical studies may include other microscopic scenarios at the tip, as for example an interpolation between the neutral and the inhibition scenario, and the coupling of multiple protofilaments. Similarly, it will be important to learn more about interactions of molecular motors with the MT [57–59] during dynamic instability [60–62] and with networks of MTs [63,64].

Acknowledgements. We thank Matthias Rank, Anna Sophia Gayek and Mohan Gupta for helpful comments on the manuscript.

Funding statement. This project was supported by the Deutsche Forschungsgemeinschaft in the framework of the SFB 863.

References

- Desai A, Mitchison T. 1997 Microtubule polymerization dynamics. *Annu. Rev. Cell Dev. Biol.* **13**, 83–117. (doi:10.1146/annurev.cellbio.13.1.83)
- Goshima G, Scholey JM. 2010 Control of mitotic spindle length. *Ann. Rev. Cell Dev. Biol.* **26**, 21–57. (doi:10.1146/annurev-cellbio-100109-104006)
- de Forges H, Bouissou A, Perez F. 2012 Interplay between microtubule dynamics and intracellular organization. *Int. J. Biochem. Cell Biol.* **44**, 266–274. (doi:10.1016/j.biocel.2011.11.009)
- Tischer C, Brunner D, Dogterom M. 2009 Force- and kinesin-8-dependent effects in the spatial regulation of fission yeast microtubule dynamics. *Mol. Syst. Biol.* **5**, 250. (doi:10.1038/msb.2009.5)
- Laan L *et al.* 2012 Cortical dynein controls microtubule dynamics to generate pulling forces that position microtubule asters. *Cell* **148**, 502–514. (doi:10.1016/j.cell.2012.01.007)
- Pavin N, Laan L, Ma R, Dogterom M, Jülicher F. 2012 Positioning of microtubule organizing centers by cortical pushing and pulling forces. *New J. Phys.* **14**, 105025. (doi:10.1088/1367-2630/14/10/105025)
- Howard J, Hyman AA. 2007 Microtubule polymerases and depolymerases. *Curr. Opin. Cell Biol.* **19**, 31–35. (doi:10.1016/j.cob.2006.12.009)
- Wordeman L. 2005 Microtubule-depolymerizing kinesins. *Curr. Opin. Cell Biol.* **17**, 82–88. (doi:10.1016/j.cob.2004.12.003)
- Akhmanova A, Steinmetz MO. 2008 Tracking the ends: a dynamic protein network controls the fate of microtubule tips. *Nat. Rev. Mol. Cell Biol.* **9**, 309–322. (doi:10.1038/nrm2369)
- Subramanian R, Kapoor T. 2012 Building complexity: insights into self-organized assembly of microtubule-based architectures. *Dev. Cell* **23**, 874–885. (doi:10.1016/j.devcel.2012.10.011)
- Varga V, Helenius J, Tanaka K, Hyman AA, Tanaka TU, Howard J. 2006 Yeast kinesin-8 depolymerizes microtubules in a length-dependent manner. *Nat. Cell Biol.* **8**, 957–962. (doi:10.1038/ncb1462)
- Gupta ML, Carvalho P, Roof DM, Pellman D. 2006 Plus end-specific depolymerase activity of Kip3, a kinesin-8 protein, explains its role in positioning the yeast mitotic spindle. *Nat. Cell Biol.* **8**, 913–923. (doi:10.1038/ncb1457)
- Walczak CE, Gayek S, Ohi R. 2013 Microtubule-depolymerizing kinesins. *Annu. Rev. Cell Dev. Biol.* **29**, 417–441. (doi:10.1146/annurev-cellbio-101512-122345)
- Leduc C, Padberg-Gehle K, Varga V, Helbing D, Diez S, Howard J. 2012 Molecular crowding creates traffic jams of kinesin motors on microtubules. *Proc. Natl Acad. Sci. USA* **109**, 6100–6105. (doi:10.1073/pnas.1107281109)
- Cooper JR, Wagenbach M, Asbury CL, Wordeman L. 2010 Catalysis of the microtubule on-rate is the major parameter regulating the depolymerase activity of MCAK. *Nat. Struct. Mol. Biol.* **17**, 77–82. (doi:10.1038/nsmb.1728)
- Varga V, Leduc C, Bormuth V, Diez S, Howard J. 2009 Kinesin-8 motors act cooperatively to mediate length-dependent microtubule depolymerization. *Cell* **138**, 1174–1183. (doi:10.1016/j.cell.2009.07.032)
- Reese L, Melbinger A, Frey E. 2011 Crowding of molecular motors determines microtubule depolymerization. *Biophys. J.* **101**, 2190–2200. (doi:10.1016/j.bpj.2011.09.009)
- Stumpff J, Du Y, English C, Maliga Z, Wagenbach M, Asbury C, Wordeman L, Ohi R. 2011 A tethering mechanism controls the processivity and kinetochore-microtubule plus-end enrichment of the kinesin-8 Kif18A. *Mol. Cell* **43**, 764–775. (doi:10.1016/j.molcel.2011.07.022)
- Su X, Qiu W, Gupta ML, Pereira-Leal JB, Reck-Peterson SL, Pellman D. 2011 Mechanisms underlying the dual-mode regulation of microtubule dynamics by kip3/kinesin-8. *Mol. Cell* **43**, 751–763. (doi:10.1016/j.molcel.2011.06.027)
- Mayr MI, Storch M, Howard J, Mayer TU. 2011 A non-motor microtubule binding site is essential for the high processivity and mitotic function of kinesin-8 Kif18A. *PLoS ONE* **6**, e27471. (doi:10.1371/journal.pone.0027471)
- Weaver LN, Ems-McClung SC, Stout JR, Leblanc C, Shaw SL, Gardner MK, Walczak CE. 2011 Kif18A uses a microtubule binding site in the tail for plus-end localization and spindle length regulation. *Curr. Biol.* **21**, 1500–1506. (doi:10.1016/j.cub.2011.08.005)
- Su X, Ohi R, Pellman D. 2012 Move in for the kill: motile microtubule regulators. *Trends Cell Biol.* **22**, 567–575. (doi:10.1016/j.tcb.2012.08.003)
- Gard DL, Kirschner MW. 1987 A microtubule-associated protein from *Xenopus* eggs that specifically promotes assembly at the plus-end. *J. Cell Biol.* **105**, 2203–2215. (doi:10.1083/jcb.105.5.2203)
- Vasquez RJ, Gard DL, Cassimeris L. 1994 XMAP from *Xenopus* eggs promotes rapid plus end assembly of microtubules and rapid microtubule polymer turnover. *J. Cell Biol.* **127**, 985–993. (doi:10.1083/jcb.127.4.985)
- Tournebise R *et al.* 2000 Control of microtubule dynamics by the antagonistic activities of XMAP215 and XKCM1 in *Xenopus* egg extracts. *Nat. Cell Biol.* **2**, 13–19. (doi:10.1038/71330)
- Kinoshita K, Habermann B, Hyman AA. 2002 XMAP215: a key component of the dynamic microtubule cytoskeleton. *Trends Cell Biol.* **12**, 267–273. (doi:10.1016/S0962-8924(02)02295-X)
- Brouhard GJ, Stear JH, Noetzel TL, Al-Bassam J, Kinoshita K, Harrison SC, Howard J, Hyman AA. 2008 XMAP215 is a processive microtubule polymerase. *Cell* **132**, 79–88. (doi:10.1016/j.cell.2007.11.043)
- Li W, Moriwaki T, Tani T, Watanabe T, Kaibuchi K, Goshima G. 2012 Reconstitution of dynamic microtubules with drosophila XMAP215, EB1, and sentin. *J. Cell Biol.* **199**, 849–862. (doi:10.1083/jcb.201206101)
- Zanic M, Widlund PO, Hyman AA, Howard J. 2013 Synergy between XMAP215 and EB1 increases microtubule growth rates to physiological levels. *Nat. Cell Biol.* **15**, 688–693. (doi:10.1038/ncb2744)
- Komarova Y *et al.* 2009 Mammalian end binding proteins control persistent microtubule growth. *J. Cell Biol.* **184**, 691–706. (doi:10.1083/jcb.200807179)
- Kinoshita K, Arnal I, Desai A, Drechsel DN, Hyman AA. 2001 Reconstitution of physiological microtubule dynamics using purified components. *Science* **294**, 1340–1343. (doi:10.1126/science.1064629)
- Niwa S, Nakajima K, Miki H, Minato Y, Wang D, Hirokawa N. 2012 Kif19a is a microtubule-depolymerizing kinesin for ciliary length control. *Dev. Cell* **23**, 1167–1175. (doi:10.1016/j.devcel.2012.10.016)
- Melbinger A, Reese L, Frey E. 2012 Microtubule length regulation by molecular motors. *Phys. Rev. Lett.* **108**, 258104. (doi:10.1103/PhysRevLett.108.258104)
- Krapivsky PL, Redner S, Ben-Naim E. 2010 *A kinetic view of statistical physics*. Cambridge, UK: Cambridge University Press.
- Chou T, Mallick K, Zia RKP. 2011 Non-equilibrium statistical mechanics: from a paradigmatic model to biological transport. *Rep. Prog. Phys.* **74**, 116601. (doi:10.1088/0034-4885/74/11/116601)
- Lipowsky R, Klumpp S, Nieuwenhuizen T. 2001 Random walks of cytoskeletal motors in open and closed compartments. *Phys. Rev. Lett.* **87**, 108101. (doi:10.1103/PhysRevLett.87.108101)
- Parmeggiani A, Franosch T, Frey E. 2003 Phase coexistence in driven one-dimensional transport. *Phys. Rev. Lett.* **90**, 086601. (doi:10.1103/PhysRevLett.90.086601)
- Parmeggiani A, Franosch T, Frey E. 2004 Totally asymmetric simple exclusion process with Langmuir

- kinetics. *Phys. Rev. E* **70**, 046101. (doi:10.1103/PhysRevE.70.046101)
39. Pierobon P, Mobilia M, Kouyos R, Frey E. 2006 Bottleneck-induced transitions in a minimal model for intracellular transport. *Phys. Rev. E* **74**, 031906. (doi:10.1103/PhysRevE.74.031906)
 40. Gillespie DT. 2007 Stochastic simulation of chemical kinetics. *Annu. Rev. Phys. Chem.* **58**, 35–55. (doi:10.1146/annurev.physchem.58.032806.104637)
 41. Mitchison T, Kirschner M. 1984 Dynamic instability of microtubule growth. *Nature* **312**, 237–242. (doi:10.1038/312237a0)
 42. Stumpff J, von Dassow G, Wagenbach M, Asbury C, Wordeman L. 2008 The kinesin-8 motor Kif18A suppresses kinetochore movements to control mitotic chromosome alignment. *Dev. Cell* **14**, 252–262. (doi:10.1016/j.devcel.2007.11.014)
 43. Gardner MK, Charlebois BD, Janosi IM, Howard J, Hunt AJ, Odde DJ. 2011 Rapid microtubule self-assembly kinetics. *Cell* **146**, 582–592. (doi:10.1016/j.cell.2011.06.053)
 44. Du Y, English CA, Ohi R. 2010 The kinesin-8 Kif18A dampens microtubule plus-end dynamics. *Curr. Biol.* **20**, 374–380. (doi:10.1016/j.cub.2009.12.049)
 45. Derrida B, Domany E, Mukamel D. 1992 An exact solution of a one-dimensional asymmetric exclusion model with open boundaries. *J. Stat. Phys.* **69**, 667–687. (doi:10.1007/BF01050430)
 46. Schütz G, Domany E. 1993 Phase transitions in an exactly soluble one-dimensional exclusion process. *J. Stat. Phys.* **72**, 277–296. (doi:10.1007/BF01048050)
 47. Hager JS, Krug J, Popkov V, Schütz GM. 2001 Minimal current phase and universal boundary layers in driven diffusive systems. *Phys. Rev. E* **63**, 056110. (doi:10.1103/PhysRevE.63.056110)
 48. Krug J. 1991 Boundary-induced phase transitions in driven diffusive systems. *Phys. Rev. Lett.* **67**, 1882–1885. (doi:10.1103/PhysRevLett.67.1882)
 49. Kolomeisky AB, Schütz GM, Kolomeisky EB, Straley JP. 1998 Phase diagram of one-dimensional driven lattice gases with open boundaries. *J. Phys. A: Math. Gen.* **31**, 6911–6920. (doi:10.1088/0305-4470/31/33/003)
 50. Popkov V, Schütz GM. 1999 Steady-state selection in driven diffusive systems with open boundaries. *Europhys. Lett.* **48**, 257–263. (doi:10.1209/epl/i1999-00474-0)
 51. Wood AJ. 2009 A totally asymmetric exclusion process with stochastically mediated entrance and exit. *J. Phys. A: Math. Theor.* **42**, 445002. (doi:10.1088/1751-8113/42/44/445002)
 52. Dogterom M, Leibler S. 1993 Physical aspects of the growth and regulation of microtubule structures. *Phys. Rev. Lett.* **70**, 1347–1350. (doi:10.1103/PhysRevLett.70.1347)
 53. Stumpff J, Wagenbach M, Franck A, Asbury CL, Wordeman L. 2012 Kif18A and chromokinesins confine centromere movements via microtubule growth suppression and spatial control of kinetochore tension. *Dev. Cell* **22**, 1017–1029. (doi:10.1016/j.devcel.2012.02.013)
 54. Bieling P, Telley IA, Surrey T. 2010 A minimal midzone protein module controls formation and length of antiparallel microtubule overlaps. *Cell* **142**, 420–432. (doi:10.1016/j.cell.2010.06.033)
 55. Marshall WF. 2004 Cellular length control systems. *Annu. Rev. Cell Dev. Biol.* **20**, 677–693. (doi:10.1146/annurev.cellbio.20.012103.094437)
 56. Li X, Kolomeisky AB. 2013 Mechanisms and topology determination of complex chemical and biological network systems from first-passage theoretical approach. *J. Chem. Phys.* **139**, 144106. (doi:10.1063/1.4824392)
 57. Vilfan A, Frey E, Schwabl F, Thormählen M, Song YH, Mandelkow E. 2001 Dynamics and cooperativity of microtubule decoration by the motor protein kinesin. *J. Mol. Biol.* **312**, 1011–1026. (doi:10.1006/jmbi.2001.5020)
 58. Bormuth V, Nitzsche B, Ruhnow F, Mitra A, Storch M, Rammner B, Howard J, Diez S. 2012 The highly processive kinesin-8, Kip3, switches microtubule protofilaments with a bias toward the left. *Biophys. J.* **103**, L4–L6. (doi:10.1016/j.bpj.2012.05.024)
 59. Roos W, Campàs O, Montel F, Woehlke G, Spatz J, Bassereau P, Cappello G. 2008 Dynamic kinesin-1 clustering on microtubules due to mutually attractive interactions. *Phys. Biol.* **5**, 046004. (doi:10.1088/1478-3975/5/4/046004)
 60. Gardner MK, Zanic M, Gell C, Bormuth V, Howard J. 2011 Depolymerizing kinesins Kip3 and MCAK shape cellular microtubule architecture by differential control of catastrophe. *Cell* **147**, 1092–1103. (doi:10.1016/j.cell.2011.10.037)
 61. Kuan H-S, Betterton MD. 2013 Biophysics of filament length regulation by molecular motors. *Phys. Biol.* **10**, 036004. (doi:10.1088/1478-3975/10/3/036004)
 62. Li X, Kolomeisky AB. 2013 Theoretical analysis of microtubules dynamics using a physical–chemical description of hydrolysis. *J. Phys. Chem. B* **117**, 9217–9223. (doi:10.1021/jp404794f)
 63. Neri I, Kern N, Parmeggiani A. 2013 Modeling cytoskeletal traffic: an interplay between passive diffusion and active transport. *Phys. Rev. Lett.* **110**, 098102. (doi:10.1103/PhysRevLett.110.098102)
 64. Greulich P, Ciandrini L, Allen RJ, Romano MC. 2012 Mixed population of competing totally asymmetric simple exclusion processes with a shared reservoir of particles. *Phys. Rev. E* **85**, 011142. (doi:10.1103/PhysRevE.85.011142)

3.4. Effects of phase transitions on length fluctuations

Having analyzed the length of microtubules for different conditions at the lattice tip, it is interesting to learn more about the physical mechanisms that lead to these cases of accurate and fluctuating regulation. Within this section it is briefly outline how our understanding of phase transitions as obtained above, leads to deeper insights on the emergence of fluctuations in the microtubule length.

As a first hypothesis it is considered that boundary induced phase transitions influence the dynamics of the filament and the accumulation of motors at the tip, see Fig. 3.2 for an illustration. Two scenarios can be distinguished: Either length regulation sets while the system is in the IN phase (IN regulation), or length regulation starts at, or after the system underwent the transition to the EX phase (IN/EX regulation).

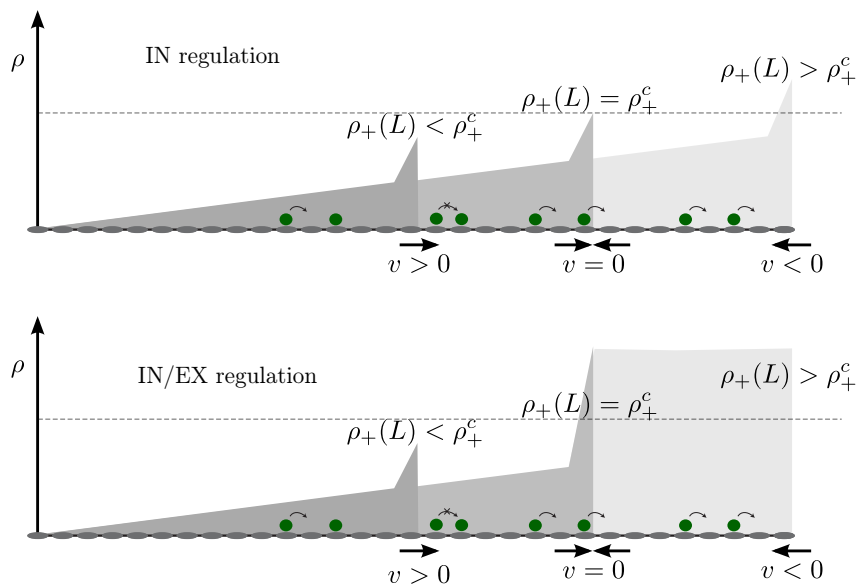


Figure 3.2.: UPPER PANEL: IN REGULATION. The microtubule is regulated in the IN phase where the density profile and the tip density are both length dependent. LOWER PANEL: IN/EX REGULATION. The microtubule is regulated at the transition between the IN and the EX phase. The density profile is length-dependent until a threshold length L^c , and independent of the lattice length for $L > L^c$.

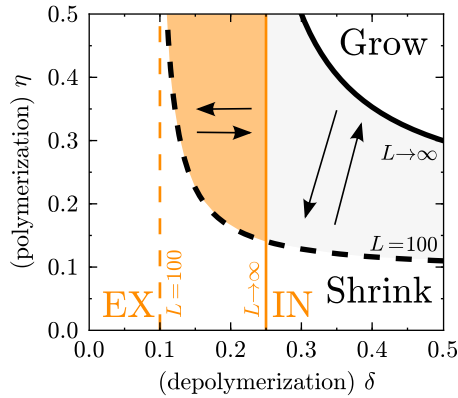


Figure 3.3.: PHASE DIAGRAM for microtubule growth and shrinking and the IN/EX boundary induced transition as seen for a microtubule of size $L \rightarrow \infty$ and $L = 100$ („exclusive“ case). Arrows indicate how these lines change during growth and depolymerization. The shaded area indicates a region where the system grows in the IN phase and shrinks in the EX phase. Otherwise the system grows and shrinks in the IN phase only.

For specificity the „exclusive“ case is considered in the following analysis. The above hypothesis motivates to reanalyze the phase transitions as obtained in the previous sections. This time, however, the transition lines between EX and IN phase and the critical growth rate η^c are considered in a length dependent manner. To illustrate how transition lines change with lattice length, a further simplification is made by restricting the analysis to a situation where no bulk induced phase transitions occurs, *i.e.* $\rho_{La} = 0.25$ with $\omega_{on} = 0.001$. For short microtubules the density profile increases linearly, however, it saturates $\rho_{La} < 1/2$. Length dependent phase transitions can now be monitored in a simple way by comparing two situations, one for long microtubules and another one for short microtubules. First consider $L \rightarrow \infty$, in this case we recover the situation as calculated in the previous section, with $\rho_- = \rho_{La}$. The transition lines between the IN and the EX phase as well as growing and shrinking are given by the solid lines in Fig. 3.3. For comparison, the dashed lines correspond to the same situation, however, for a microtubule of length $L = 100$.

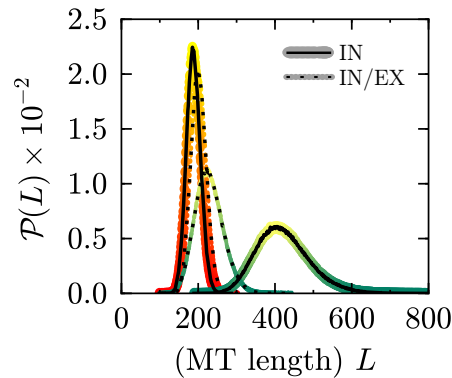


Figure 3.4.: LENGTH DISTRIBUTION of the microtubule for the IN and the IN/EX regulation in the „exclusive“ and „non-exclusive“ scenario. Parameters are for exclusive: IN $\delta = 0.3$, $\eta = 0.4$, IN/EX $\delta = 0.2$, $\eta = 0.4$, and for non-exclusive: IN $\delta = 0.4$, $\gamma = 0.125$, IN/EX $\delta = 0.2$, $\eta = 0.125$.

To see whether and how these two different regulatory mechanisms can be distinguished, it is necessary to monitor the filament length distribution and fluctuations at high accuracy. Figure 4.5 shows length distributions for both cases, IN regulation and IN/EX regulation, for the two cases discussed in the previous section „exclusive“ and „non-exclusive“. For the latter case there is basically no difference between IN and the IN/EX regulation. However, for the exclusive case the data shows that the length distribution is much broader and skewed during IN regulation as compared to a narrow and peaked length distribution for the IN/EX regulation.

So far it appears that, indeed, the scenario of a length-dependent – but boundary induced – transition influences length-regulation in a rather subtle way: In the presence of the transition, filaments stay short and fluctuate only little. Further the different scenarios from the previous sections can hardly be distinguished based on the data. There is however one situation in which a marked difference is observed. For the exclusive scenario fluctuations are only enhanced in the absence of the length dependent IN/EX transitions.

The above results indicate that length dependent processes can readily be investigated using the mean-field results obtained in this Thesis. This broad applicability leaves hope that also more complicated situations can be analyzed with the set of methods developed here. It might be worthwhile to consider biochemical networks that regulate microtubule tips. This would

enhance the simple two state model for that was developed here towards multiple competing states. Another rather speculative approach could also be to incorporate nucleotide dynamics and the protofilament structure of microtubules atop to the different length dependent scenarios. Finally, the above result also provides an unusual perspective on fluctuations in driven diffusive systems. While typically at a phase transitions fluctuations are enhanced and systems exhibit long-range correlations, here the opposite situation occurs: A phase transition pins the length of the system such that length fluctuations are reduced. The reason for this can be identified as the discontinuous transition between IN and EX phase. It will be interesting to investigate these fluctuations further with respect to the role of Langmuir kinetics for example and the critical current at the transition line.

3.5. Traffic dynamic instability

Microscopic details are extremely important in the system studied here. A remarkable result that underpins this statement is that depolymerizing motors can length-regulate or exhibit bistable behavior if only the addition of tubulin is inhibited by the presence of a motor at the tip.

Bistable driven diffusive systems have been found before in terms of the Nagel-Schreckenberg model [224] for example, or in systems of bidirectional transport [225], where it is intuitive that bistable behavior can occur. When different particles move into opposite directions and they have to share a bottleneck for example, stochastic effects are important at the bottleneck site [226] that will either block one species, or the other. A simple scenario, where intermittent density fluctuations play a role, is a TASEP with a dynamic bottleneck that switches on and off at certain rates [227].

In the model investigated here, stochastic effects at the microtubule tip are identified to trigger bistable behavior. Where bistability means that multiple phases can be stable and stochastically switch from one phase to the other. Within a mean-field approach these stochastic effects that stem from attachment and detachment events at the tip can be explained. It is remarkable that these stochastic effects at one site, *i.e.* on a microscopic scale, amplify to ensue macroscopic changes in the density of the system.

The dynamics of this model has a marked similarity to dynamic instability of microtubules. And actually, the boundary conditions correspond to microtubule dynamic instability [52], only the origin of the phenomenon studied here emerges from collective motor dynamics rather than nucleotide states.

On the following pages a manuscript is provided [228].

Traffic Dynamic Instability

Louis Reese^{1,2,*}, Anna Melbinger^{1,3}, and Erwin Frey^{1,2†}

¹*Arnold-Sommerfeld-Center for Theoretical Physics and Center for NanoScience, Department of Physics, Ludwig-Maximilians-Universität München, Theresienstr. 37, 80333 Munich, Germany;* ²*Nanosystems Initiative Munich (NIM), Ludwig-Maximilians-Universität München, Schellingstraße 4, D-80333 Munich, Germany;* ³*Department of Physics, University of California, San Diego, California 92093, USA*

Here we study a driven lattice gas model for microtubule depolymerizing molecular motors, where traffic jams of motors induce stochastic switching between microtubule growth and shrinkage. We term this phenomenon “traffic dynamic instability” because it is reminiscent of microtubule dynamic instability [T. Mitchison and M. Kirschner, *Nature* 312, 237 (1984)]. The intermittent dynamics of growth and shrinking emerges from the interplay between the arrival of motors at the microtubule tip, motor induced depolymerization, and motor detachment from the tip. The switching dynamics correlates with low and high motor density on the lattice. This leads to an effectively bistable particle density in the system. A refined domain wall theory predicts this transient appearance of different phases in the system. The theoretical results are supported by stochastic simulations.

I. INTRODUCTION

Microtubule (MT) depolymerizing enzymes [1–3] are considered important for MT length-regulation [4–6]. These enzymes function in parallel to MT dynamic instability [7], which is the hydrolysis-driven stochastic switching of MTs between a growing and a shrinking state [8, 9]. The class of MT depolymerizing enzymes [3] contains the kinesin-8 protein family, which are molecular motors that walk towards the MT plus-end [10–12]. These have been studied in detail in the biological literature, see Ref. [13] and references therein.

Suitable theoretical models to describe the collective movement of molecular motors on filaments are driven lattice gases [14–18]. Such models explain the formation of traffic jams on MTs [19–21] as observed in experiments [21, 22]. Recently also lattice gases of dynamic system size were studied. For example when individual particles trigger lattice growth by forming new lattice sites at the lattice end [23–26], or remove lattice sites [27–29].

The interplay between lattice growth and shrinking was investigated in a variety of settings, e.g. when particles stabilize shrinking lattices [30], or depolymerize growing lattices [5, 6, 31, 32]. An analogy to these molecular motor systems can be found in queuing theory, where the length of a queue is dynamic [33] and waiting times are of central interest [34].

Here we study a simplified stochastic model for a dynamic MT tip and MT depolymerizing molecular motors. The model is based on the *totally asymmetric*

simple exclusion process (TASEP) [35] and includes specific stochastic processes that account for the growth and shrinking of the lattice. Particularly, we study a kinetic model where the following MT tip related processes are included: 1) motors depolymerize the MT at the tip, 2) motors inhibit MT growth if bound to the tip, and 3) motors have a finite dwell time at the tip. Remarkably, the system investigated here displays stochastic switching between extended periods of MT growth and MT shrinking. This intermittent dynamics is reminiscent of MT dynamic instability [8], yet its origin is different and relies on the *dynamics of motors* at the MT tip: We identify the spontaneous formation of motor traffic jams at the MT tip as a “catastrophe” event, because it leads to shrinking of the MT. On the other hand, we identify the stochastic detachment of a motor from the tip as a “rescue” event, because it initiates MT growth in the model. The predictions of the model can be tested in biochemical reconstitution experiments [36] and could help to identify detailed MT-motor interactions as they become increasingly accessible to experiments, see e.g. Ref. [37].

This work is organized as follows. In section II the details of the model are presented. In the results section we present the phenomenon of “traffic dynamic instability” (III A). Then, the mean field solution of the model is introduced and discussed (III B). In sections III C and III D we numerically study the formation of shocks and develop a domain wall theory which quantifies our observations. In particular, this domain wall theory allows to identify metastable regimes in the phase space of the system as is shown in the following sections: In section III E we identify a phase of stripe formation due to particular velocities of domain wall motion in the system. The intermittent phases are analyzed in greater detail analytically as well as numerically in sections III F and III G. Finally we discuss our results and conclude in section IV.

* l.reese@tudelft.nl

Present address: Department of Bionanoscience, Kavli Institute of Nanoscience, Delft University of Technology, Delft, The Netherlands

† frey@lmu.de

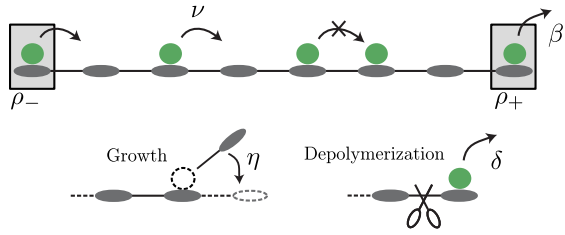


FIG. 1. Molecular motors on the MT lattice. At the left motors enter the lattice from a constant reservoir ρ_- , which mimics the motor density in bulk of the MT. The motor density at the tip (MT plus-end) is denoted ρ_+ . Motors detach from the MT tip at rate β . The MT grows in *absence* of a motor at rate η and is depolymerized by a motor at rate δ .

II. MODEL

We consider a lattice gas model for molecular motors close to the MT plus-end as illustrated in Fig. 1. Motors move from the bulk of the MT (left) to the plus-end (right) at rate $\nu = 1$ if the next site is empty. This choice of ν sets the timescale of all other rate constants. The dynamics can be formulated in terms of occupation numbers n_i , where $n_i = 1$ and $n_i = 0$ denote the presence and absence of a particle, respectively. At the left, the system is coupled to a constant particle reservoir ρ_- , which emulates the bulk of the MT. At the right, the model corresponds to the MT plus-end, where particles detach at rate β . The above model is known as the *totally asymmetric simple exclusion process* (TASEP) and plays a paradigmatic role in non-equilibrium statistical mechanics [38–41]. Furthermore, we denote the probability that a motor occupies the tip-site with ρ_+ and the probability to find a motor in bulk of the lattice ρ_b . We consider a lattice of constant size N , which is co-moving with the plus-end of the MT. At the left boundary, the system loses a particle if the lattice grows and the leftmost site is occupied. In case of a depolymerization event, the lattice moves to the left, where one lattice site is added. The newly added site is occupied with probability ρ_- . At the right boundary, two more processes can happen: (i) Particles remove the terminal site with rate δ [29]. (ii) If the tip-site is *empty* the lattice grows at rate η [6]. These dependencies of MT growth and shrinking on motor occupation at the tip can also be interpreted as the two different nucleotide states of MT tips [8]: in the GTP state the filament grows, corresponding to the absence of a motor in our model; in the GDP state the filament shrinks, corresponding to a motor bound to the tip in our model. The dynamics of motors on the lattice, however, renders our model different from GTP hydrolysis dependent switching, and, therefore, distinct from MT dynamic instability. In the model presented here switching between growth and shrinking (catastrophe) is due to the spontaneous formation of traffic jams on growing MTs. Switching from shrinking to growth (rescue) is due to detachment of a motor from the tip.

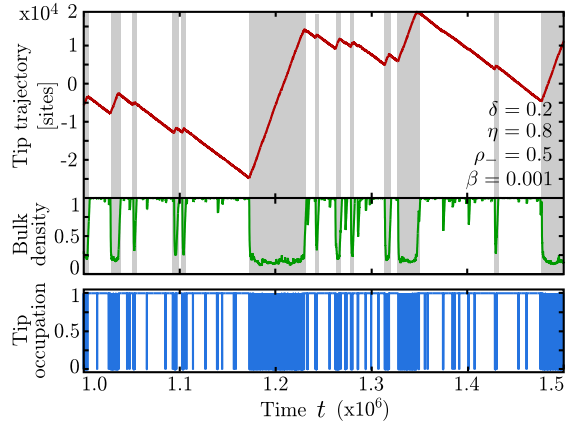


FIG. 2. Stochastic simulations show intermittent dynamics. Switching between periods of growth and shrinking are reminiscent of MT dynamic instability and indicate bistable behavior of the system: The three panels show the trajectory of the lattice tip, the bulk motor density on the MT ρ_b , and the motor occupation of the tip n_+ . Shaded areas indicate periods of growth that involve low bulk density $\rho_b \approx 0.2$. System size is $N = 200$.

III. RESULTS

A. Intermittent dynamics

In stochastic simulations of the model we observe intermittent dynamics. In Fig. 2 this is illustrated for three key observables, which are the trajectory of the MT tip, the average bulk density of motors on the lattice $\rho_b = \frac{1}{N} \sum_i n_i$, and the motor occupation at the tip $n_+ \in \{0; 1\}$, see Fig. 2. Periods of depolymerization are distinguished from periods of growth by a high bulk density $\rho_b \approx 1$ and persistent occupation of the tip $n_+ = 1$, cf. the white and shaded areas in Fig. 2, respectively. The underlying switching processes of the system can be understood intuitively in terms of a separation of timescales: If the tip site is occupied, $n_+ = 1$, it constitutes a bottleneck [42, 43] behind which particles pile up due to motor traffic and slow depolymerization. For rare tip detachment ($\beta \ll 1$) this bottleneck persists and eventually induces a high density of motors in bulk, $\rho_b \approx 1$. The high bulk density manifests the shrinking state of the filament. However, the system may stochastically switch to growth. This can happen on the occasion that the bottleneck at the tip site is removed through tip detachment (rate β). Then the tip site becomes empty, $n_+ = 0$, which entails that the lattice is in its growing state. The timescale of this rescue event is β^{-1} . Similarly, it is possible to obtain a qualitative understanding of catastrophe events: At high growth rates η , motors can not keep up with the growing tip. The system assumes a steady state where the bulk density is significantly smaller than in the depolymerizing state, $\rho_b \approx 0.2$, see Fig. 2. Stochastic switching into the shrinking state

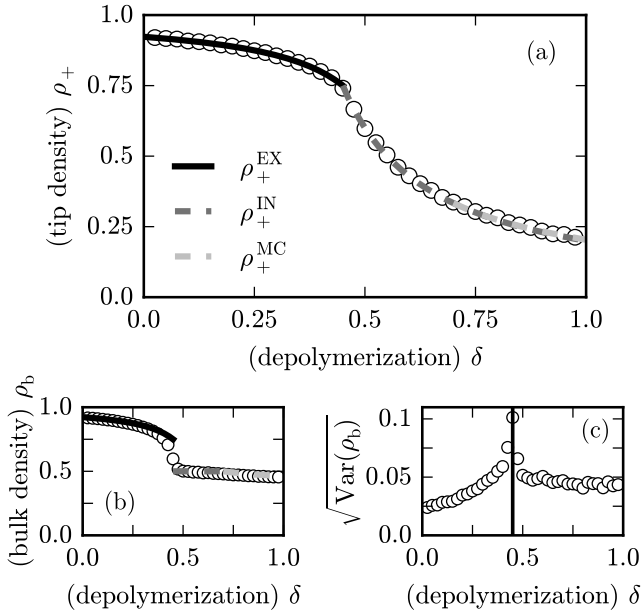


FIG. 3. (a) Comparison of stochastic simulations (symbols) and analytic results (lines) obtained for the tip densities from mean-field calculations; see Eqs. (4), (5), and (7). For $\eta = 0.35$, $\rho_- = 0.5$, $\beta = 0.05$, and $N = 400$ we find very good agreement between theory and simulations. The transition between the IN and the MC phase can hardly be recognized; we plotted both functions and elaborate on the exact criterion later. (b) Data for bulk densities (symbols) also confirms the validity of mean-field calculations [lines as in panel (a)]. The transition between the EX and the IN phase is discontinuous in the bulk densities in agreement with what is known from TASEP: At the transition between the EX and the IN phase, both phases coexist and are separated by a diffusing domain-wall (DW). (c) The DW ensues density fluctuations, which we measured in terms of the normalized standard deviation of the bulk density. At the EX/IN-transition density fluctuations show a pronounced peak (indicated by the vertical line).

may happen if a single motor reaches the tip site and induces traffic jam formation, which reverses growth to shrinking. Thus, the timescale of catastrophe is given by the arrival rate of motors at the tip, j_+ . This arrival rate is sensitive to current fluctuations and the system size N [44].

B. Limitations of the mean-field approach

In a first step to understand the dynamics of the system, we determine the tip-densities, ρ_+ , within a mean-field approach [5]. There are three generic phases of motor dynamics on the lattice: a low density phase (IN phase), a high density phase (EX phase), and a maximal current phase (MC phase). The dynamics of such a system is likewise dependent on particle input ρ_- , the particle exit rate β , or the capacity of particle flow on the lattice, respectively [38–41]. As shown recently, this requires an analysis of bulk and boundary currents in the system [5]. Employing a mean-field approximation for nearest neighbor occupation numbers, $\langle n_i n_{i+1} \rangle = \langle n_i \rangle \langle n_{i+1} \rangle$, the bulk current of the system reads [6]

$$J_b(\rho_b, \rho_+) = \rho_b(1 - \rho_b) + \delta\rho_b\rho_+ - \eta\rho_b(1 - \rho_+), \quad (1)$$

where the terms on the right hand side stand for particle hopping with on-site exclusion, depolymerization, and polymerization of the MT. Note that the latter depend on the probability that a motor is bound to the tip. In terms of particle movements, depolymerization and polymerization correspond to parallel updates of all motors on the lattice towards, or away from the lattice tip, respectively.

The current of particles that leave the system at the MT tip depends on depolymerization and detachment events and the tip density,

$$J_{\text{exit}}(\rho_+) = (\delta + \beta)\rho_+. \quad (2)$$

The tip densities in the IN and the EX phase are obtained in a straightforward manner [5, 6]. In the IN phase $\rho_b = \rho_-$, and in the EX phase $\rho_b = \rho_+$. Bulk and tip currents balance in the steady state due to particle conservation,

$$J_b(\rho_b, \rho_+) = J_{\text{exit}}(\rho_+), \quad (3)$$

and can be solved for the tip density. As results one obtains

$$\rho_+^{\text{IN}} = \frac{\rho(\rho + \eta - 1)}{\rho(\delta + \eta) - \delta - \beta}, \quad (4)$$

and

$$\rho_+^{\text{EX}} = 1 - \frac{\beta}{1 - \delta - \eta}. \quad (5)$$

In the MC phase the current through the system is determined by the transport capacity of the lattice defined from an extremal current principle [5, 6], $\partial_{\rho_b} J_b = 0$. This condition ensues bulk and tip densities in the MC phase

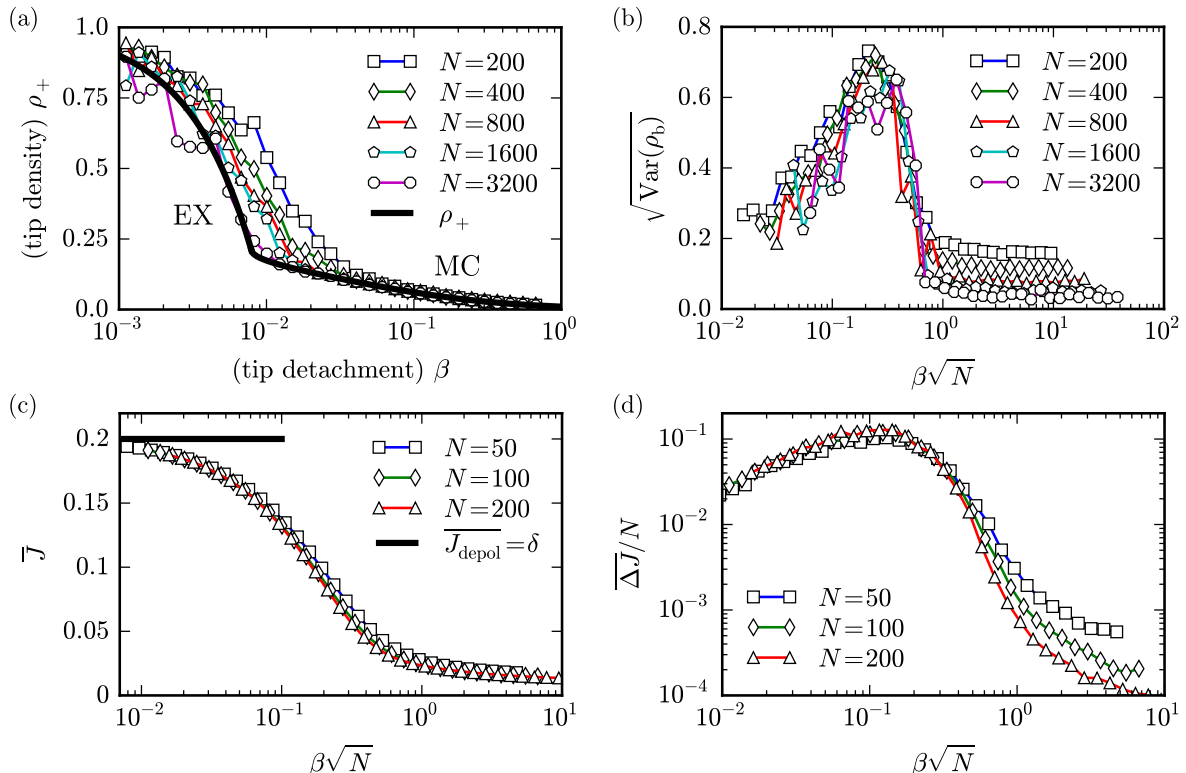


FIG. 4. Deviation from the mean-field approximation depending on detachment rates β , for growth rate $\eta = 0.79$, and depolymerization rate $\delta = 0.2$. Panel (a) shows how the data for tip densities deviates from the analytic results for a set of system sizes. The deviation from mean-field occurs at the transition between the EX phase and the MC phase, Eqs. (5) and (7), respectively. Note that the deviation from mean-field result depends on the system size N . (b) Bulk density fluctuations in terms of the normalized standard deviation of ρ_b . An heuristic scaling analysis, where we rescaled the detachment rate as $\beta\sqrt{N}$, shows data collapse for the onset of characteristic density fluctuations. (c) The average current through the system \bar{J} measured from stochastic simulations was evaluated from 10^3 realization of the process, where $\bar{J} = \langle Q \rangle / \Delta t$. The number of particles that leave the system from the tip through depolymerization or detachment is denoted Q and was measured in time intervals $\Delta t = 10^6$. Scaling is obtained by plotting the data versus $\beta\sqrt{N}$. Panel (d) shows the scaled current fluctuations $\Delta\bar{J}/N$ of the dataset presented in (c), with $\Delta\bar{J} = (\langle Q^2 \rangle - \langle Q \rangle^2) / \Delta t$. The data also reveals scaling with $\beta\sqrt{N}$ and supports the scaling relation between tip detachment and system size.

$$\rho_b^{\text{MC}} = \frac{\beta + \delta - \sqrt{(\beta + \delta)(\beta + \eta(\delta + \eta - 1))}}{\delta + \eta}, \quad (6)$$

$$\rho_+^{\text{MC}} = \frac{2\beta + \delta(\eta + 1) + (\eta - 1)\eta - 2\sqrt{(\beta + \delta)[\beta + \eta(\delta + \eta - 1)]}}{(\delta + \eta)^2}. \quad (7)$$

To test the validity of the mean-field approach we compare the analytic results for the tip density, ρ_+ , with stochastic simulation data. For slow growth rates we find excellent agreement between the calculations and the data, cf. Fig. 3(a). The transition between EX and IN phase is discontinuous as known for TASEP, see Fig. 3(b). For a later comparison with the intermittent regime, we also evaluated characteristic density fluctuations across the EX/IN transition, see Fig. 3(c). These observations are in agreement with the low-density high-density coexistence in the classical TASEP [39–41], which corresponds to the case of $\delta = \eta = 0$ and $\rho_- = \beta$ in our model. In

Fig. 3 density fluctuations show a pronounced peak at a critical depolymerization rate $\delta_c = \rho_- - \beta$, which can be attributed to the EX/IN transition. Our observation of intermittent behavior, suggests that the mean-field approximation becomes invalid at particular parameter values. Thereby the detachment rate of motors from the tip, β , plays a critical role. To understand the emergence of intermittent behavior, and the eventual break-down of the mean-field approximation, we studied the system as a function of system size N and β in stochastic simulations [45]. Figure 4(a) shows how the data for the tip densities ρ_+ , deviate from the analytic results for a growth

rate $\eta = 0.79$ and a depolymerization rate $\delta = 0.2$. While there is good agreement for relatively large motor detachment rates $\beta > 0.03$, analytic results and the data deviate significantly for smaller values of β . To exclude the possibility that these deviations from mean-field results are due to finite size effects, we also recorded the bulk density and the particle current through the system as well as the fluctuations of these two quantities. As already shown above in Fig. 2, the bulk density switches between states of high and low density in the intermittent regime. Thus, we hypothesize that density and current fluctuations are characteristic for the intermittent regime. To test this hypothesis we evaluated the bulk density with respect to fluctuations in terms of the normalized standard deviation $\sqrt{\text{Var}(\rho_b)} = \sqrt{\langle \rho_b^2 \rangle - \langle \rho_b \rangle^2} / \langle \rho_b \rangle$. The results are shown in Fig. 4(b). We found that for all studied system sizes, ranging from $N = 200$ to $N = 3200$, fluctuations peak at a particular value of β . This excludes the possibility that the observed phenomenon is a finite size effect. Furthermore, by plotting the data versus the rescaled detachment rate, $\beta\sqrt{N}$, we found data collapse for the onset as well as for the peak of the fluctuations. This heuristic analysis ensues the following system size dependent law for the onset of intermittent dynamics

$$\beta_c \propto N^{-1/2}. \quad (8)$$

The numerical measurement of the average current in the system, \bar{J} , and the current fluctuations $\Delta\bar{J}$, confirms the above scaling behavior, see Fig. 4(c) and (d). Note, that the onset of intermittency also depends on the actual values of δ and η , as will be shown later.

C. Formation of shocks

The appearance and dissolution of motor traffic jams at MT tips, provides a mechanism for stochastic switching between states of growth and shrinking. Recent studies have investigated TASEP systems with similarly complex shock dynamics, see [43, 46–48]. In the following we briefly discuss methods and results of some of those references and briefly elaborate on the differences to our work.

Turci *et al.* [43] investigated a system with a defect which underlies on/off kinetics on an otherwise static lattice with TASEP dynamics. Intermittent density fluctuations are observed, including strong deviations from the classic mean-field approach. To improve beyond a mean-field approach, the authors employ an intermittent mean-field approach which allows to calculate the average current in the system during intermittency. Sahoo *et al.* [47] investigated a defect which in addition to attachment/detachment kinetics also diffuses. In their model traffic jams form and dissolve stochastically in the bulk of the lattice. The bulk defects considered in the above references [43, 47] lead to phenomena which are similar to our observations at the MT tip. The difference

to our work is that in [43] and [47] the defects are road-blocks, whereas in our model the kinetic processes at the MT tip can function as a defect.

Pinkoviezky and Gov [46] investigated a system with defect particles on a constantly growing lattice, where the defect property is passed from one particle to the next against the direction of transport. This ensues defect propagation and interesting DW dynamics in the bulk of the lattice. A simple mean-field approach fails to describe the system, but a careful analysis of the different spatial domains that evolve allows an analysis of the defect dynamics. The main differences to our model are, the feedback between lattice dynamics and tip occupation, and that the MT tip site is the only defect in the system we study.

In the following we propose a domain wall theory to explore phase diagrams of TASEP systems where tip dynamics and bulk dynamics are coupled through shortening or growth processes. The theory reveals dynamical phase transitions in the model and thereby explains why simulation data deviate from the mean-field calculations, cf. Fig. 4(a). On the level of individual trajectories, however, the mean-field results can be verified: The velocities of domain walls can be read out directly from kymographs. Our approach generalizes previous work on domain wall theory [49, 50] towards an understanding of driven diffusive systems of interacting particles on dynamically evolving lattices.

D. Domain wall theory

Because analytic expressions for the currents, the tip densities, and the bulk densities are known for the different phases, we employ a *domain wall* (DW) theory and *extremal current principle* [38, 49–51]. In short, DW theory determines how shocks and density perturbations evolve in the system: The direction in which a shock moves and the direction in which a density perturbation spreads determine the existence and stability of the different phases [49]. In other words, we are interested in the sign of various DW velocities v_{DW} , and the sign the collective velocity v_{coll} which tells about the spreading of density perturbations. In the model considered here the bulk currents are not independent of the tip density, as in the TASEP. Microscopically this means that the occupation number of the tip $n_+ \in \{0, 1\}$ influences DW motion and thus the phase behavior of the system, see the kymograph in Fig. 5 for example. The figure shows stochastic switching in the tip occupation number. Switching between $n_+ = 0$ and $n_+ = 1$ is indicated by arrows and dashed horizontal lines. The solid lines are guides to the eye indicating the correlation between tip occupation and distinct DW velocities in the bulk of the lattice. If switching events occur within a relatively short time window, multiple DWs coexist in the bulk of the lattice as indicated by the numbers ① and ② in Fig. 5. The

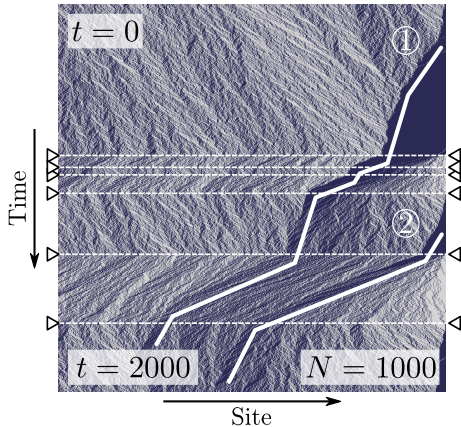


FIG. 5. Kymograph of the model in a regime with strong density fluctuations. The data shows how two traffic jams nucleate at the MT tip and propagate into the bulk of the system before they dissolve. Dashed lines and triangles indicate switching of the tip occupation between $n_+ = 1$ and $n_+ = 0$. Shock formation and propagation in the bulk of the lattice is highlighted by white solid lines. Parameters are $\beta = 0.005$, $\rho_- = 0.5$, $\delta = 0.2$, $\eta = 0.79$.

DW velocity can be analyzed analytically, it is given by

$$v_{\text{DW}} = \frac{J^{\text{left}} - J^{\text{right}}}{\rho^{\text{left}} - \rho^{\text{right}}}, \quad (9)$$

where *left* and *right* denote the densities and currents on either side of a DW. The sign of v_{DW} determines whether a shock in the system travels to the left ($v_{\text{DW}} < 0$) or the right ($v_{\text{DW}} > 0$). For our purposes the typical procedure by Kolomeisky *et al.* [49] needs to be modified, because the currents J on either side of the DW depend explicitly on the tip density ρ_+ as illustrated in Fig. 6. In the following we investigate v_{DW} between the MC phase and the EX phase, since we have seen that this transition is involved in the stochastic switching between a growing and a shrinking state of the lattice, cf. Fig. 7. For the moment, consider the MC phase at the left side of a DW and the EX phase at its right. This implies that the tip density is in the EX phase $\rho_+ = \rho_+^{\text{EX}}$. The DW velocity $v_{\text{left/right}}$ then reads

$$v_{\text{MC/EX}} = \frac{J(\rho_b^{\text{MC}}, \rho_+^{\text{EX}}) - J(\rho_b^{\text{EX}}, \rho_+^{\text{EX}})}{\rho_b^{\text{MC}} - \rho_b^{\text{EX}}}. \quad (10)$$

Note that both currents, J^{left} and J^{right} , depend on the same tip density, ρ_+^{EX} , but differ with respect to the bulk densities $\rho_b^{\text{left}} = \rho_b^{\text{MC}}$ and $\rho_b^{\text{right}} = \rho_b^{\text{EX}}$. Vice versa, if the MC phase is on the right side of the DW the tip density is $\rho_+ = \rho_+^{\text{MC}}$. With the EX phase at the left, the DW velocity is

$$v_{\text{EX/MC}} = \frac{J(\rho_b^{\text{EX}}, \rho_+^{\text{MC}}) - J(\rho_b^{\text{MC}}, \rho_+^{\text{MC}})}{\rho_b^{\text{EX}} - \rho_b^{\text{MC}}}. \quad (11)$$

Evaluating the DW velocities in the system by employing the current given in Eq. (1) and the tip and bulk densities

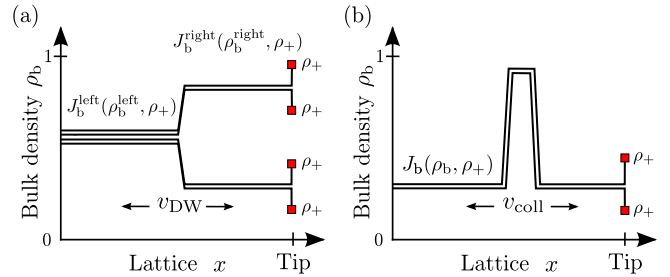


FIG. 6. Illustration of possible domain walls (a) and a density perturbation (b) in a background density ρ_b . The spike-like behavior of the density profile at the lattice tip is also illustrated. Note the particular role of the tip density ρ_+ : it influences the currents in the system.

for the individual phases, we are able to construct the phase diagram. In the following we provide an attempt for a characterization of the arising phases.

E. Stripe phase

As suggested from the data shown in the kymograph of Fig. 7, there is a regime in which the system completely switches from the MC phase to the EX phase for small β . Because the switching appears as a band of motor particles across the lattice, we refer to this regime as a stripe phase, cf. Fig. 7(a). A reasonable and simple condition for the stripe phase is that all three domain walls need a negative DW velocity. This is evident from the kymograph of Fig. 7. For $\beta = 0$ this condition cannot be fulfilled:

$$v_{\text{IN/EX}} = -\rho + \delta, \quad (12)$$

$$v_{\text{EX/MC}} = -\eta, \quad (13)$$

$$v_{\text{MC/EX}} = 0, \quad (14)$$

where right after the switching event to growth [Eq. (13)] we assumed $\rho_b^{\text{right}} = \rho_+ = 0$, and right after the switching event to depolymerization [Eq. (14)] we assumed $\rho_b^{\text{right}} = \rho_+ = 1$, as suggested from the data. The first two of the above equations indeed show a negative DW velocity as expected. The MC/EX domain wall, however, does not show a negative velocity as observed in the simulations. Let us note that for $\beta = 0$ we find a critical growth rate $\eta^s = 1 - \delta$ (dashed line in Fig. 8) or likewise, a critical depolymerization rate $\delta^s = 1 - \eta$ [6]. To better explore the possibility of $v_{\text{MC/EX}} < 0$ we study the case $\beta > 0$. We find that for finite values of β the critical line broadens up into a regime in which $v_{\text{MC/EX}} < 0$ is possible. In terms of the growth rate, the conditions for this regime can be found from $v_{\text{MC/EX}} = 0$ and that $v_{\text{MC/EX}}$ has to be real in the relevant parameter regime. It follows that the parameter region of $v_{\text{MC/EX}} \leq 0$ is

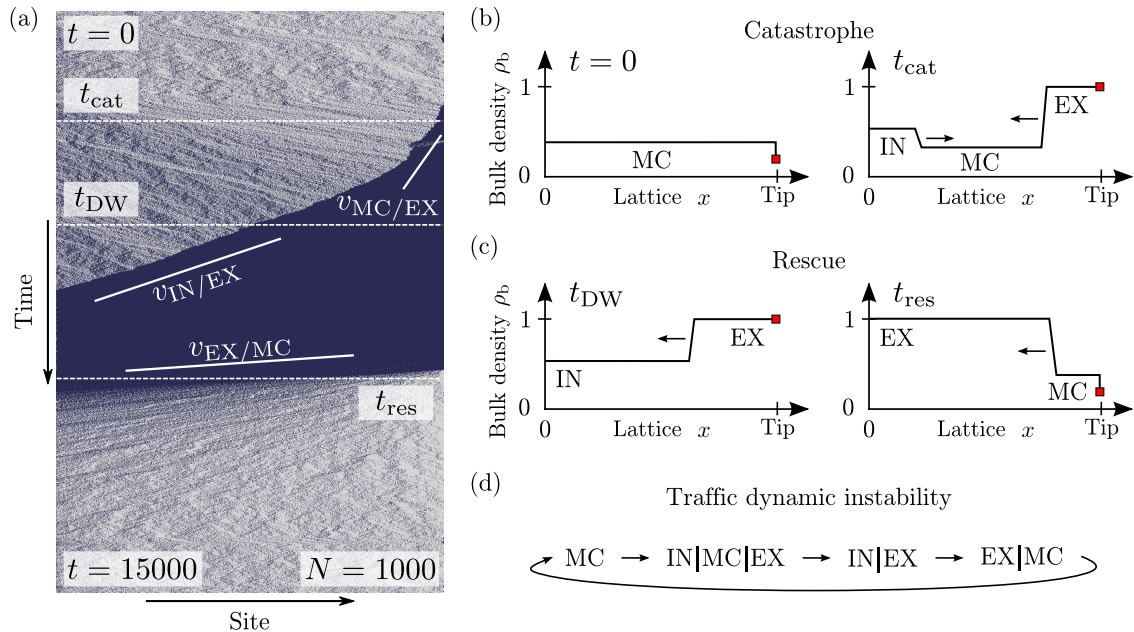


FIG. 7. (a) Kymograph of stochastic switching from lattice growth to shrinking and back. Solid lines indicate the velocities at which DWs propagate in the bulk of the lattice. For the time points indicated by thin dashed lines the density profiles are illustrated in panels (b) and (c) as indicated. Panel (b) shows the DW dynamics before and after the catastrophe event. In (c) the DW dynamics before and after the rescue event is illustrated. (d) Illustrates the consecutive phase changes in the system which we call “traffic dynamic instability”, indicative of the fact that the system does *not* settle into its non-equilibrium stationary states. Parameters in (a) are $\beta = 0.001$, $\rho_- = 0.5$, $\delta = 0.2$, $\eta = 0.79$.

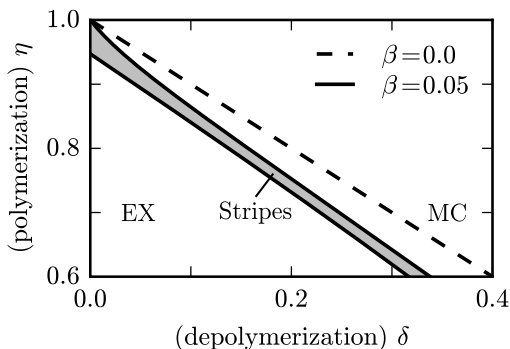


FIG. 8. Phase diagram for the stripe phase. For $\beta = 0$ the system shows a discontinuous transition between EX and MC phase, where stripes emerge right at the critical line (dashed). In the case $\beta > 0$ a distinct region in phase space exists in which the system robustly forms stripe patterns due to the creation of shocks at the MT plus end and a subsequent switch to polymerization.

given by

$$\eta \geq \frac{1}{2} \left(1 - \delta + \sqrt{-4\beta + (1 - \delta)^2} \right), \quad (15)$$

$$\eta \leq 1 - \delta \left(1 + \frac{\beta}{\beta - \delta^2 + \delta} \right). \quad (16)$$

The above relations provide the condition for stripe formation in the system based solely on domain wall the-

ory, see shaded area in Fig. 8. Although we find qualitative agreement with individual kymographs, compare Fig. 7(a) and illustrations in Fig. 7(b), (c) and (d), the stochastic nature of the phenomenon makes it hard to quantitatively confirm this regime numerically. The major difficulty thereby is that the regime of intermittent dynamics is not only confined to the stripe phase but extends to above and below in phase space. In these regimes the system does not reach a non-equilibrium steady state either, but is continuously driven between different phases in course of time. This view is fortified in the following section.

F. Intermittent phase

To characterize the non-equilibrium state in which the system does not settle into a particular (non-equilibrium) stationary state, we distinguish domain walls between different phases considering the IN, EX, and MC phase. An illustration of the possible domain walls in the system is shown in Fig. 6(a). In particular, we are interested in the direction of DW motion. This quantity determines if a transient DW moves to the left or to the right in the system.

Thus, we investigated the sign of v_{DW} for the six possible combinations of DWs in the system. Our results are summarized in Tab. I. In the following we discuss the cases related to the EX phase, because they are par-

ticularly relevant to understand the intermittent regime. We begin with the DW between the EX and the MC phase. Notably neither of the two phases, MC or EX at the right hand side of the system, is stable against the other phase on the left hand side of the system. This means, that depending on the initial preparation of the system, MC/EX or EX/MC, the final state of the system is MC or EX, respectively, and thus ergodicity seems to be broken. Similar observations were made recently for an exclusive queuing model [52]. The parameter regime where the phenomenon occurs can be determined from the conditions $v_{\text{MC/EX}} > 0$ and $v_{\text{EX/MC}} > 0$. We find a critical growth rate η^c , which reads

$$\eta^c = 1 - \delta - \frac{\beta}{1 - \delta - \beta}. \quad (17)$$

Further, the criterion for the EX/MC phase transition, in the absence of particle detachment from the tip, coincides with the change of sign in $v_{\text{EX/MC}}$ from positive to negative:

$$\eta^* = 1 - \delta. \quad (18)$$

Consequently for $\eta > \eta^*$ the MC phase is stable as noted previously [6]. The system behavior for $\eta < \eta^c$ remains to be determined. As shown in Tab. I there is also the possibility that an IN phase exists in the system below a critical growth rate $\eta < \eta_{\text{IN}}^c$. This finding is in agreement with our earlier observation that density and current fluctuations are large in this parameter regime, cf. Fig. 4. Here we refrain from a more detailed investigation of the IN phase and study the role of fluctuations for the EX phase instead, because only if the EX phase is *unstable* intermittency is possible. To this end we analyze the collective velocity in the EX phase. The collective velocity is defined as

$$v_{\text{coll}} = \partial_{\rho_b} J_b(\rho_b, \rho_+). \quad (19)$$

It probes the stability of a small density perturbation in a background bulk density, see Fig. 6(b) for an illustration. Quite generally, the EX phase is characterized by negative collective velocity, $v_{\text{coll}}^{\text{EX}} < 0$, because in a high background density a small perturbation moves to the left [49]. However, in contrast to typical TASEP systems, this is not the case in our model. In the regime of $\eta^c < \eta < \eta^*$, the velocity of a perturbation is positive $v_{\text{coll}}^{\text{EX}} > 0$, indicating that density perturbations in the system travel to the right. Interestingly the critical growth rate which determines $v_{\text{coll}}^{\text{EX}} = 0$ coincides with the critical growth rate as obtained from the DW analysis above, η^c .

Until now we have relied on the principles of classical DW analysis to determine the phase behavior of the system. We have learned that between the EX and the MC phase, for $\eta^c < \eta < \eta^*$, DW velocities and the collective velocity of the EX phase show interesting behavior. For $\eta > \eta^*$ the system is robustly in the MC phase [6], and for $\eta < \eta^c$ the EX phase is stable in the system. In the case $\eta^c < \eta < \eta^*$, however, the system does not

TABLE I. Summary of results for DW motion. η^c refers to the value determined by the EX/MC case given by Eq. (17). The boxed cases indicate mutually unstable cases of DW motion.

Domain wall	$\eta < \eta^c$	$\eta^c < \eta < \eta^*$	$\eta > \eta^*$
MC EX	n.a.	$\overleftarrow{\text{F}}$	$\overleftarrow{\text{F}}$
EX MC	n.a.	$\overrightarrow{\text{F}}$	$\overrightarrow{\text{F}}$
		MC & EX	MC
IN EX	$\overleftarrow{\text{F}}$	$\overleftarrow{\text{F}}$	$\overleftarrow{\text{F}}$
EX IN	$\overrightarrow{\text{F}}$	$\overrightarrow{\text{F}}$	$\overrightarrow{\text{F}}$
	EX & IN	EX	EX & IN ^a
MC IN	n.a.	$\overleftarrow{\text{F}}$	$\overleftarrow{\text{F}}$
IN MC	n.a.	$\overrightarrow{\text{F}}$	$\overrightarrow{\text{F}}$
		MC	MC

^a Note this combination is not realistic, because neither the EX nor the IN phase exist in this parameter regime [6].

settle into a stationary state, but is continuously driven between different transient states. So far this behavior can be summarized as follows

$$\begin{array}{ll} \eta > \eta^* & \text{MC,} \\ \eta^c < \eta < \eta^* & \text{MC \& EX,} \\ \eta < \eta^c & \text{EX.} \end{array}$$

As discussed in the previous sections, it appears from stochastic realizations of the system (Fig. 5), that perturbations at the MT tip render the bulk of the system unstable and promote the observed intermittent behavior of the system. This importance of the boundaries in driven diffusive systems was recognized by Krug [38]. And the model we study here adds dynamic complexity to boundary induced phase transitions [38]. Therefore we try to include stochastic switching at the MT tip into the analysis of the collective velocity as discussed above. In the following we show how the collective velocity is affected from switching events at the tip, by assuming that the tip density ρ_+ is characterized by only two states, given by the tip occupation number, $n_+ = 1$ and $n_+ = 0$. Thus we assume that the tip density takes only values $\rho_+ = 1$ and $\rho_+ = 0$, which leads to the following equations for the collective velocity:

$$v_{\text{coll}}(\rho_+ = 1) = 1 - 2\rho_b + \delta, \quad (20)$$

$$v_{\text{coll}}(\rho_+ = 0) = 1 - 2\rho_b - \eta. \quad (21)$$

The above equations illustrate that stochastic switching between an empty and an occupied MT tip can promptly affect the sign of the collective velocity. This can be seen immediately, because depolymerization (rate δ) and polymerization (rate η) contribute with different signs to v_{coll} .

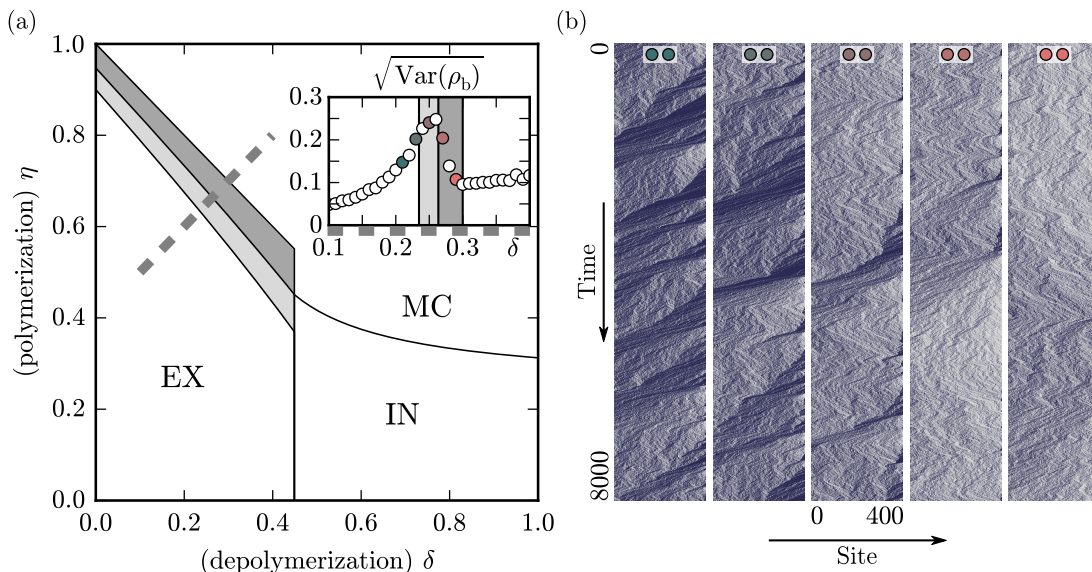


FIG. 9. (a) Phase diagram of the model in terms of depolymerization and growth rates for $\rho_- = 0.5$ and $\beta = 0.05$. The shaded areas show regimes of intermittent dynamics as calculated in the main text. The topology of the diagram with respect to high density (EX), low density (IN) and maximal current density (MC) phases correspond to the case of $\beta = 0$ [6]. The inset shows how bulk density fluctuations are increased in the intermittent regime. A comparison with Fig. 3(c) reveals that fluctuations are enhanced by almost a factor of four as compared to the discontinuous EX/IN transition. Data was recorded for system size $N = 400$ and $\eta = 0.4 + \delta$ along the thick dashed line. (b) Representative kymographs across the intermittent regime. Parameter values correspond to those of the filled circles in the inset of panel (a).

This means that depending on the state of the MT tip – occupied or empty – perturbations may either stabilize or destabilize the bulk density. This can be illustrated in a straight forward manner for the IN phase, when we choose $\rho_b = \rho_- = 1/2$ for example. In this case the sign of v_{coll} depends *only* on the tip density: For $\rho_+ = 1$ and $\rho_b = \rho_b^{\text{IN}}$ the lattice is in the shrinking state, while particles on the lattice still travel towards the tip at unit velocity. Consequently perturbation travel to the right with $v_{\text{coll}} = \delta$. This follows directly from Eq. (20) and is in line with the kymographic data presented above. For $\rho_+ = 0$ the lattice is in the growing state, and particles on the lattice travel towards the tip at a reduced velocity $1 - \eta$. As can be seen from Eq. (21), density perturbation travel to the left with negative collective velocity $v_{\text{coll}} = -\eta$, again in agreement with the kymographic data. Now let us apply this argument for the EX phase, where the situation is more intricate. The sign-change of the collective velocity, $v_{\text{coll}}(\rho_b^{\text{EX}}, \rho_+ = 0) < 0$ and $v_{\text{coll}}(\rho_b^{\text{EX}}, \rho_+ = 1) > 0$, is restricted to a particular regime $\eta^\dagger < \eta < \eta^c$, with

$$\eta^\dagger = 1 - \delta - \frac{2\beta}{1 - \delta}, \quad (22)$$

while the remaining part of the parameter space is not affected. As a consequence the EX phase is destabilized by molecular switching events at the MT tip in this regime. This means that for growth rates $\eta^\dagger < \eta < \eta^c$ the molecular noise due to motor occupation at the tip renders the EX phase unstable. This mechanism is complementary

to the above argument for DW velocities. In Fig. 9(a) we show the phase diagram with the EX, MC and IN phase as well as the different intermittent regimes. In the inset we quantified density fluctuations across the intermittent region in phase space. The different regimes, $\eta^\dagger < \eta < \eta^c$ (light gray) and $\eta^c < \eta < \eta^*$ (darker gray), can be identified reasonably well, given the complexity of the dynamics. As will be shown in the next section it is instrumental to employ higher order moments and a direct evaluation of bulk density distributions to distinguish between the regimes. Figure 9(b) shows kymographic data of typical trajectories in the intermittent regime. This direct visualization of the process is hard to analyze computationally, but in the eye of the beholder, domain walls and qualitative differences in current fluctuations can be readily recognized.

G. Bistability and collective motion

To complete the picture of the intermittent regime, we performed extensive stochastic simulations to obtain the bulk density distribution, see Fig. 10(a). We further analyze the data using the bimodality parameter $b = (\mu_3^2 + 1)/\mu_4$, where $\mu_{3,4}$ are the third and fourth standardized central moments of the density distribution. Figure 10(b) displays the results. The intermittent regime is indicated by light and dark gray regions in the plot. At δ^\dagger , b increases with increasing δ and η , it peaks at δ^c and drops to a constant value $b = 1/3$ for $\delta > \delta^*$.

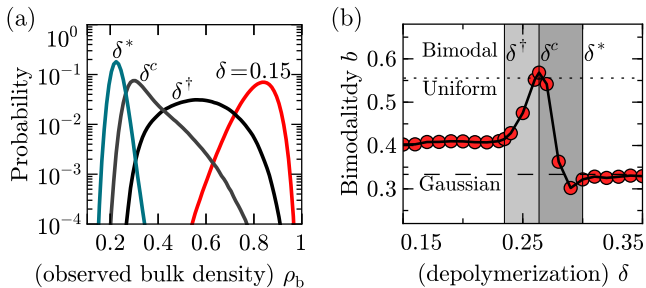


FIG. 10. (a) Distribution of the bulk density from trajectories as long as 10^8 time steps for $\beta = 0.05$ (thick). (b) The bimodality parameter b , supports the role of fluctuations during traffic dynamic instability: $b = 1/3$ corresponds to a Gaussian distribution and $b = 5/9$ to a uniform distribution. A distribution with $b > 5/9$, as reached for δ^c , can be considered bimodal. Simulations were conducted at system size $N = 400$ and $\eta = 0.4 + \delta$.

The latter value corresponds to a Gaussian distribution. The above analysis corroborates our findings for the intermittent regime: Stochastic switching between different phases ensues large density fluctuations which can be recognized in terms of a bistable bulk density distribution.

Finally, we wish to address the scaling relation we have found for density and current fluctuations in the beginning of the paper [Fig. 4]. Although we have discussed the origin of fluctuations and intermittent dynamics in the system, an explanation for the characteristic scaling $\beta_c \propto N^{-1/2}$ for the onset of density fluctuations has remained elusive. In order to gain at least some phenomenological insight, kymographic data was recorded for a set of system sizes and $\beta = \frac{1}{4}N^{-1/2}$, what approximately corresponds to the onset of the regime of strong fluctuation. The results are shown in Fig. 11. In particular, we chose the fields of view in a mainly growing state, where the system is most likely in the MC phase. A close inspection reveals that density fluctuations on the lattice do not vanish in a diffusive manner, but rather perform erratic zig-zag motion on the lattice, as indicated by the symbols. This is opposed to the situation $\beta > \beta_c$, where perturbations drift to the left of the system. Similarly for $\beta < \beta_c$ the shrinking phase becomes more likely and perturbations move towards the tip of the lattice. The data shown in Fig. 11 suggests that individual density fluctuations are maintained and held in the bulk of the system through the combined dynamics of growth and shrinking. A detailed analysis however lies beyond the scope of this paper. We think that a theory in which perturbations were considered as quasi-particles or collective excitations of the system are likely to provide a deeper understanding of the $N^{-1/2}$ relation.

IV. DISCUSSION AND CONCLUSION

In this article we presented a driven lattice gas inspired from microtubule depolymerizing motors (kinesin-8), and based on the *totally asymmetric simple exclusion process*. The system exhibits boundary-induced intermittent dynamics, with stochastic switching between different phases of motor traffic and between lattice growth and shrinking. The standard mean-field approach explains density and current profiles of the system, but misses a proper description of the intermittent regime. We introduce an extended domain wall theory complemented by an extremal current principle which predicts the intermittent regime, in which multiple phases coexist. This phase coexistence can not be resolved with time- or ensemble-averages, because in such data, it appears the system deviates from the usually well-behaved mean-field case. However, an interpretation of individual realizations of the process (like in a single molecule experiment) allows to apply the mean-field results to the data.

Intermittency in driven systems has been reported before. For example in bidirectional transport [53–55], and in cellular automata for traffic flow [56, 57]. The reasons for the interesting dynamics in these systems are particle interactions in bulk of the systems – in contrast to the situation considered here, where the system is triggered at the boundary. Quite generally, the presence of bottlenecks leads to interesting effects which affect the particle densities in driven systems [58–60]. This includes dynamic bottlenecks in bulk [43, 55, 61, 62], at system boundaries [63–65], as well as dynamically evolving bottlenecks [46–48]. In our case we could attribute the intermittent dynamics to bulk density fluctuations which arise through molecular noise at the lattice tip, i.e. switching between tip occupations $n_+ = 1$ and $n_+ = 0$. The sources of this noise is motor detachment and arrival at the tip. In our model, the bulk density fluctuations can be attributed to a region in phase space in which different phases of motor traffic coexist, or in other words, multiple phases can be transiently stable for a given set of parameters. To identify these dynamical phase transitions and track them analytically we neglected attachment and detachment kinetics of the motors, and thus assumed a constant density profile.

In a biological situation where molecular motors interact with MTs, this assumption is valid when the length of the filament exceeds a critical length $\propto \omega_a^{-1}$, where ω_a is the attachment rate of motors to the MT [29]. We checked numerically that the intermittent regime also occurs in the case of a constant density profile with explicit motor attachment and detachment. This can be understood from a lattice gas point of view, where motor detachment from the tip is equivalent to the creation of a “hole” at the tip: A hole can reach the tip by particle detachment in bulk and subsequent transport of the hole to the tip through depolymerization of the lattice.

The stochastic switching between growth and shrinking in our model emerges from collective effects of molec-

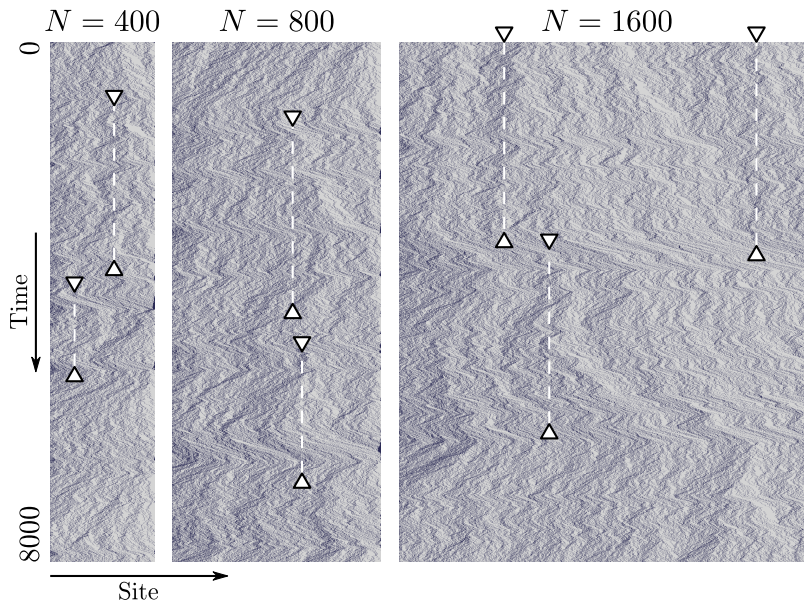


FIG. 11. At the system size dependent critical detachment rate $\beta_c(N)$, perturbations underlie erratic zig-zag motion in the bulk of the system as highlighted by the triangles and vertical dashed lines. Shown are kymographic data for several system sizes as indicated. Periods of depolymerization and polymerization alternate in a way that density perturbations are maintained within the system. Perturbations seem to perform random walks that are created and annihilated stochastically. Simulation parameters were $\delta = 0.2$, $\eta = 0.79$, $\rho_- = 0.5$, and, from left to right, $\beta_c(400) = 0.0125$, $\beta_c(800) = 0.008838$, $\beta_c(1600) = 0.00625$.

ular motor traffic. For MT dynamic instability in contrast the mechanism of stochastic switching between growing and shrinking can be attributed to the nucleotide state of the MT lattice [66]. A comparison by numbers could be thought of within the mathematical framework provided by Dogterom and Leibler [67], where the parameters are growth and shrinking speeds v_+ , v_- , and the frequencies of catastrophe f_{+-} and rescue f_{-+} . Our model relates microscopically to these macroscopic parameters. The speed of the MT tip is a function of the motor density at the MT tip and given by $v(\rho_+) = \eta(1 - \rho_+) - \delta\rho_+$ [6]. Depending on whether the system is in a high density phase or a low density phase $v(\rho_+)$ can be negative or positive. For the switching frequencies the mapping is only possible for the rescue frequency. It can be directly attributed to the parameter of particle detachment from the tip $f_{-+} \propto \beta$. Catastrophe in contrast is initiated by particle arrival at the tip and initiation of a traffic jam. Thereby current fluctuations are important and more elaborate techniques are necessary to calculate these [44].

A future challenge is to understand the interplay between the MT lattice, MT tips, and MT associated proteins. The characteristics of each of these parts

contribute significantly to MT dynamics, but the relations between them are still obscure; necessary information is available: protein localization mechanisms at MT tips [68], enzymatic functions of tip related enzymes [69, 70], and dynamic information about the MT tip structure [71, 72].

The present model constitutes an example how enzymes may influence MT dynamics. The mechanism we found is complementary to known mechanisms of MT regulation, but may contribute to MT regulation in a similar way as does MT dynamic instability [8].

ACKNOWLEDGMENTS

L.R. is grateful to Matthias Rank and Emanuel Reithmann for numerous valuable discussions and input on a previous version of this manuscript and to Anatoly B. Kolomeisky for an inspiring discussion in the prelude of this work and comments on the manuscript. Financial support by the Deutsche Forschungsgemeinschaft in the framework of the SFB 863, project number B02, is gratefully acknowledged.

[1] A. Desai, S. Verma, T. J. Mitchison, and C. E. Walczak, *Cell* **96**, 69 (1999).

[2] L. Wordeman, *Curr. Opin. Cell Biol.* **17**, 82 (2005).

[3] C. E. Walczak, S. Gayek, and R. Ohi, *Annu. Rev. Cell*

- Dev. Biol. **29**, 417 (2013).
- [4] J. Howard and A. A. Hyman, *Curr. Opin. Cell Biol.* **19**, 31 (2007).
- [5] A. Melbinger, L. Reese, and E. Frey, *Phys. Rev. Lett.* **108**, 258104 (2012).
- [6] L. Reese, A. Melbinger, and E. Frey, *Interface Focus* **4**, 20140031 (2014).
- [7] A. Desai and T. Mitchison, *Annu. Rev. Cell Dev. Biol.* **13**, 83 (1997).
- [8] T. Mitchison and M. Kirschner, *Nature* **312**, 237 (1984).
- [9] T. L. Hill, *Proc. Natl. Acad. Sci. USA* **81**, 6728 (1984); T. L. Hill and Y. Chen, *Proc. Natl. Acad. Sci. USA* **81**, 5772 (1984).
- [10] V. Varga, J. Helenius, K. Tanaka, A. A. Hyman, T. U. Tanaka, and J. Howard, *Nat. Cell Biol.* **8**, 957 (2006).
- [11] M. L. Gupta, P. Carvalho, D. M. Roof, and D. Pellman, *Nat. Cell Biol.* **8**, 913 (2006).
- [12] M. I. Mayr, S. Hümmel, J. Bormann, T. Grüner, S. Adio, G. Woehlke, and T. U. Mayer, *Curr. Biol.* **17**, 488 (2007); J. Stumpff, G. von Dassow, M. Wagenbach, C. Asbury, and L. Wordeman, *Dev. Cell* **14**, 252 (2008); C. Tischer, D. Brunner, and M. Dogterom, *Mol. Syst. Biol.* **5**, 250 (2009).
- [13] X. Su, R. Ohi, and D. Pellman, *Trends Cell Biol.* **22**, 567 (2012).
- [14] B. Derrida, *Phys. Rep.* **301**, 65 (1998).
- [15] G. Schütz, in *Phase Transitions and Critical Phenomena*, Vol. 19, edited by C. Domb and J. Lebowitz (Academic Press, London, 2001) pp. 1–251.
- [16] R. A. Blythe and M. R. Evans, *J. Phys. A: Math. Theor.* **40**, R333 (2007).
- [17] P. L. Krapivsky, S. Redner, and E. Ben-Naim, *A kinetic view of statistical physics* (Cambridge University Press, 2010).
- [18] T. Chou, K. Mallick, and R. K. P. Zia, *Rep. Prog. Phys.* **74**, 116601 (2011).
- [19] A. Parmeggiani, T. Franosch, and E. Frey, *Phys. Rev. Lett.* **90**, 86601 (2003); *Phys. Rev. E* **70**, 46101 (2004).
- [20] R. Lipowsky, S. Klumpp, and T. Nieuwenhuizen, *Phys. Rev. Lett.* **87**, 108101 (2001); S. Klumpp and R. Lipowsky, *J. Stat. Phys.* **113**, 233 (2003).
- [21] C. Leduc, K. Padberg-Gehle, V. Varga, D. Helbing, S. Diez, and J. Howard, *Proc. Natl. Acad. Sci. USA* **109**, 6100 (2012).
- [22] R. Subramanian, S.-C. Ti, L. Tan, S. Darst, and T. Kapoor, *Cell* **154**, 377 (2013).
- [23] K. E. P. Sugden, M. R. Evans, W. C. K. Poon, and N. D. Read, *Phys. Rev. E* **75**, 31909 (2007).
- [24] K. E. P. Sugden and M. R. Evans, *J. Stat. Mech.: Theory and Experiment* **2007**, P11013 (2007).
- [25] M. Schmitt and H. Stark, *Europhys. Lett.* **96**, 28001 (2011).
- [26] S. Muhuri, *Europhys. Lett.* **101**, 38001 (2013).
- [27] G. Klein, K. Kruse, G. Cuniberti, and F. Jülicher, *Phys. Rev. Lett.* **94**, 108102 (2005).
- [28] L. E. Hough, A. Schwabe, M. A. Glaser, J. R. McIntosh, and M. D. Betterton, *Biophys. J.* **96**, 3050 (2009).
- [29] L. Reese, A. Melbinger, and E. Frey, *Biophys. J.* **101**, 2190 (2011).
- [30] S. Nowak, P.-W. Fok, and T. Chou, *Phys. Rev. E* **76**, 31135 (2007).
- [31] D. Johann, C. Erlenkämper, and K. Kruse, *Phys. Rev. Lett.* **108**, 258103 (2012); C. Erlenkämper, D. Johann, and K. Kruse, *Phys. Rev. E* **86**, 051906 (2012).
- [32] C. Arita, A. Lück, and L. Santen, *ArXiv e-prints* (2015), arXiv:1504.08189 [cond-mat.stat-mech].
- [33] C. Arita and A. Schadschneider, *Phys. Rev. E* **83**, 051128 (2011); *J. Stat. Mech.* **2012**, P12004 (2012); *EPL (Europhys. Lett.)* **104**, 30004 (2013).
- [34] J. de Gier and C. Finn, *J. Stat. Mech.* **2014**, P07014 (2014).
- [35] C. MacDonald, J. Gibbs, and A. Pipkin, *Biopolymers* **6**, 1 (1968).
- [36] C. Gell, V. Bormuth, G. J. Brouhard, D. N. Cohen, S. Diez, C. T. Friel, J. Helenius, B. Nitzsche, H. Petzold, J. Ribbe, E. Schäffer, J. H. Stear, A. Trushko, V. Varga, P. O. Widlund, M. Zanic, and J. Howard, *Methods in Cell Biology*, Vol. 95 (2010) pp. 221–245.
- [37] M. K. Gardner, M. Zanic, C. Gell, V. Bormuth, and J. Howard, *Cell* **147**, 1092 (2011).
- [38] J. Krug, *Phys. Rev. Lett.* **67**, 1882 (1991).
- [39] B. Derrida, E. Domany, and D. Mukamel, *J. Stat. Phys.* **69**, 667 (1992).
- [40] B. Derrida, M. R. Evans, V. Hakim, and V. Pasquier, *J. Phys. A: Math. Gen.* **26**, 1493 (1993).
- [41] G. Schütz and E. Domany, *J. Stat. Phys.* **72**, 277 (1993).
- [42] P. Pierobon, M. Mabilia, R. Kouyos, and E. Frey, *Phys. Rev. E* **74**, 31906 (2006).
- [43] F. Turci, A. Parmeggiani, E. Pitard, M. C. Romano, and L. Ciandrini, *Phys. Rev. E* **87**, 012705 (2013).
- [44] M. Gorissen, A. Lazarescu, K. Mallick, and C. Vanderzande, *Phys. Rev. Lett.* **109**, 170601 (2012); M. Gorissen and C. Vanderzande, *J. Phys. A: Math. Theor.* **44**, 115005 (2011); A. Lazarescu and K. Mallick, *J. Phys. A: Math. Theor.* **44**, 315001 (2011).
- [45] D. Gillespie, *J. Comp. Phys.* **22**, 403 (1976); D. T. Gillespie, *J. Phys. Chem.* **81**, 2340 (1977).
- [46] I. Pinkoviezky and N. S. Gov, *Phys. Rev. E* **89**, 052703 (2014).
- [47] M. Sahoo, J. Dong, and S. Klumpp, *J. Phys. A: Math. Theor.* **48**, 015007 (2015).
- [48] A. A. van den Berg and S. M. Depken, *Biophys. J.* **108**, 535a (2015).
- [49] A. B. Kolomeisky, G. M. Schütz, E. B. Kolomeisky, and J. P. Straley, *J. Phys. A: Math. Gen.* **31**, 6911 (1998).
- [50] V. Popkov and G. M. Schütz, *Europhys. Lett.* **48**, 257 (1999).
- [51] J. S. Hager, J. Krug, V. Popkov, and G. M. Schütz, *Phys. Rev. E* **63**, 056110 (2001).
- [52] C. Schultens, A. Schadschneider, and C. Arita, *Physica A: Statistical Mechanics and its Applications* **433**, 100 (2015).
- [53] M. Evans, D. Foster, C. Godrèche, and D. Mukamel, *Phys. Rev. Lett.* **74**, 208 (1995).
- [54] R. D. Willmann, G. M. Schütz, and S. Großkinsky, *EPL (Europhys. Lett.)* **71**, 542 (2005); S. Großkinsky, G. M. Schütz, and R. D. Willmann, *J. Stat. Phys.* **128**, 587 (2007).
- [55] A. Jelić, C. Appert-Rolland, and L. Santen, *EPL (Europhys. Lett.)* **98**, 40009 (2012).
- [56] R. Barlovic, L. Santen, A. Schadschneider, and M. Schreckenberg, *Eur. Phys. J. B* **5**, 793 (1998).
- [57] C. Appert and L. Santen, *Phys. Rev. Lett.* **86**, 2498 (2001).
- [58] S. A. Janowsky and J. L. Lebowitz, *Phys. Rev. A* **45**, 618 (1992).
- [59] G. Schütz, *Journal of Statistical Physics* **71**, 471 (1993).
- [60] A. B. Kolomeisky, *Journal of Physics A: Mathematical*

- and General **31**, 1153 (1998).
- [61] L. Zhang, J. de Gier, and T. M. Garoni, *Physica A: Statistical Mechanics and its Applications* **401**, 82 (2014).
 - [62] R. Chatterjee, A. K. Chandra, and A. Basu, *Journal of Statistical Mechanics: Theory and Experiment* **2015**, P01012 (2015).
 - [63] V. Popkov, M. Salerno, and G. M. Schütz, *Phys. Rev. E* **78**, 011122 (2008).
 - [64] A. J. Wood, *J. Phys. A: Math. Theor.* **42**, 445002 (2009).
 - [65] H. Ito and K. Nishinari, *Phys. Rev. E* **89**, 042813 (2014).
 - [66] M. K. Gardner, M. Zanic, and J. Howard, *Curr. Opin. Cell Biol.* **25**, 14 (2013).
 - [67] M. Dogterom and S. Leibler, *Phys. Rev. Lett.* **70**, 1347 (1993).
 - [68] E. Reithmann, L. Reese, and E. Frey, *Biophys. J.* **108**, 787 (2015).
 - [69] M. Zanic, P. O. Widlund, A. A. Hyman, and J. Howard, *Nat. Cell Biol.* **15**, 1 (2013).
 - [70] C. Duellberg, M. Trokter, R. Jha, I. Sen, M. O. Steinmetz, and T. Surrey, *Nat. Cell Biol.* **16**, 804 (2014).
 - [71] S. P. Maurer, N. I. Cade, G. Bohner, N. Gustafsson, E. Boutant, and T. Surrey, *Curr. Biol.* **24**, 372 (2014).
 - [72] G. Alushin, G. Lander, E. Kellogg, R. Zhang, D. Baker, and E. Nogales, *Cell* **157**, 1117 (2014).

Nucleation of Filaments

– How Phase Transitions Regulate the Cytoskeleton

Nucleation phenomena have been studied in great detail in order to understand the formation and growth of crystals. With the advent of computers it became possible to perform molecular dynamics simulations and to test the thermodynamic theories on nucleation. A variety of classic nucleation problems were addressed like this, for example protein crystals formation [229], or the freezing of water [230]. More recent investigations focused on salt crystallization in confinement [231]. The nucleation mechanisms of filaments, however has remained at large since the seminal work by Oosawa and Kasai [232].

Because studying nucleation in experiments is difficult, the kinetic details of filament nucleation have remained elusive. Recently, however, kinetic modeling has proven a versatile tool to investigate the polymerization dynamics of filaments in very small systems comprising ~ 10 particles [131]. For such small systems, analytic results could be obtained for first-passage times of the assembly dynamics. Here, a similar approach is pursued with focus on the nucleation reaction and the number of monomers available in the system.

We are interested in the nucleation of actin filaments. The nucleation of actin filaments is known to play an important role *in vivo*, for example in force generation [107] and cell motility [233]. Recent thermodynamic estimates predicted that actin dimers and trimers are very unstable molecules with a lifetime of 10^{-8} seconds [234]. This is in stark contrast to the situation in the cell, where nucleation factors are present, such as ARP2/3. These proteins have been measured to stabilize the dimeric and trimeric forms of actin and thus promote the nucleation of filaments [235].

For the study presented here, an individual-based particle approach is employed, where the number of monomers is conserved in the system. Motivated by the aforementioned results on dimeric and trimeric actin and nucleation proteins, it is systematically investigated how the stability of

oligomeric species influences the filament polymerization kinetics. Once a filament has formed, it performs a random walk. There are three different phases in the nucleation process that can be distinguished, and understood intuitively:

- i)* If dimers and trimers are very stable, all monomers are sequestered. There are no filaments in the system.
- ii)* If dimers and trimers are very unstable, then all monomers absorb into one filament which is initiated stochastically.
- iii)* At intermediate lifetimes of dimers and trimers there is a constant pool of filaments. The system balances at a point where the number of filaments that go extinct equals the number of nucleating filaments.

These three cases of the kinetic model presented in the following effectively account for all known features of the actin nucleation process. *In vitro*, when nucleation is a rare event [234]. *In vivo* when nucleation is regulated by protein nucleation factors [235], or when sequestering proteins like thymosin β_4 reduce the pool of monomers available for polymerization.

4.1. Model definition

Figure 4.1 depicts the kinetic model for filament nucleation. We consider a closed system that explicitly contains M free monomers in a small volume V to mimic the situation of living cells [143, 152] and artificial systems like for example lipid vesicles and emulsion droplets [126, 152, 236, 237]. The molecular species involved in the nucleation reaction are free monomers (M), dimers (D), and trimers (T). Oligomers containing more than three monomers are considered as filaments (F). In the following we set the volume of the system to unity $V = 1$ and employ a particle based picture of the nucleation reaction. As a consequence of this particle based picture the typical unit for concentrations „mole“ is circumvented. Growth and shrinking of filaments is implemented as random walk, i.e. growth and shrink rates are set to unity, $k^+ = 1 \text{ sec}^{-1}$ and $k_f^- = 1 \text{ sec}^{-1}$. The rates of dimer and trimer formation are $k^+ = 1 \text{ sec}^{-1}$, however, with a fixed number of particles, dimer formation is implemented via a reaction probability rate constant, $k_{\text{micro}}^+ = 2k^+$, times a combinatorial factor of all possible reactions, $\frac{1}{2}M(M-1)$ [238]. For trimer formation, the number of possible reactions is $D \times M$ and the reaction rate and the reaction probability rate constant are equal. The parameters that determine nucleation in the system are the

4.2. Phase transitions

The lifetimes of dimer and trimer molecules are found to critically influence the long time behavior of the system in terms of the number of filaments F that form. Simulation data reveals that the number of filaments F depends on the dimer/trimer dissociation rate k^- (Fig. 4.2A) in an interesting way. For k^- small and large the number of filaments is small. For intermediate values, however, the number of filaments reaches a maximal value which depends on the initial number of monomers M . This observation is also confirmed when k_1^- and k_2^- are varied independently (Fig. 4.2B). The data suggests three qualitatively distinct regimes which we discuss in the following:

First, for very stable dimers or trimers (i.e. $k^- \ll 1$) the system does not form filaments, because all monomers are sequestered into dimers and trimers. Consequently monomers are not available for filament growth and the system suffers from a lack of monomers which inhibits the formation of critical nuclei for growth [241]. Note that the stochastic formation of filaments is nevertheless possible.

Second, for very unstable dimers and trimers (i.e. $k^- \gg 1$) only one filament forms which contains almost all monomers. This behavior can be understood intuitively. Because dimers and trimers are unstable, filaments only form as long as a large pool of monomers is available that allows the system to overcome the nucleation barrier. In the course of the dynamics, however, the system reaches a state where all monomers are built into filaments and the nucleation barrier prohibits the *de novo* formation of filaments. As a result, filaments may only grow at the cost of other filaments. As filaments perform one-dimensional random walks they are recurrent [242], which means they will reach an unstable oligomeric state with probability 1 and subsequently disappear at the benefit of a single largest filament containing all monomers. Note that this coarsening dynamics may cover very long timescales which depend non-trivially on both, the initial amount of monomers and the dimer/trimer lifetimes.

In the third regime filaments coexist and continuously nucleate and disintegrate. The system reaches a dynamic state where the number of newly formed filaments balances the number of filaments that decay. Consequently the average number of filaments $\langle F \rangle$ is roughly constant and greater than one.

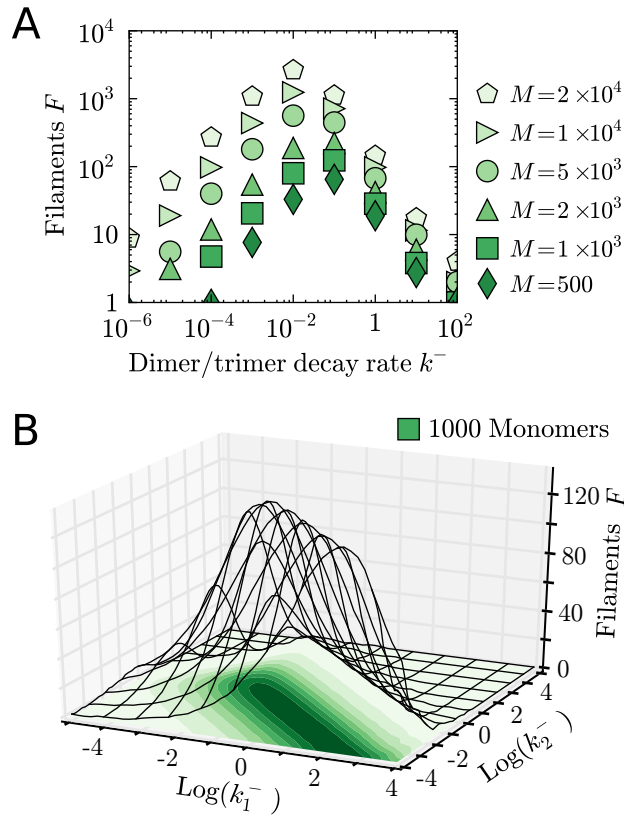


Figure 4.2.: The Number of filaments F is determined by dimer and trimer dissociation rates. (A) There is a pronounced peak in the number of filaments depending on dimer and trimer dissociation rate, k^- . The number of initial monomers is also indicated. (B) If dimer and trimer lifetimes differ, $k_1^- \neq k_2^-$, the maximum in the number of filaments persists, as well as the different regimes described in the main text (mesh and contour map).

Scaling of the number of filaments

Which of the three regimes is assumed depends critically on the number of monomers M and the dimer/trimer dissociation rate k^- . To simplify the analysis hereafter the case of equal dimer and trimer dissociation rates is considered. Performing a heuristic scaling analysis we find a scaling function for the mean number of filaments, which renders $\langle F \rangle / M$ a universal function of the rescaled dimer/trimer dissociation rate $k^- \sqrt{M}$, see Fig. 4.3A.

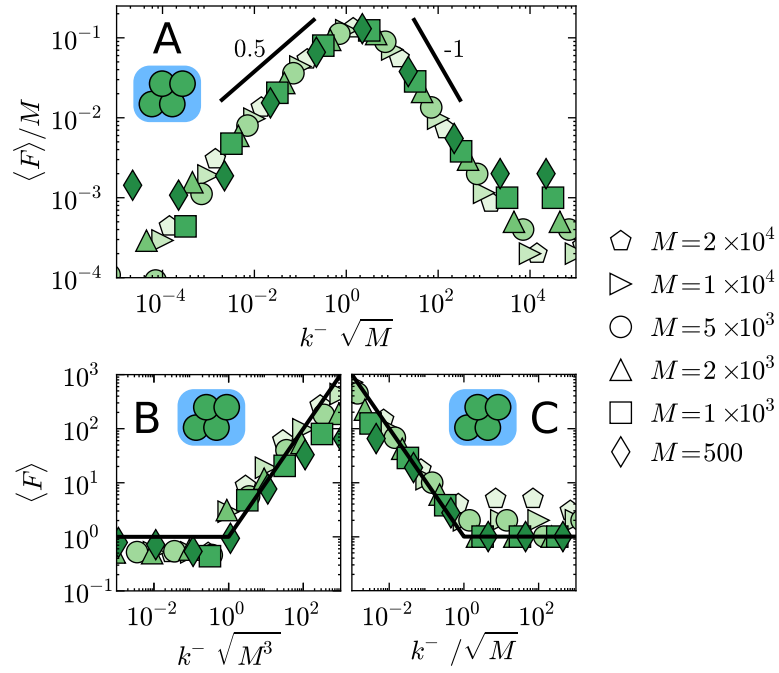


Figure 4.3.: Scaling functions for the mean number of filaments: (A) for the regime of filament coexistence, (B) at the phase transition between the monomer sequestering and the coexistence regime, and (C) at the phase transition between the coexistence and the coarsening regime. Symbols as in Fig. 4.2A; solid lines are guides to the eye.

All data points collapse onto a single curve, while the peak of $\langle F \rangle$ (cf. Fig. 4.2) is preserved. It also appears that the scaling function has a maximum. It lies approximately at $k^- \sqrt{M} = 1$, providing a criterion for a critical nucleation rate, k_{\max}^- , which maximises the number of filaments depending on the monomers in the system:

$$k_{\max}^- = \frac{1}{\sqrt{M}}. \quad (4.1)$$

The heuristic scaling approach also reveals both phase transitions, the one between the regime of monomer sequestration and filament coexistence, and the one between filament coexistence and the coarsening regime. The scaling as in Fig. 4.3B shows the nucleation transition, which occurs at a

critical dimer/trimer dissociation rate given by

$$k_{\text{nuc}}^- = \frac{1}{\sqrt{M^3}}. \quad (4.2)$$

And Fig. 4.3C shows how the coarsening transition starts at a critical dimer/trimer dissociation rate given by

$$k_{\text{cor}}^- = \sqrt{M}. \quad (4.3)$$

The above set of equations determines the phase behavior of the system with distinct phases of monomer sequestering, filament coexistence and coarsening.

Scaling of species that participate in nucleation

Figure 4.4 shows the scaling behavior of monomers, dimers, and trimers. In panel A of the figure the average number of available monomers is shown. Remarkably for $k^- < k_{\text{max}}^-$ there is less than one monomer in the system, $\langle M \rangle < 1$. Consequently the filaments are on average shrinking. This is in contrast to the observation for the regime where $k^- > k_{\text{max}}^-$: therein on average more than one monomer is available in the system $\langle M \rangle > 1$. And thus the polymers in this regime tend to grow on average. Although the absolute difference in the average amount of available monomers in the two discussed regimes is small, it significantly determines the system's dynamics and steady states. A more detailed discussion is deferred to the following section.

The scaling analyses for dimers and trimers show different behavior. While the average number of dimers scales with $1/\sqrt{M}$, the average number of trimers shows scaling with the average number of filaments, $1/M$. Notably the data collapse for trimers coincides with the scaling for the average number of filaments, see Fig. 4.3A.

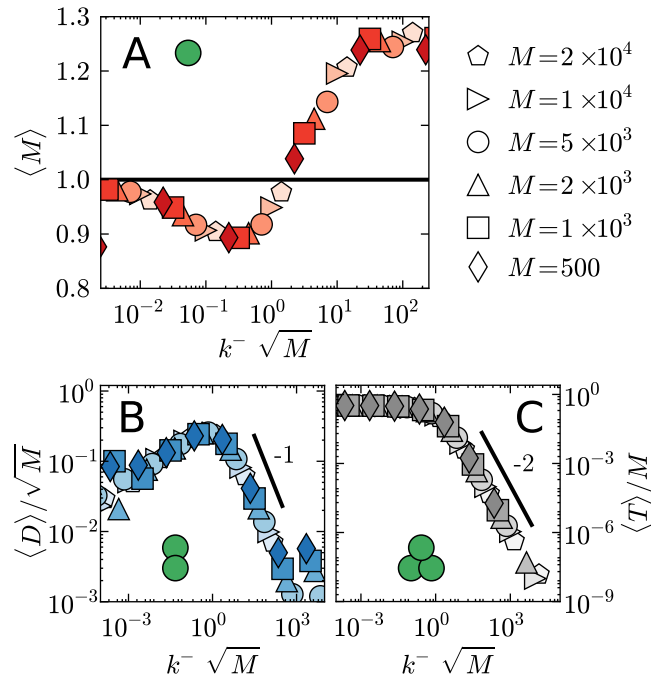


Figure 4.4.: Panels (A), (B), and (C) show scaling functions of the number of monomers and the rescaled number of dimers and trimers, respectively. In the coexistence phase all three species follow a characteristic scaling behavior depending on k^- : For $k^- < k_{\max}^-$ the mean number of monomers, $\langle M \rangle$, is less than one, while for larger k^- , $\langle M \rangle > 1$. The mean number of dimers $\langle D \rangle$ peaks at k_{\max}^- . The mean number of trimers $\langle T \rangle$ exhibits a kink at k_{\max}^- : for $k^- < k_{\max}^-$ the trimer population is roughly constant and for larger k^- the population of trimers sharply drops.

Coexistence phase

In Fig. 4.5A filament length distributions were measured in the coexistence regime for $M = 10^3$ monomers. The data shows that length distributions are exponential when $k^- > k_{\max}^-$. This is in contrast to the situation for $k^- < k_{\max}^-$ where oligomeric assemblies are favored over filaments. This picture is confirmed by simulation data (Fig. 4.5B) where the standard deviation of sets of filament trajectories was analyzed. While for $k^- > k_{\max}^-$ fluctuations are enhanced, for $k^- < k_{\max}^-$ fluctuations are damped. These observations can be readily explained with the presence of monomers in the

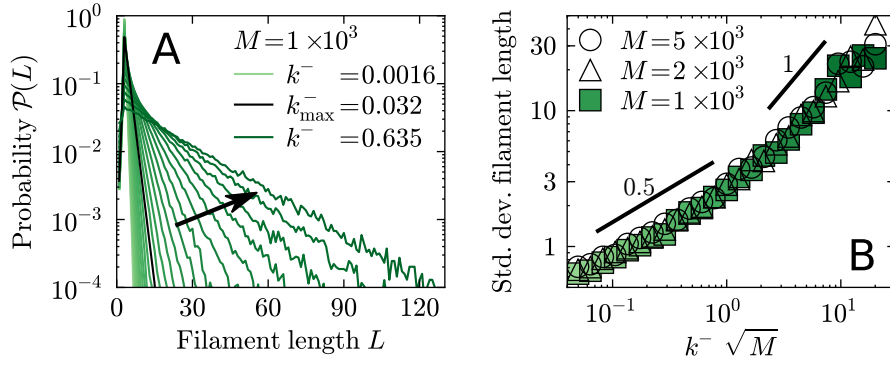


Figure 4.5.: Filament length distributions (A) and average fluctuations of individual filament's trajectories (B) depending on k^- . An ensemble average of the filament length shows that length distributions have exponential tails $\mathcal{P}(L) \propto \exp -L/\alpha$, where α is a characteristic filament length which depends on k^- (A). The arrow indicates increasing k^- . Note that the average number of monomers, dimers and trimers do not follow the distribution shown, but display distinct functional behavior; see Figs. 4.4A, B and C, respectively. Filament fluctuations, as shown in terms of the standard deviation of filament length $\sigma = \sqrt{\langle L^2 \rangle - \langle L \rangle^2}$, are shown in panel (B) and depend on whether $k^- < k_{\max}^-$ or $k^- > k_{\max}^-$. In the latter case fluctuations are enhanced due to a constantly high availability of monomers (see Fig. 4.4A). In the previous case there is on average $\langle M \rangle < 1$ monomer available in the system and therefore fluctuations are decreased. This data is consistent with an exponential length distribution for $k^- > k_{\max}^-$ and a Poisson like length distribution for $k^- < k_{\max}^-$

system. As can be deduced from the results presented in Fig. 4.4A, the increase of filament fluctuations stems from a higher availability of monomers, $\langle M \rangle > 1$, and the damping of fluctuations arises from a lower availability of monomers, $\langle M \rangle < 1$. Consequently the critical line of the maximal number of filaments k_{\max}^- separates two regimes in the coexistence phase that qualitatively differ in filament dynamics and filament length distributions: For k^- smaller than k_{\max}^- filaments are very short and might rather be called oligomers. In contrast if k^- is larger than k_{\max}^- , indeed filaments emerge that follow an exponential length distribution.

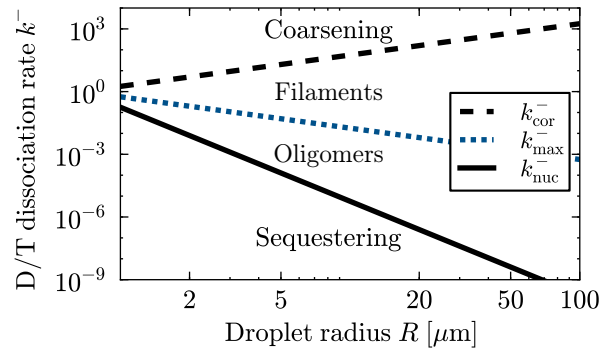


Figure 4.6.: Phase diagram of the system. The theoretical results are applied to a spherical volume with radius R containing a 10 nM solution of monomers.

Phase diagram

In Fig. 4.6 all phases of the system are summarized. To this end a spherical volume V with a 10 nM solution of molecules is considered explicitly. The critical dimer/trimer dissociation rates are plotted as a function of droplet radius R . The different phases of sequestering, filament coexistence, and coarsening can be adopted by varying the volume. Below certain critical volumes the filament coexistence phase disappears and the system either enters the coarsening or the monomer-sequestered phase. Which of the phases is adopted depends on the dissociation rate constant k^- . Within the coexistence phase, decreasing or increasing the volume constitutes a physical switch that allows the system to change from the filamentous regime to the oligomeric regime and back, respectively. The phase diagram is also useful to gain some insight on the mechanisms of nucleating proteins [111] or monomer sequestering proteins [243]. The addition of sequestering proteins allows to vertically run through all possible phases at a fixed volume V .

4.3. Application to actin filaments

By choosing appropriate dimer and trimer dissociation rates, the model effectively applies to actin filaments, which nucleate either spontaneously or via nucleator-assisted pathways. For the case of spontaneous nucleation the estimated dissociation rates are of the order of $k_1^- \approx 10^8 \text{ sec}^{-1}$, and $k_2^- \approx 10^3 \text{ sec}^{-1}$ [234]. In a first approximation one may choose $k^- = k_1^- = k_2^-$ of the order of $\sim 10^8 \text{ sec}^{-1}$. Compared with the model results, this large number is only consistent with Eq. (4.3). It implies that the system

is in the coarsening regime, given the number of monomers is larger than $M = 10^{16}$. This monomer number corresponds to an actin monomer concentration of $c = 100$ nM in experiments, which roughly corresponds to the critical concentration of actin nucleation $100 - 200$ nM [244]. Our theory suggests that this critical concentration lies in the coarsening phase of actin filament assembly.

Dimer/Trimer dissociation rates are effectively changed in the presence of nucleating proteins, because actin dimers and trimers are stabilized or mimicked by the nucleating proteins. One important example is the actin branching and nucleating protein complex ARP2/3, which effectively decreases the dimer and trimer decay rates by several orders of magnitude, $k_1^- \approx 2 \times 10^{-3} \text{ sec}^{-1}$ and $k_2^- \approx 10^{-5} \text{ sec}^{-1}$ [235]. The role of this protein in the nucleation kinetics is thus twofold: the formation of the critical nucleus is facilitated on the one hand, and free actin monomers are sequestered into dimers and trimers on the other hand. The model can be effectively applied to the case of ARP2/3 by approximating dimer/trimer dissociation rates with $k^- \sim 0.002 \text{ sec}^{-1}$. The scaling laws derived above rule out immediately that the system is in the coarsening regime. However, the two other conditions Eqs. (4.1), and (4.2) can be met depending on the amount of monomers. This renders the number of monomer a regulatory factor for the dynamics. The maximal number of filaments is obtained with $M_{\text{max}} = 2.5 \times 10^5$ monomers. Similarly, the sequestering regime, where ARP2/3 takes out all the free monomers is found for $M < M_{\text{seq}} = 63$.

4.4. Discussion

The simple model studied here for nucleation and growth of protein filaments shows a rich phase behavior when a finite amount of monomers is considered. It is found that depletion of monomers is critical for understanding the system's dynamics and steady states. Four different phases are identified. The system either consists of subcritical nuclei alone, or may undergo condensation into one large structure. In between these two extreme cases there are two more regimes in which filaments coexist either as many small filaments or as few large filaments.

The implications of these findings can be applied to diverse processes in cell biology, where the role of abundance of cytoplasmic material was unclear until recently [143]. For example recent experiments have shown that spindle size depends on the cellular amount of tubulin, and that tubulin is indeed a limiting factor [152]. In reconstitution experiments Good et al. [152] also showed that at a critical volume the amount of free tubulin incorporated in

the spindle suddenly increases, reminiscent of the coexistence to coarsening transition observed in the present model. Different experiments in fission yeast can be regarded as a system with constant volume. Burke et al. [241] have shown that there is competition for actin monomers in fission yeast, and that there are two possible phases depending on the amount of actin which is expressed in a cell. In these experiments the actin level critically influenced the morphology of the actin cytoskeleton. Filaments form at low levels of actin, whereas patch like structures emerge at high actin levels. It will be interesting to study such and other phase transitions in cells [245] theoretically, in particular with respect to the level of actually available protein. Further it is likely that not only particle number, but also different mechanisms like multivalency of enzymes play an important role [246]. Our study also contributes to the field of protein crystallography and thus to structural and molecular biology. The quest to economize purified protein lead to the development of microfluidic devices that allowed to grow protein crystals in nanoliter volumes [247, 248]. It was realized that crystals are much more likely to grow in such small volumes. The present work provides a possible explanation for this phenomenon. This is supported by recent experimental work, in which the tendency of crystallization was explicitly tested in different volumes in the nanoliter range [249], paving the way towards a more quantitative approach to crystallography.

Epilog

Within this final chapter I will try to draw conclusion from what has been learned so far from this thesis. I will also try to provide a more speculative outlook on what could be relevant extensions and consequences of the presented theoretical models. Further, I would like to point towards possible future directions of research that might be worthwhile pursuing, as far as I can see.

MICROTUBULE TIPS are indeed the place to be on a microtubule. There are so many proteins associated to them, either directly or indirectly, that it has become more and more difficult to keep an overview [88]. The analysis is not getting easier when the particular situations at different stages of the cell cycle are considered, because then the role of microtubule tips is redefined like for instance during mitosis, when they are programmed to find and interact with kinetochores at the chromosomes.

During the time of this Thesis it became clear that exclusive interactions of molecular motors ensue traffic jams of motors at microtubule tips and in the bulk of the microtubule lattice [22, 103]. This experimental finding, has been predicted in recent theoretical work [102, 140]. Together the theoretical and experimental observations of these traffic phenomena shed a new light on driven diffusive lattice gases and exclusion processes. What has previously been assumed toy models for molecular traffic has now been shown to reflect essential parts of the processes that actually happen in reconstitution experiments. This finding paves the way for a serious quantification of many different cellular processes that occur in the cytoplasm and on cytoskeletal filaments, triggered by molecular motors. The time when theoretical biophysics research employs loose and qualitative models is simple over. Because nothing can be learned from it anymore. The next stage demands quantitative and detailed understanding of molecular processes. While many recent efforts have well captured the actual biological behavior, novel insight can be gained about sub-molecular processes that happen at the nanoscale and are elusive in coarse grained models. The lack

of temporal and spatial resolution in experiments did not allow to falsify coarse grained models recently. Nowadays, the situation is different. High resolution in the temporal and spatial domain, as well as in terms of forces, is not a problem anymore. The question is rather: How shall the results be interpreted? And how can novel hypothesis be generated? In the following I present one possible hypothesis, that emerges from what has been learned in this thesis:

The *spatial arrangement* of enzymes plays an essential role in microtubule tip-related processes.

Adopting the above hypothesis, several questions can be formulated. What are the assembly principles of such spatially coordinated macromolecular structures? Minimal systems that mimic specific behavior like tip-tracking for example [6] have been investigated. These experiments suggest that end binding proteins (EBs) interact with the microtubule tip, and tethering proteins pass on their interaction with the EBs to molecular motor. Complementary to such *in vitro* findings are high resolution structures of macromolecular complexes that form on microtubule tips [250]. However, it will take a multidisciplinary effort to resolve the dynamics of these structures and their cellular implications.

One example for which a systems understanding has been achieved already are the kinetochores [219]. These supramolecular structures consist of more than 80 different protein components that have been studied and are rather well characterized with respect to their role in the complex. Some of them exhibit a role as force sensors for example, while others are similar to kinesin motors. It is a future challenge to understand the assembly and disassembly of such structures and their dynamics. It seems likely that such protein assemblies behave like amorphous materials and have a preferential structure.

For microtubules recent structural work [57] and dynamic investigations [251] reveal essential microscopic properties of the microtubule lattice. These findings and information on microtubule-protein interactions and microtubule dynamics could provide a basis for the development of a realistic and complete picture of the macromolecule „microtubule“ and its associated proteins.

It will be important to build upon simple model systems with spatial degrees of freedom, as previously achieved for a Michaelis-Menten reaction [252–254].

And last not least, when speaking of microtubule as an enzymatic substrate alone, one misses important aspects of the biological situation. The

mechanical properties of microtubules have to be accounted for as well. On different scales and in different situations, microtubule can be well described as elastic beams [255], semi-flexible polymers [256] or as bundles of protofilaments [257, 258]. Their mechanical properties were studied in terms of single molecule experiments [259, 260]. On the other hand however, biological situations are very different from the reconstructed system, in which purified components are used. To illustrate this, an example is in order. Recently, experiments showed how microtubule associated proteins influence the mechanical properties of microtubules [261] in unexpected ways. In the presence of MAP65, which is considered a cross-linker protein, the bending stiffness of a microtubule reduce by 75%, from 1.6 mm to 0.4 mm. These numbers illustrate the dramatic mechanical and structural changes associated proteins may induce when binding to microtubules and forming microtubule bundles. For the cellular functions of microtubules, and the cytoskeleton, these results are broadly relevant. However it remains to be shown to what extent and how crosslinker-induced flexibility contributes to *in vitro* microtubule mechanics.

There are many open questions in the microtubule field. As outlined above, the interactions between microtubules and related enzymes are plentiful. These comprise interesting enzyme related questions, where reaction-diffusion and driven lattice gas approaches could unveil cellular mechanisms in the future. And there is also an intricate coupling between those enzyme-related questions and the mechanical behavior of microtubules. So far microtubules have been assessed in terms of polymer physics, but novel, interesting insights might be gained when polymer physics meets enzymes.

NUCLETATION of macromolecules is a phenomenon that has been studied for many years. And ever since it has been a challenge, because the nucleation reaction has to be seeded. For salt crystals seeding is simple, because it is possible to hang a piece of yarn into the saturated salt solution, and there we go, the crystal will nucleate and grow overnight. For proteins the situation is very much the same, just that these molecules are more complicated and their interactions are of complex chemical and physical nature. During the time of this thesis a novel approach to study nucleation was developed together with Dr. Alvaro Crevenna. We conceived an experimental setup that allows to study the initial steps of filament nucleation and elongation in a controlled way. The key idea is to tether nucleator proteins at the bottom of zero mode wave-guides and to monitor the system nucleate and grow. Preliminary results show the stepwise addition of single actin monomers to the seed of the nucleation. Temporal and spatial infor-

mation about the nucleation and growth of a filament is thus available and can be analyzed using theoretical descriptions from stochastic processes. These data will allow to quantify the theoretical model presented in this thesis.

Potential applications of this novel experimental technique – combined with theoretical analysis – might prove useful to study assembly dynamics beyond the cytoskeleton field. This becomes apparent when considering the complexity of macromolecules in cell biology and how they are assembled and disassembled at unprecedented accuracy.

List of Figures

1.1. Electron microscopy images of growing and shrinking microtubules.	10
1.2. Microtubule depolymerizing proteins induce protofilament rings.	13
1.3. Illustration of size determinants of the mitotic spindle.	19
2.1. Illustration of the simple exclusion process (SEP)	22
2.2. Illustration of the totally asymmetric simple exclusion process (TASEP)	23
2.3. Phase diagram of TASEP	24
2.4. Illustration of domain wall theory.	27
2.5. Illustration of density perturbations	28
3.1. Model for kinesin-8 on microtubules.	30
3.2. Phase transitions during microtubule length regulation	63
3.3. Phase diagram for kinesin-8 traffic on microtubules of different length	64
3.4. Filament length distributions for IN and IN/EX regulation.	65
4.1. Model of filament nucleation	83
4.2. Steady states after filament nucleation	85
4.3. Scaling analysis of the number of filament	86
4.4. Scaling analysis of monomers, dimers, and trimers	88
4.5. Filament length distribution and fluctuations	89
4.6. Phase diagram	90

Appendix A.

Teams of Molecular Spiders

– Transport Properties and Cooperative Effects

Please find in the following, work together with Matthias Rank which emerged from his master's thesis [262] on the motion of molecular spider teams [263].

Cooperative effects enhance the transport properties of molecular spider teams

Matthias Rank, Louis Reese, and Erwin Frey*

*Arnold Sommerfeld Center for Theoretical Physics (ASC) and Center for NanoScience (CeNS) and Department of Physics,
Ludwig-Maximilians-Universität München, Theresienstraße 37, 80333 München, Germany*

(Received 12 December 2012; published 8 March 2013)

Molecular spiders are synthetic molecular motors based on DNA nanotechnology. While natural molecular motors have evolved towards very high efficiency, it remains a major challenge to develop efficient designs for man-made molecular motors. Inspired by biological motor proteins such as kinesin and myosin, molecular spiders comprise a body and several legs. The legs walk on a lattice that is coated with substrate which can be cleaved catalytically. We propose a molecular spider design in which n spiders form a team. Our theoretical considerations show that coupling several spiders together alters the dynamics of the resulting team significantly. Although spiders operate at a scale where diffusion is dominant, spider teams can be tuned to behave nearly ballistic, which results in fast and predictable motion. Based on the separation of time scales of substrate and product dwell times, we develop a theory which utilizes equivalence classes to coarse-grain the microstate space. In addition, we calculate diffusion coefficients of the spider teams, employing a mapping of an n -spider team to an n -dimensional random walker on a confined lattice. We validate these results with Monte Carlo simulations and predict optimal parameters of the molecular spider team architecture which makes their motion most directed and maximally predictable.

DOI: [10.1103/PhysRevE.87.032706](https://doi.org/10.1103/PhysRevE.87.032706)

PACS number(s): 87.16.Nn, 82.39.Fk, 05.40.Fb, 02.50.Ey

I. INTRODUCTION

How the motion of molecules along predefined traffic routes emerges and how these molecules self-organize has become an experimentally tractable question due to advances in nanotechnology. Molecular motors that have evolved inside cells and perform well-defined tasks [1] inspired the engineering of DNA devices performing motor business on the nanoscale [2–4]: So-called DNA walkers have been built that move or diffuse along a substrate [5–7]. Among the first autonomous synthetic walkers was a motor design that used a catalytic reaction to cleave a substrate in order to move forward [8]. Since then, a plethora of different motor molecules have been built from scratch in the laboratory. They not only serve technological advances, but also shed light on the basic principles of molecular movement, e.g., of biological molecular motors. One class of molecules that attracted a great deal of attention is molecular spiders [9]. They combine the catalytic activity of nucleic acids with a multivalent design: Attached to a body are several legs of single-stranded DNA. These DNA legs can bind to and catalytically cleave a substrate. This can be repeated over and over again, which in turn generates processive motion: While individual legs dissociate from the substrate on a time scale of seconds, the multipedal architecture ensures tight binding of the spider to the substrate for hours [9]. Recent experiments used DNA origami to build quasi-one-dimensional tracks for molecular spiders [10]. A prescribed substrate landscape allows one to assign special tasks to a spider and, for instance, control its movement. The simple yet well-defined design makes it possible to study spiders in great detail and probe theoretical predictions.

Molecular spiders have also been theoretically studied extensively in recent years. Antal *et al.* [11] and Antal and

Krapivsky [12] were the first to propose an abstract model that describes the dynamics of molecular spiders. They analyzed the spiders' kinetics for various architectures and found a variety of interesting effects which arise due to the mutual exclusion of spider legs on the lattice and the presence of the substrate. Substrates are cleaved slowly in comparison to hopping from already cleaved sites. This distinction leads to subtle memory effects that affect the spiders' dynamics and result in a bias towards the substrate [12]. When the spider is in an all-cleaved area, principles emerging from simple exclusion processes [13,14] allow a derivation of the spiders' diffusion constants [11,15].

In the meantime, mechanistically more detailed systems have been considered. These include the variation of the rate constants involved in the chemical reactions [16,17] and boundary conditions [17], as well as the number and length of legs [18]. Samii *et al.* [17] investigated the spiders' stepping gait and considered inchworm as well as hand-over-hand spiders. Semenov *et al.* [16] showed that spiders experience a rather extended time period of superdiffusion given that the cleavage rate r is small. More complex spiders in quasi-one [19] and in two dimensions [20] have also been studied. Moreover, there have been studies focusing on mathematical aspects such as recurrence, transience, and ergodicity [21,22], as well as random environments [23,24]. These investigations have examined molecular spiders independently from their chemical motivation as a general class of multivalent random walkers [19].

The rich variety and diversity of these recent studies show that molecular spiders are a versatile system to study artificial molecular motors both theoretically as well as experimentally. However, many challenges still remain in improving their efficiency and tailoring the spiders' design for possible biotechnological applications [7].

In this study, we examine dynamic and stochastic properties of a molecular spider team design: n molecular spiders are constrained due to their joint attachment to a single linking

*frey@lmu.de

node which may be considered as a primitive model of a cargo. The resulting spider-spider interactions lead to collective effects which enhance the motor properties of the n -spider team. We show that spider teams are faster and move more persistently along their track than individual spiders. We also predict that the spider teams move at reduced randomness and thus are candidates for applications that require reliable, i.e., predictable motion [4].

This paper is organized as follows: In Sec. II we provide a detailed picture of how molecular spiders function and give a comprehensive introduction to the existing theoretical models before we define an n -spider team. Subsequently, in Sec. III A we present our main results: spider teams have enhanced motor properties. To explain these numerical observations, we present a comprehensive analysis of the stochastic dynamics of a spider team. In particular, we perform a reduction of the state space of the spider teams and thereby calculate the mean number of consecutive directed steps a spider team performs while attached to the substrate boundary (Sec. III B). Moreover, we explore the validity of the resulting network representation of the spider team dynamics and also show how it breaks down (Sec. III C). In addition to this approach, we provide an exact mapping of the n -spider team to an n -dimensional confined random walk (Sec. III D). This enables us to quantify the diffusion coefficient which describes the motion of a spider team during diffusive periods (Sec. III E). Finally, in Sec. IV we bridge theoretical and experimental observables and predict the existence of optimal parameters which maximize the spider teams' predictability. Finally (Sec. V), we conclude and identify connections to related fields.

II. MODEL DEFINITION

Our model is based on the theoretical description of molecular spiders introduced by Antal *et al.* [11] and Antal and Krapivsky [12] that was motivated by experiments of Pei *et al.* [9]. They propose a spider design that consists of a central body and l legs that are attached to it. Each leg has a certain length and thus the overall spider can span a maximal distance s . In the experiment, a spider is exposed to a (one-dimensional) lattice, to which a substrate is attached. Since binding of leg and substrate happens through the Watson-Crick mechanism [25], only one leg may bind to a lattice site at a time. In the model, this corresponds to an exclusion process in that the movement of one spider leg is constrained by the spider's remaining legs. The lattice prevails in two states: with and without substrate. Legs which bind to lattice sites with substrate can remove it (chemically: they cleave it, only a shorter part remains bound to the lattice), which happens along with unbinding from that site at rate r . By contrast, spiders unbind from sites without substrate (i.e., from product sites) at rate 1. In the model, a substrate is *always* cleaved when a leg steps away from it, and rebinding of a leg to a new lattice site happens instantaneously. Two different rules to rebind to a new lattice site have to be distinguished: Spiders' legs either have a certain ordering, i.e., they cannot "overtake" each other; these spiders are termed *inchworm* spiders [11,12,16]. Alternatively, spider legs have no ordering, i.e., they can step over each other; those spiders have been called "quick spiders" [11] or "hand-over-hand"

spiders [17,18] in previous studies. Both types of spiders show quite different behavior [18] and have to be well distinguished. In this paper, we will concentrate on inchworm spiders.

In our model a leg which has just unbound from the lattice rebinds to the lattice instantaneously. Furthermore, we allow a spider's leg to rebind to any lattice site as long as the new leg configuration does not violate any of the restrictions imposed by the leg length or the ordering of the legs (in particular, this implies that rebinding to the lattice site from which the leg just unbound is possible [26]); this can be motivated from experiments where the typical time scales for binding to substrates exceed those for diffusion by orders of magnitude [17]. In addition, our choice obviates unphysical situations that might occur for spider teams due to the complete blockage of a leg.

Hollow circles (\circ) denote unoccupied lattice sites and filled circles (\bullet) indicate that a leg is attached to that site. The presence of substrate is marked with a hat, i.e., $\hat{\bullet}$ or $\hat{\circ}$. Throughout this paper, we consider bipedal spiders (i.e., $l = 2$) with a maximal leg span of $s = 2$. Spiders may thus only arise in either the spanned ($\bullet\circ\bullet$) or the relaxed ($\bullet\bullet$) configuration. For this case, the geometry of the cleaved sites, which is usually called *product sea*, is an interval on the one-dimensional lattice; it gives rise to memory effects which stem from irreversible substrate cleavage [11].

Samii *et al.* [18] suggested that the lattice could be prepared with substrates on the right, and products on the left-hand side from the very beginning, and called this initial condition *P-S lattice*. This asymmetry makes some calculations easier, and it provides a symmetry breaking direction already at the beginning of the dynamics. We are going to use this kind of lattice throughout the paper.

Taken together, the spiders which we examine in this study are bipedal ($l = 2$) inchworm spiders with a maximal span of $s = 2$, which walk on a one-dimensional P-S lattice. Every spider's leg may rebind to any accessible lattice site as long as the ordering is preserved, including the site from where it just unbound.

Based on this model for molecular spiders, we propose a minimal model for a team of molecular spiders. Several, say n , molecular spiders are linked to a (virtual) cargo with an inelastic leash (i.e., a string; sometimes this is also called cable [27]) of a well-defined length. Each of these spiders runs on its own one-dimensional track. This is similar to biological molecular motors like kinesin-1 [28,29] that walk along one-dimensional microtubule filaments [1]. We call these ensembles of spiders that jointly pull a cargo a spider team. For a cartoon of a team of two spiders, see Fig. 1(a).

Note that the role of the "cargo" is not primarily to put load on the spiders; actually we set the mass of the cargo equal to zero. In contrast, the cargo mediates the interaction among the n spiders comprising the team: Since the strings used for linking the spiders to the cargo are inelastic with some length a , any two of the spiders' bodies may mostly be $2a$ away from each other. From the bodies, the furthestmost reachable lattice site is given by the spiders' legs' length, call it b , so that the *maximal* distance between the leftmost and the rightmost leg of all the spiders in the team is given by $2(a + b) =: d$. Mathematically, letting λ_i (ρ_i) denote the position of the i th

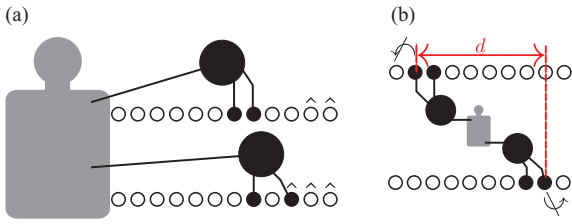


FIG. 1. (Color online) Cartoon of the spider team model and definition of the leash length d . (a) Two spiders are attached to a joint cargo with an inelastic string. Both spiders walk on their respective one-dimensional track. Hats indicate the presence of substrate. (b) The finite length of the linking string induces a maximal distance between the spiders' bodies which gives rise to a maximal span of the spider team, characterized by the "leash length" d .

spider's left (right) leg, this restriction reads

$$|\rho_i - \lambda_j| \leq d \quad \forall i, j. \quad (1)$$

Note that this is a global constraint which restricts the spider team, in contrast to the local constraint limiting the span of an individual spider,

$$|\rho_i - \lambda_i| \leq s \equiv 2 \quad \forall i. \quad (2)$$

The definition of d is visualized for a two-spider team in Fig. 1(b). For simplicity of language, and to capture an intuitive understanding especially for two-spider teams, we will call d the *leash length* in the following.

III. RESULTS

A. Enhanced properties of n -spider teams

We performed extensive numerical simulations to characterize the dynamic properties of n -spider teams. Our simulation data show that the constraint arising through the leash that holds the spider team together induces collective effects among the n spiders. We find that the incorporation of a spider into a team enhances many of the motor properties: The mean traveled distance of a spider team exceeds that of single spiders by far, up to orders of magnitude, for a rather small cleavage rate $r = 0.01$ [see Figs. 2(a) and 2(b)]. In addition, a spider team's movement is a lot more "predictable." This can be inferred from the width of the probability distributions, see Fig. 2(a), and the shaded areas depicted in Fig. 2(b), which illustrate the standard deviation of the mean displacement.

Another important quantity is the mean square displacement (MSD) of the spider teams [see Fig. 2(c)]. It shows a steep increase at intermediate time scales, similar but stronger and longer lasting compared to recent results by Semenov *et al.* [16] for single spiders: In this regime spiders move superdiffusively. To quantify the time-dependent effects of superdiffusion, we evaluated the "slope" of the variance in a double logarithmic scaling, i.e., the effective exponent

$$\alpha(t) = \frac{d \log \langle [x(t) - \langle x(t) \rangle]^2 \rangle}{d \log t}, \quad (3)$$

which provides a measure for diffusivity (see also Refs. [16,19,30]). Figure 2(d) shows $\alpha(t)$ for a single spider and several different spider teams. Remarkably, the four-spider team travels almost ballistically ($\alpha \approx 2$) for rather

long times and the periods of "instantaneous superdiffusion" of spider teams (i.e., times with $\alpha > 1.1$ [16]) last much longer compared to single spiders. The nontrivial shape of $\alpha(t)$ indicates the multitude of dynamic processes that are involved in the spider team's dynamics: Initially, $\alpha \approx 1$ for $t \lesssim 1$ for all configurations, reflecting the very first hop of the spiders' left legs. In succession, until $t \lesssim r^{-1} = 100$, the spiders' right legs have typically not yet cleaved a substrate, whereas the left legs jump back and forth, hence the variance is approximately constant and thus $\alpha < 1$ (for these two regimes, see also a more explicit discussion in Ref. [16]). Had we chosen other starting conditions for the spiders, the behavior at short time would look different. Likewise, also the following regime until $t \lesssim 10^2 \dots 10^3$ results from the fixed starting conditions: While at early times the spider team does not feel the leash and all spiders can move independently from each other, at some point the leash is fully spanned and the spiders at the most extreme position (i.e., those contributing most to the variance) are retarded. This leads to a transient decrease of α . This regime is unique to spider teams since it is an effect constituted by the leash. Finally, for large times $t \gtrsim 10^2 \dots 10^3$, the memory of initial conditions is lost and α becomes maximal. Clearly, the maximal value of α is greatest for $n = 4$ of the displayed configuration. As time increases further, α decreases slowly which is due to the fact that more and more spiders move away from the product-substrate boundary (see also Ref. [16]). Figure 2(e) shows the velocity of the spider team by means of the derivative of the mean displacement with respect to time. Clearly, the velocity of a four-spider team outperforms that of a single spider by more than one order of magnitude.

These pronounced effects are in a way surprising: At first sight, one might speculate that the coupling leash which imposes an additional constraint on the spiders would handicap the spider team's motion and make it slower. This is clearly not the case. To the contrary, the dynamic properties of the spider teams are enhanced. In the remainder of this section we will explain this behavior using analytical arguments.

B. Boundary periods

a. Single spiders. Key to the understanding of an individual molecular spider's motion is to unravel the mechanism for biased motion. To this end we distinguish between two qualitatively different dynamic states of the spiders: Looking at single trajectories of molecular spiders we find that there are periods of time in which the spider's motion is strongly directed, and other periods with undirected, diffusive motion [see Fig. 2(f)]. In the following, we will call these dynamic states *boundary periods* and *diffusive periods*, respectively. To define the notion of these periods, it is convenient to distinguish between the steps of the spider's legs and the step of the spider as a whole. We define a *spider step* as a transition from a spread configuration ($\circ \bullet \bullet \circ$) to another spread configuration shifted by one lattice unit forwards or backwards, i.e., $\circ \bullet \bullet \circ$ or $\bullet \bullet \circ \circ$, irrespective of the sites being products or substrates. During a diffusive period all the spider's legs are attached to product sites and therefore the spider steps with equal probability in both directions [11]. In contrast, biased spider motion can emerge in the vicinity of the boundary between product and substrate sites. We define a boundary

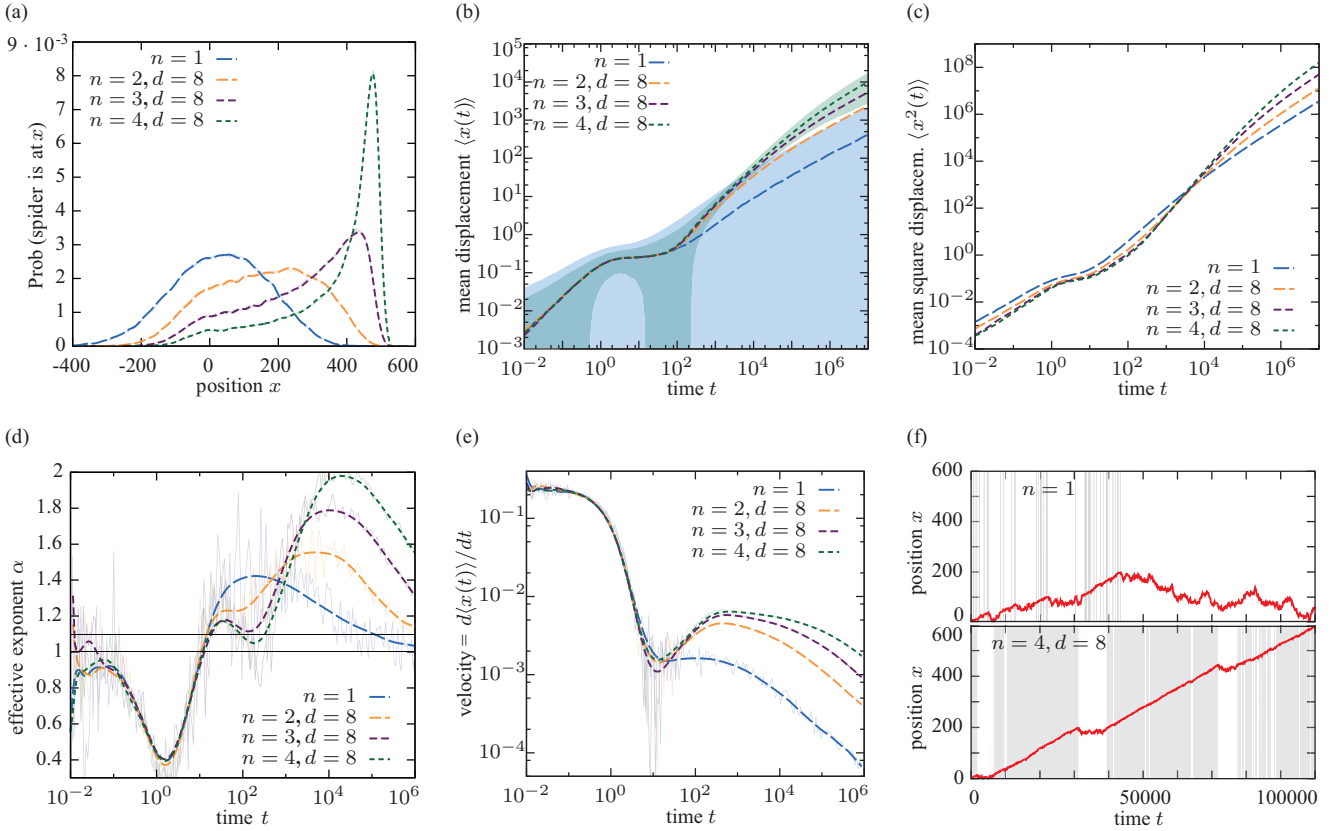


FIG. 2. (Color online) Dynamic properties of spider teams. Positions are given in lattice units throughout this work; time is defined by setting the hopping rate from products to 1. Thin shaded lines show data from finite difference approximations; thick lines show smoothing Bezier curves. (a) Probability distributions (histograms) of spiders to be at position x at time $t = 10^6$; simulation data were binned with a box size 1. Depicted are distributions for a single spider ($n = 1$) and spider teams comprised of $n = 2, 3, 4$ spiders and leash length $d = 8$, and cleavage rate $r = 0.01$. While the single spider distribution follows nearly a Gaussian centered close to the origin, the distributions of spider teams are clearly skewed and shifted towards larger x . The asymmetry stems from the P-S preparation of the lattice at $t = 0$ (products at the left, substrates at the right) [17]. (b) Mean displacement as a function of time (lines). The shaded areas represent the standard deviation around the mean displacement for a single spider and the four-spider team, respectively, and provide a measure for the randomness of the spiders' motion. Note that the *visual* impression of the standard deviation is rather that of a relative deviation, since the plot is in double logarithmic scale. (c) MSD as a function of time, $\langle x^2(t) \rangle$. (d) The variance's effective exponent $\alpha(t)$ [see Eq. (3)]. For diffusion, $\langle [x(t) - \langle x(t) \rangle]^2 \rangle \propto t^1$, hence $\alpha = 1$; superdiffusion corresponds to $\alpha > 1.1$ [16], and ballistic motion to $\alpha = 2$. The superdiffusive regime of spider teams lasts longer than that of single spiders; large spider teams reach nearly ballistic motion for significantly long times. For a more detailed discussion, see the main text. (e) Mean velocity of the spiders as a function of time. The mean velocity is defined as the time derivative of the mean displacement, $d\langle x(t) \rangle/dt$. Spider teams outperform single spiders by an order of magnitude. (f) Sample trajectory of a single spider (top), and a four-spider team with $d = 8$ (bottom). Periods in which the spider (team) is in the vicinity of the product-substrate boundary are shaded.

period as follows: It starts with a spread configuration where the right spider leg is attached to a substrate ($\cdots \circ \bullet \circ \bullet \hat{\circ} \cdots$), and ends when the spider has fully stepped away from the substrate boundary ($\cdots \bullet \circ \bullet \hat{\circ} \cdots$) (the dots indicate that the block of displayed lattice sites may have been shifted during the boundary period), as illustrated in Fig. 3(a). As a consequence, during a boundary period the substrate boundary is shifted by an integer number of lattice units forward.

For single spiders the bias can be measured by calculating the *first passage probability*, p_+ , for the spider to progress one step forward during a boundary period, i.e., $p_+ = \text{Prob}\{\bullet \circ \bullet \hat{\circ} \not\rightarrow \bullet \circ \bullet \hat{\circ} \rightarrow \circ \bullet \circ \hat{\circ}\}$ [see also Fig. 3(a) for an illustration of the corresponding dynamic processes]. By analyzing all possible sequences of transitions, Antal and Krapivsky found an explicit expression for the bias, namely, $p_+(r) = \frac{5+r}{8+4r}$ [12], valid for spiders with legs always jumping

to *neighboring* sites. Similar calculations can be performed for spiders whose legs may also rebind to the *same* site again (like those we consider throughout this paper), leading to $\tilde{p}_+(r) = \frac{5+3r}{8+8r}$. The mathematical expressions for p_+ and \tilde{p}_+ differ only slightly; in particular, they are equal in the limits $\lim_{r \rightarrow 0} \tilde{p}_+(r) = \lim_{r \rightarrow 0} p_+(r) = \frac{5}{8}$ and $\tilde{p}_+(r = 1) = p_+(r = 1) = \frac{1}{2}$ [31].

There is a special feature of single spiders which makes the definition of p_+ straightforward in this case: The spread configuration $\bullet \circ \bullet$ of the spider's legs is unique, since a spider step to the right corresponds to a translation of both legs to the right, and hence the configuration before and after a step is the same [cf. Fig. 3(a) states (i), (iii), and (vii)]. As we will show below, this is a property which unfortunately does not extend to spider teams.

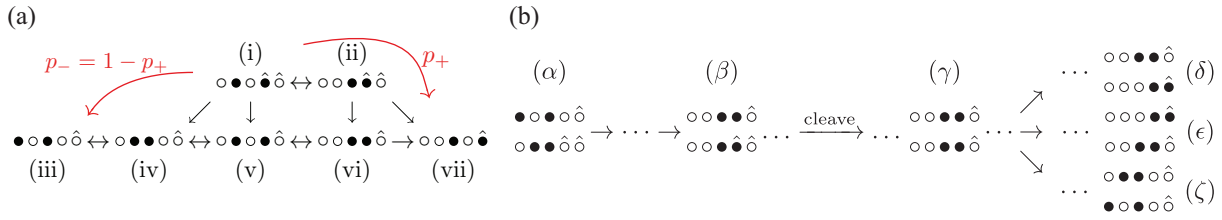


FIG. 3. (Color online) Definition of a boundary period. (a) Path of a single spider through a boundary period. The period *always* starts in state (i). From there, the spider can change to (ii), and back. When the right leg cleaves the substrate, the spider arrives at (iv), (v), (vi), or (vii). Arriving at (vii) corresponds to continuing the same boundary period from a new substrate [with “(vii) being the new (i)”], since (vii) and (i) are equivalent up to translation. Hence, the number of steps is raised by one upon arriving at (vii). If, by contrast, the spider reaches (iii), the boundary period ends and a diffusive period begins. The probability to make a successful step, i.e., to reach (vii) before (iii), is the bias p_+ calculated by Antal and Krapivsky [12]. The number of steps during a boundary period is then the number of transitions (i) \rightarrow (vii), without reaching (iii) in between. This is equivalent to the number of cleavages during a boundary period, not counting the very last cleavage (which is not counted since by definition the spider steps away from the boundary after the last cleavage, and we only count forward steps). (b) Example of a boundary period of a two-spider team. (α) None of the spiders is in a boundary period, hence none of them experiences a bias. Thus, the spider *team* is in a diffusive period. When the lower spider reaches a substrate (β) it enters a boundary period. Thus, also the spider *team* enters a boundary period. In succession, the lower spider’s right leg happens to cleave the substrate (γ). The lower spider can then find its way to a new substrate (δ) what constitutes a $\frac{1}{2}$ successful step for the spider team and preserves the boundary period. If the upper spider, in this case, steps to a substrate (ϵ), this does not yet, however, constitute a step. This is because although the spider team is in a boundary period, the *upper* spider has not been in a boundary period itself during this team’s boundary period. Since a step essentially reflects a cleavage, no step can be integrated in this case. If the lower spider steps away from the new substrate (ζ), the spider team enters a diffusive period. In analogy to single spiders, the number of steps during a spider team’s boundary period is equivalent to the number of cleavages during that period, divided by the number of spiders, and not counting each spider’s *last* cleavage event.

A quantity which does not require this uniqueness is the mean number of consecutive directed steps that a spider performs during one boundary period. This quantity will be denoted $\langle S \rangle$ in the following. With

$$p_j = (p_+)^j (1 - p_+) \quad (4)$$

being the probability that the spider walks precisely j steps during a boundary period, before it leaves the boundary and enters a diffusive period, $\langle S \rangle$ can be calculated as

$$\langle S(p_+) \rangle = \sum_{j=0}^{\infty} j p_j = \frac{p_+}{1 - p_+} \quad (5)$$

for single spiders. Let us emphasize that $\langle S \rangle$ is different from the mean “number of steps the spider makes in the B state” [16], $\langle S_B \rangle$, as defined by Semenov *et al.*, which counts the number of leg movements (“leg steps” in our terminology). By contrast, $\langle S \rangle$ only counts a step if *both* legs have been shifted to the right without having moved to the left (“spider steps”), i.e., the number of times the spider consecutively reaches (vii) before (iii), starting from (i) in Fig. 3(a).

The number of consecutive spider steps, $\langle S \rangle$, is equivalent to the number of cleavage events during a boundary period. Not counted is the last cleavage before the spider leaves the boundary period, since this corresponds to a backward step of the spider [cf. Eq. (4)].

b. Spider teams. Clearly, the motion of a single spider is biased only during boundary periods, and undirected during diffusive periods. However, it is manifest that a spider *team*’s motion is not completely diffusive as long as *any of the spiders comprising the team* is in a boundary period. Hence, we consider the spider *team* being in a boundary period if at least one of its spiders resides in a boundary period. In order to compare the performance of individual spiders with that of

spider teams, it is now essential to find a way how to count the number of a spider team’s steps during a boundary period. Basically, a team moves forward by one step if the boundary between substrate and product sites is shifted forward by one lattice unit on average. To this end we count every cleavage event but for each spider’s last cleavage before the *team* leaves the boundary period. In analogy to a single spider, the latter avoids counting those events where the spider team moves away from the boundary and thereby steps backward [cf. Fig. 3(b)]. The number of steps of a spider team is then given by the number of such cleavage events divided by the number of spiders in a team, in accord with fractional steps of molecular motors like kinesin [32]. For example,



corresponds to two steps of the lower spider and thus one step for the spider team.

As we consider two or more coupled spiders, the translational symmetry of the state before and after a complete step ($\bullet \circ \hat{\circ} \hat{\circ}$ and $\circ \bullet \hat{\circ}$, respectively, for a single spider) is broken, likewise the uniqueness of the state which is the first during a boundary period ($\bullet \circ \hat{\circ}$ for a single spider), is lost. For example,



all are possible states at the beginning of a boundary period. It is therefore no longer possible to calculate the probability to step to the right (denoted p_+ for single spiders) without further specification of these initial states. For spider teams the probability for a forward step explicitly depends on the particular state from which it starts.

This complexity prohibits an analytic treatment of the stochastic dynamics in general. However, if the relative rate of substrate cleavage is small compared to the rate of hopping from product sites, i.e., $r \ll 1$, the dynamics become amenable to a theoretical analysis. While in this limit the motion of the boundary between substrate and product sites is slow, the dynamics of spider legs bound to product sites are fast. This suggests to group states into classes characterized by the slow variable, i.e., the distance between the ends of the product seas, denoted by Δ . In addition, it turns out to be convenient to introduce subclasses according to the number of spiders attached to substrates, σ . In the following we will illustrate this for teams comprised of $n = 2$ spiders and a leash length $d = 2$. All states

$$\begin{array}{cccc} \circ \bullet \circ \hat{\circ} \hat{\circ} & \sim & \circ \circ \bullet \bullet \hat{\circ} \hat{\circ} & \sim & \circ \bullet \circ \hat{\circ} \hat{\circ} & \sim & \circ \circ \bullet \hat{\circ} \hat{\circ} \\ \circ \bullet \circ \hat{\circ} \hat{\circ} & \sim & \circ \bullet \circ \hat{\circ} \hat{\circ} & \sim & \circ \circ \bullet \hat{\circ} \hat{\circ} & \sim & \circ \circ \bullet \hat{\circ} \hat{\circ} \end{array} \quad (8)$$

comprise the class

$$\left[\begin{array}{c} \circ \bullet \circ \hat{\circ} \hat{\circ} \\ \circ \bullet \circ \hat{\circ} \hat{\circ} \end{array} \right] =: [0_2] = [\Delta_\sigma]. \quad (9)$$

Likewise, configurations with $\Delta = 0$ and $\sigma = 1$, i.e., with only one spider having a leg at the boundary, are possible:

$$\left[\begin{array}{c} \circ \bullet \circ \hat{\circ} \hat{\circ} \\ \circ \bullet \bullet \hat{\circ} \hat{\circ} \end{array} \right] =: [0_1]. \quad (10)$$

Here, we made use of the invariance under renumbering of spiders, it is irrelevant if we label the ‘‘upper’’ spider as 1 and the ‘‘lower’’ as 2, or the other way round. Hence, irrespective of whether the lower or the upper spider’s leg is bound to a substrate, both contribute to class $[0_1]$. That same renumbering symmetry can also be applied when one considers states where the lower and the upper product seas do not end at the same position. This leads to the classes

$$\left[\begin{array}{c} \circ \bullet \circ \hat{\circ} \hat{\circ} \\ \circ \bullet \bullet \hat{\circ} \hat{\circ} \end{array} \right] =: [1_2] \quad \text{and} \quad \left[\begin{array}{c} \circ \bullet \bullet \hat{\circ} \hat{\circ} \\ \circ \bullet \bullet \hat{\circ} \hat{\circ} \end{array} \right] =: [1_1], \quad (11)$$

as well as

$$\left[\begin{array}{c} \circ \circ \bullet \bullet \hat{\circ} \hat{\circ} \\ \circ \bullet \hat{\circ} \hat{\circ} \end{array} \right] =: [2_1]. \quad (12)$$

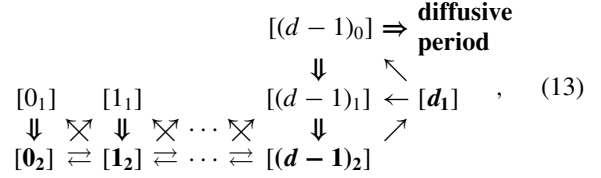
This completes the list of possible classes with $\sigma \neq 0$ since the constraint $d = 2$ imposed by the leash forbids class $[2_2]$, as well as classes $[\Delta_\sigma]$ with $\Delta > 2$. For general d , class $[d_2]$ and classes with $\Delta > d$ are not allowed.

One can show that the classification of states by means of the distance of the product seas’ ends and the number of spiders at the boundary is reflexive, symmetric, and transitive, and hence defines an equivalence relation. Therefore, we tentatively used the symbols \sim and $[\cdot]$ in the previous equations.

Instead of a large number of ‘‘micro’’ states, we are now left with only five equivalence classes which include all the spider states at the boundary. The reduction of complexity can be pushed even further: classes $[\Delta_1]$ with only one leg attached to the substrate are only transient in the sense that they will always decay into classes with two legs attached $[\Delta_2]$ (as long as $\Delta < d$). Consider, for example, a spider team in class $[0_1]$ where one spider’s right leg is attached to a substrate while the other spider’s legs are free to move on product sites. Since the diffusion time of legs on products is small compared

to the expected residence time $1/r$ of the leg on the substrate, the transition $[0_1] \rightarrow [0_2]$ is almost certain and happens on a time scale ~ 1 (fast compared to substrate cleavage).

All possible transitions between the classes can be visualized as the following reaction scheme:



where Δ is constant along a column and σ along a row, respectively. As explained above, vertical transitions from $[\Delta_1]$ to $[\Delta_2]$ are fast [emphasized with double arrows in Eq. (13)]. In contrast, horizontal and diagonal transitions involving substrate cleaving events and hence leading to $\Delta \rightarrow \Delta \pm 1$ are slow. Since vertical transitions occur with certainty and fast, we can eliminate the transient classes $[\Delta_1]$ and reduce to a reaction scheme for the most stable subclass of each class, shown in boldface in Eq. (13) and signified $[\Delta]$ in the following:

$$[0] \xrightleftharpoons[\frac{1}{2}]{\frac{1}{2}} [1] \xrightleftharpoons[\frac{1}{2}]{\frac{1}{2}} \dots \xrightleftharpoons[\frac{1}{2}]{\frac{1}{2}} [d-1] \xrightleftharpoons[\Pi]{\frac{1}{2}} [d] \xrightarrow{1-\Pi} \text{diffusive period} \quad (14)$$

The numbers above and below the arrows are transition probabilities into the respective classes, reflecting that each of the two spiders may cleave a substrate with equal probability for $\Delta < d$. The class $[d]$ has to be treated separately as it constitutes a gate from the boundary into the diffusive period.

Our next set of tasks is now threefold: First, in order for our classification scheme to be a consistent reduction of the stochastic processes, all states comprising the gate class $[d] = [d_1]$ should have the same *survival probability* Π , i.e., the same probability not to exit into a diffusive period. This is indeed the case for sufficiently small cleavage rates r : In the limit $r \rightarrow 0$, substrate cleavage events are rare compared to hopping from product sites. Therefore, the dynamics exhibit a time scale separation where all the legs attached to products quickly visit any accessible lattice site while the legs on substrate sites remain stuck. In other words, the dynamics within class $[d_1]$ are ergodic and equilibrate, and all micro states effectively reduce to one coarse-grained ‘‘macro’’ state, namely, the class $[d_1]$. Second, we have to calculate the survival probability Π by analyzing all the various routes between the micro states. Third, in order to determine the mean number of consecutive steps $\langle S \rangle$, the reduced reaction scheme of Eq. (14) has to be solved.

We now address the calculation of the survival probability Π . In principle, this can be done for arbitrary complex spider teams. For the purpose of illustration, we continue the example from above with two spiders and a leash length $d = 2$. We consider all states comprising class $[2_1]$. These are

$$\begin{array}{lll} \textcircled{1} = \begin{array}{c} \circ \circ \bullet \bullet \hat{\circ} \\ \circ \bullet \hat{\circ} \hat{\circ} \end{array}, & \textcircled{2} = \begin{array}{c} \circ \circ \bullet \bullet \hat{\circ} \\ \circ \bullet \hat{\circ} \hat{\circ} \end{array}, & \textcircled{3} = \begin{array}{c} \circ \bullet \bullet \circ \hat{\circ} \\ \circ \bullet \hat{\circ} \hat{\circ} \end{array}, \\ \textcircled{4} = \begin{array}{c} \bullet \circ \bullet \circ \hat{\circ} \\ \circ \bullet \hat{\circ} \hat{\circ} \end{array}, & \textcircled{5} = \begin{array}{c} \bullet \circ \bullet \circ \hat{\circ} \\ \circ \bullet \hat{\circ} \hat{\circ} \end{array}, & \textcircled{6} = \begin{array}{c} \circ \bullet \bullet \circ \hat{\circ} \\ \bullet \circ \hat{\circ} \hat{\circ} \end{array}, \\ \textcircled{7} = \begin{array}{c} \bullet \circ \bullet \circ \hat{\circ} \\ \bullet \circ \hat{\circ} \hat{\circ} \end{array}, & \textcircled{8} = \begin{array}{c} \bullet \circ \bullet \circ \hat{\circ} \\ \bullet \circ \hat{\circ} \hat{\circ} \end{array}, & \end{array} \quad (15)$$

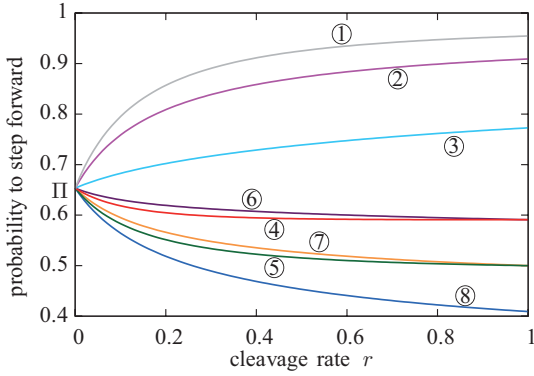


FIG. 4. (Color online) Justification for the equivalence classes in the limit $r \rightarrow 0$. Shown are the analytically calculated probabilities that a spider team ($n = d = 2$) successfully completes one step during a boundary period, starting from the specific states ①–⑧ as given in Eq. (15). Each line corresponds to a state of the equivalence class $[2_1]$ [cf. Eq. (12)]. In the limit $r \rightarrow 0$, the probability to step forward for all eight states collapses to a fixed value $\Pi \approx 0.65$.

and their respective “mirrored” states, i.e., the states with spiders 1 and 2 interchanged. Let us illustrate the calculation for the particular initial state ①. Legs unbind from products at rate 1 and from substrates with rate r . Hence, from this configuration, the probability that the upper right, or the lower right leg is the first one to unbind is $1/(3+r)$ and $r/(3+r)$, respectively. The left legs unbind first with probability $1/(3+r)$ each. If now, for instance, the lower right leg detaches, it may either reattach to the very same lattice site again, or it may step one site to the right. In either case it cleaves a substrate. Both processes happen with equal probability. Hence, altogether, the transition probability for the lower right leg to step to the right is given by $r/2(3+r)$. The analysis can be continued from the resulting states until either a step is completed or the team has left the boundary period, finally leading to a high dimensional system of linear equations. The results obtained by solving the ensuing sets of equations are shown in Fig. 4 for all initial states comprising class $[d_1]$.

Clearly, as r approaches 0, all survival probabilities, i.e., all probabilities to make a step within the team’s boundary period, approach a single value

$$\Pi = \frac{115}{176} \approx 0.65. \quad (16)$$

This result is reassuring, as it confirms our heuristic arguments on the equilibration of states within class $[d_1]$, and thereby justifies combining several different states into one class in the limit $r \rightarrow 0$.

All the complexity of calculating the mean number of steps $\langle S \rangle$ of a spider team during a boundary period has now been reduced to analyzing the various routes between the *equivalence classes*. Since each transition [33] in Eq. (14) corresponds to a directed step done during a boundary period, the number of these steps $\langle S \rangle$ is equivalent to the number of (undirected) jumps performed by a simple random walker with reflective and absorbing boundary conditions on the left, and right ends of the reaction scheme, respectively. As detailed in the Appendix, the general solution for the mean number of

TABLE I. Comparison of analytic and simulation results for the mean number of steps during a boundary period, $\langle S \rangle$. Analytic values were derived in the limit $r \rightarrow 0$; simulation results were obtained for very small $r \lesssim 10^{-4}$. Simulations and analytical calculations show excellent agreement.

	$\langle S(r \rightarrow 0)_d^n \rangle$, analytic	$\langle S(r \lesssim 10^{-4})_d^n \rangle$, simulation
$n = 1$	$\frac{5}{3} \approx 1.6667$	1.6672 ± 0.0015
$n = 2, d = 2$	$\frac{291}{61} \approx 4.770$	4.769 ± 0.003
$n = 2, d = 3$	$\frac{3170931}{443341} \approx 7.152$	7.146 ± 0.005
$n = 2, d = 4$	$\frac{4055316673}{414459263} \approx 9.785$	9.785 ± 0.008
$n = 3, d = 2$	$\frac{340881}{48391} \approx 7.044$	7.042 ± 0.006
$n = 3, d = 3$	$\frac{16.3745\dots}{1.34258\dots} \approx 12.196$	12.204 ± 0.012

steps during a boundary period in the limit $r \rightarrow 0$, and for arbitrary d , reads

$$\langle S(d, r \rightarrow 0) \rangle = \frac{\Pi}{1 - \Pi} + (d - 1) \frac{1}{1 - \Pi}. \quad (17)$$

For our example of a two-spider team with $d = 2$, we obtain, using Eq. (16),

$$\langle S(r \rightarrow 0)_{d=2}^{n=2} \rangle = \frac{291}{61} \approx 4.77. \quad (18)$$

We also analyzed more complex spider teams with size $n = 2, 3$ and up to a leash length of $d = 4$, and found even larger mean step numbers, compared to $\frac{5}{3}$ for a single spider. Obviously, during boundary periods even the simplest spider teams behave significantly more directed and progress a lot further on average, compared to individual spiders. This result is remarkable since directed motion is desirable for applications and a rare feature at the nanoscale. The analytical results are summarized in Table I where they are also compared with Monte Carlo simulations which match them at a very high accuracy.

C. Validity of the equivalence classes

With increasing d , the spiders forming a team become more and more independent since it is increasingly unlikely that a spider “feels” the constraint of its teammates. In particular, the probability Π that a spider in class $[d_1]$ reaches $[(d - 1)_2]$ without exiting the boundary period [cf. Eq. (14)], converges towards the probability p_+ that a single spider makes a step to the right which is $\frac{5}{8}$ for $r \rightarrow 0$. Hence, assuming $\Pi = \frac{5}{8}$ for large d , Eq. (17) would imply that the mean number of steps increases linearly with d . Indeed, in the asymptotic limit $r \rightarrow 0$ this agrees well with the simulation data. However, with increasing r deviations from this linear behavior become more and more significant (cf. Fig. 5).

This can be explained as follows: For increasing leash length d , the configuration space accessible to the spider team becomes progressively larger, so that it takes longer to completely exploit it, i.e., the *equilibration time* grows. Conversely, the average time of substrate cleavage scales as $1/r$. With increasing r and/or d these two time scales become comparable. The assumption of time scale separation, on which the reduction of the dynamics to equivalence classes was based, then becomes invalid. In conclusion, the equivalence class concept which we derived in the previous sections provides a very good approximation for small but finite

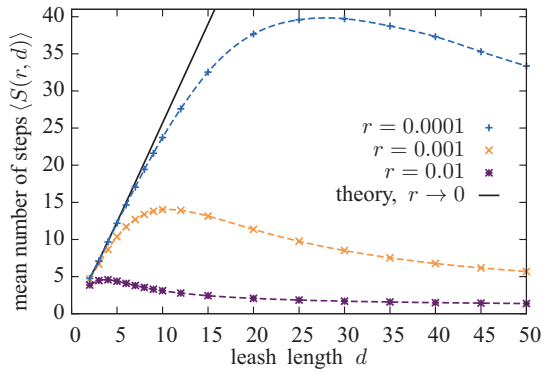


FIG. 5. (Color online) Validity of the equivalence class formalism. Shown are the simulation results for the mean number of steps (S) for a two-spider team and different values of d and cleavage rates $r = 0.0001, 0.001, 0.01$; broken lines are a guide to the eye. The theoretical result derived within the equivalence class formalism for $r \rightarrow 0$ (black) is exact for $d = 2, 3, 4$ (Table I), and we assumed $\Pi = \frac{5}{8}$ for $d \geq 5$ [Eq. (17)].

substrate cleavage rates r , as long as the leash length d is not too large.

D. An exact mapping to a confined random walker

For a bipedal spider with a maximal span of $s = 2$, a single coordinate, the “center of mass” coordinate, fully describes the position of the spider’s legs. Hence, it is possible to map the motion of the single spider’s legs on $\frac{1}{2}\mathbb{Z}$, the set of integers and half-integers, with hopping of the legs corresponding to changes of the center of mass [11,12]. This mapping can be

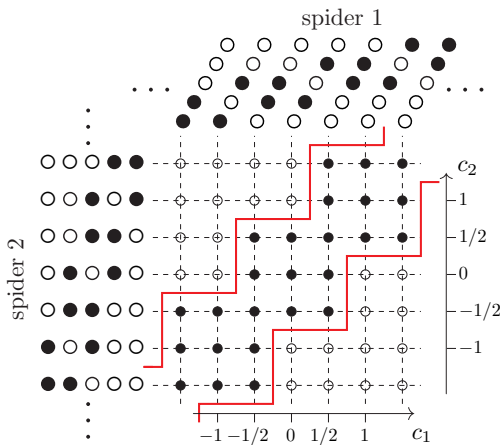


FIG. 6. (Color online) A spider team can be mapped to a random walk in a confined environment: Transitions of a spider’s leg correspond to a change of its center-of-mass coordinate c_i of $\pm \frac{1}{2}$. Shown is the mapping of a two-spider team with a leash length $d = 2$. The shape of the environment (solid) follows from the leash constraint which confines the span of the spider team. From $d = 2$ follows that the leftmost left and the rightmost right legs of the two spiders may be at most two lattice sites apart. With that restriction, the allowed configurations of the team follow directly, as can be seen with some explicit configurations in the left and the top part of the figure.

extended for a spider team: The position of an n -spider team is characterized by a position on an n -dimensional square lattice where each of the n axes corresponds to the center of mass of one of the spiders comprising the team. The dynamics of a spider team then corresponds to a trajectory on that lattice. However, due to the leash constraint, not all sites on this lattice are accessible to the spider team. To illustrate this, let us for the moment focus on a two-spider team with leash length $d = 2$. Fixing the first spider’s center of mass c_1 , the other spider’s center of mass c_2 is restricted to be near c_1 due to the leash constraint. We have to distinguish between two cases. Spider 1 is either in a spread or a relaxed configuration, e.g., $c_1 = 0$ or $c_1 = \frac{1}{2}$, respectively. If it is in the spread configuration $c_1 = 0$, then the other spider may be in one of three configurations: $c_2 \in \{-\frac{1}{2}, 0, \frac{1}{2}\}$. For the relaxed configuration $c_1 = \frac{1}{2}$, there are five configurations possible for the second spider: $-\frac{1}{2}, 0, \frac{1}{2}, 1,$ and $\frac{3}{2}$. Geometrically, this leads to a staircase shape for the accessible set of states. For arbitrary d , the step width of this staircase generalizes to $4d - 3$ and $4d - 5$ (cf. Fig. 6).

While in Sec. III E this mapping will be employed to calculate diffusion constants during diffusive periods, we use it here to illustrate the concept of equivalence classes again. To this end, the mapping is generalized to incorporate substrates as illustrated in shaded colors in Fig. 7: Each substrate can be drawn as a box. This is seen as follows: Because each spider being at a specific substrate site may either be in a spread or

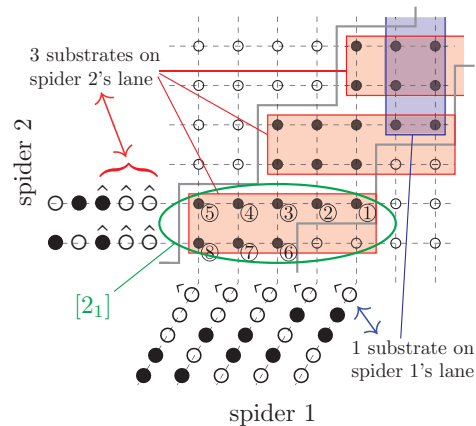


FIG. 7. (Color online) Substrate in the staircase random walker picture ($n = d = 2$ as before). Like in Fig. 6, explicit configurations are shown for some points. In addition, boxes are drawn which correspond to the substrates on spider 1’s (vertical blue box), or spider 2’s (horizontal red boxes) lane. This can be understood as follows: When a spider is attached to a substrate with its right leg, it can be either in the spread or the relaxed configuration. Hence a substrate at position c has to be indicated at *two* points in the center of mass space, namely, at $c - \frac{1}{2}$ and $c - 1$; therefore the substrate boxes have width 2. Encircled in the figure are the eight states which have spider 2 at $\bullet \circ \hat{\circ} \hat{\circ} \hat{\circ}$ or $\circ \circ \hat{\bullet} \hat{\circ} \hat{\circ}$, respectively, and spider 1 in one of the five states $\bullet \bullet \circ \circ \hat{\circ}, \dots, \circ \circ \bullet \bullet \hat{\circ}$. The resulting states correspond clearly to those of Eq. (15) and Fig. 4. In the figure, there are three horizontal red boxes (substrates on spider 2’s lane), and only one vertical blue box (substrate on lane 1). Hence, the difference of the product sea’s ends is $\Delta = 2$. Since the encircled states ①–⑧ have, by direct reading, *only* spider 2 at a substrate (i.e., they are only contained in $\sigma = 1$ box), they form the equivalence class $[\Delta_r] = [2_1]$.

a relaxed configuration, a substrate has to be indicated at *two* different locations in the center of mass space (thus the width of every box equals 2). Furthermore, since spider 1 being or not being at a substrate does not affect spider 2, every box indicating a substrate at spider 1's track has to be of a size that it contains all allowed configurations of spider 2, and vice versa.

We now return to an example discussed in Sec. III B: Equation (15) shows all configurations in which spider 1 has cleaved two more substrates than spider 2 and only spider 2 is attached to a substrate. We referred to this set of configurations as the equivalence class $[\Delta_\sigma] = [2_1]$. This situation is illustrated in Fig. 7, where there are $\Delta = 2$ more boxes (i.e., substrates) for spider 2 than for spider 1. The eight allowed configurations contained by the ellipse in this figure are only contained in *one* box ($\sigma = 1$), such that these states provide a geometrical interpretation of the equivalence class $[2_1]$. Leaving the boundary period in this picture corresponds to removing the encircled box (i.e., cleaving the substrate) and stepping down (i.e., away from the substrate boundary).

E. Diffusive periods

We now employ the mapping of the spider team motion to a confined random walk in order to analyze the spider team's dynamics during a diffusive period. Let us first examine the transition rates between neighboring points in the confined random walk picture. Consider, for example, the point

$$(c_1, c_2) = (0, 0) = \begin{array}{cc} \circ & \circ \\ \circ & \circ \end{array} \quad (19)$$

in Fig. 6. From this configuration, every *leg* may unbind from its product with rate 1, and then rebind to either the same product site again, or move to the allowed neighboring site at equal *probability* $\frac{1}{2}$. In the confined random walk picture, this leads to transition *rates* of $1 \times \frac{1}{2}$ along each connection between adjacent sites from $(0, 0)$. The same argument applies to any site within the allowed region, so that the transition rate between any two lattice sites equals $\frac{1}{2}$ [cf. Fig. 8(a)]. This leads to the following master equation for the occupation probability P_{c_1, c_2} on the confined lattice:

$$\frac{d}{dt} P_{c_1, c_2} = \sum_{\langle c_1, c_2 \rangle} \frac{1}{2} (P_{\langle c_1, c_2 \rangle} - P_{c_1, c_2}), \quad (20)$$

where the sum runs over all nearest neighbors $\langle c_1, c_2 \rangle$ of (c_1, c_2) . In order to calculate the diffusion coefficient $D = \frac{1}{2} \lim_{t \rightarrow \infty} \frac{d}{dt} \langle x^2(t) \rangle$ we determine the time derivative of the mean square displacement of the spider team:

$$\frac{d}{dt} \langle x^2(t) \rangle = \sum_{(c_1, c_2) \in \mathcal{C}} x_{c_1, c_2}^2 \sum_{\langle c_1, c_2 \rangle} \frac{1}{2} (P_{\langle c_1, c_2 \rangle} - P_{c_1, c_2}), \quad (21)$$

where $x_{c_1, c_2} = \frac{1}{2}(c_1 + c_2)$ is the position of the spider team on the molecular track for given values of c_1 and c_2 , and the summation extends over all (c_1, c_2) within the allowed region \mathcal{C} . This equation can be reorganized such that

$$\frac{d}{dt} \langle x^2(t) \rangle = \sum_{\mathcal{C}} P_{c_1, c_2} \sum_{\langle c_1, c_2 \rangle} \frac{1}{2} (x_{\langle c_1, c_2 \rangle}^2 - x_{c_1, c_2}^2). \quad (22)$$

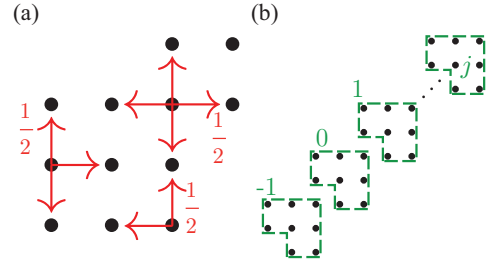


FIG. 8. (Color online) Diffusion in the staircase environment. (a) Transition rates between the sites of the staircase environment. Along every arrow drawn, the rate is $\frac{1}{2}$ leading to local detailed balance. (b) The staircase can be split into elementary cells, numbered with integers.

To evaluate this expression we split the lattice into elementary cells as shown in Fig. 8(b), and use that for asymptotically large times $t \rightarrow \infty$, the probability density P varies only little between neighboring elementary cells. This follows from translational symmetry; every cell obeys the same master equation. The master equation, Eq. (20), then implies a nearly uniform probability distribution within each elementary cell j [34]. Upon assuming a constant value P_j within each unit cell, carrying out the sum over an arbitrary elementary cell j leads to a further simplification

$$\sum_{\mathcal{C}_j} P_j \sum_{\langle c_1, c_2 \rangle} \frac{1}{2} (x_{\langle c_1, c_2 \rangle}^2 - x_{c_1, c_2}^2) = \frac{1}{2} P_j, \quad (23)$$

independent of j . Altogether, we obtain

$$\begin{aligned} \lim_{t \rightarrow \infty} \frac{d}{dt} \langle x^2(t) \rangle &\approx \sum_{j=-\infty}^{\infty} \frac{1}{2} P_j \stackrel{(*)}{\approx} \sum_{j=-\infty}^{\infty} \sum_{\mathcal{C}_j} \frac{1}{8} P_{c_1, c_2} \\ &= \frac{1}{16} \sum_{\mathcal{C}} P_{c_1, c_2} \stackrel{(\dagger)}{=} \frac{1}{16} = 2D, \end{aligned} \quad (24)$$

where in (*) we used that each elementary cell comprises eight points, and in (†) we employed the normalization condition for P . This procedure can be generalized for arbitrary d . The formula for the diffusion constants for $n = 2$ then reads

$$D(d) = \frac{1}{16} + \frac{1}{32(1-d)}. \quad (25)$$

This theoretical result agrees well with simulation data for the diffusion constant D , as a function of the leash length d (see Fig. 9).

IV. OPTIMIZATION OF DIRECTED MOTION

In the previous sections we mainly focused on ensemble properties of spider teams. However, in experiments or applications one has to deal with single realizations of the stochastic process, i.e., single trajectories [cf. Fig. 2(f)]. Since it is desirable to achieve a molecular motor design that works reliably, one would like to minimize the randomness of the trajectory, i.e., the motion's standard deviation

$$\sigma = \sqrt{\langle (x - \langle x \rangle)^2 \rangle}. \quad (26)$$

It is interesting to ask how the microscopic properties of the spider team (n, d) influence σ : Can we optimize the

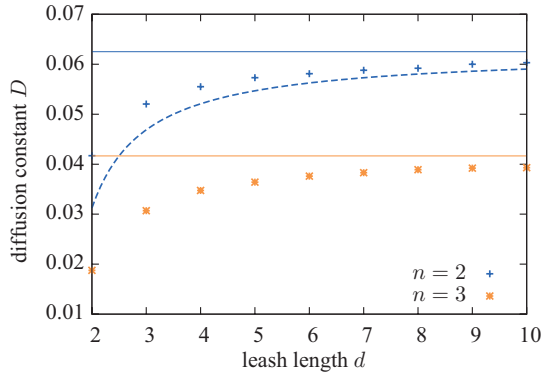


FIG. 9. (Color online) Diffusion constants as a function of the leash length d for $n = 2$ and 3 spiders. The dashed line shows the theoretical result for $n = 2$ [Eq. (25)]; solid lines are asymptotics for $d \rightarrow \infty$. Our theoretical approximation is in good agreement with simulation data (points).

performance of a spider team? Is there an optimal choice of parameters n and d which reduces the randomness of a spider teams' motion to a minimum?

The randomness is determined by the interplay between the dynamics of the spider team during its different episodes of motion, i.e., the boundary periods and the diffusive periods. For each episode we found a characteristic feature: During boundary periods the spider team motion is essentially ballistic which can be quantified in terms of the mean number of consecutive steps $\langle S \rangle$ [cf. Eq. (17)]. In contrast, during a diffusive period the spider team performs a random walk with a diffusion constant D [cf. Eq. (25)].

We have already learned in Sec. III C and Fig. 5 that there is an optimal choice of parameters for the number of consecutive directed steps during a boundary period (see Fig. 5). One could now naively conclude that the predictability of a spider team's motion can as well be optimized with the same set of parameters. However, this argument would overlook the impact of the diffusive periods. Indeed, there are several effects which influence the randomness during these episodes:

(i) In Sec. III E we noted that the diffusion constant D grows with the leash length d [Eq. (25) and Fig. 9]. Since D determines the mean square displacement during a diffusive period, increasing d would then also imply a *greater* randomness, σ .

(ii) Conversely, a higher diffusion coefficient during diffusive periods speeds up all dynamic processes. Thus, in a given time window, larger d make it more probable for a spider team to return to the boundary and start moving ballistically [35].

The combined effect of these two processes can be estimated by analyzing a random walker with an absorbing boundary. In one dimension, one finds that $\langle x^2(t) \rangle \propto \sqrt{Dt}$ [36,37]. Hence, (i) and (ii) together would lead to an *increase* of σ with d .

(iii) Consider the geometrical interpretation of the transition from the boundary period to the diffusive period as given in Fig. 7. In this picture, entering a diffusive period corresponds to removing the lowermost red box, and stepping to one of the three points below states ⑥–⑧. Right after this transition, the average minimal distance $\langle x_0 \rangle$ of the spider team from the

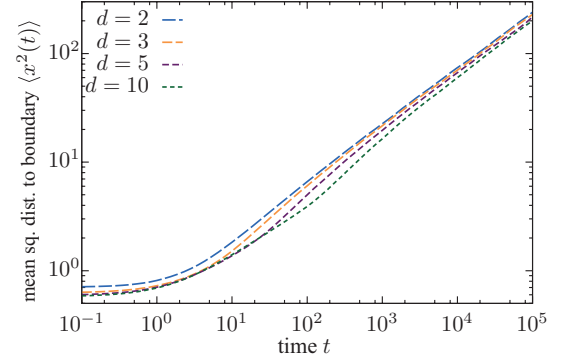


FIG. 10. (Color online) Randomness during a diffusive period. Shown is the mean-squared minimal distance to the boundary of a random walker in the staircase environment ($n = 2$), Fig. 6. The walkers start randomly along every point which provides an entrance to the diffusive period (for $d = 2$, these are the three points below states ⑥–⑧ in Fig. 7); they are absorbed when they reach the boundary (which is the second substrate box in Fig. 7; note that the lowermost box has been removed when the walker entered the diffusive period). Obviously, the mean-squared distance is greater the smaller d is. Increasing d thus decreases the randomness.

boundary is therefore given by

$$\langle x_0 \rangle = \frac{1}{4} \left(3 + \frac{3}{4d-5} \right), \quad (27)$$

as can be inferred from counting the different transition pathways. Hence, with increasing d , the spider team entering the diffusive period is closer to the boundary, and is thereby more likely to reenter a boundary period quickly.

(iv) In Sec. III D we have shown that with increasing leash length d the number of pathways in state space to reenter a boundary period also increases. Pictorially, this can be inferred from the mapping of the spider team's motion to a random walker in a staircase environment: The longer the leash length

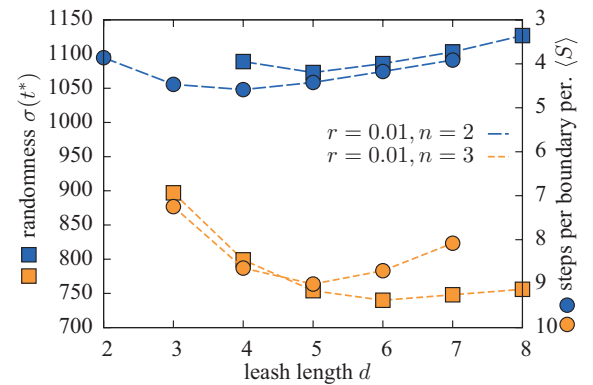


FIG. 11. (Color online) Standard deviation σ of the spider teams' movement and the mean number of steps $\langle S \rangle$ as a function of the leash length d . Both σ and $\langle S \rangle$ show extrema. To emphasize the correspondence between the minimum of σ and the maximum of $\langle S \rangle$ (cf. Fig. 5), the $\langle S \rangle$ axis is drawn in reverse (see right scale). σ is measured at the time t^* when the mean displacement $\langle x \rangle$ equals 1000. This choice is arbitrary; for smaller values the minima of σ persist, but are less pronounced [cf. Fig. 2(b)].

TABLE II. Optimal values of d for $n = 2$ and 3, and several values of r . Compared are the values of d which maximize the mean number of steps during a boundary period, and that which minimize the randomness (for a comparison see Fig. 11). Clearly, both values of d are closely correlated, where $d_{(S)}^{\text{opt}}$ is only slightly smaller than d_{σ}^{opt} .

r	$n = 2$		$n = 3$	
	$d_{(S)}^{\text{opt}}$	d_{σ}^{opt}	$d_{(S)}^{\text{opt}}$	d_{σ}^{opt}
0.001	$\sim 10-11$	~ 13		
0.01	4	5	5	6
0.02	3	4	3-4	4-5
0.05	2	3		
0.1	2	3	2	3
0.2	2	2	2	3

d the larger is the ‘‘angle’’ under which a random walker sees the boundary of the staircase. Thus, when the random walker takes an arbitrary direction the probability that it walks toward the boundary is increasing with d .

Since there is no unique trend in the various effects discussed above in (i)–(iv), it is difficult to conclude what would be the dominant effect of the diffusive period on the randomness. Therefore, we numerically determine the randomness of the spider team during diffusive periods [38]; this quantity is depicted in Fig. 10. We observe that the mean squared distance from the boundary is smaller for larger d at all times. This implies that—considering only diffusive periods—increasing d leads to a *reduction* of the randomness. From this we can infer that the effects (iii) and (iv), which decrease the randomness of the process with increasing d , overcompensate the effects (i) and (ii).

Altogether we can now conclude the influence of the diffusive periods as follows:

$$d \nearrow \Rightarrow \sigma \searrow .$$

Analogously we can decipher the influence of boundary periods. Going back to Fig. 5 we observe

$$d < d_{(S)}^{\text{opt}} : d \nearrow \Rightarrow \langle S \rangle \nearrow \Rightarrow \sigma \searrow ,$$

$$d > d_{(S)}^{\text{opt}} : d \nearrow \Rightarrow \langle S \rangle \searrow \Rightarrow \sigma \nearrow .$$

These considerations explain that *if* there is an optimal value d_{σ}^{opt} at which the randomness becomes minimal, it must be found beyond $d_{(S)}^{\text{opt}}$. This is in agreement with our data: Figure 11 shows the existence of a minimum of the randomness, and its positioning with respect to $d_{(S)}^{\text{opt}}$. Remarkably, the positions of both optima are strongly correlated (see Table II).

In conclusion, our analysis shows that the randomness of the spider team is mainly determined by the mean number of steps $\langle S \rangle$ during boundary periods. Diffusive periods have only a small effect on the randomness and change the optimal parameters only slightly.

V. CONCLUSIONS

Based on existing models for molecular spiders [11,12], we proposed a model for a spider team that explores the collective behavior of cooperating spiders: In our model, bipedal spiders are jointly attached to a (zero-mass) linking cargo. Each spider

walks on its own one-dimensional track. This leads to a spacial constraint which can be characterized by the maximal span d of the resulting spider team.

Depending on the cleavage rate of the substrate $r < 1$, the number of coupled spiders n , and the leash length d , we found that the coupling leads to a significant enhancement of many of the spider’s motor properties: Spider teams show a significant increase of their mean displacement; their motion is a lot less random; the ensemble’s velocity can be increased by more than an order of magnitude; and the superdiffusive behavior lasts longer for orders of magnitude in time. Unlike single spiders, cooperating spiders could therefore—at least in theory—be employed for executing well-defined tasks reliably.

Like their individual counterparts [16], spider teams’ motion can be characterized as being in either a boundary or a diffusive period. We found that the characteristic quantity is the mean number of consecutive directed steps $\langle S \rangle$ which a spider team performs during a boundary period. In simplified language, $\langle S \rangle$ integrates the number of steps which the spider teams walk, as long as it stays in the vicinity of the coming boundary between substrate and product sites. $\langle S \rangle$ is closely related to the bias p_+ of single spiders [12]. For small r , we succeeded in calculating $\langle S \rangle$ analytically through an equivalence class formalism which made use of the time scale separation of dwell times on products and substrates. This formalism is exact for $r \rightarrow 0$, regardless of the number of coupled spiders and the tightness of the coupling. We explicitly calculated values for various small spider teams, and find excellent agreement with simulation data. For small but finite cleavage rates r , the formalism still holds as an approximation for relatively tight coupling. We found that in this case there is an optimal value for the coupling tightness d which maximizes the mean number of steps.

Next, we provided a mapping of the stochastic motion of an n -spider team to a random walker in an n -dimensional environment. The motion is confined between parallel boundaries which have the shape of staircases. This mapping is exact and allows a complementary interpretation for the equivalence classes: Substrates can be drawn as boxes which are easy to enter for random walkers but impossible to leave without removing, which happens slowly on a time scale r^{-1} . It is then straightforward to see that an equivalence class corresponds to an intersection of boxes (cf. Fig. 7). The staircase picture also allows one to quantify the dynamics during the diffusive periods of spider teams: In that case, boxes can be ignored and spider teams correspond to ordinary diffusive random walkers on the confined lattice. We calculated the diffusion constants for two-spider teams and find good agreement with simulation data.

The analysis of the mean number of consecutive steps during a boundary period $\langle S \rangle$ (which shows a maximum for some value of the leash length d), taken together with the diffusion constants D (which grow with d) allow for a comprehensive explanation of our observations. We show that the optimal value of d that minimizes the randomness (which involves boundary and diffusive periods) differs only slightly from the leash length maximizing the mean number of steps during a boundary period (see Fig. 11).

The staircase picture also illustrates that despite the difference in complexity, a single spider and a spider team can

both be described by similar effective random walk models: The motion of a bipedal spider which has a nontrivial stepping gait can be fully described by its center of mass coordinate which performs simple one-dimensional random walks [12]. Likewise, the motion of an n -spider team which involves complicated interactions between the spiders can equivalently be described by another single coordinate which performs n -dimensional random walks that are, however, geometrically confined due to the leash constraint.

Our results show that the primary factor for improving the motor properties of molecular spiders is the accessibility of substrate sites for the spider legs: While single spiders only have access to one substrate at a time, an n -spider team can reach n substrates. This would imply that there is a significant difference between truly one-dimensional spiders [12] and quasi-one-dimensional spiders [10]. This is enforced by a very recent study of Olah *et al.* [19] who examined molecular spiders on a narrow two-dimensional lattice. As well, it is in full accordance with recent data by Samii *et al.* [18] who concentrated on hand-over-hand spiders: They showed that motor properties of this class of spiders which have access to more than one substrate site at a time are superior to inchworm spiders which can only reach one substrate at once [17,18].

The results presented here can be extended in multiple ways. In analogy to individual spiders, further studies could concentrate on varying design specifics like the number or the length of legs [18]. Likewise, the underlying chemical processes [9,10] could be modeled in greater molecular detail also for spider teams. Similarly, the team's spiders' stepping gait could be varied, potentially profiting from studies about the motion of individual hand-over-hand spiders with more than two legs [18] which seem to be difficult to realize in the experiment.

Unlike other studies (e.g., [16]) which have extensively investigated the role of the cleavage rate r , our focus was different and the variation of r was only a side aspect of this work. Nevertheless, our analysis hints towards a scaling behavior which maps the quantity $\langle S(r,d) \rangle$ to a universal form $\tilde{S}(\tilde{d})$ which is independent of r . In this spirit, it would also be interesting to study the connection of the optimal leash length and the cleavage rate r . It appears that this relation might be rather simple for a wide parameter range, although its mathematical formulation seems to be very complex. The difficulty is that the simplified formulation of the problem presented here, i.e., the equivalence classes, cannot be applied directly. One possibility to address this problem might lie in drawing analogies from related models such as the burnt-bridge model [39]. For example, it has been studied for dimeric motor molecules [40] and as an exclusion process [41].

Our results might also be relevant to study collective properties of molecular motor assemblies theoretically (cf. e.g. Ref. [42] or Ref. [43], and references therein). These models are relevant to understand the interplay between biological motor molecules such as kinesin, dynein, and myosin inside cells [44,45]. In contrast to spiders, biological motors are fueled by ATP hydrolysis; they can build up significant pulling forces due to strong mechanochemical coupling [46]. In particular, recent experiments addressed the complex interplay of multiple coupled kinesin motor proteins where the motors are coupled via a DNA leash of certain length. It is interesting

to note how in these experiments teams of two kinesin motors outperform a single motor in terms of run length and pulling forces [47–49]. Similarly, cooperative effects also improve the properties of two coupled burnt-bridge motors modeling collagenase transport [40].

In conclusion, we believe that our model of coupling molecular spiders provides insight on how cooperative behavior evolves on the molecular scale. We hope that our ideas about molecular spiders help advance a young and fast growing field in which much focus is put on the construction of novel, more efficient molecular designs [4]. We believe that our findings are not limited to the case of molecular spiders, but apply to molecular machines working together in general.

ACKNOWLEDGMENTS

We thank Anatoly Kolomeisky for fruitful discussions and comments on the manuscript. This project was supported by the the German Excellence Initiative via the program “Nanosystems Initiative Munich” (NIM). M.R. gratefully acknowledges a scholarship by the Cusanuswerk.

APPENDIX: DERIVATION OF EQ. (17)

We analyze the graph for a two-spider team with arbitrary d as depicted in Eq. (14). According to this graph, transitions $[i] \rightarrow [i \pm 1]$ are equally likely as long as $i < d$, whereas $[d] \rightarrow [d - 1]$ happens at probability Π . During every transition, the spider team performs a fractional step $\frac{1}{n} = \frac{1}{2}$. Only during the transition $[d] \rightarrow [d - 1]$, no step is integrated; in return, $[d - 1] \rightarrow [d]$ leads to a whole step for the team. This is due to the very definition of the number of steps during a boundary period, which comprises all cleavages but for each spider's last cleavage before the team enters the diffusive period.

With these preparations, we can now establish the probabilities $p(j|[i])$ that a spider team, being in class $[i]$, performs exactly j steps before leaving into the diffusive period. These read

$$\begin{aligned} p(j|[0]) &= p(j - \frac{1}{2}|[1]), \\ p(j|[i]) &= \frac{1}{2}(p(j - \frac{1}{2}|[i - 1]) + p(j - \frac{1}{2}|[i + 1])), \\ p(j|[d - 1]) &= \frac{1}{2}(p(j - \frac{1}{2}|[d - 2]) + p(j|[d])), \\ p(j|[d]) &= \Pi p(j - 1|[d - 1]) \end{aligned} \quad (\text{A1})$$

where $0 < i < d - 1$. The *mean* number of steps $\langle S(x) \rangle$ which a spider team walks from class $[x]$ until going to the diffusive period is then given by

$$\langle S(x) \rangle = \sum_{j=0, \frac{1}{2}, \dots}^{\infty} j p(j|[x]). \quad (\text{A2})$$

Inserting Eq. (A2) into Eq. (A1), and by renumbering indexes we obtain

$$\begin{aligned} \langle S(0) \rangle &= \frac{1}{2} + \langle S(1) \rangle, \\ \langle S(i) \rangle &= \frac{1}{2} + \frac{1}{2} \langle S(i - 1) \rangle + \frac{1}{2} \langle S(i + 1) \rangle, \\ \langle S(d - 1) \rangle &= \frac{1}{4} + \frac{1}{2} \langle S(d - 2) \rangle + \frac{1}{2} \langle S(d) \rangle, \\ \langle S(d) \rangle &= \Pi + \Pi \langle S(d - 1) \rangle, \end{aligned} \quad (\text{A3})$$

where again $0 < i < d - 1$. Solving this system of equations, we obtain the recursion relation

$$\langle S(k) \rangle = \langle S(k+1) \rangle + k + \frac{1}{2} \quad (\text{A4})$$

for $0 \leq k < d - 2$. Substituting this into the remaining equations leads to

$$\langle S(d) \rangle = \frac{\Pi d}{1 - \Pi}, \quad (\text{A5})$$

and finally

$$\langle S(d-1) \rangle = \frac{d}{1 - \Pi} - 1 = (d-1) \frac{1}{1 - \Pi} + \frac{\Pi}{1 - \Pi}. \quad (\text{A6})$$

Since a spider always enters a boundary period in class $[d-1]$ in the limit $r \rightarrow 0$ [cf. Eq. (13)], the last equation is equivalent to $\langle S \rangle$, Eq. (17).

-
- [1] J. Howard, *Mechanics of Motor Proteins and the Cytoskeleton* (Sinauer Associates, Sunderland, MA, 2001).
- [2] J. Bath and A. J. Turberfield, *Nat. Nanotech.* **2**, 275 (2007).
- [3] R. D. Astumian, *Biophys. J.* **98**, 2401 (2010).
- [4] A. V. Pinheiro, D. Han, W. M. Shih, and H. Yan, *Nat. Nanotech.* **6**, 763 (2011).
- [5] W. B. Sherman and N. C. Seeman, *Nano Lett.* **4**, 1203 (2004).
- [6] J.-S. Shin and N. A. Pierce, *J. Am. Chem. Soc.* **126**, 10834 (2004).
- [7] M. von Delius and D. A. Leigh, *Chem. Soc. Rev.* **40**, 3656 (2011).
- [8] Y. Tian, Y. He, Y. Chen, P. Yin, and C. Mao, *Angew. Chem., Int. Ed. Engl.* **44**, 4355 (2005).
- [9] R. Pei, S. K. Taylor, D. Stefanovic, S. Rudchenko, T. E. Mitchell, and M. N. Stojanovic, *J. Am. Chem. Soc.* **128**, 12693 (2006).
- [10] K. Lund, A. J. Manzo, N. Dabby, N. Michelotti, A. Johnson-Buck, J. Nangreave, S. Taylor, R. Pei, M. N. Stojanovic, N. G. Walter, E. Winfree, and H. Yan, *Nature (London)* **465**, 206 (2010).
- [11] T. Antal, P. L. Krapivsky, and K. Mallick, *J. Stat. Mech.: Theory Exp.* (2007) P08027.
- [12] T. Antal and P. L. Krapivsky, *Phys. Rev. E* **76**, 021121 (2007).
- [13] T. Chou, K. Mallick, and R. K. P. Zia, *Rep. Prog. Phys.* **74**, 116601 (2011).
- [14] M. Mobilia, T. Reichenbach, H. Hirsch, T. Franosch, and E. Frey, *Banach Cent. Publ.* **80**, 101 (2008).
- [15] B. Derrida, M. Evans, and K. Mallick, *J. Stat. Phys.* **79**, 833 (1995).
- [16] O. Semenov, M. J. Olah, and D. Stefanovic, *Phys. Rev. E* **83**, 021117 (2011).
- [17] L. Samii, H. Linke, M. J. Zuckermann, and N. R. Forde, *Phys. Rev. E* **81**, 021106 (2010).
- [18] L. Samii, G. A. Blab, E. H. C. Bromley, H. Linke, P. M. G. Curmi, M. J. Zuckermann, and N. R. Forde, *Phys. Rev. E* **84**, 031111 (2011).
- [19] M. J. Olah and D. Stefanovic, arXiv:1211.3482.
- [20] T. Antal and P. L. Krapivsky, *Phys. Rev. E* **85**, 061927 (2012).
- [21] C. Gallesco, S. Müller, and S. Popov, *ESAIM: Probab. Stat.* **15**, 390 (2011).
- [22] I. Ben-Ari, K. Boushaba, A. Matzavinos, and A. Roitershtein, *Bull. Math. Biol.* **73**, 1932 (2011).
- [23] C. Gallesco, S. Müller, S. Popov, and M. Vachkovskaia, *ALEA, Lat. Am. J. Probab. Math. Stat.* **8**, 129 (2011).
- [24] R. Juhász, *J. Stat. Mech.: Theory Exp.* (2007) P11015.
- [25] J. D. Watson and F. H. C. Crick, *Nature (London)* **171**, 737 (1953).
- [26] This differs from the original model of Antal *et al.* [11] who allowed rebinding only to *different* sites.
- [27] C. B. Korn, S. Klumpp, R. Lipowsky, and U. S. Schwarz, *J. Chem. Phys.* **131**, 245107 (2009).
- [28] M. Brunnbauer, R. Dombi, T.-H. Ho, M. Schliwa, M. Rief, and Z. Ökten, *Mol. Cell* **46**, 147 (2012).
- [29] S. Ray, E. Meyhöfer, R. Milligan, and J. Howard, *J. Cell Biol.* **121**, 1083 (1993).
- [30] J.-P. Bouchaud and A. Georges, *Phys. Rep.* **195**, 127 (1990).
- [31] Note that $r = 0$ is unphysical since it would not allow substrate cleavage. Therefore, the limit $r \rightarrow 0$ has to be understood as a time separation limit where substrate cleavage is much slower than stepping of legs from product sites, i.e., $r \ll 1$.
- [32] C. Leduc, F. Ruhnnow, J. Howard, and S. Diez, *Proc. Natl. Acad. Sci. USA* **104**, 10847 (2007).
- [33] Following the definition of a step done by a spider team in Sec. III B, no step is counted along with the transition $[d-1] \rightarrow [d]$, since this is potentially the last cleavage event of the spider which caused this transition. To compensate this (if this spider makes another cleavage), the transition $[d] \rightarrow [d-1]$ is counted as two (half) steps.
- [34] Note that global equilibrium is never reached in this system due to the open boundaries.
- [35] Note that although the random walker is recurrent its recurrence time is infinite [50].
- [36] N. G. van Kampen, *Stochastic Processes in Physics and Chemistry* (Elsevier, New York, 2007).
- [37] S. Redner, *A Guide to First-Passage Processes* (Cambridge University Press, Cambridge, 2009).
- [38] It is convenient to run the simulations in the staircase picture (cf. Fig. 7). We assume that each of the three points below ⑥-⑧ in this figure is an equally likely starting point, and set up an absorbing boundary at the lowermost substrate box.
- [39] T. Antal and P. L. Krapivsky, *Phys. Rev. E* **72**, 046104 (2005).
- [40] A. Y. Morozov and A. B. Kolomeisky, *J. Stat. Mech.* (2007) P12008.
- [41] J. H. P. Schulz, A. B. Kolomeisky, and E. Frey, *Europhys. Lett.* **95**, 30004 (2011).
- [42] F. Berger, C. Keller, S. Klumpp, and R. Lipowsky, *Phys. Rev. Lett.* **108**, 208101 (2012).
- [43] T. Guérin, J. Prost, P. Martin, and J.-F. Joanny, *Curr. Opin. Cell Biol.* **22**, 14 (2010).
- [44] S. P. Gross, M. Vershinin, and G. T. Shubeita, *Curr. Biol.* **17**, R478 (2007).
- [45] E. L. F. Holzbaur and Y. E. Goldman, *Curr. Opin. Cell Biol.* **22**, 4 (2010).

- [46] A. B. Kolomeisky and M. E. Fisher, *Annu. Rev. Phys. Chem.* **58**, 675 (2007).
- [47] A. R. Rogers, J. W. Driver, P. E. Constantinou, D. Kenneth Jamison, and M. R. Diehl, *Phys. Chem. Chem. Phys.* **11**, 4882 (2009).
- [48] J. W. Driver, D. K. Jamison, K. Uppulury, A. R. Rogers, A. B. Kolomeisky, and M. R. Diehl, *Biophys. J.* **101**, 386 (2011).
- [49] D. K. Jamison, J. W. Driver, and M. R. Diehl, *J. Biol. Chem.* **287**, 3357 (2012).
- [50] G. Polya, *Math. Ann.* **84**, 149 (1921).

Appendix B.

Diffusion and Capture

– How Diffusive Enzymes Regulate Filaments

Please find in the following, work together with Emanuel Reithmann on proteins that diffuse on filaments and are captured at the filament end [264]. This model can be applied to diffusing polymerases and depolymerases on actin and microtubule filaments [265]. A more detailed description can be found in Emanuel's master's thesis [91].

Biophysical Letter

Quantifying Protein Diffusion and Capture on Filaments

Emanuel Reithmann,^{1,2} Louis Reese,^{1,2} and Erwin Frey^{1,2,*}¹Arnold Sommerfeld Center for Theoretical Physics and Center for NanoScience, Department of Physics and ²Nanosystems Initiative Munich, Ludwig-Maximilians-Universität München, Munich, Germany

ABSTRACT The functional relevance of regulating proteins is often limited to specific binding sites such as the ends of microtubules or actin-filaments. A localization of proteins on these functional sites is of great importance. We present a quantitative theory for a diffusion and capture process, where proteins diffuse on a filament and stop diffusing when reaching the filament's end. It is found that end-association after one-dimensional diffusion is the main source for tip-localization of such proteins. As a consequence, diffusion and capture is highly efficient in enhancing the reaction velocity of enzymatic reactions, where proteins and filament ends are to each other as enzyme and substrate. We show that the reaction velocity can effectively be described within a Michaelis-Menten framework. Together, one-dimensional diffusion and capture beats the (three-dimensional) Smoluchowski diffusion limit for the rate of protein association to filament ends.

Received for publication 2 July 2014 and in final form 18 December 2014.

*Correspondence: frey@lmu.de

The catalytic activity of enzymes is often restricted to specific binding sites. The ends of microtubules (MTs) for example are binding sites for a plethora of MT-associated proteins (MAPs) (1). At MT ends, MAPs can catalyze biochemical processes (2), or serve as substrates for other enzymes. This makes an efficient association of MAPs to MT tips important. Experiments suggest that one-dimensional diffusion of MAPs on MTs facilitates tip-targeting (3,4). This idea goes back to the concept of “reduction in dimensionality” suggested by Adam and Delbrück (5) and has been largely applied (6,7). However, a quantitative understanding of tip-binding mediated by diffusion on the filament and subsequent capture at the tip has remained elusive (3,8–16).

Here we show that capturing at the tip is crucial for tip-localization of proteins. We present a theory where diffusion and capture is accurately quantified with an effective association rate constant and provide a result that depends only on experimentally accessible parameters. For proteins that are enzymatically active at filament ends, our theory predicts that diffusion and capture leads to an enhancement of the enzymatic reaction velocity due to stronger tip-localization. We observe that the reaction velocity in dependence of the enzyme concentration closely follows a Michaelis-Menten curve and quantify the contribution of one-dimensional diffusion to tip-localization and enzymatic processes downstream thereof.

To model the diffusive motion of proteins on a filament, we consider a one-dimensional lattice of length l with lattice spacing $a = 8.4$ nm (Fig. 1 A). The lattice corresponds to a single protofilament of a stabilized MT in the absence of dynamic instability. Proteins perform a random walk on the

lattice with a hopping rate ϵ , the diffusion constant is $D = \epsilon a^2$. Each site can be occupied by only one protein, as the system is an exclusion process (17). Proteins attach to and detach from the lattice at rates $\omega_{\text{on}}c$ and ω_{off} , respectively, where c is the concentration of proteins in solution. The tip of the MT is represented by the first lattice site in our model. To account for its particular structure, different on- and off-rates are assumed there, expressed as $k_{\text{on}}c$ and k_{off} . Proteins that bind to the tip are captured, i.e., not allowed to hop on the lattice, but still may detach into solution. This important condition is a critical difference between our model and previous approaches ((3,16); and see also the [Supporting Material](#)).

The central goal of this letter is to quantify the relative contributions of diffusion and capture (tip-attachment after diffusion on the lattice) and end-targeting (attachment after diffusion in solution) (Fig. 1 B) to tip-localization. To this end we calculated the probability to find a protein at the end of a protofilament (the tip density ρ_+). In the absence of diffusion and capture, the Langmuir isotherm is obtained,

$$\rho_+(c) = \frac{c}{K + c}, \quad (1)$$

where $K = k_{\text{off}}/k_{\text{on}}$ is the dissociation constant of the protein at the tip. However, as noted previously (3,4), such a model is incomplete as it does not account for the additional

Editor: E. Ostap.

© 2015 by the Biophysical Society

<http://dx.doi.org/10.1016/j.bpj.2014.12.053>

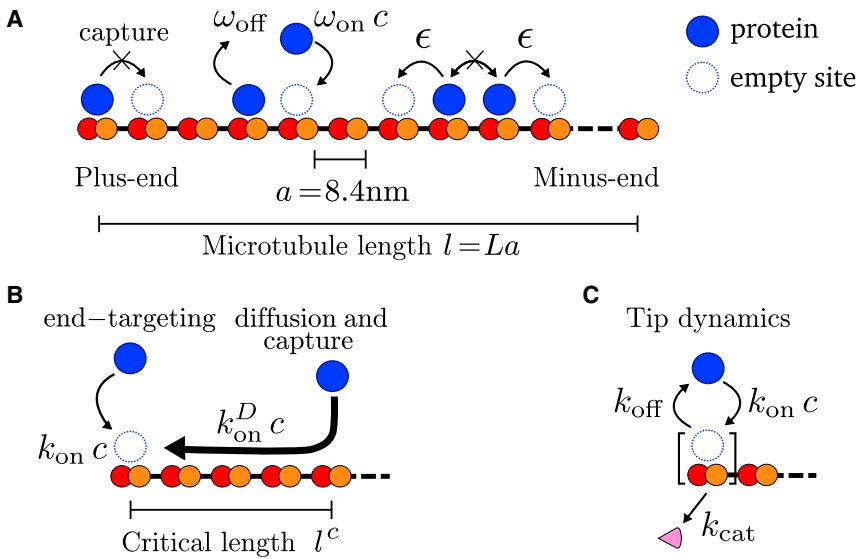


FIGURE 1 (A) Schematic of a microtubule (MT) with diffusive tip-binding proteins. In the bulk of the lattice, proteins attach to empty sites and detach. Proteins hop to neighboring sites but obey exclusion. At the plus-end, particles are captured. (B) Illustration of direct tip-attachment from solution and via diffusion and capture. (C) Proteins bind reversibly at the plus-end. While a protein is attached there, a reaction is catalyzed at rate k_{cat} . To see this figure in color, go online.

protein flux along protofilaments mediated by diffusion and capture. We have analyzed this flux by stochastic simulations of the model (Fig. 1). Surprisingly, we find that over a broad range of concentrations c , the additional protein current to an unoccupied reaction site J^D effectively obeys first-order kinetics, i.e., $J^D = k_{\text{on}}^D c$ (Fig. S2 in the Supporting Material). This observation implies that despite the complexity of the diffusion-reaction process one approximately retains the functional form of the Langmuir isotherm. Accounting for the diffusion-capture contribution to the rate of protein attachment leads to an effective dissociation constant,

$$K^{\text{eff}} = k_{\text{off}} / (k_{\text{on}} + k_{\text{on}}^D). \quad (2)$$

We have calculated the diffusion-capture rate k_{on}^D analytically, by exploiting the observed approximate linear reaction kinetics. We find

$$k_{\text{on}}^D = \frac{\omega_{\text{on}} D / a^2}{\omega_{\text{off}} + \sqrt{\omega_{\text{off}} D / a^2}}. \quad (3)$$

Refer to the Supporting Material for a detailed derivation of Eqs. 1–3. Together, Eqs. 1–3 comprise an effective theory for the association of proteins to the tip, which accounts for direct end-targeting as well as the diffusion-capture process. With Eq. 3, we are able to quantitatively predict the relative contribution of diffusion and capture to tip-binding for different proteins that diffuse on filaments. The results are shown in Fig. 2: 90–99% of molecules bind to the tip through one-dimensional diffusion, given they follow diffusion and capture.

Tip-localization due to diffusion and capture as predicted by our theory has important implications for enzymatically active proteins. We extended the model to investigate enzy-

matic reactions at the MT tip, where the protein-tip complex catalyzes a product at rate k_{cat} (Fig. 1 C). In detail, we assume that the protein does not leave the tip after catalyzing a reaction, but only through detachment into solution. These model assumptions are consistent with filament polymerizing enzymes that act processively, such as XMAP215 for MTs (9,10), and VASP (15) and formins (18) for actin filaments. The assumption of a constant length l in our model is excellent if the rate of diffusion is fast compared to the polymerization rate.

With the above model assumptions, the reaction velocity v is determined by the tip density, $v = \rho_+ k_{\text{cat}}$. We can apply our previous results, Eqs. 1–3, to obtain

$$v(c) = k_{\text{cat}} \rho_+(c) = \frac{k_{\text{cat}} c}{K^{\text{eff}} + c}. \quad (4)$$

The above equation is reminiscent of a single-molecule Michaelis-Menten equation (19,20) when K^{eff} is reinterpreted as the Michaelis constant and substrate and enzyme concentrations are interchanged. In this way, our theory constitutes an effective Michaelis-Menten theory, accounting for end-targeting and diffusion and capture. Instead of solving a complex many-body problem, it suffices to apply a mathematical framework that is analogous to (single-molecule) Michaelis-Menten kinetics. The details of diffusion and capture are accurately included in the effective on-rate

$$k_{\text{on}}^{\text{eff}} = k_{\text{on}} + k_{\text{on}}^D.$$

This result is in accordance with experimental results for several enzymatically active proteins where Michaelis-Menten curves were observed for the reaction speed depending on the enzyme concentration (8,9). Inspired by the processive (de)polymerase activity of (M)CAK XMAP215, we assume that enzyme and substrate are not

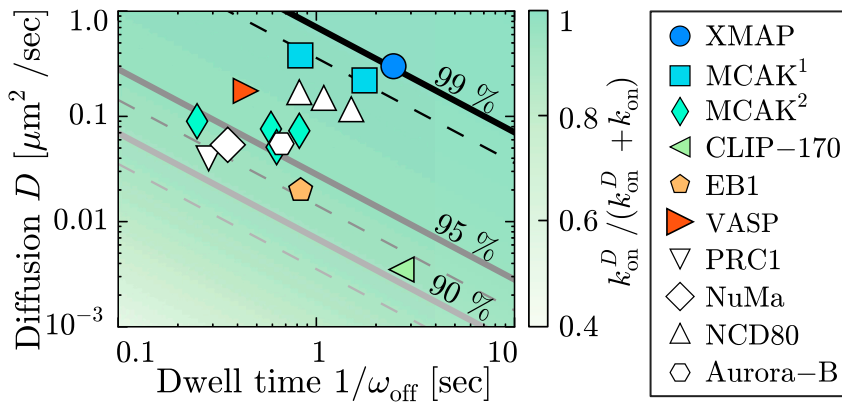


FIGURE 2 The model predicts the relative contribution to tip localization of proteins due to diffusion and diffusion and capture (color code and solid lines), $k_{\text{on}}^D / (k_{\text{on}}^D + k_{\text{on}})$ with $k_{\text{on}} = \omega_{\text{on}}$ (dashed line for actin: $a = 6$ nm). Proteins that are captured at the filament end (solid symbols) and proteins where evidence for capturing is lacking (open symbols) are shown. Proteins that in addition have a direct enzymatic activity at the filament end are XMAP215 (9,10), MCAK¹ (3), and MCAK² (8) on MTs, and VASP on actin filaments (15; S.D. Hansen and R.D. Mullins, University of California San Francisco School of Medicine, personal communication, 2014). There exist also proteins that diffuse on MTs

without enzymatic activity at MT ends, but with roles downstream of tip-localization, e.g., in the protein network of MT tips (1): Ndc80 (11), CLIP-170 (12), NuMA, PRC1, EB1 (13), and Aurora-B (14). To see this figure in color, go online.

decomposed in the reaction step. However, it is straightforward to include a decomposition in the theory: the corresponding effective dissociation constant would read

$$K^{\text{eff}} = (k_{\text{off}} + k_{\text{cat}}) / k_{\text{on}}^{\text{eff}}.$$

Our analytical results, Eqs. 2–4, agree well with simulation results of the stochastic model, as shown in Fig. 3, A and B. We find that the diffusion and capture mechanism dramatically increases $k_{\text{on}}^{\text{eff}}$ and thereby reduces the effective dissociation constant typically by more than one order of magnitude, e.g., for XMAP215 we find $K^{\text{eff}} \approx 10^{-2} K$ (see Table S1 in the Supporting Material for parameter values). In the case of long dwell-times ω_{off}^{-1} and fast diffusion ϵ , K^{eff} reduces to a particularly simple form

$$K^{\text{eff}} = (k_{\text{off}} / \omega_{\text{on}}) / \sqrt{\epsilon / \omega_{\text{off}}}, \quad (5)$$

where the denominator is the square-root of the average number of diffusive steps a protein performs on the filament.

Note that one-dimensional diffusion without capturing (16) does not lead to a particle flux on the filament (Fig. S4), and hence the reaction velocity is not increased (Fig. 3 A). Further, the particle flux might be limited by the length of the filament: below a threshold length l^c (which is smaller than typical in vivo lengths of MTs), we observe a length-dependent behavior of the reaction velocity (Fig. S3), where our theory is not valid.

Our analysis reveals diffusion and capture as an efficient mechanism to circumvent the diffusion limit for the rate of end-targeting: Smoluchowski's theory of three-dimensional diffusion physically limits the rate of direct tip-attachment from solution (21). As shown here, one-dimensional diffusion along a filament and subsequent capture at the filament end overcomes this limitation. This has been shown experimentally for MCAK (3). Our work provides an applicable

theory for reaction kinetics facilitated by diffusion and capture: specific parameter values for diffusion, tip-association, and dwell times can be accounted for (see Eqs. 3 and 4). Employing a broader perspective, our results may also be

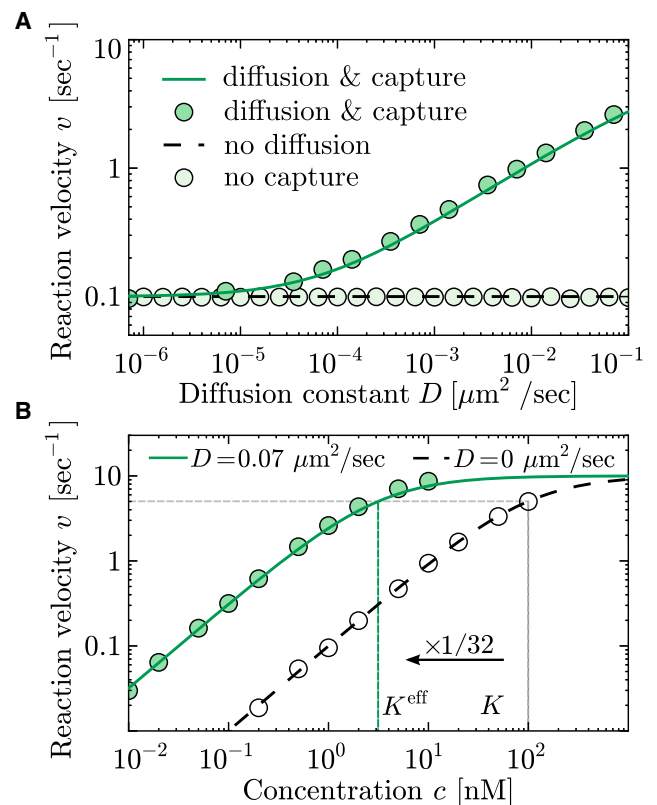


FIGURE 3 (A) Comparison of the reaction velocity with (solid) and without (dashed) lattice diffusion and with and without capturing at the tip (circles, simulation data; lines, analytic results). (B) Reaction velocity v in dependence on the protein concentration c . Analytic results (lines) are confirmed by simulation data (circles). Parameters are $L = 1000$, $\omega_{\text{off}} = k_{\text{off}} = 1$ s⁻¹, $k_{\text{cat}} = 10$ s⁻¹, $\omega_{\text{on}} = k_{\text{on}} = 0.01$ s⁻¹ nm⁻¹, and $c = 1$ nM. To see this figure in color, go online.

applicable to other systems where one-dimensional diffusion is important (6), including transcription factor binding on DNA (22).

SUPPORTING MATERIAL

Supporting Materials and Methods, four figures, and one table are available at [http://www.biophysj.org/biophysj/supplemental/S0006-3495\(15\)00063-6](http://www.biophysj.org/biophysj/supplemental/S0006-3495(15)00063-6).

ACKNOWLEDGMENTS

The authors thank Scott Hansen and Dyche Mullins for helpful correspondence on diffusing actin binding proteins.

This research was supported by the Deutsche Forschungsgemeinschaft via project No. B02 within the SFB 863.

REFERENCES

1. Akhmanova, A., and M. O. Steinmetz. 2008. Tracking the ends: a dynamic protein network controls the fate of microtubule tips. *Nat. Rev. Mol. Cell Biol.* 9:309–322.
2. Howard, J., and A. A. Hyman. 2007. Microtubule polymerases and depolymerases. *Curr. Opin. Cell Biol.* 19:31–35.
3. Helenius, J., G. Brouhard, ..., J. Howard. 2006. The depolymerizing kinesin MCAK uses lattice diffusion to rapidly target microtubule ends. *Nature.* 441:115–119.
4. Cooper, J. R., and L. Wordeman. 2009. The diffusive interaction of microtubule binding proteins. *Curr. Opin. Cell Biol.* 21:68–73.
5. Adam, G., and M. Delbrück. 1968. Reduction of dimensionality in biological diffusion processes. In *Structural Chemistry and Molecular Biology*. Freeman, New York, pp. 198–215.
6. von Hippel, P. H., and O. G. Berg. 1989. Facilitated target location in biological systems. *J. Biol. Chem.* 264:675–678.
7. Mirny, L., M. Slutsky, ..., A. Kosmrlj. 2009. How a protein searches for its site on DNA: the mechanism of facilitated diffusion. *J. Phys. A Math. Theor.* 42:434013.
8. Cooper, J. R., M. Wagenbach, ..., L. Wordeman. 2010. Catalysis of the microtubule on-rate is the major parameter regulating the depolymerase activity of MCAK. *Nat. Struct. Mol. Biol.* 17:77–82.
9. Brouhard, G. J., J. H. Stear, ..., A. A. Hyman. 2008. XMAP215 is a processive microtubule polymerase. *Cell.* 132:79–88.
10. Widlund, P. O., J. H. Stear, ..., J. Howard. 2011. XMAP215 polymerase activity is built by combining multiple tubulin-binding TOG domains and a basic lattice-binding region. *Proc. Natl. Acad. Sci. USA.* 108:2741–2746.
11. Powers, A. F., A. D. Franck, ..., C. L. Asbury. 2009. The Ndc80 kinetochore complex forms load-bearing attachments to dynamic microtubule tips via biased diffusion. *Cell.* 136:865–875.
12. Dixit, R., B. Barnett, ..., E. L. F. Holzbaur. 2009. Microtubule plus-end tracking by CLIP-170 requires EB1. *Proc. Natl. Acad. Sci. USA.* 106:492–497.
13. Forth, S., K.-C. Hsia, ..., T. M. Kapoor. 2014. Asymmetric friction of nonmotor MAPs can lead to their directional motion in active microtubule networks. *Cell.* 157:420–432.
14. Noujaim, M., S. Bechstedt, ..., G. J. Brouhard. 2014. Microtubules accelerate the kinase activity of Aurora-B by a reduction in dimensionality. *PLoS ONE.* 9:e86786.
15. Hansen, S. D., and R. D. Mullins. 2010. VASP is a processive actin polymerase that requires monomeric actin for barbed end association. *J. Cell Biol.* 191:571–584.
16. Klein, G. A., K. Kruse, ..., F. Jülicher. 2005. Filament depolymerization by motor molecules. *Phys. Rev. Lett.* 94:108102.
17. Krapivsky, P. L., S. Redner, and E. Ben-Naim. 2010. *A Kinetic View of Statistical Physics*. Cambridge University Press, Cambridge, UK.
18. Vavylonis, D., D. R. Kovar, ..., T. D. Pollard. 2006. Model of formin-associated actin filament elongation. *Mol. Cell.* 21:455–466.
19. Kou, S. C., B. J. Cherayil, ..., X. S. Xie. 2005. Single-molecule Michaelis-Menten equations. *J. Phys. Chem. B.* 109:19068–19081.
20. Michaelis, L., and M. L. Menten. 1913. The kinetics of invertase action [Die Kinetik der Invertinwirkung]. *Biochem. Z.* 49:333–369.
21. von Smoluchowski, M. 1917. Attempt to derive a mathematical theory of coagulation kinetics [Versuch einer mathematischen Theorie der Koagulationskinetik]. *Z. Phys. Chem.* 92:129–168.
22. Hammar, P., P. Leroy, ..., J. Elf. 2012. The Lac repressor displays facilitated diffusion in living cells. *Science.* 336:1595–1598.

Spatial correlations in protein diffusion and capture on filaments

Emanuel Reithmann, Louis Reese, and Erwin Frey*

*Arnold Sommerfeld Center for Theoretical Physics (ASC) and Center for NanoScience (CeNS),
Department of Physics, Ludwig-Maximilians-Universität München, Theresienstrasse 37,
80333 München, Germany and Nanosystems Initiative Munich (NIM),
Ludwig-Maximilians-Universität München, Schellingstraße 4, 80333 Munich, Germany*

One dimensional diffusive motion of enzymes on microtubules is a widespread motif of microtubule regulating proteins. To quantify the impact of filament diffusion we investigate a stochastic lattice gas model that accounts for enzymatic activities at microtubule ends such as polymerization and depolymerization. We find that filament diffusion with subsequent capturing generates significant spatial correlations and develop an analytic approximation to account for such influences. This proves essential to obtain agreement between theory and experiment. We observe that diffusion and capture operates most efficiently at cellular enzyme concentrations.

PACS numbers: 05.40.-a, 87.16.Uv, 87.10.Mn

The diffusive motion of proteins on filamentous structures in the cell is vital for several cellular functions like gene regulation [1] and cytoskeletal dynamics [2, 3]: Transcription factors are likely to employ one dimensional diffusion on the DNA to find their target site in a highly specific manner and to determine the kinetics of gene regulation [4]. Similarly, actin and microtubule binding proteins diffuse on the respective filaments and fulfill regulatory functions at the filament ends. The benefit of such a low dimensional diffusive motion to specific binding was — on a theoretical level — first addressed by Adam and Delbrück. They suggested that a reduction in dimensionality of the diffusive motion enhances the effective association rate of particles to binding sites on the membrane or on DNA and filaments (see Refs. [6] for recent reviews on the topic). Since then many studies addressed biological questions where bulk-filament [7–12] or bulk-membrane association [13, 14] are important.

Concerning cytoskeletal architectures the efficient association and localization of enzymes to specific sites is relevant to a variety of cellular processes throughout the cell cycle and for cell motility and dynamics [15]. Recently, it was suggested that filament diffusion is utilized by two key players [3, 16] involved in regulation of microtubule dynamics, MCAK and XMAP: For both proteins the association rate for the enzymatic reaction sites is significantly faster than binding via three dimensional diffusion [17, 18]. This is important as both proteins accomplish vital tasks in acting as depolymerases (MCAK) [19] and polymerases (XMAP) [20], respectively, whilst bound to the microtubule end. Note that this mechanism is also assumed to be relevant for actin associated proteins [21].

However, diffusive motion on filaments does not lead to such a dramatic increase of association rates *per se*: As shown previously [22], it is crucial that the proteins are captured at the respective reaction site subsequent to their one-dimensional diffusive motion. In this work, we employ a one dimensional lattice gas [23, 24] to investi-

gate the influence of diffusion and capture in a dynamic system where growth or shrinkage is triggered by interactions of proteins with the lattice end [25–29]. This study follows a twofold motivation: Firstly, we seek for a mathematical understanding of the capture process and its implications. Secondly, based on a fully quantitative model without free parameters we try to illuminate the specific biomolecular mechanism employed by XMAP and MCAK.

Our results show that the capture process significantly complicates the theoretical situation as it inherently leads to large-scale spatial correlations in the system. Opposed to previous work which did either not account for protein capturing [25, 26] or only accounted for it heuristically [22] we specifically develop a mathematical framework that systematically includes the main determinants of such systems. Together with the extension towards dynamic systems, this conceptual advancement allows us to quantitatively explain *in vitro* experiments with XMAP and MCAK [18, 30]. Our analysis suggests that diffusion and capture was optimized evolutionary for MCAK and XMAP, which might point to its importance *in vivo*.

Model definition. We consider a one dimensional lattice gas, as depicted in Fig. 1. The lattice spacing is denoted as a . In the case of microtubules a is the size of a tubulin dimer, 8.4 nm. The configuration of enzymes on the lattice is described by occupation numbers n_i , taking values $n_i = 0$ for empty, and $n_i = 1$ for occupied sites. The particles symmetrically hop to neighboring sites in the semi-infinite system at rate ω and interact via hard-core repulsion. We implement Langmuir kinetics to model a surrounding reservoir of particles with a constant concentration c . In detail, particles attach to and detach from the lattice at rates $\omega_a c$ and ω_d , respectively [8, 9]. Sites $i \geq 3$ are considered as bulk and sites $i = 1, 2$ are considered *boundary* sites. At these boundary sites the dynamics is different from that in bulk because hopping from site $i = 1$ to site $i = 2$ is not allowed, as suggested recently for MT depolymerizing and polymer-

izing enzymes [17, 18]. This is a critical feature of the model, as the capturing process is essential to obtain a localization of proteins at the tip [22]. Particles detach from the first lattice site at a distinct off-rate, $\bar{\omega}_d \neq \omega_d$. In the following we wish to introduce the notion that site $i = 1$ is a *reaction* site at which lattice may polymerize or depolymerize. To simplify the further discussion we specify our description to the polymerizing case as induced by XMAP [18]. However, the main results and computations are independent of whether polymerization or depolymerization occurs — an equivalent formulation can also be found for the depolymerase MCAK [31]. The key feature of our model is that particle occupation at the tip, n_1 , triggers lattice growth at rate δ . This implies that the average speed of lattice growth is proportional to the average particle occupation $\langle n_1 \rangle$ and polymerization rate in the presence of XMAP, δ . As shown in recent experiments, XMAP acts *processively*, i.e. one molecule adds multiple rounds of tubulin dimers to the MT end [18]. Similar observations have been made for MCAK [17, 30]. To allow for such a behavior the particle at the tip is instantaneously shifted to newly incorporated lattice sites in our model. With these stochastic rules we can set up the equations of motion for the average occupation numbers. All equations will be formulated in the frame of reference comoving with the dynamic lattice end. In the bulk of the lattice, $i \geq 3$, we obtain

$$\frac{d}{dt} \langle n_i \rangle = \epsilon(\langle n_{i+1} \rangle - 2\langle n_i \rangle + \langle n_{i-1} \rangle) + \delta(\langle n_1 n_{i-1} \rangle - \langle n_1 n_i \rangle) + \omega_a c(1 - \langle n_i \rangle) - \omega_d \langle n_i \rangle. \quad (1)$$

This equation comprises contributions from hopping with exclusion (terms proportional to ϵ), a displacement current due to polymerization (terms proportional to δ) as well as particle attachment and detachment (terms proportional to ω_a and ω_d , respectively). The dynamics for tip occupations couples these bulk dynamics in the fol-

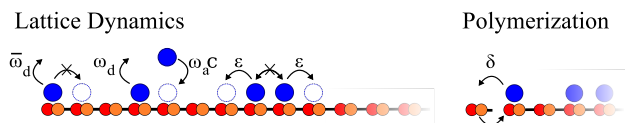


FIG. 1. Graphical representation of the XMAP model. XMAP particles bind to empty lattice sites with rate $\omega_a c$, where c is the particle concentration in solution, and detach with rate ω_d . While attached to the lattice, the proteins perform an unbiased random walk with hopping rate ω , respecting hard-core repulsion. We assume a distinct off rate at the first site, denoted by $\bar{\omega}_d$. Particles bound there are prohibited to perform hopping. *Polymerization* at rate δ occurs only if the first site is occupied. At the same time, the XMAP particle stimulating polymerization stays bound to the tip. A similar model can be defined for MCAK, where lattice depolymerization occurs if the lattice end is occupied, see Supporting Material for details.

lowing manner:

$$\frac{d}{dt} \langle n_1 \rangle = \epsilon(\langle n_2 \rangle - \langle n_1 n_2 \rangle) + \omega_a c(1 - \langle n_1 \rangle) - \bar{\omega}_d \langle n_1 \rangle, \quad (2a)$$

$$\frac{d}{dt} \langle n_2 \rangle = \epsilon(\langle n_3 \rangle - 2\langle n_2 \rangle + \langle n_2 n_1 \rangle) - \delta \langle n_1 n_2 \rangle + \omega_a c(1 - \langle n_2 \rangle) - \omega_d \langle n_2 \rangle \quad (2b)$$

$$\frac{d}{dt} \langle n_1 n_2 \rangle = \epsilon(\langle n_1 n_3 \rangle - \langle n_1 n_2 \rangle) + \delta \langle n_1 n_2 \rangle + \omega_a c(\langle n_1 \rangle + \langle n_2 \rangle - 2\langle n_1 n_2 \rangle) * (\omega_d + \bar{\omega}_d) \langle n_1 n_2 \rangle. \quad (2c)$$

Note that the contribution of hopping particles changes at the tip due to the capturing mechanism. Moreover, the processive polymerization scheme implies the creation of an empty lattice site at $i = 2$ after the addition of a new site. The occupation at the terminal site remains unchanged upon polymerization. We quantify our model with the experimental data available for XMAP [18, 32], see Supporting Material for all parameter values.

In a first step we test the quality of standard approximation techniques for driven lattice gases against stochastic simulation data obtained from Gillespie's algorithm [33]. The set of equations which determines the lattice occupations, Eq. 1 and Eqs. 2(a-c), is not closed, but the dynamics of the density $\rho_i = \langle n_i \rangle$ is coupled to the dynamics of the correlation function $g_i = \langle n_1 n_i \rangle$. In fact, there is an infinite hierarchy of equations, which, in general, precludes obtaining an exact solution [34], see e.g. Ref. [35]. A common and often quite successful approximation scheme for exclusion processes is to assume that there are no correlations and one may factorize all correlation functions, $\langle n_1 n_i \rangle \approx \langle n_1 \rangle \langle n_i \rangle$. In this *mean-field* (MF) approximation one obtains a closed set of differential equations for the particle density ρ_i which may be solved subject to the boundary conditions; see Supporting Material for details. Fig. 2 shows the average occupation number of the first site $\langle n_1 \rangle$ as a function of the bulk concentration c . A comparison with our stochastic simulation data shows that the MF solution strongly overestimates $\langle n_1 \rangle$ and thereby the average polymerization speed $v = \delta a \langle n_1 \rangle$.

One might suspect that the reason for the failure of the MF calculation are correlations close to the catalytic site where XMAP acts as a polymerase. Local correlations can efficiently be accounted for by employing a *finite segment mean-field* (FSMF) theory [37, 38]. The idea is to retain all correlations close to the catalytic site by solving the full master equation for the first N sites and to use the mean-field assumption only outside of this segment. The density profile is then obtained by matching the full solution and the MF solution [25, 29]; see Supporting Material for details. While the results show the right tendency towards the numerical data the improvement as compared to the MF results is insignificant. These observations strongly suggest that correlations extend far beyond the immediate vicinity of the catalytic site.

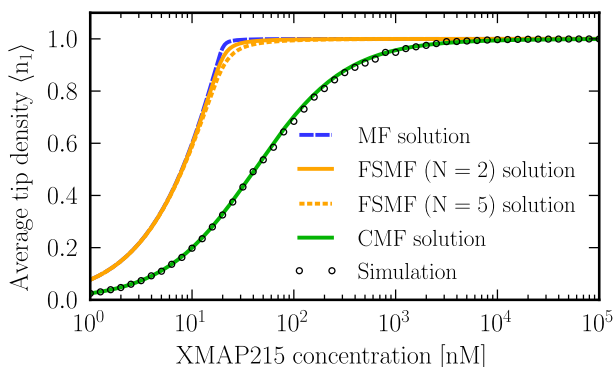


FIG. 2. Average occupation of the first lattice site $\langle n_1 \rangle$. This quantity determines the polymerization velocity via $v = \delta \langle n_1 \rangle$. Simple mean-field theory as well as FSMFT for segment sizes of $N = 2, 5$ do not agree with the data from stochastic simulations (dots), while the CMF approximation provides accurate results. Parameter values are detailed in the Supporting Material [36]

To account for these correlations we extend the MF theory by keeping both the density and the correlation function as dynamic variables. In order to close the set of equations we employ the following heuristic factorization scheme which we confirmed by stochastic simulations: $\langle n_1 n_2 n_i \rangle \approx \langle n_1 n_2 \rangle \langle n_i \rangle$ and $\langle n_2 n_i \rangle \approx \langle n_2 \rangle \langle n_i \rangle$; see Supporting Material. With the above closure relations one obtains for the bulk dynamics to leading order in the continuum limit

$$\partial_t \rho(x, t) = D \partial_x^2 \rho - v_0 \partial_x g + \omega_a c (1 - \rho) - \omega_d \rho, \quad (3a)$$

$$\begin{aligned} \partial_t g(x, t) = D \partial_x^2 g - v_0 \partial_x g + \epsilon \rho (\langle n_2 \rangle - \langle n_1 n_2 \rangle) \\ + \omega_a c (\rho + \langle n_1 \rangle - 2g) - (\omega_d + \bar{\omega}_d) g, \end{aligned} \quad (3b)$$

where $\rho(x, t) = \langle n_{i+1} \rangle$ and $g(x, t) = \langle n_1 n_{i+1} \rangle$ with $x = a(i-1)$ for $i \geq 3$. Eqs. 3 can be derived from the discrete equations for the density ρ_i , Eq. 3a, and the correlator g_i , see Supporting Material for details. We have also introduced the macroscopic diffusion constant $D = \epsilon a^2$ and the maximum polymerization speed $v_0 = \delta a$. Due to the capturing mechanism a continuous approximation of is not valid at sites $i = 1, 2$. Therefore we keep the local dynamics, Eqs. 2(a-c), for the boundary sites. These equations constrain the boundary conditions of $\rho(x)$ and $g(x)$ at $x = a$. For the semi-infinite geometry we further impose that the density equilibrates at the Langmuir isotherm, $\lim_{x \rightarrow \infty} \rho(x) = \rho_{La} = \omega_a c / (\omega_a c + \omega_d)$, and that correlations vanish asymptotically, $\lim_{x \rightarrow \infty} g(x) = \langle n_1 \rangle \rho_{La}$.

Solving the equations of this *correlated MF* (CMF) theory for the steady state tip density we obtain the results shown in Fig. 2. They are in excellent agreement with the data of the stochastic simulations. We conclude that there are long-ranged correlations along the

microtubule and that they are essential in explaining the observed average tip density.

Fig. 3(a) shows the density profile along the lattice obtained by stochastic simulations and the CMF approach. The particle occupation is obtained with high precision within the CMF framework along the whole lattice. Note that there is a discontinuity at the boundary sites which is due to particle capturing and which demonstrates the strong tip-localization of the proteins. This also shows, that a continuous description of the density is not valid at sites $i = 1, 2$.

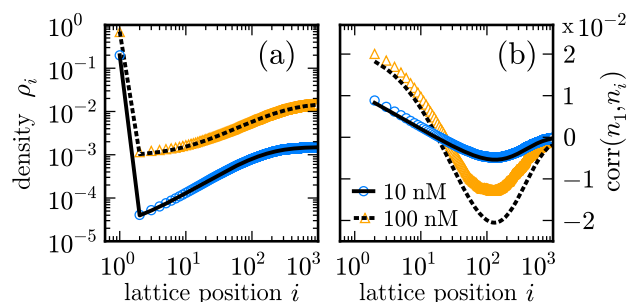


FIG. 3. Panel (a) shows the density profile of XMAP along the growing MT lattice for a XMAP concentration of 10 and 100 nM (see Supporting Material [36] for parameter values [18, 32]). XMAP strongly localizes at the MT tip and the density profile has a discontinuity between the tip site ($i = 1$) and the lattice site next to the tip ($i = 2$). In the bulk of the lattice the density obeys a diffusive (exponential) density profile [25]. Panel (b) shows the correlation coefficient $\text{corr}(n_1, n_i)$ (see Eq. (4)) along the growing MT lattice, complementing the density profiles in (a). The data as well as the analytic results indicate that the system develops correlations that extend over hundreds of lattice sites. In (a) and (b) data points are obtained from stochastic simulations; lines are analytic solutions to Eqs. (3a) and (3b), respectively.

We now discuss the behavior of correlations between the occupations at the reaction site and in the bulk. The Pearson product-momentum correlation coefficient quantifies these correlations:

$$\text{corr}(n_1, n_i) = \frac{\text{cov}(n_1, n_i)}{\sigma(n_1)\sigma(n_i)}, \quad (4)$$

where $\text{cov}(\cdot, \cdot)$ is the covariance, and $\sigma(\cdot)$ is the standard deviation. $\text{corr}(n_1, n_i)$ ranges from -1 to $+1$, with these values implying perfect anti-correlation or correlation of n_1 and n_i , respectively. Data and theory for the hypothesized tip-bulk correlations are shown in Fig. 3(b). Remarkably, the correlation coefficient shows intricate behavior covering a broad region at the tip — including anti-correlations. These effects can be qualitatively understood in terms of competition between different influences on the tip occupation. In the model diffusing particles are captured by the tip, i.e. they are prohibited to leave the reaction site via lattice movement. This

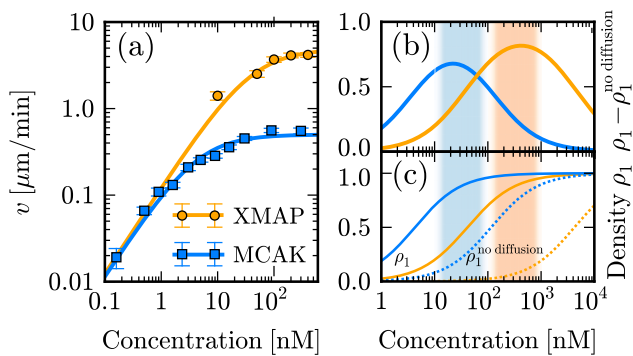


FIG. 4. In panel (a) we present concentration dependent polymerization and depolymerization velocities obtained from our theoretical analysis in comparison with existing experimental data for XMAP [18, 32] and MCAK [30], respectively. We find excellent agreement of the CMF theory with experiments. Panel (b) shows the efficiency of the one dimensional reaction site targeting mechanism as the deviation of ρ_1 obtained from our theoretical analysis from the density of proteins on the reaction site without diffusion $\rho_1^{\text{no diffusion}} = \omega_a c / (\bar{\omega}_d + \omega_a c)$. The maximum efficiency coincides with the physiological concentration range of both proteins: 100 – 1000 nM for XMAP [16] and 10 – 100 nM for MCAK [39] (shaded areas). In (c) the concentration dependency of the reaction site density with lattice diffusion (ρ_1 , solid lines) and without lattice diffusion ($\rho_1^{\text{no diffusion}}$, dashed lines) is depicted. Kinetic parameters are given in the Supporting Material [36].

ensues positive correlations with respect to the first lattice site and sites in its vicinity. On the other hand this effect is antagonized by negative correlations caused by the creation of empty lattice sites due to polymerization. With diffusion taking place on a faster time scale as compared to polymerization the positive correlations dominate for short distances. Further it becomes evident why the MF approach and the FSMFT do not lead to the correct tip density: Correlations extend into the system on a length-scale which lies beyond the scope of those approaches. As opposed to this, the CMF approach qualitatively captures significant correlations and thereby reproduces simulation data.

Comparison with experimental data. With this theory at hand, we now turn to a comparison of our theoretical efforts with experimental data [18, 32]. To show the generality of our method additionally apply it for a different MT regulating protein, MCAK, that depolymerizes MTs [17, 30]. To this end we adapt our model for the case of depolymerizing diffusing proteins [31]. We find perfect quantitative agreement of our theoretical approach with the measured polymerization and depolymerization velocities, see Fig. 4(a). The filament facilitates enzyme association to the MT tip via a diffusion and capture mechanism as can be concluded from our investigations. Fig. 4(b) shows the effect of diffusion on the effi-

ciency of tip association: We plot the difference between tip densities in the presence of diffusion (ρ_1^{CMF}) and in the absence of diffusion ($\rho_1^{\text{L}^a}$) when only direct binding to the tip is allowed. We find that the ensuing curve has a pronounced maximum indicating an optimal concentration range where the enhancement of the tip density peaks due to diffusion on the MT. Strikingly, this maximum coincides with the physiological concentration range for both proteins, XMAP (100 – 1000 nM [16]) and MCAK (10 – 100 nM [39]). We hypothesize, that there is an evolutionary pressure that optimized diffusion and capture for MCAK and XMAP which might indicate the importance of the filament diffusion also *in vivo*.

Summary and Conclusion. In this work, we study the regulatory influence of microtubule polymerases and depolymerases that are subject of a one-dimensional diffusion and capture process on microtubules. To model these biological situations we employ a lattice gas based on a *symmetric simple exclusion process* [24]. We find that the occupation of the microtubule tip with a protein spatially correlates with the occupation of the microtubule lattice. This correlation decays slowly along the lattice and has a large impact on the occupation of the microtubule tip. This is of relevance as the latter quantity determines the velocity of enzyme-dependent microtubule growth or shrinking. We derive a generalized set of hydrodynamic equations which couple the evolution of the particle density with the evolution of relevant correlations. In that way it is possible to globally account for those correlations. Similar correlations have been identified in two-dimensional diffusive systems [40].

We find excellent agreement of our analytic approach and stochastic simulations with *in vitro* experiments. In these experiments growth and shrink velocities were measured for the polymerase XMAP as well as the depolymerase MCAK in a concentration dependent manner. Remarkably, quantitative agreement is achieved without any fit parameter: all parameters used here were directly extracted from the experiments. As a result, we conclude that the diffusive motion and subsequent capturing of enzymes on the microtubule lattice constitutes a highly efficient mechanism to target the microtubule tip. The analytic approach and stochastic simulations allow for a quantification of this effect: The increase of the tip occupation due to facilitated diffusion is most efficient at physiological concentrations.

Our findings are not limited to microtubules and their related enzymes, but might also be relevant for other enzymatic processes with spatial degrees of freedom and non-equilibrium physics.

This project was supported by the Deutsche Forschungsgemeinschaft in the framework of the SFB 863.

-
- * frey@lmu.de
- [1] P. H. von Hippel and O. G. Berg, *J. Biol. Chem.* **264**, 675 (1989).
 - [2] J. R. Cooper and L. Wordeman, *Curr. Opin. Cell Biol.* **21**, 68 (2009).
 - [3] J. Howard and A. A. Hyman, *Curr. Opin. Cell Biol.* **19**, 31 (2007).
 - [4] A. D. Riggs, H. Suzuki, and S. Bourgeois, *J. Mol. Biol.* **48**, 67 (1970).
 - [5] G. Adam and M. Delbrück, in *Structural chemistry and molecular biology* (Freeman, 1968) pp. 198–215.
 - [6] L. Mirny *et al.*, *J. Phys. A: Math. Theor.* **42**, 434013 (2009); A. B. Kolomeisky, *Phys. Chem. Chem. Phys.* **13**, 2088 (2011); O. Bénichou *et al.*, *Rev. Mod. Phys.* **83**, 81 (2011); M. Sheinman *et al.*, *Rep. Prog. Phys.* **75**, 026601 (2012).
 - [7] P. H. Richter and M. Eigen, *Biophys. Chem.* **2**, 255 (1974); O. G. Berg, R. B. Winter, and P. H. Von Hippel, *Biochemistry* **20**, 6929 (1981).
 - [8] R. Lipowsky, S. Klumpp, and T. Nieuwenhuizen, *Phys. Rev. Lett.* **87**, 108101 (2001).
 - [9] A. Parmeggiani, T. Franosch, and E. Frey, *Phys. Rev. Lett.* **90**, 86601 (2003); *Phys. Rev. E* **70**, 46101 (2004).
 - [10] L. Bintu, N. E. Buchler, H. G. Garcia, U. Gerland, T. Hwa, J. Kondev, and R. Phillips, *Curr. Opin. Genet. Dev.* **15**, 116 (2005).
 - [11] I. Neri, N. Kern, and A. Parmeggiani, *Phys. Rev. Lett.* **110**, 098102 (2013).
 - [12] P. Hammar, P. Leroy, A. Mahmutovic, E. G. Marklund, O. G. Berg, and J. Elf, *Science* **336**, 1595 (2012).
 - [13] S. Mayor, J. F. Presley, and F. R. Maxfield, *J. Cell Biol.* **121**, 1257 (1993).
 - [14] J. Halatek and E. Frey, *Cell Rep.* **1**, 741 (2012).
 - [15] C. G. Dos Remedios *et al.*, *Physiol. Rev.* **83**, 433 (2003); A. Akhmanova and M. O. Steinmetz, *Nat. Rev. Mol. Cell Biol.* **9**, 309 (2008).
 - [16] K. Kinoshita, I. Arnal, A. Desai, D. N. Drechsel, and A. A. Hyman, *Science* **294**, 1340 (2001).
 - [17] J. Helenius, G. J. Brouhard, Y. Kalaidzidis, S. Diez, and J. Howard, *Nature* **441**, 115 (2006).
 - [18] G. J. Brouhard, J. H. Stear, T. L. Noetzel, J. Al-Bassam, K. Kinoshita, S. C. Harrison, J. Howard, and A. A. Hyman, *Cell* **132**, 79 (2008).
 - [19] J. D. Wilbur and R. Heald, *eLife* **2**, e00290 (2013).
 - [20] S. B. Reber *et al.*, *Nat. Cell Biol.* **15**, 1116 (2013).
 - [21] S. Romero *et al.*, *Cell* **119**, 419 (2004); D. Vavylonis *et al.*, *Mol. Cell* **21**, 455 (2006); S. D. Hansen and R. D. Mullins, *J. Cell Biol.* **191**, 571 (2010); H. Mizuno *et al.*, *Science* **331**, 80 (2011).
 - [22] E. Reithmann, L. Reese, and E. Frey, *Biophys. J.* **108**, 787 (2015).
 - [23] T. Chou, K. Mallick, and R. K. P. Zia, *Rep. Prog. Phys.* **74**, 116601 (2011).
 - [24] B. Derrida, *Phys. Rep.* **301**, 65 (1998).
 - [25] G. Klein, K. Kruse, G. Cuniberti, and F. Jülicher, *Phys. Rev. Lett.* **94**, 108102 (2005).
 - [26] M. Schmitt and H. Stark, *Europhys. Lett.* **96**, 28001 (2011).
 - [27] K. E. P. Sugden, M. R. Evans, W. C. K. Poon, and N. D. Read, *Phys. Rev. E* **75**, 31909 (2007).
 - [28] L. Reese, A. Melbinger, and E. Frey, *Biophys. J.* **101**, 2190 (2011); A. Melbinger, L. Reese, and E. Frey, *Phys. Rev. Lett.* **108**, 258104 (2012); L. Reese, A. Melbinger, and E. Frey, submitted (2014).
 - [29] S. Nowak, P.-W. Fok, and T. Chou, *Phys. Rev. E* **76**, 31135 (2007).
 - [30] J. R. Cooper, M. Wagenbach, C. L. Asbury, and L. Wordeman, *Nat. Struct. Mol. Biol.* **17**, 77 (2010).
 - [31] E. Reithmann, L. Reese, and E. Frey, to be published.
 - [32] P. O. Widlund, J. H. Stear, A. Pozniakovsky, M. Zanic, S. Reber, G. J. Brouhard, A. a. Hyman, and J. Howard, *Proc. Nat. Acad. Sci. USA* **108**, 2741 (2011).
 - [33] D. T. Gillespie, *Annu. Rev. Phys. Chem.* **58**, 35 (2007).
 - [34] This can be seen if one considers the dynamic equations for the correlators, e.g. $\frac{d}{dt}\langle n_1 n_i \rangle$. These 2-point correlators each depend on higher order correlators. The hierarchy continues until one reaches the L -point correlator, where L is the system size. As a consequence the size of the hierarchy of equations is $2^L - 1$.
 - [35] B. Derrida, M. R. Evans, V. Hakim, and V. Pasquier, *J. Phys. A: Math. Gen* **26**, 1493 (1993).
 - [36] Supporting Material can be found at ...
 - [37] T. Chou and G. Lakatos, *Phys. Rev. Lett.* **93**, 198101 (2004).
 - [38] G. Lakatos, T. Chou, and A. Kolomeisky, *Phys. Rev. E* **71**, 011103 (2005).
 - [39] A. W. Hunter, M. Caplow, D. L. Coy, W. O. Hancock, S. Diez, L. Wordeman, and J. Howard, *Mol. Cell* **11**, 445 (2003).
 - [40] D. C. Markham, M. J. Simpson, and R. E. Baker, *Phys. Rev. E* **87**, 062702 (2013); D. C. Markham, M. J. Simpson, P. K. Maini, E. A. Gaffney, and R. E. Baker, *Phys. Rev. E* **88**, 052713 (2013).

Bibliography

- [1] T. D. Pollard, „No question about exciting questions in cell biology,“ *PLoS Biol.* **11**, e1001734 (2013).
- [2] B. Alberts, A. Johnson, J. Lewis, M. Raff, K. Roberts, and P. Walter, *Molecular Biology of the Cell*, 4th ed. (Garland Science, 2002).
- [3] J. Howard and A. A. Hyman, „Microtubule polymerases and depolymerases.“ *Curr. Opin. Cell Biol.* **19**, 31–5 (2007).
- [4] R. D. Vale, T. S. Reese, and M. P. Sheetz, „Identification of a novel force-generating protein, kinesin, involved in microtubule-based motility,“ *Cell* **42**, 39–50 (1985).
- [5] T. P. Loisel, R. Boujemaa, D. Pantaloni, and M.-F. Carrier, „Reconstitution of actin-based motility of *Listeria* and *Shigella* using pure proteins,“ *Nature* **401**, 613–616 (1999).
- [6] P. Bieling, L. Laan, H. Schek, E. L. Munteanu, L. Sandblad, M. Dogterom, D. Brunner, and T. Surrey, „Reconstitution of a microtubule plus-end tracking system in vitro.“ *Nature* **450**, 1100–5 (2007).
- [7] J. R. James and R. D. Vale, „Biophysical mechanism of T-cell receptor triggering in a reconstituted system,“ *Nature* (2012), 10.1038/nature11220.
- [8] A. Mogilner, J. Allard, and R. Wollman, „Cell polarity: Quantitative modeling as a tool in cell biology,“ *Science* **336**, 175–179 (2012).
- [9] A. M. Turing, „The chemical basis of morphogenesis,“ *Phil. Trans. R. Soc. Lond. B* **237**, 37–72 (1952).
- [10] J. D. Murray, *Mathematical Biology*, Vol. 2 (Springer, 2002).
- [11] F. J. Nédélec, T. Surrey, A. C. Maggs, and S. Leibler, „Self-organization of microtubules and motors.“ *Nature* **389**, 305–8 (1997).
- [12] Surrey, Thomas and Nédélec, Francois and Leibler, Stanislas and Karsenti, Eric, „Physical Properties Determining Self-Organization of Motors and Microtubules,“ *Science* **292**, 1167–1171 (2001).
- [13] M. K. Gardner, D. C. Bouck, L. V. Paliulis, J. B. Meehl, E. T. O’Toole, J. Haase, A. Soubry, A. P. Joglekar, M. Winey, E. D. Salmon, K. Bloom, and D. J. Odde, „Chromosome Congression by Kinesin-5 Motor-Mediated Disassembly of Longer Kinetochores Microtubules,“ *Cell* **135**, 894–906 (2008).
- [14] R. Loughlin, R. Heald, and F. Nédélec, „A computational model predicts *Xenopus* meiotic spindle organization.“ *J. Cell Biol.* **191**, 1239–49 (2010).
- [15] A. Mogilner, „Mathematics of cell motility: have we got its number?“ *J.*

- Math. Biol. **58**, 105–134 (2009).
- [16] A. Mogilner, R. Wollman, and W. F. Marshall, „Quantitative modeling in cell biology: What is it good for?“ *Dev. Cell* **11**, 279 – 287 (2006).
- [17] D. G. Drubin and G. Oster, „Experimentalist meets theoretician: A tale of two scientific cultures,“ *Mol. Biol. Cell* **21**, 2099–2101 (2010).
- [18] J. Halatek and E. Frey, „Highly canalized mind transfer and mine sequestration explain the origin of robust mincde-protein dynamics,“ *Cell Rep.* **1**, 741–752 (2012).
- [19] J. Halatek and E. Frey, „Effective 2d model does not account for geometry sensing by self-organized proteins patterns,“ *Proc. Natl. Acad. Sci. USA* **111**, E1817 (2014).
- [20] J. Liu, Y. Sun, D. G. Drubin, and G. F. Oster, „The mechanochemistry of endocytosis,“ *PLoS Biol.* **7**, e1000204 (2009).
- [21] M. K. Gardner, B. D. Charlebois, I. M. Janosi, J. Howard, A. J. Hunt, and D. J. Odde, „Rapid Microtubule Self-Assembly Kinetics,“ *Cell* **146**, 582–592 (2011).
- [22] C. Leduc, K. Padberg-Gehle, V. Varga, D. Helbing, S. Diez, and J. Howard, „Molecular crowding creates traffic jams of kinesin motors on microtubules,“ *Proc. Natl. Acad. Sci. USA* **109**, 6100–6105 (2012).
- [23] L. Laan, N. Pavin, J. Husson, G. Romet-Lemonne, M. van Duijn, M. P. López, R. D. Vale, F. Jülicher, S. L. Reck-Peterson, and M. Dogterom, „Cortical dynein controls microtubule dynamics to generate pulling forces that position microtubule asters.“ *Cell* **148**, 502–14 (2012).
- [24] N. Pavin, L. Laan, R. Ma, M. Dogterom, and F. Jülicher, „Positioning of microtubule organizing centers by cortical pushing and pulling forces,“ *New J. Phys.* **14**, 105025 (2012).
- [25] T. Freisinger, B. Klünder, J. Johnson, N. Müller, G. Pichler, G. Beck, M. Costanzo, C. Boone, R. A. Cerione, E. Frey, and R. Wedlich-Söldner, „Establishment of a robust single axis of cell polarity by coupling multiple positive feedback loops,“ *Nat. Commun.* **4**, 1807 (2013).
- [26] B. Klünder, T. Freisinger, R. Wedlich-Söldner, and E. Frey, „Gdi-mediated cell polarization in yeast provides precise spatial and temporal control of cdc42 signaling,“ *PLoS Comput. Biol.* **9**, e1003396 (2013).
- [27] J. Brugués, V. Nuzzo, E. Mazur, and D. J. Needleman, „Nucleation and transport organize microtubules in metaphase spindles.“ *Cell* **149**, 554–64 (2012).
- [28] O. Campàs, T. Mammoto, S. Hasso, R. A. Sperling, D. O’Connell, A. G. Bischof, R. Maas, D. A. Weitz, L. Mahadevan, and D. E. Ingber, „Quantifying cell-generated mechanical forces within living embryonic tissues.“ *Nature Methods* **11**, 183–189 (2013).
- [29] D. A. Fletcher and R. D. Mullins, „Cell mechanics and the cytoskeleton.“ *Nature* **463**, 485–92 (2010).

- [30] F. Huber, J. Schnauß, S. Rönicke, P. Rauch, K. Müller, C. Fütterer, and J. Käs, „Emergent complexity of the cytoskeleton: from single filaments to tissue,“ *Adv. Phys.* **62**, 1–112 (2013).
- [31] N. Cartwright, *How the Laws of Physics Lie* (Oxford University Press, 1983).
- [32] S. S. Shen-Orr, R. Milo, S. Mangan, and U. Alon, „Network motifs in the transcriptional regulation network of escherichia coli,“ *Nat. Genetics* **31**, 64–68 (2002).
- [33] J. Howard and A. A. Hyman, „Dynamics and mechanics of the microtubule plus end,“ *Nature* **422**, 753–8 (2003).
- [34] R. D. Vale, „The molecular motor toolbox for intracellular transport,“ *Cell* **112**, 467–480 (2003).
- [35] D. Chrétien, F. Metoz, F. Verde, E. Karsenti, and R. Wade, „Lattice defects in microtubules: protofilament numbers vary within individual microtubules,“ *J. Cell Biol.* **117**, 1031–1040 (1992).
- [36] N. W. Ashcroft and N. D. Mermin, *Solid State Physics* (Saunders College, Philadelphia, 1976).
- [37] C. Tropini, E. A. Roth, M. Zanic, M. K. Gardner, and J. Howard, „Islands containing slowly hydrolyzable GTP analogs promote microtubule rescues.“ *PLoS ONE* **7**, e30103 (2012).
- [38] M. K. Gardner, M. Zanic, and J. Howard, „Microtubule catastrophe and rescue,“ *Curr. Opin. Cell Biol.* **25**, 14 – 22 (2013), cell architecture.
- [39] M. Bettencourt-Dias and D. M. Glover, „Centrosome biogenesis and function: centrosomics brings new understanding.“ *Nat. Rev. Mol. Cell Biol.* **8**, 451–63 (2007).
- [40] I. Vitale, L. Galluzzi, M. Castedo, and G. Kroemer, „Mitotic catastrophe: a mechanism for avoiding genomic instability.“ *Nat. Rev. Mol. Cell Biol.* **12**, 385–92 (2011).
- [41] R. Heald, R. Tournebize, A. Habermann, E. Karsenti, and A. Hyman, „Spindle assembly in xenopus egg extracts: respective roles of centrosomes and microtubule self-organization,“ *J. Cell Biol.* **138**, 615–628 (1997).
- [42] C. E. Oakley and B. R. Oakley, „Identification of gamma-tubulin, a new member of the tubulin superfamily encoded by mipA gene of *Aspergillus nidulans*.“ *Nature* **338**, 662–4 (1989).
- [43] H. Ishikawa and W. F. Marshall, „Ciliogenesis: building the cell’s antenna.“ *Nat. Rev. Mol. Cell Biol.* **12**, 222–34 (2011).
- [44] D. Adams, „The Hitchhiker’s Guide to the Galaxy,“ in *The Hitchhiker’s Guide to the Galaxy* (Pan Books, 1979).
- [45] S. Westermann and K. Weber, „Post-translational modifications regulate microtubule function.“ *Nat. Rev. Mol. Cell Biol.* **4**, 938–47 (2003).
- [46] C. Janke and J. C. Bulinski, „Post-translational regulation of the microtubule cytoskeleton: mechanisms and functions.“ *Nat. Rev. Mol. Cell Biol.*

- 12**, 773–86 (2011).
- [47] P. O. Widlund, M. Podolski, S. Reber, J. Alper, M. Storch, A. A. Hyman, J. Howard, and D. N. Drechsel, „One-step purification of assembly-competent tubulin from diverse eukaryotic sources,“ *Mol. Biol. Cell* **23**, 4393–4401 (2012).
- [48] M. Erent, D. R. Drummond, and R. A. Cross, „S. pombe kinesins-8 promote both nucleation and catastrophe of microtubules.“ *PLoS ONE* **7**, e30738 (2012).
- [49] L. Peris, M. Wagenbach, L. Lafanechère, J. Brocard, A. T. Moore, F. Kozielski, D. Job, L. Wordeman, and A. Andrieux, „Motor-dependent microtubule disassembly driven by tubulin tyrosination,“ *J. Cell Biol.* **185**, 1159–1166 (2009).
- [50] E. L. Grishchuk, M. I. Molodtsov, F. I. Ataulakhanov, and J. R. McIntosh, „Force production by disassembling microtubules.“ *Nature* **438**, 384–8 (2005).
- [51] S.-M. Kalisch, L. Laan, and M. Dogterom, „Force Generation by Dynamic Microtubules In Vitro,“ in *Microtubule Dynamics*, Methods in Molecular Biology, Vol. 777, edited by A. Straube (Humana Press, 2011) pp. 147–165.
- [52] T. Mitchison and M. Kirschner, „Dynamic instability of microtubule growth.“ *Nature* **312**, 237–42 (1984).
- [53] E. C. Garner, C. S. Campbell, and R. D. Mullins, „Dynamic instability in a dna-segregating prokaryotic actin homolog,“ *Science* **306**, 1021–1025 (2004).
- [54] D. Chrétien, S. D. Fuller, and E. Karsenti, „Structure of growing microtubule ends: two-dimensional sheets close into tubes at variable rates.“ *J. Cell Biol.* **129**, 1311–1328 (1995).
- [55] R. Padinhateeri, A. B. Kolomeisky, and D. Lacoste, „Random hydrolysis controls the dynamic instability of microtubules,“ *Biophys. J.* **102**, 1274 – 1283 (2012).
- [56] S. P. Maurer, P. Bieling, J. Cope, A. Hoenger, and T. Surrey, „GTPgammaS microtubules mimic the growing microtubule end structure recognized by end-binding proteins (EBs).“ *Proc. Natl. Acad. Sci. USA* **108**, 3988–93 (2011).
- [57] S. P. Maurer, F. J. Fourniol, G. Bohner, C. A. Moores, and T. Surrey, „EBs recognize a nucleotide-dependent structural cap at growing microtubule ends.“ *Cell* **149**, 371–82 (2012).
- [58] A. Dimitrov, M. Quesnoit, S. Moutel, I. Cantaloube, C. Poüs, and F. Perez, „Detection of GTP-Tubulin Conformation in Vivo Reveals a Role for GTP Remnants in Microtubule Rescues,“ *Science* **322**, 1353 (2008).
- [59] M. Zanic, J. H. Stear, A. A. Hyman, and J. Howard, „EB1 Recognizes the Nucleotide State of Tubulin in the Microtubule Lattice,“ *PLoS ONE* **4**, e7585 (2009).

- [60] D. E. Koshland, T. J. Mitchison, and M. W. Kirschner, „Polewards chromosome movement driven by microtubule depolymerization in vitro.“ *Nature* **331**, 499–504 (1988).
- [61] C. S. Peskin and G. F. Oster, „Force production by depolymerizing microtubules: load-velocity curves and run-pause statistics,“ *Biophys. J.* **69**, 2268–2276 (1995).
- [62] T. L. Hill, „Introductory analysis of the gtp-cap phase-change kinetics at the end of a microtubule,“ *Proc. Natl. Acad. Sci. USA* **81**, 6728–6732 (1984).
- [63] H. Flyvbjerg, T. E. Holy, and S. Leibler, „Stochastic dynamics of microtubules: A model for caps and catastrophes,“ *Phys. Rev. Lett.* **73**, 2372–2375 (1994).
- [64] H. Flyvbjerg, T. E. Holy, and S. Leibler, „Microtubule dynamics: Caps, catastrophes, and coupled hydrolysis,“ *Phys. Rev. E* **54**, 5538–5560 (1996).
- [65] T. Antal and P. Krapivsky, „Molecular spiders with memory,“ *Phys. Rev. E* **76**, 21121 (2007).
- [66] T. Antal, P. L. Krapivsky, and K. Mallick, „Molecular Spiders in One Dimension.“ *J. Stat. Mech.* **2007**, P08027 (2007).
- [67] V. Jemseena and M. Gopalakrishnan, „Microtubule catastrophe from protofilament dynamics,“ *Phys. Rev. E* **88**, 032717 (2013).
- [68] X. Li and A. B. Kolomeisky, „Theoretical analysis of microtubules dynamics using a physicalchemical description of hydrolysis,“ *J. Phys. Chem. B* **117**, 9217–9223 (2013).
- [69] I. M. János, D. Chrétien, and H. Flyvbjerg, „Modeling elastic properties of microtubule tips and walls,“ *Eur. Biophys. J.* **27**, 501–513 (1998).
- [70] V. VanBuren, L. Cassimeris, and D. J. Odde, „Mechanochemical model of microtubule structure and self-assembly kinetics,“ *Biophys. J.* **89**, 2911 – 2926 (2005).
- [71] B. T. Castle and D. J. Odde, „Brownian dynamics of subunit addition-loss kinetics and thermodynamics in linear polymer self-assembly.“ *Biophys. J.* **105**, 2528–40 (2013).
- [72] J. Howard and A. A. Hyman, „Growth, fluctuation and switching at microtubule plus ends.“ *Nat. Rev. Mol. Cell Biol.* **10**, 569–74 (2009).
- [73] S. Klumpp and R. Lipowsky, „Cooperative cargo transport by several molecular motors,“ *Proc. Natl. Acad. Sci. USA* **102**, 17284–17289 (2005).
- [74] C. Hentrich and T. Surrey, „Microtubule organization by the antagonistic mitotic motors kinesin-5 and kinesin-14,“ *J. Cell Biol.* **189**, 465–480 (2010).
- [75] P. Bieling, I. A. Telley, and T. Surrey, „A Minimal Midzone Protein Module Controls Formation and Length of Antiparallel Microtubule Overlaps,“ *Cell* **142**, 420–432 (2010).
- [76] R. Subramanian, E. M. Wilson-Kubalek, C. P. Arthur, M. J. Bick, E. A. Campbell, S. A. Darst, R. A. Milligan, and T. M. Kapoor, „Insights into

- antiparallel microtubule crosslinking by PRC1, a conserved nonmotor microtubule binding protein." *Cell* **142**, 433–43 (2010).
- [77] L. Wordeman, „Microtubule-depolymerizing kinesins." *Curr. Opin. Cell Biol.* **17**, 82–8 (2005).
- [78] C. E. Walczak, S. Gayek, and R. Ohi, „Microtubule-depolymerizing kinesins," *Annu. Rev. Cell Dev. Biol.* **29**, 417–441 (2013).
- [79] A. Desai, S. Verma, T. J. Mitchison, and C. E. Walczak, „Kin I Kinesins Are Microtubule-Destabilizing Enzymes," *Cell* **96**, 69–78 (1999).
- [80] C. A. Moores, M. Yu, J. Guo, C. Beraud, R. Sakowicz, and R. A. Milligan, „A Mechanism for Microtubule Depolymerization by KinI Kinesins," *Mol. Cell* **9**, 903–909 (2002).
- [81] C. Peters, K. Brejc, L. Belmont, A. J. Bodey, Y. Lee, M. Yu, J. Guo, R. Sakowicz, J. Hartman, and C. A. Moores, „Insight into the molecular mechanism of the multitasking kinesin-8 motor." *EMBO J.* **29**, 3437–47 (2010).
- [82] A. W. Hunter, M. Caplow, D. L. Coy, W. O. Hancock, S. Diez, L. Wordeman, and J. Howard, „The kinesin-related protein MCAK is a microtubule depolymerase that forms an ATP-hydrolyzing complex at microtubule ends." *Mol. Cell* **11**, 445–57 (2003).
- [83] J. Helenius, G. Brouhard, Y. Kalaidzidis, S. Diez, and J. Howard, „The depolymerizing kinesin MCAK uses lattice diffusion to rapidly target microtubule ends." *Nature* **441**, 115–9 (2006).
- [84] C. T. Friel and J. Howard, „The kinesin-13 MCAK has an unconventional ATPase cycle adapted for microtubule depolymerization." *EMBO J.* **30**, 3928–39 (2011).
- [85] J. R. Cooper, M. Wagenbach, C. L. Asbury, and L. Wordeman, „Catalysis of the microtubule on-rate is the major parameter regulating the depolymerase activity of MCAK." *Nat. Struct. Mol. Biol.* **17**, 77–82 (2010).
- [86] G. Klein, K. Kruse, G. Cuniberti, and F. Jülicher, „Filament Depolymerization by Motor Molecules," *Phys. Rev. Lett.* **94**, 108102 (2005).
- [87] L. E. Hough, A. Schwabe, M. A. Glaser, J. R. McIntosh, and M. D. Betterton, „Microtubule depolymerization by the kinesin-8 motor kip3p: A mathematical model," *Biophys. J.* **96**, 3050–3064 (2009).
- [88] A. Akhmanova and M. O. Steinmetz, „Tracking the ends: a dynamic protein network controls the fate of microtubule tips," *Nat. Rev. Mol. Cell Biol.* **9**, 309–322 (2008).
- [89] C. Tischer, D. Brunner, and M. Dogterom, „Force- and kinesin-8-dependent effects in the spatial regulation of fission yeast microtubule dynamics." *Mol. Syst. Biol.* **5**, 250 (2009).
- [90] G. J. Brouhard, J. H. Stear, T. L. Noetzel, J. Al-Bassam, K. Kinoshita, S. C. Harrison, J. Howard, and A. A. Hyman, „XMAP215 is a processive microtubule polymerase." *Cell* **132**, 79–88 (2008).

- [91] E. Reithmann, *Correlations at the Edge of Lattice Gases – How Tip-Tracking Proteins Influence Microtubule Dynamics*, Master’s thesis, Ludwig-Maximilians Universität München (2013).
- [92] V. Varga, J. Helenius, K. Tanaka, A. A. Hyman, T. U. Tanaka, and J. Howard, „Yeast kinesin-8 depolymerizes microtubules in a length-dependent manner.“ *Nat. Cell Biol.* **8**, 957–62 (2006).
- [93] M. L. Gupta, P. Carvalho, D. M. Roof, and D. Pellman, „Plus end-specific depolymerase activity of Kip3, a kinesin-8 protein, explains its role in positioning the yeast mitotic spindle.“ *Nat. Cell Biol.* **8**, 913–23 (2006).
- [94] V. Varga, C. Leduc, V. Bormuth, S. Diez, and J. Howard, „Kinesin-8 motors act cooperatively to mediate length-dependent microtubule depolymerization.“ *Cell* **138**, 1174–83 (2009).
- [95] M. I. Mayr, S. Hümmer, J. Bormann, T. Grüner, S. Adio, G. Woehlke, and T. U. Mayer, „The human kinesin Kif18A is a motile microtubule depolymerase essential for chromosome congression.“ *Curr. Biol.* **17**, 488–98 (2007).
- [96] J. Stumpff, G. von Dassow, M. Wagenbach, C. Asbury, and L. Wordeman, „The kinesin-8 motor Kif18A suppresses kinetochore movements to control mitotic chromosome alignment.“ *Dev. Cell* **14**, 252–62 (2008).
- [97] Y. Du, C. A. English, and R. Ohi, „The kinesin-8 Kif18A dampens microtubule plus-end dynamics.“ *Curr. Biol.* **20**, 374–80 (2010).
- [98] A. Unsworth, H. Masuda, S. Dhut, and T. Toda, „Fission yeast kinesin-8 Klp5 and Klp6 are interdependent for mitotic nuclear retention and required for proper microtubule dynamics.“ *Mol. Biol. Cell* **19**, 5104–15 (2008).
- [99] X. Su, W. Qiu, M. L. Gupta, J. B. Pereira-Leal, S. L. Reck-Peterson, and D. Pellman, „Mechanisms underlying the dual-mode regulation of microtubule dynamics by kip3/kinesin-8.“ *Mol. Cell* **43**, 751–63 (2011).
- [100] L. N. Weaver, S. C. Ems-McClung, J. R. Stout, C. Leblanc, S. L. Shaw, M. K. Gardner, and C. E. Walczak, „Kif18A Uses a Microtubule Binding Site in the Tail for Plus-End Localization and Spindle Length Regulation.“ *Curr. Biol.* **21**, 1500–6 (2011).
- [101] M. I. Mayr, M. Storch, J. Howard, and T. U. Mayer, „A non-motor microtubule binding site is essential for the high processivity and mitotic function of kinesin-8 Kif18A.“ *PLoS ONE* **6**, e27471 (2011).
- [102] A. Parmeggiani, T. Franosch, and E. Frey, „Phase Coexistence in Driven One-Dimensional Transport,“ *Phys. Rev. Lett.* **90**, 86601 (2003).
- [103] R. Subramanian, S.-C. Ti, L. Tan, S. Darst, and T. Kapoor, „Marking and Measuring Single Microtubules by PRC1 and Kinesin-4,“ *Cell* **154**, 377 – 390 (2013).
- [104] C. S. Peskin, G. M. Odell, and G. F. Oster, „Cellular motions and thermal fluctuations: the Brownian ratchet.“ *Biophys. J.* **65**, 316–24 (1993).

- [105] M. J. Footer, J. W. J. Kerssemakers, J. A. Theriot, and M. Dogterom, „Direct measurement of force generation by actin filament polymerization using an optical trap.“ *Proc. Natl. Acad. Sci. USA* **104**, 2181–6 (2007).
- [106] A. Mogilner and G. Oster, „Cell motility driven by actin polymerization.“ *Biophys. J.* **71**, 3030–45 (1996).
- [107] A. Mogilner and G. Oster, „Force generation by actin polymerization II: the elastic ratchet and tethered filaments.“ *Biophys. J.* **84**, 1591–605 (2003).
- [108] O. Campàs, L. Mahadevan, and J.-F. Joanny, „Actin network growth under load.“ *Biophys. J.* **102**, 1049–58 (2012).
- [109] M. M. A. E. Claessens, M. Bathe, E. Frey, and A. R. Bausch, „Actin-binding proteins sensitively mediate F-actin bundle stiffness.“ *Nat. Materials* **5**, 748–53 (2006).
- [110] K. M. Schmoller, O. Lieleg, and A. R. Bausch, „Structural and viscoelastic properties of actin/filamin networks: cross-linked versus bundled networks.“ *Biophys. J.* **97**, 83–9 (2009).
- [111] R. D. Mullins and S. D. Hansen, „In vitro studies of actin filament and network dynamics.“ *Curr. Opin. Cell Biol.* **25**, 6–13 (2013).
- [112] J. Stigler, F. Ziegler, A. Gieseke, J. C. M. Gebhardt, and M. Rief, „The complex folding network of single calmodulin molecules.“ *Science* **334**, 512–6 (2011).
- [113] M. Grandbois, M. Beyer, M. Rief, H. Clausen-Schaumann, and H. E. Gaub, „How Strong Is a Covalent Bond?“ *Science* **283**, 1727–1730 (1999).
- [114] L. Rognoni, J. Stigler, B. Pelz, J. Ylänne, and M. Rief, „Dynamic force sensing of filamin revealed in single-molecule experiments.“ *Proc. Natl. Acad. Sci. USA* **109**, 19679–84 (2012).
- [115] D. Dulin, J. Lipfert, M. C. Moolman, and N. H. Dekker, „Studying genomic processes at the single-molecule level: introducing the tools and applications.“ *Nat. Rev. Genetics* **14**, 9–22 (2013).
- [116] K. C. Neuman and A. Nagy, „Single-molecule force spectroscopy: optical tweezers, magnetic tweezers and atomic force microscopy.“ *Nat. Methods* **5**, 491–505 (2008).
- [117] E. Evans and K. Ritchie, „Dynamic strength of molecular adhesion bonds,“ *Biophys. J.* **72**, 1541 – 1555 (1997).
- [118] G. Hummer and A. Szabo, „Free energy reconstruction from nonequilibrium single-molecule pulling experiments,“ *Proc. Natl. Acad. Sci. USA* **98**, 3658–3661 (2001).
- [119] S. Inoué, „Video image processing greatly enhances contrast, quality, and speed in polarization-based microscopy.“ *J. Cell Biol.* **89**, 346–356 (1981).
- [120] R. D. Allen, N. S. Allen, and J. L. Travis, „Video-enhanced contrast, differential interference contrast (avec-dic) microscopy: A new method capable of analyzing microtubule-related motility in the reticulopodial network of *allogromia laticollaris*,“ *Cell Motility* **1**, 291–302 (1981).

- [121] C. Grashoff, B. D. Hoffman, M. D. Brenner, R. Zhou, M. Parsons, M. T. Yang, M. A. McLean, S. G. Sligar, C. S. Chen, T. Ha, and M. A. Schwartz, „Measuring mechanical tension across vinculin reveals regulation of focal adhesion dynamics.“ *Nature* **466**, 263–6 (2010).
- [122] A. G. York, P. Chandris, D. D. Nogare, J. Head, P. Wawrzusin, R. S. Fischer, A. Chitnis, and H. Shroff, „Instant super-resolution imaging in live cells and embryos via analog image processing.“ *Nat. Methods* **10**, 1122–6 (2013).
- [123] A. Chmyrov, J. Keller, T. Grotjohann, M. Ratz, E. D’Este, S. Jakobs, C. Eggeling, and S. W. Hell, „Nanoscopy with more than 100,000 ‘doughnuts’.“ *Nat. Methods* **10**, 737–40 (2013).
- [124] Y. Wu, P. Wawrzusin, J. Senseney, R. S. Fischer, R. Christensen, A. Santella, A. G. York, P. W. Winter, C. M. Waterman, Z. Bao, D. A. Colón-Ramos, M. McAuliffe, and H. Shroff, „Spatially isotropic four-dimensional imaging with dual-view plane illumination microscopy.“ *Nat. Biotech.* **31**, 1032–8 (2013).
- [125] A. D. McNaught and A. Wilkinson, *IUPAC. Compendium of Chemical Terminology*, 2nd (the ”Gold Book”) ed. (Blackwell Scientific Publications, Oxford, 1997).
- [126] A. Fallah-Araghi, K. Meguellati, J.-C. Baret, A. E. Harrak, T. Mangeat, M. Karplus, S. Ladame, C. M. Marques, and A. D. Griffiths, „Enhanced chemical synthesis at soft interfaces: A universal reaction-adsorption mechanism in microcompartments,“ *Phys. Rev. Lett.* **112**, 028301 (2014).
- [127] R. Grima and S. Schnell, „Modelling reaction kinetics inside cells,“ *Essays Biochem.* **45**, 41–56 (2008).
- [128] R. Ramaswamy, N. González-Segredo, I. F. Sbalzarini, and R. Grima, „Discreteness-induced concentration inversion in mesoscopic chemical systems.“ *Nat. Commun.* **3**, 779 (2012).
- [129] T. Chou and M. R. D’Orsogna, „Coarsening and accelerated equilibration in mass-conserving heterogeneous nucleation,“ *Phys. Rev. E* **84**, 011608 (2011).
- [130] M. R. D’Orsogna, G. Lakatos, and T. Chou, „Stochastic self-assembly of incommensurate clusters,“ *J. Chem. Phys.* **136**, 084110 (2012).
- [131] R. Yvinec, M. R. D’Orsogna, and T. Chou, „First passage times in homogeneous nucleation and self-assembly,“ *J. Chem. Phys.* **137**, 244107 (2012).
- [132] M. R. D’Orsogna, B. Zhao, B. Berenji, and T. Chou, „Combinatoric analysis of heterogeneous stochastic self-assembly,“ *J. Chem. Phys.* **139**, 121918 (2013).
- [133] D. A. Adams, B. Schmittmann, and R. K. P. Zia, „Far-from-equilibrium transport with constrained resources,“ *J. Stat. Mech.* **2008**, P06009 (2008).
- [134] L. J. Cook, R. K. P. Zia, and B. Schmittmann, „Competition between multiple totally asymmetric simple exclusion processes for a finite pool of

- resources," *Phys. Rev. E* **80**, 031142 (2009).
- [135] L. J. Cook and R. K. P. Zia, „Competition for finite resources," *J. Stat. Mech.* **2012**, P05008 (2012).
- [136] L. J. Cook, J. J. Dong, and A. LaFleur, „Interplay between finite resources and a local defect in an asymmetric simple exclusion process," *Phys. Rev. E* **88**, 042127 (2013).
- [137] C. Brackley, M. Romano, C. Grebogi, and M. Thiel, „Limited Resources in a Driven Diffusion Process," *Phys. Rev. Lett.* **105**, 78102 (2010).
- [138] C. A. Brackley, M. C. Romano, and M. Thiel, „Slow sites in an exclusion process with limited resources," *Phys. Rev. E* **82**, 051920 (2010).
- [139] P. Greulich, L. Ciandrini, R. J. Allen, and M. C. Romano, „Mixed population of competing totally asymmetric simple exclusion processes with a shared reservoir of particles," *Phys. Rev. E* **85**, 011142 (2012).
- [140] R. Lipowsky, S. Klumpp, and T. Nieuwenhuizen, „Random Walks of Cytoskeletal Motors in Open and Closed Compartments," *Phys. Rev. Lett.* **87**, 108101 (2001).
- [141] S. Klumpp and R. Lipowsky, „Traffic of molecular motors through tube-like compartments," *J. Stat. Phys.* **113**, 233–268 (2003).
- [142] Y.-H. M. Chan and W. F. Marshall, „How Cells Know the Size of Their Organelles," *Science* **337**, 1186–1189 (2012).
- [143] N. W. Goehring and A. A. Hyman, „Organelle Growth Control through Limiting Pools of Cytoplasmic Components," *Curr. Biol.* **22**, R330–R339 (2012).
- [144] S. Dumont and T. J. Mitchison, „Force and Length in the Mitotic Spindle," *Curr. Biol.* **19**, R749–R761 (2009).
- [145] G. Goshima and J. M. Scholey, „Control of mitotic spindle length." *Ann. Rev. Cell Dev. Biol.* **26**, 21–57 (2010).
- [146] M. Wuehr, Y. Chen, S. Dumont, A. C. Groen, D. J. Needleman, A. Salic, and T. J. Mitchison, „Evidence for an upper limit to mitotic spindle length," *Curr. Biol.* **18**, 1256–1261 (2008).
- [147] G. Greenan, C. P. Brangwynne, S. Jaensch, J. Gharakhani, F. Jülicher, and A. A. Hyman, „Centrosome Size Sets Mitotic Spindle Length in *Caenorhabditis elegans* Embryos," *Curr. Biol.* **20**, 353–358 (2010).
- [148] G. Goshima, R. Wollman, N. Stuurman, J. M. Scholey, and R. D. Vale, „Length control of the metaphase spindle." *Curr. Biol.* **15**, 1979–88 (2005).
- [149] S. B. Domnitz, M. Wagenbach, J. Decarreau, and L. Wordeman, „MCAK activity at microtubule tips regulates spindle microtubule length to promote robust kinetochore attachment." *J. Cell Biol.* **197**, 231–7 (2012).
- [150] R. Loughlin, J. D. Wilbur, F. J. McNally, F. J. Nédélec, and R. Heald, „Katanin contributes to interspecies spindle length scaling in *Xenopus*." *Cell* **147**, 1397–407 (2011).
- [151] S. B. Reber, J. Baumgart, P. O. Widlund, A. Pozniakovsky, J. Howard,

- A. A. Hyman, and F. Jülicher, „Xmap215 activity sets spindle length by controlling the total mass of spindle microtubules,“ *Nat. Cell Biol.* **15**, 1116–1122 (2013).
- [152] M. C. Good, M. D. Vahey, A. Skandarajah, D. A. Fletcher, and R. Heald, „Cytoplasmic Volume Modulates Spindle Size During Embryogenesis,“ *Science* **342**, 856–860 (2013).
- [153] A. L. Hodgkin and R. D. Keynes, „The potassium permeability of a giant nerve fibre,“ *The Journal of Physiology* **128**, 61–88 (1955).
- [154] S. Alexander and P. Pincus, „Diffusion of labeled particles on one-dimensional chains,“ *Phys. Rev. B* **18**, 2011–2012 (1978).
- [155] R. K. Pathria, *Statistical Mechanics*, 2nd ed. (Butterworth Heineman, Oxford, UK, 1996).
- [156] F. Höfling and T. Franosch, „Anomalous transport in the crowded world of biological cells.“ *Rep. Prog. Phys.* **76**, 046602 (2013).
- [157] C. MacDonald, J. Gibbs, and A. Pipkin, „Kinetics of biopolymerization on nucleic acid templates,“ *Biopolymers* **6**, 1 (1968).
- [158] J. Krug, „Boundary-induced phase transitions in driven diffusive systems,“ *Phys. Rev. Lett.* **67**, 1882–1885 (1991).
- [159] P. L. Krapivsky, S. Redner, and E. Ben-Naim, *A kinetic view of statistical physics* (Cambridge University Press, 2010).
- [160] A. B. Kolomeisky, G. M. Schütz, E. B. Kolomeisky, and J. P. Straley, „Phase diagram of one-dimensional driven lattice gases with open boundaries,“ *J. Phys. A: Math. Gen.* **31**, 6911 (1998).
- [161] B. Derrida, E. Domany, and D. Mukamel, „An exact solution of a one-dimensional asymmetric exclusion model with open boundaries,“ *J. Stat. Phys.* **69**, 667–687 (1992).
- [162] G. Schütz and E. Domany, „Phase transitions in an exactly soluble one-dimensional exclusion process,“ *J. Stat. Phys.* **72**, 277–296 (1993).
- [163] B. Derrida, M. R. Evans, V. Hakim, and V. Pasquier, „Exact solution of a 1d asymmetric exclusion model using a matrix formulation,“ *J. Phys. A: Math. Gen.* **26**, 1493 (1993).
- [164] L. B. Shaw, R. K. P. Zia, and K. H. Lee, „Totally asymmetric exclusion process with extended objects: A model for protein synthesis,“ *Phys. Rev. E* **68**, 021910 (2003).
- [165] T. Chou and G. Lakatos, „Clustered bottlenecks in mrna translation and protein synthesis,“ *Phys. Rev. Lett.* **93**, 198101 (2004).
- [166] G. Lakatos, T. Chou, and A. Kolomeisky, „Steady-state properties of a totally asymmetric exclusion process with periodic structure,“ *Phys. Rev. E* **71**, 011103 (2005).
- [167] P. C. Bressloff and J. M. Newby, „Stochastic models of intracellular transport,“ *Rev. Mod. Phys.* **85**, 135–196 (2013).
- [168] B. Schmittmann and R. K. P. Zia, „Statistical mechanics of driven diffusive

- systems," in *Phase Transitions and Critical Phenomena*, Vol. 17, edited by C. Domb and J. Lebowitz (Academic Press, London, 1995).
- [169] B. Derrida, „An exactly soluble non-equilibrium system: The asymmetric simple exclusion process," *Phys. Rep.* **301**, 65–83 (1998).
- [170] G. Schütz, „Exactly solvable models for many-body systems far from equilibrium," in *Phase Transitions and Critical Phenomena*, Vol. 19, edited by C. Domb and J. Lebowitz (Academic Press, London, 2001) pp. 1–251.
- [171] R. A. Blythe and M. R. Evans, „Nonequilibrium steady states of matrix-product form: a solver's guide," *J. Phys. A: Math. Theor.* **40**, R333 (2007).
- [172] T. Chou, K. Mallick, and R. K. P. Zia, „Non-equilibrium statistical mechanics: from a paradigmatic model to biological transport," *Rep. Prog. Phys.* **74**, 116601 (2011).
- [173] R. K. Zia, J. Dong, and B. Schmittmann, „Modeling translation in protein synthesis with tasep: a tutorial and recent developments," *J. Stat. Phys.* **144**, 405–428 (2011).
- [174] M. Gorissen, A. Lazarescu, K. Mallick, and C. Vanderzande, „Exact current statistics of the asymmetric simple exclusion process with open boundaries," *Phys. Rev. Lett.* **109**, 170601 (2012).
- [175] K. Nishinari, Y. Okada, A. Schadschneider, and D. Chowdhury, „Intracellular transport of single-headed molecular motors kif1a," *Phys. Rev. Lett.* **95**, 118101 (2005).
- [176] T. Reichenbach, T. Franosch, and E. Frey, „Exclusion Processes with Internal States," *Phys. Rev. Lett.* **97**, 50603 (2006).
- [177] P. Greulich, A. Garai, K. Nishinari, A. Schadschneider, and D. Chowdhury, „Intracellular transport by single-headed kinesin kif1a: Effects of single-motor mechanochemistry and steric interactions," *Phys. Rev. E* **75**, 041905 (2007).
- [178] T. Reichenbach, E. Frey, and T. Franosch, „Traffic jams induced by rare switching events in two-lane transport," *New J. Phys.* **9**, 159 (2007).
- [179] S. Klumpp, Y. Chai, and R. Lipowsky, „Effects of the chemomechanical stepping cycle on the traffic of molecular motors," *Phys. Rev. E* **78**, 041909 (2008).
- [180] L. Ciandrini, I. Stansfield, and M. C. Romano, „Role of the particles stepping cycle in an asymmetric exclusion process: A model of mrna translation," *Phys. Rev. E* **81**, 051904 (2010).
- [181] A. Melbinger, T. Reichenbach, T. Franosch, and E. Frey, „Driven transport on parallel lanes with particle exclusion and obstruction," *Phys. Rev. E* **83**, 031923 (2011).
- [182] L. Ciandrini, M. C. Romano, and A. Parmeggiani, „Stepping and crowding: statistical kinetics from an exclusion process perspective," arXiv preprint arXiv:1312.1911 (2013).
- [183] I. Pinkoviezky and N. S. Gov, „Modelling interacting molecular motors

- with an internal degree of freedom,“ *New J. Phys.* **15**, 025009 (2013).
- [184] D. Oriola and J. Casademunt, „Cooperative force generation of kif1a brownian motors,“ *Phys. Rev. Lett.* **111**, 048103 (2013).
- [185] D. Oriola and J. Casademunt, „Cooperative action of kif1a brownian motors with finite dwell time,“ *Phys. Rev. E* **89**, 032722 (2014).
- [186] P. Ashwin, C. Lin, and G. Steinberg, „Queueing induced by bidirectional motor motion near the end of a microtubule,“ *Phys. Rev. E* **82**, 051907 (2010).
- [187] M. Schuster, S. Kilaru, P. Ashwin, C. Lin, N. J. Severs, and G. Steinberg, „Controlled and stochastic retention concentrates dynein at microtubule ends to keep endosomes on track,“ *EMBO J.* **30**, 652–664 (2011).
- [188] C. Lin, G. Steinberg, and P. Ashwin, „Bidirectional transport and pulsing states in a multi-lane asep model,“ *J. Stat. Mech.* **2011**, P09027 (2011).
- [189] B. Embley, A. Parmeggiani, and N. Kern, „Understanding totally asymmetric simple-exclusion-process transport on networks: Generic analysis via effective rates and explicit vertices,“ *Phys. Rev. E* **80**, 041128 (2009).
- [190] P. Greulich and L. Santen, „Active transport and cluster formation on 2D networks.“ *Eur. Phys. J. E* **32**, 191–208 (2010).
- [191] I. Neri, N. Kern, and A. Parmeggiani, „Totally Asymmetric Simple Exclusion Process on Networks,“ *Phys. Rev. Lett* **107**, 068702 (2011).
- [192] I. Neri, N. Kern, and A. Parmeggiani, „Exclusion processes on networks as models for cytoskeletal transport,“ *New Journal of Physics* **15**, 085005 (2013).
- [193] I. Neri, N. Kern, and A. Parmeggiani, „Modeling cytoskeletal traffic: An interplay between passive diffusion and active transport,“ *Phys. Rev. Lett.* **110**, 098102 (2013).
- [194] L. J. Cook and R. K. P. Zia, „Feedback and fluctuations in a totally asymmetric simple exclusion process with finite resources,“ *J. Stat. Mech.* **2009**, P02012 (2009).
- [195] C. A. Brackley, L. Ciandrini, and M. Carmen Romano, „Multiple phase transitions in a system of exclusion processes with limited reservoirs of particles and fuel carriers,“ *J. Stat. Mech.* **2012**, P03002 (2012).
- [196] T. Galla, „Fluctuations in meta-population exclusion processes,“ *J. Stat. Mech.* **2012**, P03008 (2012).
- [197] C. Arita, J. Bouttier, P. L. Krapivsky, and K. Mallick, „Asymmetric exclusion process with global hopping,“ *Phys. Rev. E* **88**, 042120 (2013).
- [198] A. Parmeggiani, T. Franosch, and E. Frey, „Totally asymmetric simple exclusion process with Langmuir kinetics,“ *Phys. Rev. E* **70**, 46101 (2004).
- [199] A. Gabel, P. L. Krapivsky, and S. Redner, „Facilitated asymmetric exclusion,“ *Phys. Rev. Lett.* **105**, 210603 (2010).
- [200] J. Dong, S. Klumpp, and R. K. P. Zia, „Entrainment and unit velocity: Surprises in an accelerated exclusion process,“ *Phys. Rev. Lett.* **109**, 130602

- (2012).
- [201] J. Dong, S. Klumpp, and R. K. P. Zia, „Mass transport perspective on an accelerated exclusion process: Analysis of augmented current and unit-velocity phases,“ *Phys. Rev. E* **87**, 022146 (2013).
 - [202] K. E. P. Sugden and M. R. Evans, „A dynamically extending exclusion process,“ *J. Stat. Mech.* **2007**, P11013–P11013 (2007).
 - [203] K. E. P. Sugden, M. R. Evans, W. C. K. Poon, and N. D. Read, „Model of hyphal tip growth involving microtubule-based transport,“ *Phys. Rev. E* **75**, 31909 (2007).
 - [204] S. Muhuri, „Scale-invariant density profiles of a dynamically extending tasep,“ *Europhys. Lett.* **101**, 38001 (2013).
 - [205] L. Reese, A. Melbinger, and E. Frey, „Crowding of molecular motors determines microtubule depolymerization. “ *Biophys. J.* **101**, 2190–200 (2011).
 - [206] M. Schmitt and H. Stark, „Modelling bacterial flagellar growth,“ *Europhys. Lett.* **96**, 28001 (2011).
 - [207] P. I. Zhuravlev, Y. Lan, M. S. Minakova, and G. A. Papoian, „Theory of active transport in filopodia and stereocilia,“ *Proc. Natl. Acad. Sci. USA* **109**, 10849–10854 (2012).
 - [208] S. Nowak, P.-W. Fok, and T. Chou, „Dynamic boundaries in asymmetric exclusion processes,“ *Phys. Rev. E* **76**, 31135 (2007).
 - [209] A. Melbinger, L. Reese, and E. Frey, „Microtubule length regulation by molecular motors,“ *Phys. Rev. Lett.* **108**, 258104 (2012).
 - [210] D. Johann, C. Erlenkämper, and K. Kruse, „Length regulation of active biopolymers by molecular motors,“ *Phys. Rev. Lett.* **108**, 258103 (2012).
 - [211] C. Erlenkämper, D. Johann, and K. Kruse, „Impact of motor molecules on the dynamics of treadmilling filaments,“ *Phys. Rev. E* **86**, 051906 (2012).
 - [212] H.-S. Kuan and M. D. Betterton, „Biophysics of filament length regulation by molecular motors,“ *Phys. Biol.* **10**, 036004 (2013).
 - [213] S. Dorosz, S. Mukherjee, and T. Platini, „Dynamical phase transition of a one-dimensional transport process including death,“ *Phys. Rev. E* **81**, 042101 (2010).
 - [214] V. Popkov and G. M. Schütz, „Steady-state selection in driven diffusive systems with open boundaries,“ *Europhys. Lett.* **48**, 257–263 (1999).
 - [215] V. Popkov, L. Santen, A. Schadschneider, and G. M. Schütz, „Empirical evidence for a boundary-induced nonequilibrium phase transition,“ *J. Phys. A: Math. Gen.* **34**, L45–L52 (2001).
 - [216] J. S. Hager, J. Krug, V. Popkov, and G. M. Schütz, „Minimal current phase and universal boundary layers in driven diffusive systems. “ *Phys. Rev. E* **63**, 056110 (2001).
 - [217] M. Rank, L. Reese, and E. Frey, „Finite resources induce bistability in microtubule length regulation by kinesin-8 motors,“ preprint (2013).
 - [218] S. Niwa, K. Nakajima, H. Miki, Y. Minato, D. Wang, and N. Hirokawa,

- „Kif19a is a microtubule-depolymerizing kinesin for ciliary length control,“ *Dev. Cell* **23**, 1167–1175 (2012).
- [219] I. M. Cheeseman and A. Desai, „Molecular architecture of the kinetochore-microtubule interface.“ *Nat. Rev. Mol. Cell Biol.* **9**, 33–46 (2008).
- [220] C. Erlenkämper and K. Kruse, „Uncorrelated changes of subunit stability can generate length-dependent disassembly of treadmilling filaments.“ *Phys. Biol.* **6**, 046016 (2009).
- [221] B. S. Govindan, M. Gopalakrishnan, and D. Chowdhury, „Length control of microtubules by depolymerizing motor proteins,“ *Europhys. Lett.* **83**, 40006 (2008).
- [222] C. Arita, „Queueing process with excluded-volume effect,“ *Phys. Rev. E* **80**, 051119 (2009).
- [223] C. Arita and A. Schadschneider, „Density profiles of the exclusive queueing process,“ *J. Stat. Mech.* **2012**, P12004 (2012).
- [224] R. Barlovic, L. Santen, A. Schadschneider, and M. Schreckenberg, „Metastable states in cellular automata for traffic flow,“ *Eur. Phys. J. B* **5**, 793–800 (1998).
- [225] M. Evans, D. Foster, C. Godrèche, and D. Mukamel, „Spontaneous Symmetry Breaking in a One Dimensional Driven Diffusive System,“ *Phys. Rev. Lett.* **74**, 208–211 (1995).
- [226] A. Jelić, C. Appert-Rolland, and L. Santen, „A bottleneck model for bidirectional transport controlled by fluctuations,“ *EPL (Europhys. Lett.)* **98**, 40009 (2012).
- [227] F. Turci, A. Parmeggiani, E. Pitard, M. C. Romano, and L. Ciandrini, „Transport on a lattice with dynamical defects,“ *Phys. Rev. E* **87**, 012705 (2013).
- [228] L. Reese, A. Melbinger, and E. Frey, „Traffic Dynamic Instability,“ *ArXiv e-prints* (2015), arXiv:1505.01219 [cond-mat.stat-mech] .
- [229] P. R. ten Wolde and D. Frenkel, „Enhancement of protein crystal nucleation by critical density fluctuations,“ *Science* **277**, 1975–1978 (1997).
- [230] M. Matsumoto, S. Saito, and I. Ohmine, „Molecular dynamics simulation of the ice nucleation and growth process leading to water freezing.“ *Nature* **416**, 409–13 (2002).
- [231] I. Kalcher and J. Dzubiella, „NaCl crystallization in apolar nanometer-sized confinement studied by atomistic simulations,“ *Phys. Rev. E* **88**, 062312 (2013).
- [232] F. Oosawa and M. Kasai, „A theory of linear and helical aggregations of macromolecules.“ *J. Mol. Biol.* **4**, 10–21 (1962).
- [233] M. D. Welch and R. D. Mullins, „Cellular control of actin nucleation,“ *Annu. Rev. Cell Dev. Biol.* **18**, 247–288 (2002).
- [234] D. Sept and J. A. McCammon, „Thermodynamics and kinetics of actin filament nucleation.“ *Biophys. J.* **81**, 667–74 (2001).

- [235] R. D. Mullins, J. A. Heuser, and T. D. Pollard, „The interaction of Arp2/3 complex with actin: nucleation, high affinity pointed end capping, and formation of branching networks of filaments,“ *Proc. Natl. Acad. Sci. USA* **95**, 6181–6186 (1998).
- [236] L. Limozin, M. Bärmann, and E. Sackmann, „On the organization of self-assembled actin networks in giant vesicles,“ *Eur. Phys. J. E* **10**, 319–330 (2003).
- [237] J. Hazel, K. Krutkramelis, P. Mooney, M. Tomschik, K. Gerow, J. Oakey, and J. C. Gatlin, „Changes in cytoplasmic volume are sufficient to drive spindle scaling,“ *Science* **342**, 853–856 (2013).
- [238] D. T. Gillespie, „A diffusional bimolecular propensity function,“ *J. Chem. Phys.* **131**, 164109 (2009).
- [239] D. T. Gillespie, „A general method for numerically simulating the stochastic time evolution of coupled chemical reactions,“ *J. Comp. Phys.* **22**, 403–434 (1976).
- [240] J. Hu, A. Matzavinos, and H. Othmer, „A theoretical approach to actin filament dynamics,“ *J. Stat. Phys.* **128**, 111–138 (2007).
- [241] T. A. Burke, J. R. Christensen, E. Barone, C. Suarez, V. Sirotkin, and D. R. Kovar, „Homeostatic actin cytoskeleton networks are regulated by assembly factor competition for monomers.“ *Current biology : CB* **24**, 579–85 (2014).
- [242] G. Polya, „Über eine Aufgabe der Wahrscheinlichkeitsrechnung betreffend die Irrfahrt im Straßennetz,“ *Mathematische Annalen* **84**, 149–160 (1921).
- [243] L. Cassimeris, D. Safer, V. T. Nachmias, and S. H. Zigmond, „Thymosin beta 4 sequesters the majority of G-actin in resting human polymorphonuclear leukocytes.“ *J. Cell Biol.* **119**, 1261–1270 (1992).
- [244] D. Vavylonis, Q. Yang, and B. O’Shaughnessy, „Actin polymerization kinetics, cap structure, and fluctuations,“ *Proc. Natl. Acad. Sci. USA* **102**, 8543–8548 (2005).
- [245] C. P. Brangwynne, „Phase transitions and size scaling of membrane-less organelles,“ *J. Cell Biol.* **203**, 875–881 (2013).
- [246] X. Li, R. Lipowsky, and J. Kierfeld, „Critical Motor Number for Fractional Steps of Cytoskeletal Filaments in Gliding Assays,“ *PLoS ONE* **7**, e43219 (2012).
- [247] C. L. Hansen, E. Skordalakes, J. M. Berger, and S. R. Quake, „A robust and scalable microfluidic metering method that allows protein crystal growth by free interface diffusion,“ *Proc. Natl. Acad. Sci. USA* **99**, 16531–16536 (2002).
- [248] B. Zheng, L. S. Roach, and R. F. Ismagilov, „Screening of protein crystallization conditions on a microfluidic chip using nanoliter-size droplets,“ *J. Am. Chem. Soc.* **125**, 11170–11171 (2003).
- [249] Y. Zhu, L.-N. Zhu, R. Guo, H.-J. Cui, S. Ye, and Q. Fang, „Nanoliter-Scale

- Protein Crystallization and Screening with a Microfluidic Droplet Robot,“ *Scientific Reports* **4** (2014), 10.1038/srep05046.
- [250] G. Alushin and E. Nogales, „Visualizing kinetochore architecture,“ *Curr. Opin. Struct. Biol.* **21**, 661 – 669 (2011).
- [251] C. E. Coombes, A. Yamamoto, M. R. Kenzie, D. J. Odde, and M. K. Gardner, „Evolving tip structures can explain age-dependent microtubule catastrophe.“ *Curr. Biol.* **23**, 1342–8 (2013).
- [252] A. Buchner, F. Tostevin, and U. Gerland, „Clustering and optimal arrangement of enzymes in reaction-diffusion systems,“ *Phys. Rev. Lett.* **110**, 208104 (2013).
- [253] A. Buchner, F. Tostevin, F. Hinzpeter, and U. Gerland, „Optimization of collective enzyme activity via spatial localization,“ *J. Chem. Phys.* **139**, 135101 (2013).
- [254] A. Buchner, *Spatial aspects of enzymology – Optimal arrangement and conformational dynamics*, Ph.D. thesis, Ludwig-Maximilians Universität München (2013).
- [255] L. D. Landau and E. M. Lifschitz, *Elastizitätstheorie* (Akademie Verlag, Berlin, 1991).
- [256] J. Wilhelm and E. Frey, „Radial Distribution Function of Semiflexible Polymers,“ *Phys. Rev. Lett.* **77**, 2581–2584 (1996).
- [257] M. Bathe, C. Heussinger, M. M. A. E. Claessens, A. R. Bausch, and E. Frey, „Cytoskeletal bundle mechanics.“ *Biophys. J.* **94**, 2955–64 (2008).
- [258] H. Mohrbach, A. Johner, and I. M. Kulić, „Tubulin bistability and polymorphic dynamics of microtubules,“ *Phys. Rev. Lett.* **105**, 268102 (2010).
- [259] F. Gittes, B. Mickey, J. Nettleton, and J. Howard, „Flexural rigidity of microtubules and actin filaments measured from thermal fluctuations in shape.“ *J. Cell Biol.* **120**, 923–934 (1993).
- [260] F. Pampaloni, G. Lattanzi, A. Jonás, T. Surrey, E. Frey, and E.-L. Florin, „Thermal fluctuations of grafted microtubules provide evidence of a length-dependent persistence length.“ *Proc. Natl. Acad. Sci. USA* **103**, 10248–53 (2006).
- [261] D. Portran, M. Zoccoler, J. Gaillard, V. Stoppin-Mellet, E. Neumann, I. Arnal, J. L. Martiel, and M. Vantard, „MAP65/Ase1 promote microtubule flexibility,“ *Mol. Biol. Cell* **24**, 1964–1973 (2013).
- [262] M. Rank, *Statistical Mechanics of History-dependent Random Walks*, Master’s thesis, Ludwig-Maximilians Universität München (2011).
- [263] M. Rank, L. Reese, and E. Frey, „Cooperative effects enhance the transport properties of molecular spider teams,“ *Phys. Rev. E* **87**, 032706 (2013).
- [264] E. Reithmann, L. Reese, and E. Frey, „Quantifying Protein Diffusion and Capture on Filaments,“ *Biophys. J.* **108**, 787–790 (2015).
- [265] E. Reithmann, L. Reese, and E. Frey, „Spatial Correlation in Protein Diffusion and Capture on Filaments,“ to be published .